Large-Scale Hemodynamic Analysis of Cerebral Arterial Tree with Parametric Mesh Generation Technique

BY

MAHSA GHAFFARI
M.S. Amirkabir University of Technology, 2012
B.S., Azad University, Science and research branch, 2010

THESIS

Submitted as partial fulfillment of the requirements for
the degree of Doctor of Philosophy in Bioengineering
in the Graduate College of the
University of Illinois at Chicago, 2018

Chicago, IL

Defense Committee:

Prof. Andreas Linninger, Chair and Advisor
Prof. Fady T. Charbel, Neurosurgery, University of Illinois College of Medicine
Prof. Xiaohong Joe Zhou, Center for Magnetic Resonance Research
Dr. Salman Khetani, Bioengineering
Dr. Meenesh R Singh, Chemical Engineering

DEDICATED

to

My father, Mostafa

For supporting and encouraging me to believe in myself and teaching me that “giving up” can never be an option in my life.

My mother, Mahnaz

Who offered me unconditional love and support and have always been there for me. She has always given me the strength to stand firm on my own and chase my dreams.

My husband, Saeed

His unwavering love, his remarkable patience, and support during the challenges of graduate life. I am truly thankful for having you in my life.

My brothers, Mehrad & Amin

Who support me, uplift me, comfort me and bring joy to my soul. I am so thankful for your kindness.

ACKNOWLEDGMENTS

I am forever indebted to my PhD advisor, Professor Andreas Linninger, for his unwavering support, and patience throughout my research. I can never pay you back for all the help you have provided me, the experience you have helped me gain by working for you at LPPD and the precious time you spent training me. I greatly appreciate your mentorship, without you this dissertation would not have been possible.

I am also deeply indebted to Dr. Ali Alaraj for his knowledge, support, and advice throughout my PhD research. I am grateful to Dr. Charbel for his excellent advice and help with my project and Dr. Zhou for his guidance on the image processing. I would like to thank Dr. Singh and Dr. Khetani for their valuable ideas and suggestions during my preliminary examination.

I want to extend my gratitude to all my lab colleagues: Chih-Yang, Kevin, Indu, Ian, Grant, Chang-Sub, Narsi, Abhay, Nazia, Homay, Ben, Claudia, Celine, Ryan, Lea, Guren, Hita, and Nicolas. They have all provided valuable suggestions about my work and motivated me whenever necessary. It would have been impossible to complete the MRI imaging and resolving technical problems of this dissertation without Chih-Yang's knowledge and support. I will always be thankful to him. I would like to acknowledge the significant support that Kevin provided through my project. I have also had many excellent technical discussions with Ian, Narsi, Indu, Guren and Grant which greatly aided me to complete my research.

No part of this thesis would have been possible without the support of my parents, and my husband and my brothers. Their courage, strength, and energy are the greatest sources of my inspiration.

Last, but in no way least, I will forever be grateful to GOD for everything in my life.

CONTRIBUTION OF AUTHORS

Chapter 1 is an introduction summarizing the clinical importance of my dissertation. Chapter 2 is previously published paper discussing the generation of parametric meshes (M. Ghaffari, K. Tangen, A. Alaraj, X. Du, F. Charbel, A. Linninger. "Large-scale subject-specific cerebral arterial tree modeling using automated parametric mesh generation for blood flow simulation" Computers in Biology and Medicine, 2017) as well as (M. Ghaffari, C. Hsu, A. Linninger. "Automatic reconstruction and generation of structured hexahedral mesh for non-planar bifurcations in vascular network." Computer Aided Chemical Engineering, 2015) for which I was the primary author and major driver of the research. In these paper, Mr. Tangen helped in mesh quality assessment. Dr. Hsu. assisted in image processing and filtration of medical images. Dr. Alaraj shared his patient data for vascular modeling. Dr. Alaraj and Dr. Charbel contributed their knowledge in cerebral arterial tree anatomy. Dr. Du assisted in image acquisition of the blood vessel. Dr. Linninger assisted in the paper writing and provided direction to the overall research. Chapter 3 is an under-revision paper about spatial validation of parametric mesh generation method (M. Ghaffari, L. Sanchez, G. Xu, A. Alaraj, X. J. Zhou. F. Charbel, A. Linninger. "Validation of parametric mesh generation for subject-specific cerebroarterial trees using modified Hausdorff distance metrics", Computers in Biology and medicine, 2018) for which I was the primary author. Ms. Sanchez assisted in writing the paper and understanding the Hausdorrf distance metric. Mr. Xu played a significant role in completing the automatic sampling acquisition work required for the publication. Dr. Alaraj and Dr. Charbel contributed their knowledge in cerebral arterial tree anatomy. My research mentor, Dr. Linninger contributed to the writing of the manuscript and directed the research. Chapter 4 is a published paper which shows the

hemodynamic risk-factor analysis (M. Ghaffari, A. Alaraj, X. Du, X. Zhou, F. Charbel, A. Linninger. "Quantification of near- wall hemodynamic risk factors in large- scale cerebral arterial trees" International Journal of Numerical methods in Biomedical Engineering, 2018.) in which I was the first author. The authors had the same contribution as in Chapter 2. Chapter 5 represents my overall conclusions and the future directions of my thesis. Appendix 7.4 represents a series of my unpublished results of comparison between 1D and 3D simulation results. I anticipate that this line of research will be continued in the laboratory after I leave and t hat this work will ultimately be published as part of a coauthored manuscript. Totally, image processing and filtration of arterial tree were mainly performed by Dr. Hsu, details of this process are explained in "C. Hsu, M. Ghaffari, A. Alaraj, Flannery X J Zhou, A. Linninger, "Gap-free segmentation of vascular networks with automatic image processing pipeline," Computers in Biology and Medicine, 2017." "C. Hsu, B. Schneller, M. Ghaffari, A. Alaraj and A. Linninger, "Medical Image Processing for Fully Integrated Subject Specific Whole Brain Mesh Generation." Technologies, 2015." for which I was the second and third authors of the publication.

TABLE OF CONTENTS

CHAPTER **PAGE**

LIST OF TABLES

TABLE **PAGE**

LIST OF FIGURES

FIGURE **PAGE**

LIST OF ABBREVIATIONS

DSA	2d Digital Subtraction Angiography
3DRA	3d Rotational Angiography
ACA	Anterior Cerebral Artery
AVM	Arterio-Venous Malformations
CFD	Computational Fluid Dynamics
COW	Circle Of Willis
CVD	Cerebral Vascular Disease
DSA	Digital Subtraction Angiography
ICA	Internal Carotid Artery
ECA	External Carotid Artery
ACOM	Anterior Communicating Artery
PCOM	Posterior Communicating Arteries
MCA	Middle Cerebral Artery
MRA	Magnetic Resonance Angiography
MRI	Magnetic Resonance Imaging
PC	Phase Contrast
PCA	Posterior Cerebral Artery
QMRA	Quantitative Magnetic Resonance Angiography
ROC	Receiver Operating Characteristic
TOF	Time Of Flight
UNST	Unstructured Mesh
PRM	Parametric Mesh

FSI	Fluid Structure Interaction
BIF	Bifurcation
BIF-BIF	Bifurcation To Bifurcation
BIF-TERM	Bifurcation To Terminal Point
CP	Control Point
SP	Separation Point
SIMPLE	Semi-Implicit Method For Pressure Linked Equations
FPR	False Positive Rate
TPR	True Positive Rate
AUC	Area Under The Curve
WSS	Wall Shear Stress
OSI	Oscillatory Shear Index
RRT	Relative Residence Time
TAWSS	Time-Average WSS
WSSG	Wall Shear Stress Gradient
DH	Delayed Hemorrhage
FVM	Finite Volume Method
CFL	Courant-Friedrichs-Lewy
PC	Personal Computer
PSM	Parametric Structured Mesh
PSD	Pointwise Surface Distance
CRS	Cross-Sections
AUC	Area Under The Curve
DEI	Diameter Estimation Index

PDF	Probability Density Function
DIPH	Delayed Ipsilateral Parenchymal Hemorrhage
VMTK	Vascular Modelling Toolkit
PICA	Posterior Inferior Cerebellar Artery
UDF	User-Defined Functions
PI	Pulsatility Index
RI	Resistance Index
PSI	Post-Intervention
PRI	Pre-Intervention
LPPD	Laboratory of Product And Process Design
STL	Stereo Lithography
SD	Systole to Diastole Ratio

1. INTRODUCTION

In this thesis, we present a novel technique to automatically generate parametric meshes for subject-specific cerebral arterial network. This technique generates high-quality and anatomically accurate computational meshes for fast blood flow simulations extending the scope of 3D vascular modeling to a large portion of cerebral arterial trees. For this purpose, a parametric meshing procedure was developed to automatically decompose the vascular skeleton, extract geometric features and generate hexahedral meshes using a body-fitted coordinate system that optimally follows the vascular network topology.

Currently, unstructured tetrahedral meshes are the standard output of image reconstruction software (e.g. MIMICS, VMTK, Amira), but require immensely fine resolution to smoothly delineate vascular tree with accurate anatomical details. Even though unstructured surface meshes can be smoothed, interior cells cannot be aligned in the flow direction, which introduces significant numerical diffusion error [1], [2]. It is also well known that even mesh refinement of misaligned elements does not necessarily reduce mesh-dependent error in calculating wall shear stress [3]. In contrast, hexahedral structural meshes require a much smaller number of elements to reach mesh independency [4]. Grid cell alignment in flow direction can, in principle, be achieved by structured meshing (Cooper algorithm, [5] Laplace equation, [6], [7] block structure, [8], [9] NURBS [10], [11]). However, these algorithms need manual intervention to handle complex geometries and bifurcations. In fact, reconstruction of a single arterial tree with hundreds of bifurcations and segments would require several weeks of painstaking manual operation. Therefore, we propose an image processing workflow, specifically tailored for vascular trees, for the fully automatic generation of anatomically accurate network representations of the entire cerebro-vascular

circulation. We then construct a volumetric mesh *aligned in the dominant flow direction* by means of a body-fitted radial, circumferential and longitudinal coordinate system (*parametric mesh*). Hexahedral grid cells *optimally* aligned in the dominant flow direction reduces necessary mesh size, improves mesh quality and accelerates convergence.

Accurate subject-specific vascular network reconstruction is a critical task for the hemodynamic analysis of cerebroarterial circulation. Vascular skeletonization and computational mesh generation for large sections of cerebrovascular trees from magnetic resonance angiography (MRA) is an error-prone, operator-dependent, and very time-consuming task. Validation of reconstructed computational models is essential to ascertain their accuracy and precision, which directly relates to the confidence of the hemodynamic analysis. We also generate a pipeline to automatically validate and quantify the spatial accuracy of computational models of subject-specific cerebral arterial trees in this thesis.

Detailed computational fluid dynamics (CFD) analysis of isolated vascular segments has led to the design and validation of novel therapies for cerebrovascular diseases, such as pipeline stenting for aneurysm flow diversion. However, the detailed CFD that helped design such devices is not capable of assessing their impact on the large portion of cerebroarterial tree. Unintended consequences, such as delayed hemorrhage and perforator infarction, far downstream from the intervention site, have been observed after the intracranial intervention. Such circulation-wide issues of reconfigured blood flow distribution cannot be addressed by locally applied CFD methods. However, a large-scale approach that could extend rigorous CFD analysis to the large portion of vascular tree would have potential to yield previously inaccessible insights.

In the last decade, detailed hemodynamic analysis of blood flow in pathological segments close to aneurysm and stenosis has provided physicians with invaluable information about the local flow

patterns leading to vascular disease. However, these diseases have both local and global effects on the circulation of the blood within the cerebral tree. The project will demonstrate the importance of extending subject-specific hemodynamic simulations to the large-scale cerebral arterial tree with hundreds of bifurcations and vessels, as well as evaluate hemodynamic risk factors and waveform shape characteristics throughout the cerebral arterial trees. A global map of cerebral arterial blood flow distribution revealed regions of low to high hemodynamic risk that may significantly contribute to the development of intracranial aneurysms or atherosclerosis. The lesion regions not only affect blood flow streamline of the proximal sites, but also generate pulse wave shift and disturbed flow in downstream vessels. This necessitates the use of large-scale simulation to visualize both local and global effects of pathological lesions.

1.1. Significance

Large-scale cerebrovascular tree simulation can produce the significant outcome of computing well-established hemodynamic risk factors efficiently and reliably. Currently, non-invasive modality of *quantitative magnetic resonance angiography* (qMRA) is a commonly used method to quantify blood flow, however it is limited in large blood vessels and does not provide direct measurements for hemodynamic states which are responsible for the formation of *cerebrovascular disease* (CVD) such as *wall shear stress* (WSS), *time-average WSS* (TAWSS), *oscillatory shear index* (OSI), *WSS gradient* (WSSG), *relative residence time* (RRT), and secondary flow (helicity and vorticity). The critical advantage of our pipeline is that it extends the analysis of risk factors to the large-scale cerebrovascular tree as visible by angiography, potentially providing clinicians with an almost complete hemodynamic status.

Importance of risk factor analysis. Computational fluid dynamic (CFD) has become a very important methodH in assessing cerebral blood flow both for understanding normal perfusion of

the brain and for elucidating hemodynamic risk in cerebral vascular diseases such as aneurysms and stenosis. Currently, "*quantitative magnetic resonance angiography* (qMRA) is a commonly used non-invasive modality to quantify blood flow in the human vasculature, however it is limited in large blood vessels" [12] and does not provide direct measurements for hemodynamic states which are responsible for the formation of *cerebrovascular disease* (CVD) such as *wall shear stress* (WSS), *time-average WSS* (TAWSS), *oscillatory shear index* (OSI), *relative residence time* (RRT), and secondary flow (helicity and vorticity). The importance of secondary flow and WSS vector direction changes have been well shown in the literature [13]–[16]. OSI has been correlated with plaque formation [17], [18] and high WSSG initiate intracranial aneurysm formation.[19] The occurrence of the atherosclerosis-prone region strongly correlates with low TAWSS and high OSI (i.e. high RRT) [20], [21]. Clinical study of Kawaguchi et al. [22] demonstrates that there is a distinctive flow pattern between ruptured and unruptured blebs and the degree of WSS was significantly lower in the ruptured aneurysm. Animal and clinical studies have shown that sustainable secondary flow (helicity) can significantly reduce the likelihood of thrombosis formation inside vascular grafts [23], [24]. Since none of these parameters can be measured directly, we propose to augment the value of in vivo measurement by performing subject-specific CFD analysis to infer hemodynamic risk factors from actual measurements. This whole tree analysis is expected to help to identify hemodynamic abnormalities for the entire cerebral blood supply.

Importance of subject-specific modeling. Accurate cerebral arterial trees modeling requires precise subject-specific reconstruction of the cerebral vasculature which exhibits large geometrical variations between individuals. For example, the *circle of Willis* (CoW) is a significant pathway in distributing adequate cerebral blood flow supply to different territories of brain. CoW'S ability

to redistribute blood flow depends on the presence and the shape of the communicating vessels. More than half of the population possess some kind of abnormalities in the CoW [25]. In addition to the COW anatomical variance, any small changes in intracranial geometry can create a large effect on WSS and its derivatives [26]. Beyond the CoW, the pial arterial networks extending in MCA, PCA, ACA regions are highly variable for each individual. Small changes in resistance and configuration of these vascular territories give rise to different levels of collateral blood supply in vascular reserve. In order to address subject-specific risk factors, we propose to include subject-specific models of the entire vascular tree including the vascular territory of the main cerebro-arterial tree in addition to the CoW.

Due to very high temporal and spatial resolution, cerebral blood flow simulation is a valuable tool for quantifying important hemodynamic parameters for a better understanding of cerebrovascular diseases. Realistic and computerized simulation can be used to enhance traditional clinical training with real patient models. Our proposed pipeline, with many automated image reconstruction and mesh generation methods, is a great stepping-stone toward real-time flow analysis of cerebral arterial tree for neurosurgeons.

1.2. Innovation

Hemodynamics analysis of cerebrovascular disease (CVD) has become an invaluable research tool for aneurysm rupture risk, [27]–[30] and aneurysm coiling, [30]–[32] stent designs, [33], [34] and angioplasty [35]. Most current CFD simulations are limited to a short section, even though endovascular interventions for CVD's affect flow in the entire cerebral circulation. Therefore, we propose departure of classical modeling, which is limited to a single segment, to the entire tree. This also has the advantage of assessing hemodynamic analysis of surgical intervention for the large portion of the arterial tree including downstream vessels where undesired hemodynamics

risk could occur far away from the site of intervention. For example, delayed hemorrhage (DH) is reported after aneurysm surgery and flow diversion in distal vessels due to cerebral circulation changes. Entire cerebral arterial tree simulation would also enable assessment of hemodynamic factors associated with treatment and persistent patency of DH complications. The possibility of remote and delayed effects caused by endovascular intervention underscores the need for assessing hemodynamic changes not only locally but throughout the entire cerebroarterial tree. The purpose of this thesis is to extend rigorous CFD analysis from a single site to the larger portions of the entire cerebrovascular network using a combination of novel image-derived filters and mesh generation techniques.

Our central hypothesis is that our proposed pipeline with tighter integration of imaging, vascular modeling, and hemodynamic is capable of addressing hemodynamic risk factors over the entire cerebroarterial tree.

1.3. Anatomy

In this section, we will describe the anatomy of cerebral circulation, especially Circle of Willis (CoW) which is a ring-like structure for distribution of the blood through the brain. Circle of Willis provides important commutating arteries between different vascular territories in cerebrovascular tree. “The circle of Willis is an important potential collateral pathway in maintaining adequate cerebral blood flow” [36]; “its ability to redistribute blood flow depends on its morphology, the presence and size of the component vessels” [37]. More than half of population has some kind of abnormalities in the CoW [25]. Complete anterior and complete posterior parts of the COW were only seen in 68.3%, and 38.3%, respectively [36]. A close correlation has been reported between a low capacity CoW and an increased risk of stroke [36].

The incoming flow to CoW including the left internal carotid artery (LICA), the right internal carotid artery (RICA) and basilar artery (BA); in addition, "arteries leaving the CoW include the anterior cerebral arteries (RACA, LACA), middle cerebral arteries RMCA, LMCA) and posterior cerebral arteries (LPCA and RPCA)"[38] are shown in Figure 1. The CoW is a ring-like structure which may interconnect arteries of posterior communicating arteries (PCOM), and anterior communicating artery (ACOM). It also creates collateral blood supply to the cerebrovascular circulation. In other words, in case of insufficient blood flow in a region of the brain, other blood vessels can provide the blood demand to that specific region through collateral blood flow.

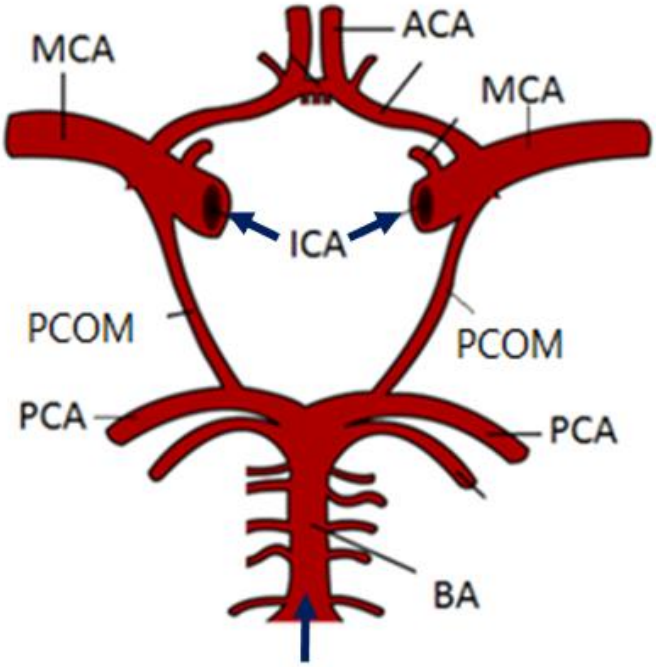

Figure 1. A schematic of the Circle of Willis. The internal carotid arteries (RICA, LICA) along with the basilar artery (BA) provide the input blood flow for the ring-like structure of Cicle of Willis (CoW). The right and left anterior, middle, and posterior cerebral arteries (RACA, RMCA, RPCA, LACA, LMCA, LPCA) stem from the CoW to reach blood flow supply to the different territories of the cerebral arterial tree.

1.4. Cerebrovascular Disease

Cerebrovascular disease (CVD) is one of the most common reason for death in the western countries. It includes a variety of severe medical condition related to blood vessels of the brain. The well-known examples of CVS are schematic stroke and sometimes hemorrhage stroke which are mostly due to stenosis (narrowing of vessels), arterio-venous malformation (AVM) and aneurysm.

1.4.1. Intracranial stenosis

Intracranial stenosis is an abnormal narrowing of blood flow inside the brain causing a lesion that reduces the lumen space such as atherosclerotic plaque. High-degree of stenosis can results in abnormal blood sounds due to the turbulent flow over the narrowed region of the vessel. In addition, cerebral stenosis will result in a reduction of blood flow and oxygen supply to a downstream region of the narrowed vessel. The carotid stenosis is the most common stenosis in the brain which is easier for a surgeon to treat than stenosis in the deep brain. There are a different surgical approach to treat stenosed blood vessels such as endarterectomy, balloon angioplasty, and stenting. In endarterectomy, endovascular surgeons remove the atherosclerotic plaque inside the vessel. During angioplasty, balloon-tipped catheter is guided toward the stenosed region and is placed within the narrowed part. Then the balloon is inflated to open the artery. Usually after removal of the balloon through the catheter. A mesh-like structured tube, stent, is placed over the plaque to keep the artery open.

“A stenosis is narrowing of a vessel lumen, which in most cases is caused by atherosclerotic plaque. The narrowing results in a reduction of blood flow and oxygen supply. Severe narrowing might even cause total occlusion of the artery. The narrowing usually builds up gradually. But it can also happen when a piece of plaque breaks off and obstructs a smaller downstream artery.

Stenosis can be treated with drug therapy or it can be treated with endarterectomy, angioplasty, or stenting as shown in Figure 2. Endarterectomy is a surgical procedure to remove atherosclerotic plaque on the inside of the artery. Angioplasty is the mechanical widening of a stenosed blood vessel, typically by expanding a balloon delivered by a catheter. Stenting is the application of a metal-mesh tube which extends the vessel" [39], [40].

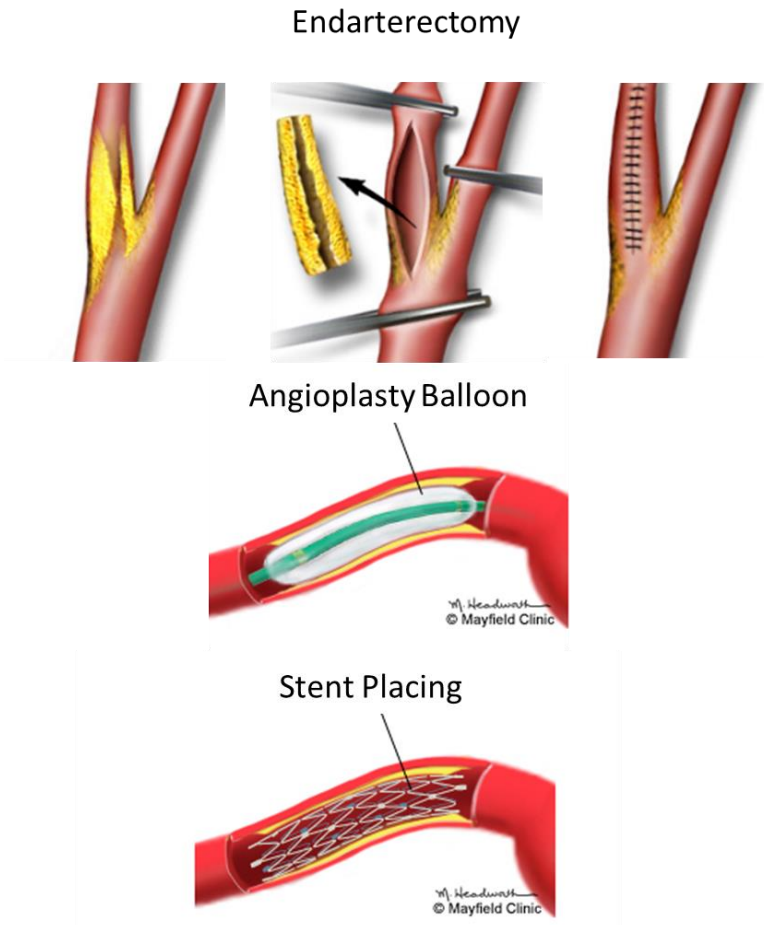

Figure 2. Schematics of stenosis treatment options, including endarterectomy, Balloon angioplasty, and stent placing [39]. Endarterectomy is a surgical procedure to remove atherosclerotic plaque on the inside of the artery. Angioplasty is the mechanical widening of a stenosed blood vessel, typically by expanding a balloon delivered by a catheter. Stenting is the application of a metal-mesh tube which extends the vessel. (Mayo Clinic)

1.4.2. Cerebral aneurysm

A cerebral aneurysm, also known as an intracranial aneurysm, is a thinning of the vessel wall in the brain that deforms and balloon out of the vessel with a high risk of rupture [41]. The balloon-shape of the vessel can put pressure on the neighboring nerve and surrounding brain tissue. Leakage of the blood flow through rupture and spilling out the blood flow to the surrounding tissue is called hemorrhage. Evaluation the risk of aneurysm rupture is highly important for surgeons. Common treatment of an aneurysm includes clipping, coiling and flow diverting as shown in Figure 3.

Surgical clipping is a procedure to close off the aneurysm neck using a metal clip to limit entering blood flow to the dome of the aneurysm. Endovascular coiling is less invasive compared to clipping. In this procedure, the surgeon inserts the catheter into the lesion to full the dome with tiny and soft platinum coils. The wire coils will prevent blood flow from entering and essentially seals off the aneurysm [42], [43].

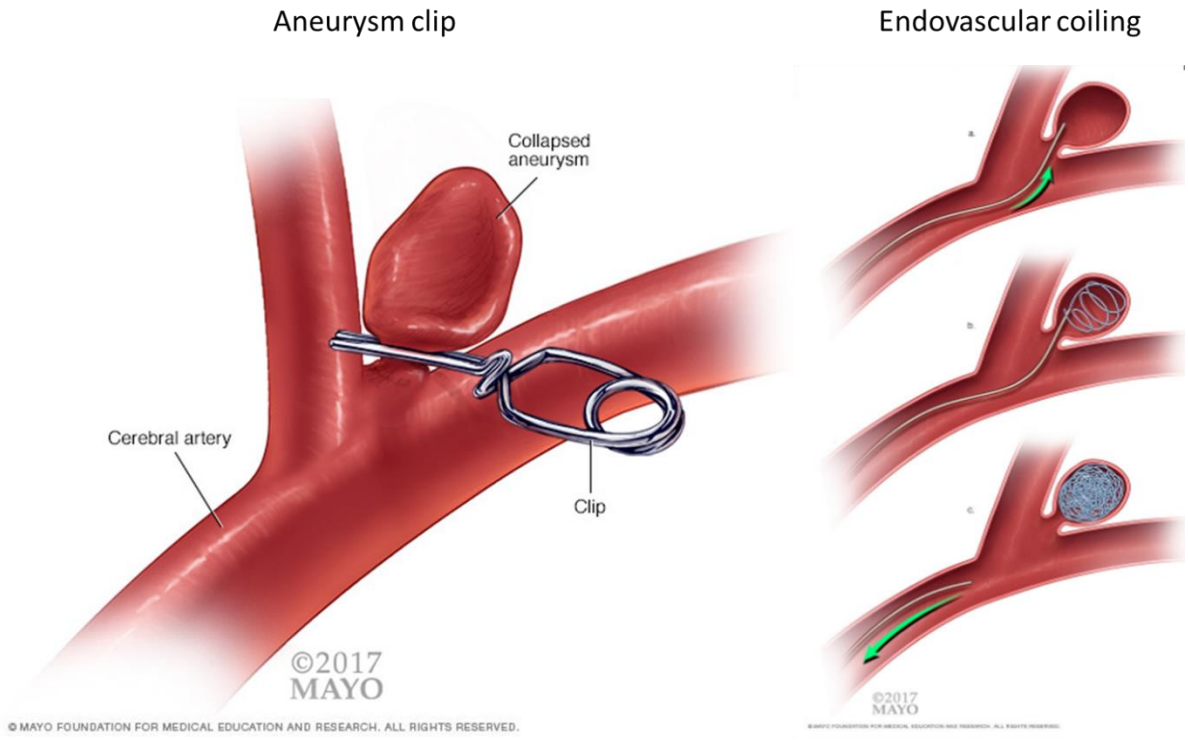

Figure 3. Schematics of clipping surgery (left) and endovascular coiling (right) to treat a cerebral aneurysm. (Mayo Clinic)

1.4.3. Arteriovenous malformations

Arteriovenous malformation (AVM) is a vascular defect which connects arteries directly to the brain without passing the capillaries as shown in Figure 4. This lesion will disturb oxygen supply to the brain tissue and has a risk of hemorrhage. Surgical approaches to treat AVM include resection or surgical removal, endovascular embolization, and stereotactic radiosurgery. Surgical removal is recommended for the area that can easily be accessed using conventional brain surgery. In embolization procedure, a catheter is positioned in one of the feeding arteries to the AVM lesion. Then a glue-like substance is injected to block the artery to prevent blood flow through the AVM which will result in reducing the size of the AVM. Stereotactic radiology uses radiation technology to destroy the AVM which is most suitable for small AVMs [44].

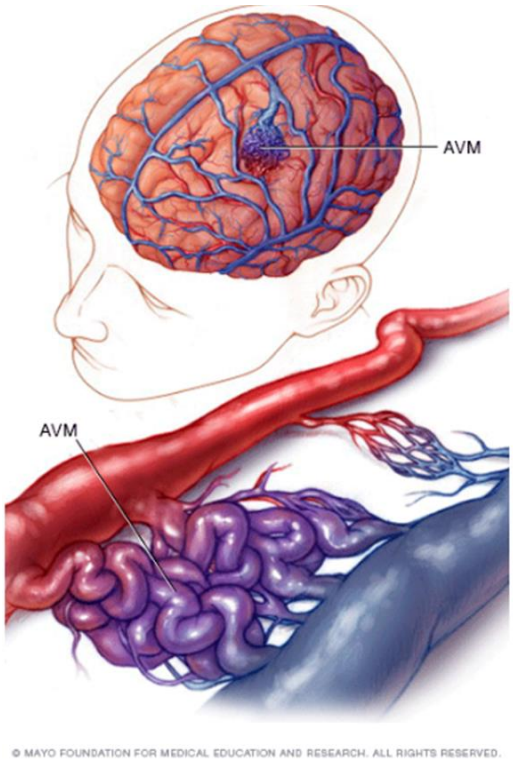

Figure 4. Arteriovenous malformation (AVM) is a premature and abnormal connection of arteries and veins. Surgical approaches to treat AVM include resection or surgical removal, endovascular embolization, and stereotactic radiosurgery (Mayo Clinic).

2. MESH GENERATION

This chapter is previously published by Ghaffari, Mahsa, et al. “Large-scale subject-specific cerebral arterial tree modeling using automated parametric mesh generation for blood flow simulation.” Computers in Biology and Medicine (2017) as well as “Automatic reconstruction and generation of structured hexahedral mesh for non-planar bifurcations in vascular network.” Computer Aided Chemical Engineering, (2015).

2.1. Abstract

In this chapter, we present a novel technique for automatic parametric mesh generation of subject-specific cerebral arterial trees. This technique generates high-quality and anatomically accurate computational meshes for fast blood flow simulations extending the scope of 3D vascular modeling to a large portion of cerebral arterial trees.

For this purpose, a parametric meshing procedure was developed to automatically decompose the vascular skeleton, extract geometric features and generate hexahedral meshes using a body-fitted coordinate system that optimally follows the vascular network topology. To validate the anatomical accuracy of the reconstructed vasculature, we performed statistical analysis to quantify the alignment between parametric meshes and raw vascular images using receiver operating characteristic curve. Geometric accuracy evaluation showed an agreement with an area under the curves value of 0.87 between the constructed mesh and raw MRA data sets.

Parametric meshing yielded on-average, 36.6% and 21.7% orthogonal and equiangular skew quality improvement over the unstructured tetrahedral meshes. The parametric meshing and processing pipeline constitutes an automated technique to reconstruct and simulate blood flow

throughout a large portion of the cerebral arterial tree down to the level of pial vessels. This study is the first step towards fast large-scale subject-specific hemodynamic analysis for clinical applications.

2.2. Introduction

Currently, unstructured tetrahedral meshes (UNST) are the standard format of domain discretization of circulatory networks in computational fluid dynamics (CFD). UNST meshes have been very successful in handling irregular vascular geometry especially pathological cases[1-5]. There are also procedures to convert UNST into unstructured polyhedral meshes to reduce the required cell elements [48]. Although unstructured grids are the most commonly used technique for complex geometries, structured hexahedral meshes offer several advantages that might be necessary for some applications. For example, structured hexahedral meshes are essential for isogeometric analysis [11]; the arrangement of near-orthogonal hexahedral cell layers make them ideal for fluid structure interaction (FSI) [49]. Hexahedral structured mesh generation for the entire vascular trees is challenging due to complex network connectivity with multiple bifurcations, loops, and vessels with high tortuosity.

Structured hexahedral meshes have proven to produce stable results in numerical analysis requiring fewer elements to reach mesh independence than UNST meshes [4]. Moreover, it has been shown [3] that UNST mesh element refinement does not necessarily reduce mesh-dependent error in calculating wall shear stress (WSS). However, WSS components are critical hemodynamic factors for predicting of endovascular lesions such as atherosclerosis [13], [17].

Randomly distributed cells introduce numerical diffusion error in CFD analysis [1], [2], [50]. The main blood flow direction in large cylindrical vessels aligns with the longitudinal axis. Face and elements alignment along the dominant flow direction improves numerical results and

accelerate numerical convergence compared with UNST [3]. Grid cell alignment in the flow direction can, in principle, be achieved by structured meshing such as using cooper algorithm [5], Laplace equation [6], [7], block structure [8], [9], [51], and NURBS [10], [11], [52]. However, most implementations require manual intervention when applied for vascular trees. Some procedures require a smoothed surface mesh for hexahedral volumetric mesh generation [53], [54], but it is extremely laborious to manually obtain a high quality surface mesh with no gaps and discontinuity from medical images for a large-scale cerebral arterial tree. Size and complex connectivity of cerebral arterial trees with hundreds of bifurcations and branches call for *automated* image segmentation and mesh processing.

Many prior techniques also suffer from limitations when dealing with complex topologies. For example, some methods are limited to planar bifurcations [3], [5], [54], [55] (bifurcation branches lying in a single plane), however, non-planar bifurcations are prevalent in the human vascular trees [56]. Other procedures fail in short segments between bifurcations [53] or segments with high tortuosity [57].

In this study, we present a *robust automatic* procedure for parametric hexahedral mesh generation of large cerebral arterial trees from medical images. We will perform parametric meshing on multiple healthy and pathological arterial trees.

The workflow for the large-scale arterial tree flow simulation from image acquisition to simulation output is illustrated in Figure 5. Imaging datasets were used for arterial tree reconstructions of six healthy volunteers and two endovascular patient cases. A novel vesselness filter [58], [59] was used to enhance the contrast of the cerebral angioarchitecture [60] down to pial arteries (400 μm). Vessel centerline and radius information of the vascular network were extracted. Then, a fully automatic parametric mesh generation technique (PRM) was deployed to

generate flow-aligned hexahedral meshes for the cerebral arterial trees. Finally, we performed blood flow simulation of cerebral arterial trees and compared the results to those obtained with UNST meshing techniques.

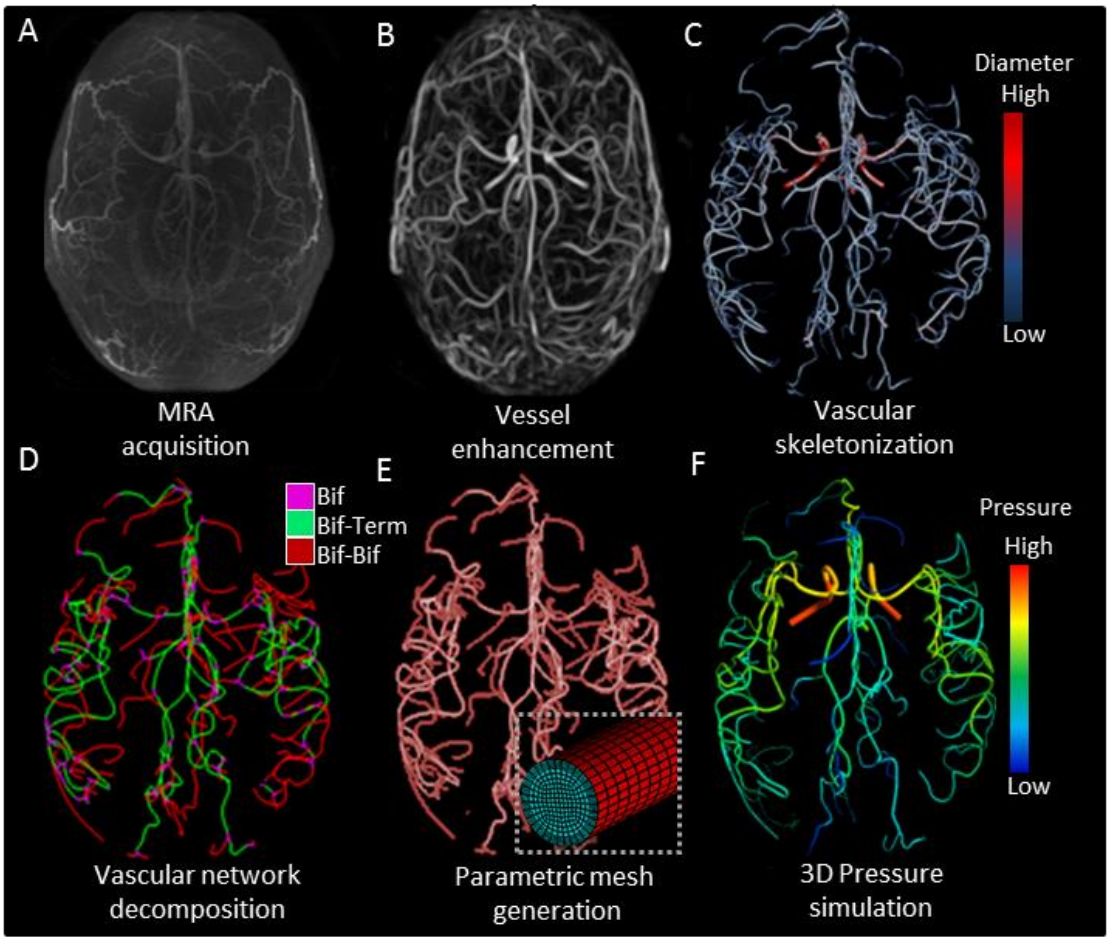

Figure 5. Workflow of subject-specific skeletonization and parametric mesh generation of cerebral arterial tree. (A) Raw MRA image acquisition of cerebral arterial tree with MRA. (B) *Vesselness* enhancement filter suppresses tissues and background to better delineate the arterial blood vessels. (C) Vascular skeletonization obtains geometrical network information such as diameters, centerline point coordinates, and segment connectivity (color-coded diameter information). (D) The vascular network is decomposed into three sections: *bifurcation (Bif)*, *bifurcation-to-terminal* (*Bif-Term)*, and *bifurcation-to-bifurcation* (*Bif-Bif*) segments. (E) Parametric meshes composed of surface and volumetric grids along body-fitted radial, circumferential and axial coordinates system. Magnified insert shows cross-section of a small artery. (F) Simulated three-dimensional pressure field at systole for the entire cerebral arterial tree in one subject.

2.3. Methods

2.3.1. Image Acquisition

Magnetic resonance angiography were acquired from six healthy human subjects on a General Electric 3T MR750 scanner using a 32 channel phased array coil (Nova Medical, Inc., Wilmington, MA, USA). Magnetic resonance angiograms (MRA) were acquired for healthy volunteers (five men and one woman between 25 to 31 year-old). In addition, clinical digital subtraction angiography (DSA) data for two retrospective pathological cases were selected. The pathological case I was a 59 year-old male diagnosed with left middle cerebral artery (MCA) stenosis. Pathological case II was a 74 year-old female who had a large aneurysm in the side branch of the right vertebral artery (VA). MRA and DSA were acquired under institutional review board.

2.3.2. Vascular filtration

To better capture a large-scale cerebrovascular tree from large to small pial arteries, we enhanced the vessel contrast with our in-house *multi-scale vesselness* filter [58], [59]. Figure 5B shows an enhanced image of the vasculature of the *subject I*, which is much brighter and clearly delineated from the background compared to the raw image data.

2.3.3. Skeletonization

2.3.3.1. Read case and network file

This part will extract diameter vector, point coordinate matrix, face matrix, and point matrix from the imported case and network file. The .m file is written CASEReaderCY and NWKReaderCY.

The *ptCoordMx* is a double-precision matrix that gives information about the node coordinates. Each row represents the global index of a point.

The *faceMx* is an integer matrix, which gives information about the connection. Each row is the global index of the face. The second column and third column refer to the indices of the two points making up the face.The *diameterVector* is a double-precision vector that contains the diameter for each face.The *pointMx* is an integer matrix contains the indices of the faces connected to a given point. The rows stand for the points. The columns signify the indices of the faces connecting to the point. If the face is positive, the flow flows out of the faces. Figure 6 illustrates a sample of *ptCoordMx*, *faceMx*, *diameterVector*, and *pointMx* in a simple network.

A

nwk.ptCoordMx

	1	2	3
1	4.3743e-21	1.1429	0
2	1.4286	1.1429	0
3	2.2857	1.7143	0
4	3.1429	2.2857	0
5	2.2857	0.5714	0
6	3.1429	0	0
7	4	1.7143	0
8	4	0.5714	0
9	4.8571	1.1429	0
10	6.2857	1.1429	0

B

nwk.faceMx

	1	2	3
1	1	1	2
2	1	2	3
3	1	2	5
4	1	3	4
5	1	5	6
6	1	6	8
7	1	4	7
8	1	7	9
9	1	8	9
10	1	9	10

C

nwk.pointMx

	1	2	3
1	-1	0	0
2	1	-2	-3
3	2	-4	0
4	4	-7	0
5	3	-5	0
6	5	-6	0
7	7	-8	0
8	6	-9	0
9	8	9	-10
10	10	0	0

D

nwk.diameterVector

	1	2	3
1	0.4000		
2	0.3500		
3	0.3900		
4	0.3500		
5	0.3800		
6	0.3800		
7	0.3500		
8	0.3500		
9	0.3900		
10	0.4000		

E

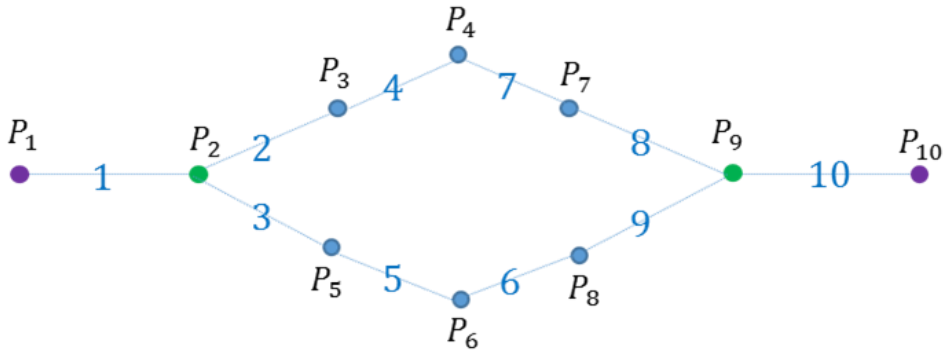

Figure 6. The storage of information for the reconstructed vessel network. (B) In *faceMx*, each row encodes the index. The second column and third column refer to the indices of the two points making up the face. (C) The *pointMx* is an integer matrix contains the indices of the faces connected to a given point. The rows stand for the points. The columns signify the indices of the faces connecting to the point. If the face is positive, the flow flows out of the face. (D) The diameters for each face stored in *diameterVector*. (E) Visualization of the network file. P_i shows the *i*-index points and faces are illustrated in dotted-line and its indexes are shown in blue numbers.

2.3.3.2. Optional scaling

The unit in this program is SI, however, in some case and network file, such as Ian Gould's brain the unit is inaccurate. Here you can convert the *diameterVector* and *pointCoordinate* to your desire unit.

2.3.3.3. Find Bifurcation and Terminal points

Simply, points with one face are Terminal points and points with three assigned faces are Bifurcation points. It also will calculate a total number of bifurcation and terminal point in a vascular network. Green and Purple nodes are bifurcations and terminal points in Figure 6, respectively.

2.3.3.4. Segment and spline generation

Segments are the vessels between either a terminal and bifurcation point or between two bifurcation points. Finally, we created Bezier splines for each segment. For each segment, we used Bezier spline approximation to generate a single spline smoothly connecting all point of a segment.

Bezier spline passes through every single point while keeping the G_1 continuity. G_1 continuity keeps the direction of the velocity tangent between neighboring Bezier curves.

In Figure 7A, seven points are shown in black in a single segment. For each point, $\vec{V}_{Prev}$ and $\vec{V}_{Next}$ data are used to compute the "direction" of control points. In Figure 7B, $\vec{V}_i = \left\|P_0^i - P_1^i\right\|$ and $\vec{V}_j = \left\|P_1^j - P_0^j\right\|$ represents the $\vec{V}_{Prev}$, and $\vec{V}_{Next}$, respectively. Equation (1), and (2) were used to compute the control point location for C_0^j and C_1^i.

$$C_0^j = \frac{\left|P_1^j - P_0^j\right|}{3} \cdot \left\|\vec{V}_i + \vec{V}_j\right\| \quad (1)$$

$$C_1^i = \frac{\left|P_1^i - P_0^i\right|}{3} \cdot \left\|\vec{V}_i + \vec{V}_j\right\| \quad (2)$$

The simple network model consists of four segments as shown in Figure 8. The spline data set for each segment are stored such as $\{P_0^i, C_0^i, C_1^i, P_1^i\}$, $\{P_0^j, C_0^j, C_1^j\ P_1^j\}$, $\{P_0^k, C_0^k, C_1^k\ P_1^k\}$ sequentially.

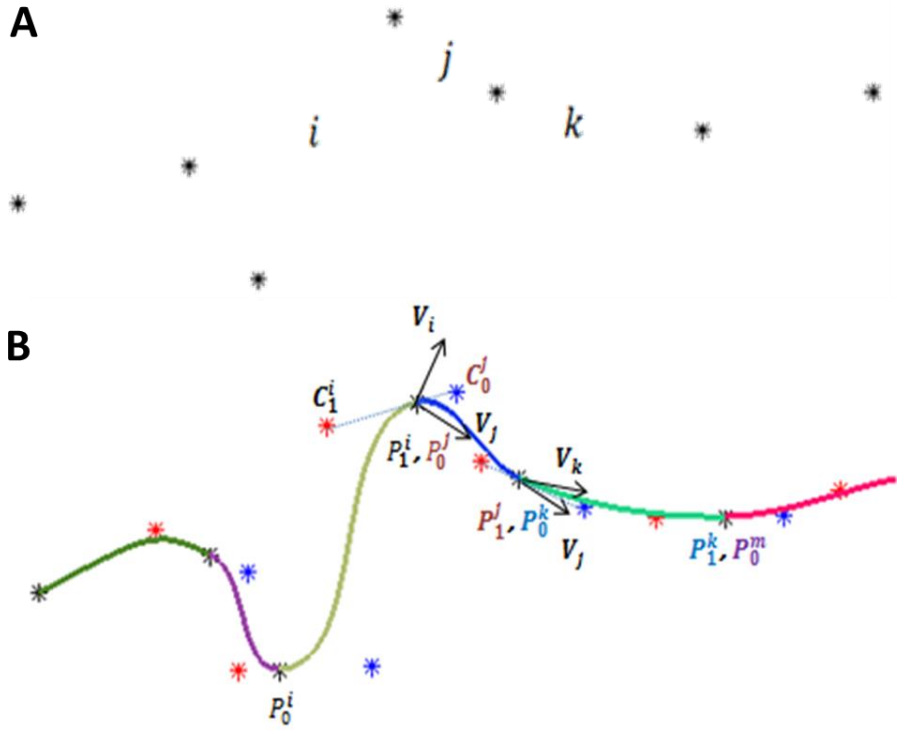

Figure 7. Illustration of local Bezier curve approximation, Bezier spline pass through all data points. (A) Black points are the data points used to create Bezier curve. (B) Shows the connection of *i* and *j* splines. Red and blue points show the $\boldsymbol{C_1}$ and $\boldsymbol{C_0}$, respectively. $\vec{\boldsymbol{V}}_{\boldsymbol{i}} = \left\|\boldsymbol{P_0^i} - \boldsymbol{P_1^i}\right\|$ is the direction of *i*-spline and $\vec{\boldsymbol{V}}_{\boldsymbol{j}} = \left\|\boldsymbol{P_1^j} - \boldsymbol{P_0^j}\right\|$ is the direction of *j*-spline. The "direction" of $\boldsymbol{C_1^i}$ and $\boldsymbol{C_0^j}$ determined by the sum of unit vectors of $\vec{\boldsymbol{V}}_{\boldsymbol{i}}$ and $\vec{\boldsymbol{V}}_{\boldsymbol{j}}$. (Similarly, $\vec{\boldsymbol{V}}_{\boldsymbol{j}}$ and $\vec{\boldsymbol{V}}_{\boldsymbol{k}}$ are used to compute the $\boldsymbol{C_1^j}$ and $\boldsymbol{C_0^k}$ coordination).

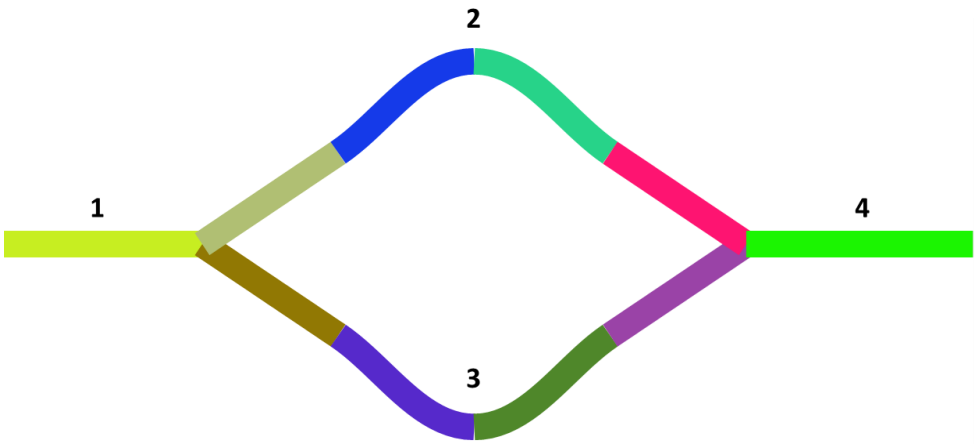

nwk.bzSplines

	1	2	3	4	5	6	7	8	9	10	11
1	1	2	2	3	0	0	0	0	0	0	0
2	3	4	4	5	5	6	7	8	8	9	10
3	3	15	15	16	16	17	18	19	19	20	21
4	14	25	25	26	0	0	0	0	0	0	0

Figure 8. The Bezier spline of the simple network model. The simple network includes four segments. Segment 1, 2, 3 4, consist of 1, 4, 4, and 1 color-coded Bezier curves. The point index of the Bezier splines was stored in *bzSplines* matrix.

2.3.3.5. Bifurcation Matrix generation

Here we will find the neighboring segment to each bifurcation point. Figure 9 is the Bifurcation matrix for the simple network, the row indexes are bifurcation index, with three columns which each is a segment connected to that bifurcation.

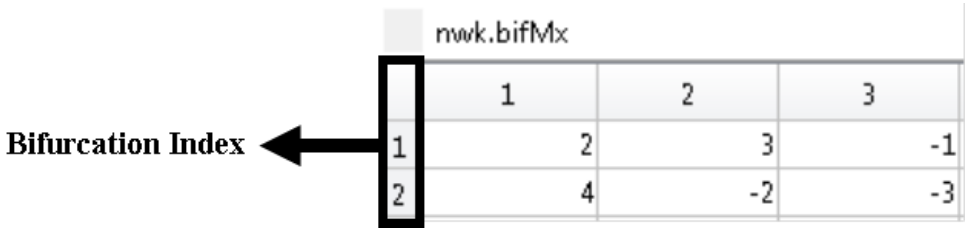

Figure 9. Bifurcation matrix generation. Each column represents the neighboring spline of the bifurcation. The positive and negative sign of the *bzSpline* index represents outflow and inflow segment to the bifurcation point.

2.3.3.6. Morphological analysis

Here you can calculate the morphological parameters such as tortuosity, curvature, torsion in each segment. Morphological index calculation of curvature, torsion, and tortuosity using Equations (3)-(5), respectively.

$$Curvature = \frac{\left\|\overrightarrow{s'} \times \overrightarrow{s''}\right\|}{\left\|\overrightarrow{s'}\right\|^3} \tag{3}$$

$$Torsion = \frac{\left(\overrightarrow{s'} \times \overrightarrow{s''}\right) \cdot \overrightarrow{s'''}}{\left\|\overrightarrow{s'} \times \overrightarrow{s''}\right\|^2} \tag{4}$$

$$Tortuosity = \frac{L}{L_0} - 1 \tag{5}$$

With $\|\vec{.}\|$ the norm of a vector, $\overrightarrow{s'}$, $\overrightarrow{s''}$, and $\overrightarrow{s'''}$ are the first, second, and third derivative of the parametric curve of the centerline. L is the total arc length and L_0 the end-first length of the vessel.

2.3.3.7. Diameter assignment for splines

In this section, the diameter of the vessels will be cleaned and filtered to remove the noise (sudden unreasonable changes in diameter), then diameters datasets assigned to each spline. Figure 10 illustrates the raw diameter and smooth diameter for two vascular segments. Table 1 summaries the process of diameter vessel cleaning and smoothing.

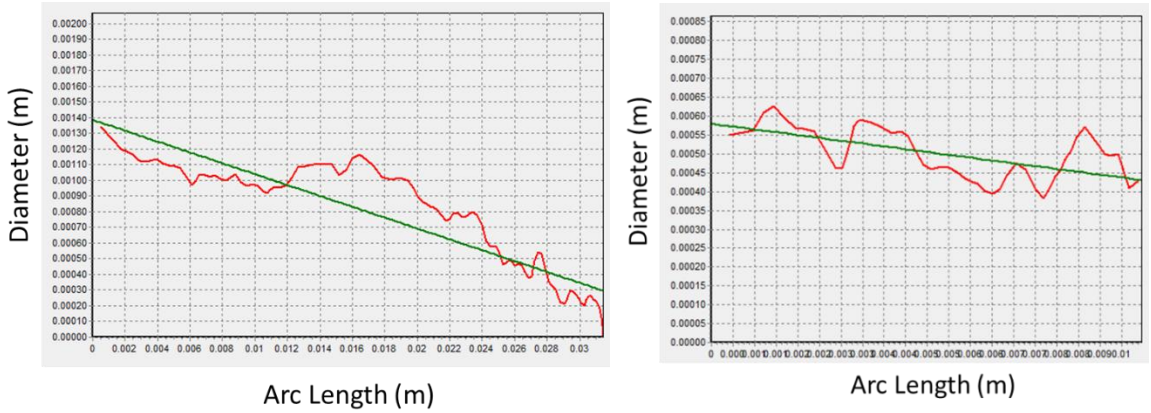

Figure 10. Diameter smoothing of the vascular segment. Red line shows the original diameter, the green line is the approximated linear fitted diameter for a vascular segment.

Table 1. Algorithm of vascular diameter cleaning and smoothing

Segment and diameter cleaning

1. Zero diameters should be checked if zero diameters are detected. Average of neighboring diameter should be replaced by that zero-diameter value.
2. Any diameter below 400μm was replaced by 400μm.
3. Total length of each segment (Length_j), and the mean of diameter (mean_Diameter_j) w calculated.
4. Using pointMx in spline form, we can get information about the neighboring splines.
   - For splines with no neighbors (Dangling branch): it should be deleted.
   - For splines with only one-side neighbors (Bifurcation to the terminal).
     if $\frac{(\text{Length}_j)}{(\text{mean\_Diameter}_j)} < 5$, then it should be deleted

Diameter smoothing

5. Moving average smoothing was performed before linear fitting of diameters. N is the total number of diameter in each segment.

$$d_i = \begin{cases} \frac{d_i + d_{i+1} + d_{i+2}}{3} & i = 1, \quad first\ diamter\ of\ the\ segment \\ \frac{d_{i-1} + d_i + d_{i+1} + d_{i+2}}{4} & i = 2, \quad second\ diamter\ of\ the\ segment \\ \frac{d_{i-2} + d_{i-1} + d_i + d_{i+1} + d_{i+2}}{5} & otherwise \\ \frac{d_{i-2} + d_{i-1} + d_i + d_{i+1}}{4} & i = N-1, \quad N-1\ diamter\ of\ the\ segment \\ \frac{d_{i-2} + d_{i-1} + d_i}{3} & i = N, \quad final\ diamete\ of\ the\ segment \end{cases}$$

Linear fitting

6. The length of each face was used as a distance-parametrized weight in our system

$$\omega_i = \frac{L_i}{\sum_{i=1}^{n} L_i} \cdot nFace$$

   Here L_i is the length of the *i-th face*, $\sum_{i=1}^{n} L_i$ is the length of a spline. $nFace$ is the number of connectivity faces in the spline. ω_i is the distance-parametrized weight.
7. Linear fitting to the diameters by using the Diameter and ω_i. Here m is the slope

$$y = mx + b$$

8. Here we checked the sign of the slope according to the morphology of the vessel
   - For splines with only one-side neighbors (Bifurcation to terminal), we should make sure that the slope (m) is negative.
   - For splines with two-side neighbors (Bifurcation to bifurcation), the maximum average diameter of each side should be calculated, calling $D_{max\_Previous}$ and D_{max_next}.

     I. If $D_{max\_Previous} > D_{max\_next}$ & the slope is positive.
     II. If $D_{max\_Previous} < D_{max\_next}$ & the slope is negative.

In a case of *I* or *II*, the linear fitting should be canceled and only moving diameter should be applied. If linear fitting results in the generation of the vessels less than 400μm, it should be replaced by 400μm**.**

2.3.3.8. Classification of the segments

The aim of network decomposition is to categorize the network branches into the bifurcation (*Bif*), bifurcation to the terminal (*Bif-Term*) and bifurcation to bifurcation (*Bif-Bif*) segment. In the previous section, we used Bezier curve approximation to generate a Bezier network, which is the representation of vessel morphology as shown in Figure 11A.

The points in cerebral skeletons are categorized into three groups of bifurcations, outlet/inlet (terminals), and connecting points. Using these points, the network branch is segmented into *Bif*, *Bif-Term*, *Bif-Bif*. The *Bif* segment is firstly assigned in the network. Three branches are connected to each bifurcation points. Generally, each branch was subdivided where the arc length of the bifurcation branch is equal to twice the local radius of the vessel [56]. The most challenging problem is subdividing a branch, which connects two close bifurcations. In this case, one-fourth of the arc length is assigned to each bifurcation and the rest is assigned to *Bif-Bif* region. *Bif* regions are green-colored in Figure 11B.

After assigning *Bif* region, remedies are categorized into either *Bif-Term* or *Bif-Bif*. *Bif-Term* is the segment connecting a bifurcation branch to an outlet or inlet. Similarly, *Bif-Bif* is the segment connecting two bifurcations together. *Bif-Term* and *Bif-Bif* are in black and blue as shown in Figure 11B.

In this section, we will explain the Bezier subdivision method while keeping G^1 continuity between segregated curves. As shown in Figure 12, *A*, *B*, *C*, and *D* are the P_0 C_0 C_1 P_1 of our primary Bezier curve. We want to split the curve while keeping G^1 based on De Casteljau Algorithm. *AB* is the halfway point of the line segment that is defined by *A* and *B* points. *AB*, *BC*, *CD* points will also be calculated. Repeatedly, this process continues until the $B(t = 0.5)$ is located. The control points of the two new curves are *AB*, *ABC* as well as *BCD* and *CD*, respectively.

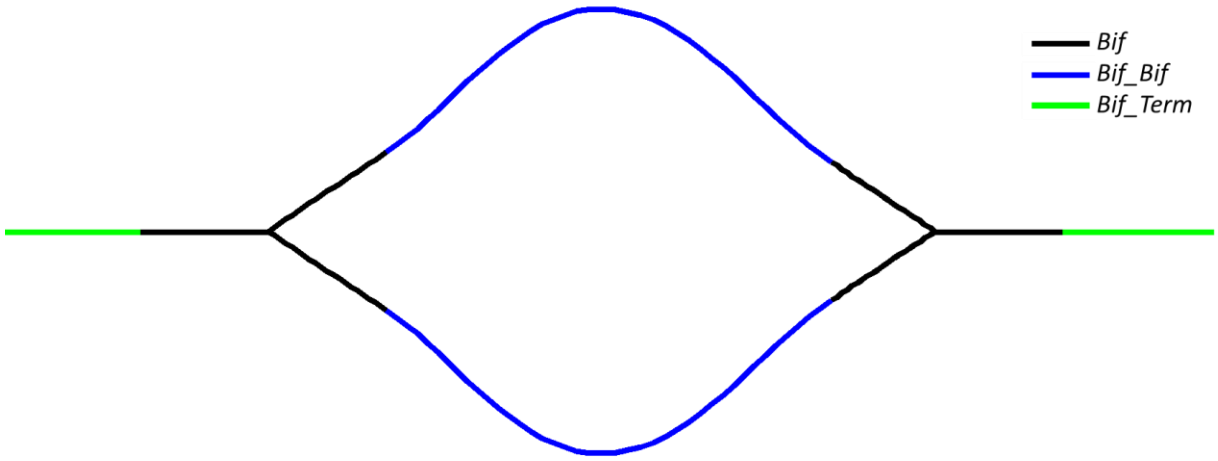

Figure 11. Illustration of Bezier network generation. (A) Bezier network generation of Circle of Willis, the more tortuous the more number of Bezier curves. Bezier curves are colored differently to show its variety, G^1 continuity is enforced between adjacent curves. (B) Network decomposition, Bezier network is decomposed into three part of bifurcation (green), bifurcation to bifurcation (blue) and bifurcation to the terminal (black).

2.3.3.9. Subdivision de Casteljau algorithm

One of the most important operations on a curve is a subdivision of curves. *De Casteljau algorithm* were implemented to separate a single Bezier curve into two Bezier curves. A Bezier curve can be evaluated at a specific parameter of *t*, between zero to one, and the curve can be split at that value using this algorithm. Figure 12 shows the subdivision of a Bezier curve at $t = 0.5$.

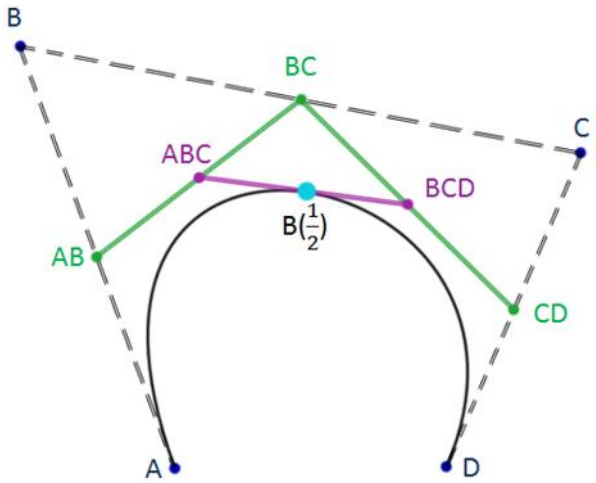

Figure 12. Bezier subdivision, the subdivision of a Bezier curve corresponding to the parameter $t = 0.5$. A, B, C, and D points are the P_0 C_0 C_1 P_1 of our primary Bezier curve. Then, AB, BC, CD point will be calculated. AB is the halfway point of the line segment that is defined by point A and B. Repeatedly, this process continues until the B(0.5) is found. The control points of the two new Bezier curves are AB, ABC as well as BCD and CD.

2.3.3.10. Obj2mesh format

Obj2 mesh is an (N × 4) matrix which N is the number of all groups in a network including bifurcation (*Bif*), Bifurcation to Bifurcation (*Bif-Bif*) and Bifurcation to Terminal (*Bif-Term*). Generally, Obj2mesh are total objects which should be meshed. In obj2mesh matrix first column indicates if the data is bifurcation (3), *Bif-Bif* (2) or *Bif-Term* (1).

In the case of bifurcation, the second column indicates the input branch and 3rd and 4th column shows two output fork branches. In bifurcation to bifurcation, the second column indicates the index *Bif-Bif* and 3th and 4th column shows that the *Bif-Bif* is attaching to which bifurcation index. This structure is the same for *Bif-Term* with only this difference is in *Bif-Term*, vessels are free in one side which is indicating with zero value in the 4th column and are only attached to one bifurcation Figure 13.

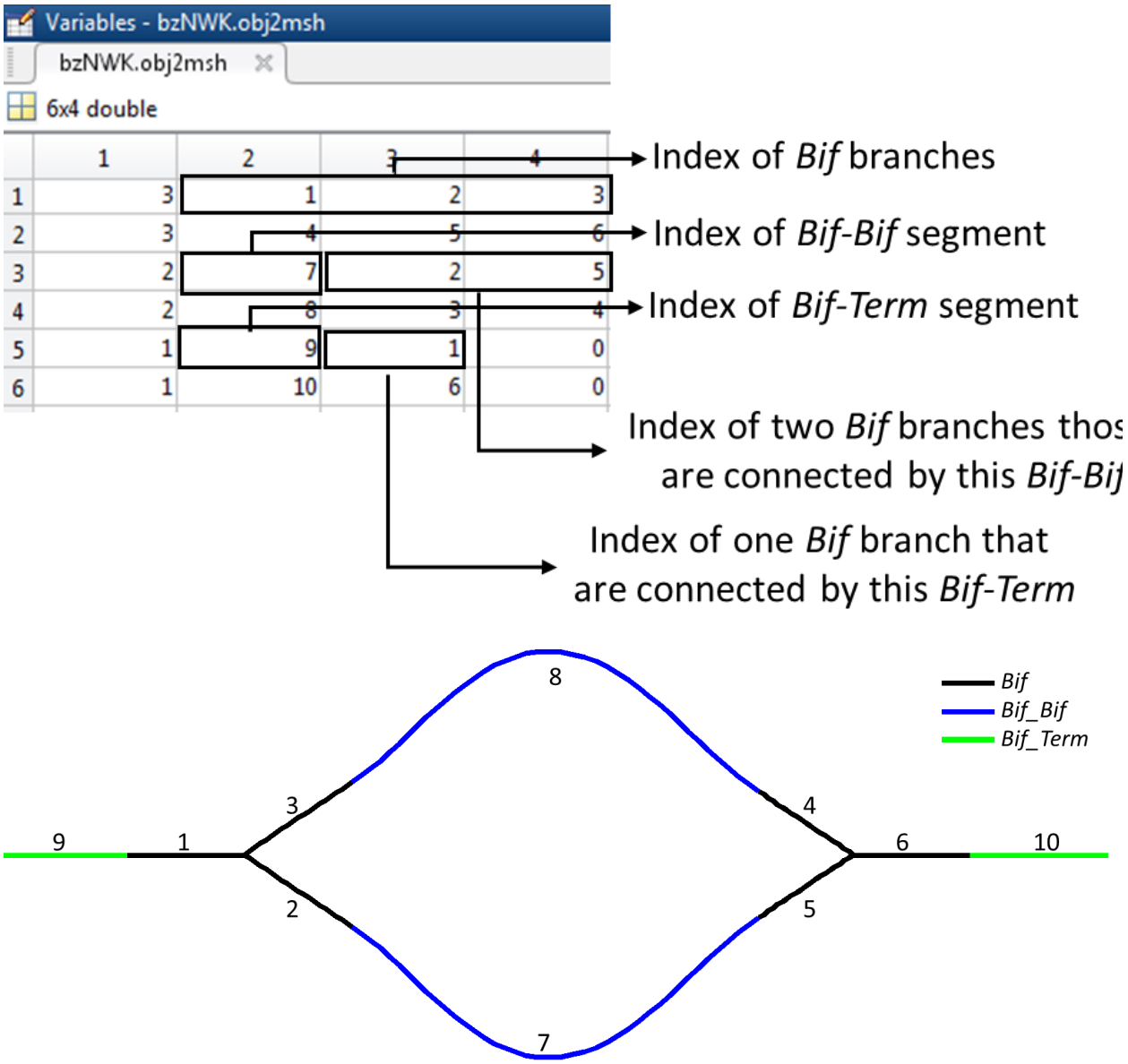

	1	2	3	4
1	3	1	2	3
2	3	4	5	6
3	2	7	2	5
4	2	8	3	4
5	1	9	1	0
6	1	10	6	0

Figure 13. The obj2msh matrix, this matrix was used to index each segmentation and the connectivity of vessels.

2.3.4. Bifurcation-Term

2.3.4.1. Import Bif-Term data set

Bif-Term segments are the portions of the vascular network connecting bifurcation branches to terminal nodes. In Figure 9, segment #9 and #10 are the two *Bif-Term* segments in the Simple Network, which are attached to #1 and #6 *Bif* branches, respectively. Here we first extract all *Bif-Term* segments and their corresponding attached *Bif* branches from Obj2msh matrix. *Bif* branch indices were deployed to access attached coupling-points. Figure 14 illustrates the coupling-points of #9 *Bif-Term*. Here we assumed that the coupling-points of #1 and #6 branches are computed. Details of the coupling-points computation are explained in *Bifurcation* section.

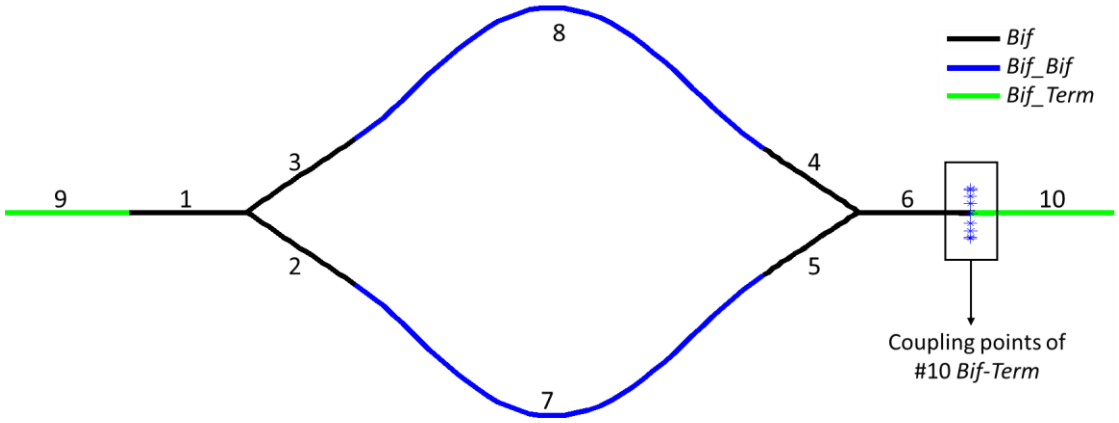

Figure 14. The coupling-points visualization. Coupling-points are the circumferential points coupling the *Bif* branch and neighboring *Bif-Term* segment.

2.3.4.2. Iso-planar mapping

Here we show how to project one single point to the cross-sectional section to enable circular cross-section generation. For this purpose, we introduce *iso-planar* mapping which has several advantages over the prior Frenet frame. A common problem of the Frenet frame is twisting [61], which we overcome by introducing a body-fitted coordinate system that moves along the curve as shown in Figure 15A and Equations (6)-(8).

$$\vec{\omega} = \vec{v}_i \times \vec{u}_i \tag{6}$$

$$\vec{u}_j = \vec{\omega} \times \vec{v}_j \tag{7}$$

$$P_j = O_j + \frac{\vec{u}_j}{\|\vec{u}_j\|} R_j \tag{8}$$

Here $\vec{v}_i$ is the normalized tangent vector at the centerpoint, O_i. $\vec{u}_i$ is a vector between the reference, P_i, and the centerpoint in the i^{th} cross-section. R_j is the vessels radius at the j^{th} cross-section. The reference point can be chosen among the circumferential points. Figure 15A illustrates the method to move the local frame between two cross-sections without twisting. It is termed *iso-planar* because P_j lies on the same plane, generated by P_i, O_i and O_j with the normal plane of $\vec{\omega}$. The use of a single plane eliminates the twisting problem at inflection points.

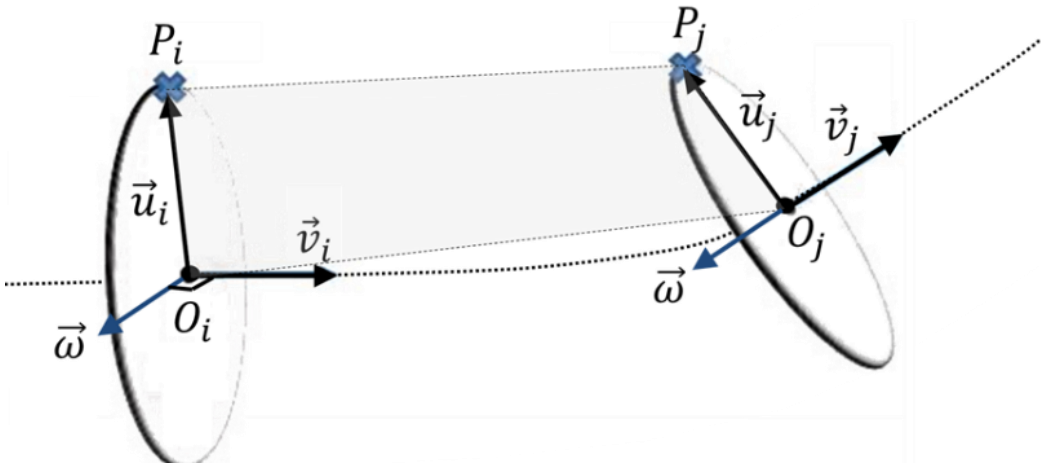

Figure 15. Iso-planar mapping. To build the mesh for a *Bif-Term* segment, a moving frame was implemented to sweep the local coordinate base vectors along the centerline. Reference point section, P_i, in the first cross-section was associated with the point, P_j, in the second cross-section using iso-planar mapping.

Figure 16B illustrates the projected points to the cross-sections referred to as reference points using isoplanar mapping. Reference points and Bezier curve information will be used to create a cross-sectional surface as shown in Figure 16C.

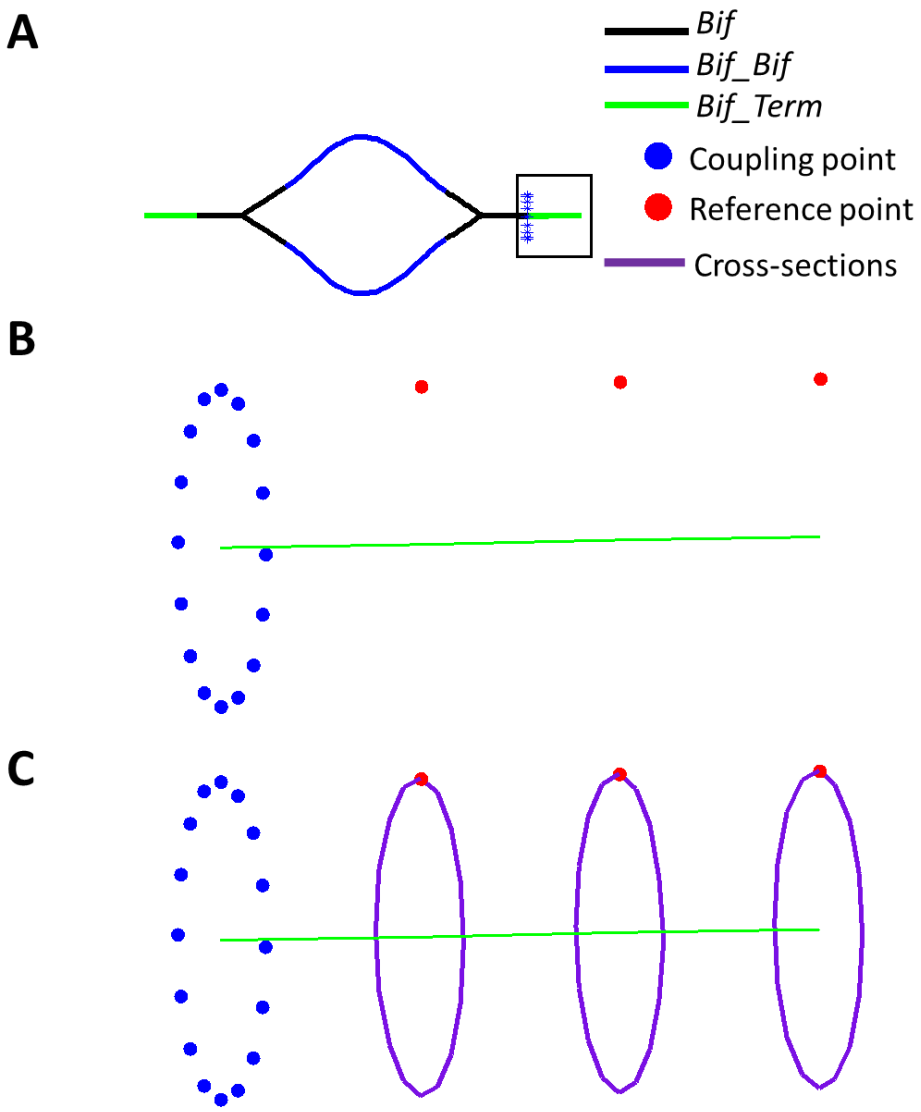

Figure 16. Cross-sectional mesh generation. (A) A *Bif-Term* segment from a simple vascular network with its corresponding coupling-points. (B) An arbitrary point was projected to the cross-sectional sections using Iso-planar Mapping to create Reference points. (C) Parametric circular curve was used to create cross-sectional surface points.

2.3.4.3. Circular cross-section generation

To develop parametric circular curve we used Equation (9).

$$P(\Theta) = R_i \cos(\Theta_i)\overrightarrow{v_i} + R_i \sin(\Theta_i)\ \overrightarrow{v_i} \times \overrightarrow{u_i} + O_i \qquad (9)$$

$\overrightarrow{u_i}$ is a unit vector from the center of the cross-section (O_i) to any point on the circle, which here is the reference point (red point in Figure 16). R_i is the local radius, $\overrightarrow{v_i}$ is a unit vector, perpendicular to the cross-sectional plane, which here is the first derivative of the Bezier curve centerline as shown in Figure 15. Figure 17 shows the final cross-sections for a tortuous vessel.

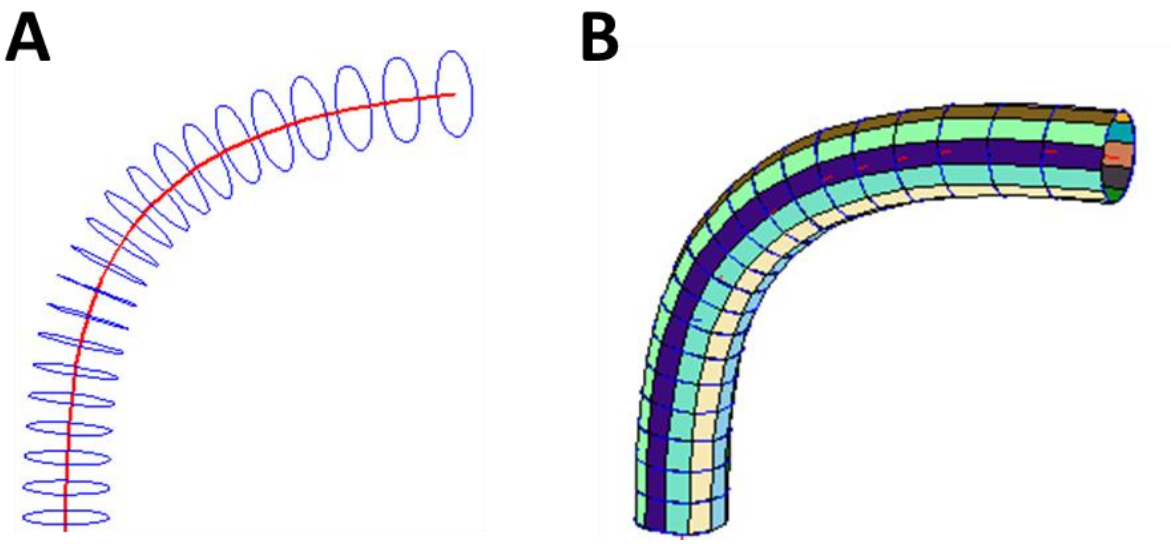

Figure 17. Surface meshes of the tortuous vessel. (A) Sweeping the circles along the Bezier curve as the first step of developing surface mesh. (B) Completed surface mesh for vessels, all cross section is perpendicular to the centerline.

2.3.5. Bifurcation

2.3.5.1. Prepossessing

Bifurcation regions were first extracted from Obj2msh as shown in Figure 13. Then, we computed the length of each branch of bifurcation, the velocity of the Bezier curves at the first and end of each branch. Next step is to create the topology of bifurcation region using separation and control points.

2.3.5.2. Compute separation and control points

Bifurcation branches require a unique procedure to define the *separation region* and maintain geometrical continuity between connected branches. The *separation region* is defined around the bifurcation point *B* by three separation points, *S*, and two control points, *CP*. The three branches of a bifurcation were indexed as *a*, *b*, and *c* as shown in Figure 19.

All three Bezier curves of the bifurcation branches are in an outward direction, starting from Bifurcation point (t = 0) to the terminal branch (t =1). Normal velocity vector of Bezier curves at bifurcation point was calculated using Equation (10). Then coordinates of separation points, S_{ab}, S_{bc}, S_{ac}, were calculated between the branches of *a*-*b*, *b*-*c*, and *a*-*c*, respectively using Equations (11) and (12), as shown in Figure 18. To complete the *separation region* geometry, the normal vector of the separation plane, $\vec{n}$, was extended by a magnitude equal to the mean radius to find control points, CP_1 and CP_2, using Equations (13)-(15) as shown in Figure 19.

$$\overrightarrow{v_a} = \frac{B_a(t=0)}{\|B_a(t=0)\|} \tag{10}$$

$$\overrightarrow{K_{ab}} = \frac{(R_a\overrightarrow{v_b} + R_b\overrightarrow{v_a})}{\|R_a\overrightarrow{v_b} + R_b\overrightarrow{v_a}\|} \tag{11}$$

$$S_{ab} = \begin{cases} B + \overrightarrow{K_{ab}} \cdot \dfrac{R_a}{\sin\left[tan^{-1}\left(\frac{R_a}{R_b}\right)\right]}, & \alpha \le 90° \\ B + \overrightarrow{K_{ab}} \cdot (R_a + R_b)/2, & \alpha > 90° \end{cases} \quad (12)$$

$$\vec{n} = (S_{ac} - S_{ab}) \times (S_{bc} - S_{ab}) \quad (13)$$

$$CP_1 = B + \vec{n} \cdot (R_a + R_b + R_c)/3 \quad (14)$$

$$CP_2 = B - \vec{n} \cdot (R_a + R_b + R_c)/3 \quad (15)$$

Where the unit tangent vectors of $\overrightarrow{v_a}, \overrightarrow{v_b}, \overrightarrow{v_c}$ are at the bifurcation point are equal to the derivative of Bezier curve at t = 0 on a, b, c branches, respectively. ||.|| denotes the Euclidean norm. α is the angle between two unit vectors of $\overrightarrow{v_a}$ and $\overrightarrow{v_b}$. R_a and R_b are the radii corresponding to the branches of a and b, respectively. CP_1 and CP_2 are the control points located above and below the separation plane.

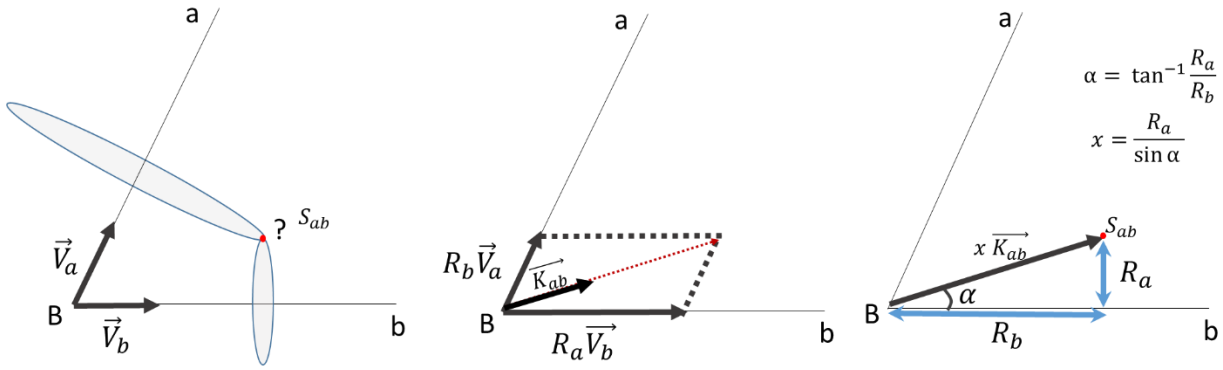

Figure 18. Illustration of separation point calculation between branches “a” to “b”.

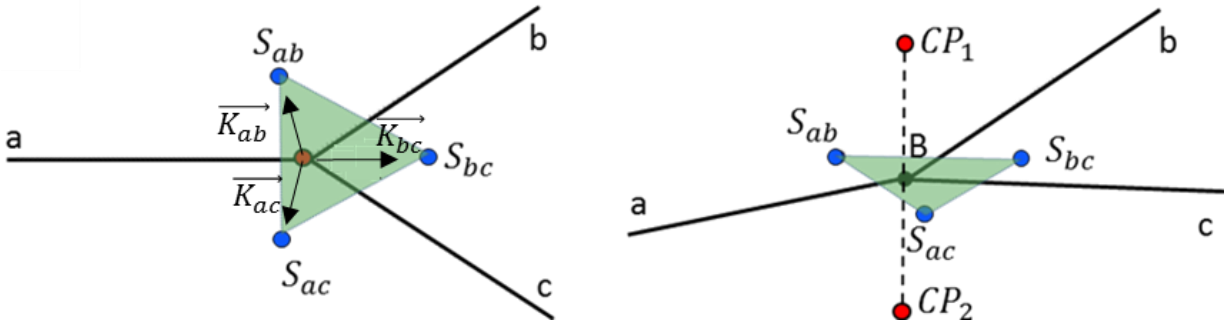

Figure 19. Separation and control points generation. Separation points, S, are located between two bifurcation branches. In the left Panel, control points, CPs, lie above and below the separation plane (transparent green plane). In the left panel, six parametric curves connecting CPs and S form the bifurcation geometry.

2.3.5.3. Correction of bifurcation geometry, detection of one-sided bifurcation

The formulae for the computations of the bifurcation geometry requires the detection of one-sided versus two-sided bifurcations. One-sided bifurcations have both outgoing branches on the same side of the incoming branch as illustrated in Figure 20A-B, and require a reflection operation to compute the separation point.

Assuming that $\vec{V}_i$ is the first derivative of the Bezier curves at the bifurcation point from an incoming branch; and $\vec{V}_j$ and $\vec{V}_k$ are the first derivative of Bezier curves for two outgoing daughter bifurcation branches, respectively, as shown in Figure 20C-D.

In a two-sided bifurcation branch, the dot-product of the T-vectors $\vec{T}_1 = (\vec{V}_i \times \vec{V}_j)$ and $\vec{T}_2 = (\vec{V}_i \times \vec{V}_k)$ is negative, $\vec{T}_1 \cdot \vec{T}_2 < 0$. This case requires no further action. A positive value of $(\vec{T}_1 \cdot \vec{T}_2)$ indicate a one-sided bifurcation orientation. For one-sided bifurcations, the minimum angle between $\vec{V}_i$ and two velocity vector of daughter branches ($\vec{V}_j$ and $\vec{V}_k$) were calculated (branch *j* in Figure 20B). Then the relevant separation point (S_{ij}, in Figure 20 D) was reflected on the other side of the branch to get the corrected separation point. The pseudo code for one-sided bifurcation detection and geometry correction is written in Table 2.

Table 2. One-sided bifurcation detection and separation point correction.

Algorithm One-sided bifurcation detection for bifurcation

Input: Three Bezier curves information for a bifurcation with tangent vector of $\vec{V}_i$ for parent branch and $\vec{V}_j$ and $\vec{V}_k$ for two daughter branches. Calculated Separation Points S_{ij}, S_{jk}, S_{ik}, and bifurcation point (B).

Output: Return correct Separation Point calculation for one-sided bifurcations.

$\vec{T}_1 \leftarrow (\vec{V}_i \times \vec{V}_j)$

$\vec{T}_2 \leftarrow (\vec{V}_i \times \vec{V}_k)$

$if\ (\vec{T}_1 \cdot \vec{T}_2) > 0$ //Indication of one-sided bifurcation

$\propto_{ij} =$ CalculateAngle$(\vec{V}_i, \vec{V}_j)$

$\propto_{ik} =$ CalculateAngle$(\vec{V}_i, \vec{V}_k)$

If $\propto_{ij} < \propto_{ik}$

$S_{ij} \leftarrow B - (S_{ij} - B)$

elseif

$S_{ik} \leftarrow B - (S_{ik} - B)$

end

return Separation Points

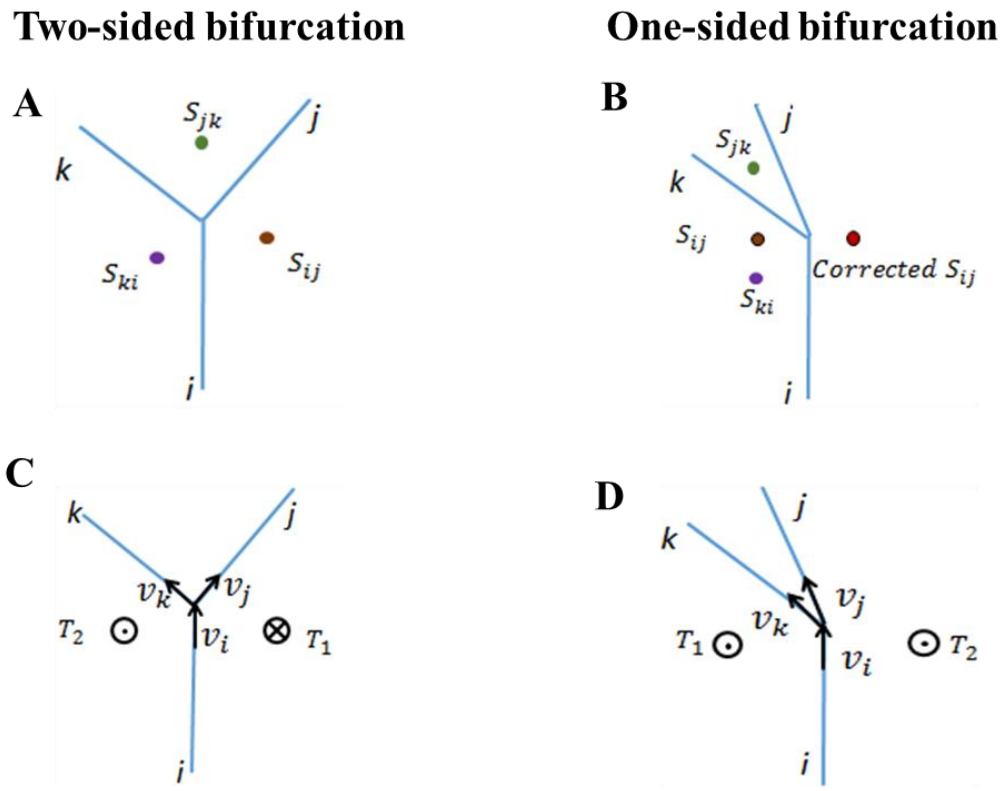

Figure 20. Bifurcation orientation detection. The aim is to distinguish between two-sided and one-sided bifurcation branches. Separation points are well defined in (A), however in one-sided bifurcation branches S_{it} is not on the right side between the "j" and "i" branches (B). To solve this problem, $\vec{T}_1 = (\vec{V}_i \times \vec{V}_j)$ and $\vec{T}_2 = (\vec{V}_i \times \vec{V}_k)$ were calculated and compared (C-D). In one-sided bifurcations, $\vec{T}_1$ and $\vec{T}_2$ vectors have the same directions. If one-sided bifurcation is detected, relevant separation point should be reflected to the other side of bifurcation to correct bifurcation topology $S_{ij} \rightarrow$ "Corrected S_{ij}".

2.3.5.4. Bifurcation-site points generation

Parametric curves are generated to connect control points to separation points. Figure 21 shows the six curves reached to build the bifurcation geometry that links CP (Control points) and S (separation points). A radial parameter, *r(t)*, was computed between each control and separation point using Equation (16). A parametric curve equation in Equation (17) determines the position of surface nodes, which will serve as guide points for the vessel surface mesh.

$$r(t) = t \cdot \|\vec{U}\| + (1-t) \cdot \|\vec{K}\|, \; t \in [0,1] \tag{16}$$

$$f(t,\Theta) = r(t)\cos(j\Theta)\ \overrightarrow{e_U} + r(t)\sin(j\Theta)\ \frac{\overrightarrow{e_T}\times\overrightarrow{e_U}}{\|\overrightarrow{e_T}\times\overrightarrow{e_U}\|} + B, \qquad j = \left\{1, 2, \dots, \frac{N}{4}\right\} \tag{17}$$

Vector $\vec{U}$ and $\vec{K}$ connect separation and control point to bifurcation point *B*, respectively, as shown in Figure 21. $\|\cdot\|$ denotes the magnitude of the vector. $\overrightarrow{e_i}$ corresponds to the unit vector of i. $\vec{T}$ denotes a unit vector to the plane of *CP*, *S*, and *B*. The parametric curve, $f(t,\theta)$, is a scalar function with two independent variables of t and θ representing the radial and angular parameters, respectively. *N* is the number of nodes on the circumference of the structured cross-section. For each quarter, *N/4* points were calculated to partition each parametric curve using Equation (17).

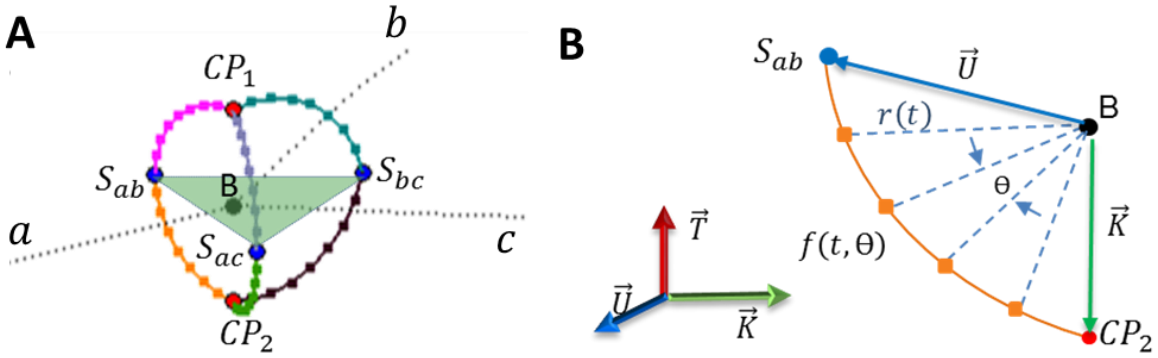

Figure 21. Bifurcation-site points generation. Six color-coded parametric curves connecting CP and S form the bifurcation geometry. The generated points using these parametric curves are referred as bifurcation-site points. (B) The schematic illustrates parametric curves between S_{ab} and CP_2.

2.3.5.5. Coupling-points generation

The purpose of this section is to generate coupling-points using bifurcation-site points in Figure 22. Coupling-points are the circumferential points coupling the *Bif* branch and neighboring *Bif-Term* segment. Here we simply projected the bifurcation site-points to the corresponding terminal branch to generate coupling-points.

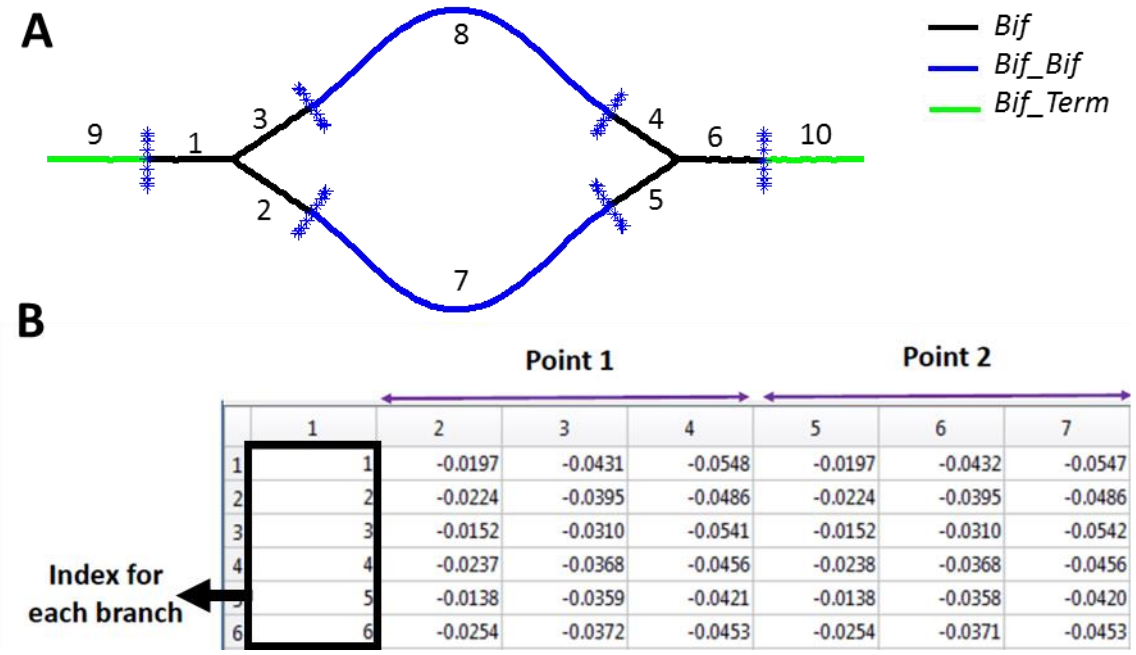

Figure 22. Coupling-points storage for Bifurcation branches. (A) Blue points are the coupling-points between *Bif* to either *Bif-Term* or *Bif-Bif* segment. (B) Coupling-points are stored in a matrix which the first column represents the index of the bifurcation branches. The point coordinates are stored sequentially.
Figure 22

Projection algorithm

To create the surface mesh for a bifurcation branch, points were projected on the inlet and outlet planes. Figure 23 shows the detailed illustration of CP_1 projected on plane labelled "a". Inlet cross-section of "a" with the center of O_a, and R_a is located on a-plane with the normal vector of $\vec{n}$. Initially, CP_1 was projected on the plane to find CP_{1a} using Equations (18) and (19). Then, thecorresponding point of CP_{1a}, on the surrounding of the inlet cross section, was found using Equation (20). Therefore, CP'_{1a} is the projection of CP_1 on the cross-section of "a".

$$\vec{q} = CP_1 - O_a \quad (18)$$

$$CP_{1a} = CP_1 - [\vec{n}(\vec{q} \cdot \vec{n})] \quad (19)$$

$$CP'_{1a} = O_a + R_a\left(\frac{CP_{1a} - O_a}{\|CP_{1a} - O_a\|}\right) \quad (20)$$

Which, $\vec{n}$ in a unit vector and "$\cdot$" is dot product. If the CP_{1a} is inside the cross-section or outside, Equation (20) still calculate the same value. The pseudo code for projection is written in Table 3.

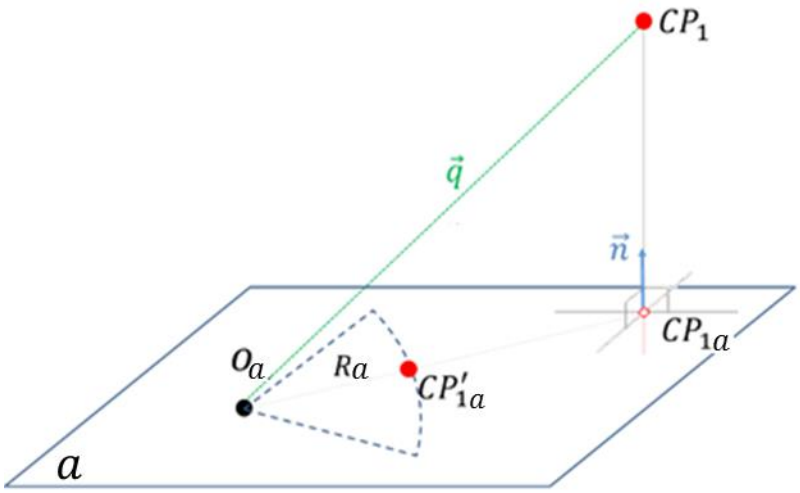

Figure 23. Projection of CP_1 point on k-inlet. Inlet cross section of k, with the center of O_a and R_k, is located on O_a-plane with the normal vector of $\vec{n}$. Initially, CP_1 was projected on the plane to find CP_{1a}. CP'_{1a} is the projection of CP_1 on circular cross-section.

Table 3. Pseudo code projection of a bifurcation site point on each inlet/outlet.

Algorithm (Find projection of a bifurcation site point on each inlet/outlet)
Input: The center of circular inlet/outlet O_a The radius of circular inlet/outlet R_a, The normal vector of the plane $\vec{n}$ Given point for projection CP_1
Output: Return a single point (CP'_{1a}) on bifurcation inlet/outlet
$\vec{q} \leftarrow CP_1 - O_k$
$CP_{1a} \leftarrow CP_1 - [\vec{n}(\vec{q} \cdot \vec{n})]$ //Project CP_1on a-plane
$CP'_{1a} \leftarrow O_a + R_a \left(\frac{CP_{1a} - O_a}{\|CP_{1a} - O_a\|}\right)$
return (CP'_{1a})

2.3.5.6. Coupling-points storage

Coupling-points are the circumferential points coupling the *Bif* branch to either *Bif-Term* or *Bif-Bif* segment. Generated coupling-points in Bif segment should be stored and used for mesh

generation of *Bif-Term* or *Bif-Bif* segment to ensure the nodal connectivity between segments. Figure 22 shows the coupling-points in a simple network.

2.3.5.7. Bifurcation surface mesh generation

In this section, we will show the stepwise procedure to develop surface meshes for bifurcations. Here, we first calculated longitudinal surface Bezier curves, then we partitioned the surface curves to the required mesh density. This method guarantees a penetration-element-free region in bifurcations.

Table 4 is the pseudo code for surface Bezier curve generation on the vessel wall of the bifurcations. Figure 24 shows the stepwise workflow to generate vessel wall mesh for bifurcations. To accomplish this section, we required several procedures such as Bezier subdivision, Casteljau algorithm, minimum distance, and offset Bezier curve algorithm. Bezier subdivision has been explained in the *Bif-Term* region. Minimum distance and offset Bezier curve algorithm are defined in this section.

Table 4. Pseudo code of generation of parallel Bezier curve for bifurcations.

Algorithm. Generation of surface Bezier curve for bifurcations.

//Return a Bezier curve ($B^I(t) = P_0^I, C_0^I, C_1^I, P_1^I$ given a Bezier curve of $B(t) = P_0, C_0, C_1, P_1$.

$P_0^{II} \leftarrow Minimum\ distance\ algorithm(P_0, B(t))$

$C_0^{II}, C_1^{II}, P_1^{II} \leftarrow Subdivision\ method(P_0^{II}, B(t))$

$C_0^I, C_1^I, P_1^I \leftarrow Offset\ Bezier\ algorithm(P_0^I, B(t))$

return $(B^I(t))$

Step I: The purpose is to find the C_0^I, C_1^I in a way that generate a Bezier curve surface perpendicular to the centerline Bezier curve.	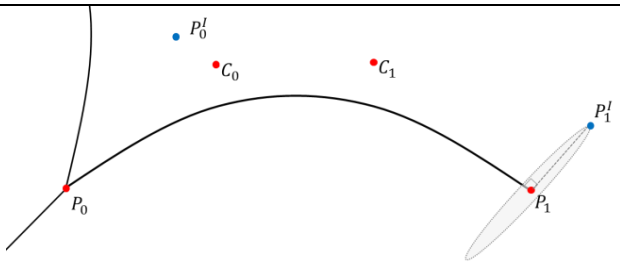
Step II: Minimum distance algorithm	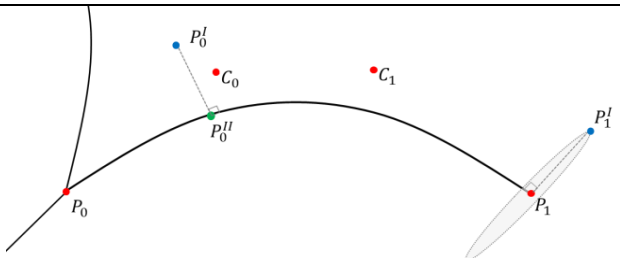
Step III: Subdivision Method	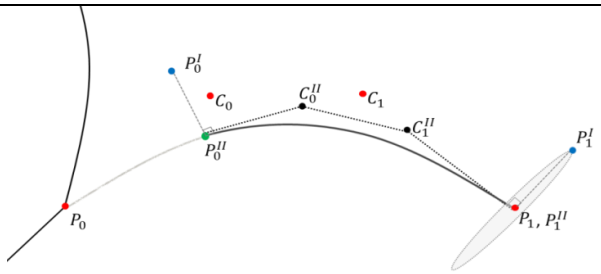
Step IV: Bezier Offset algorithm	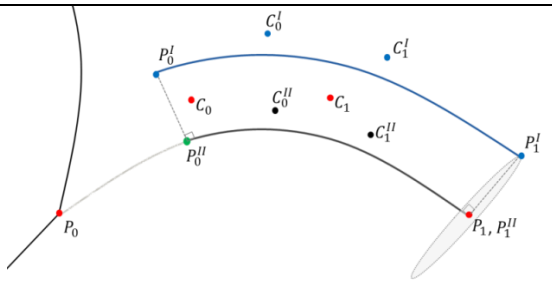
Step V: Another example	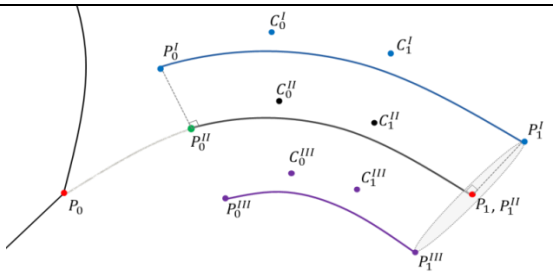

Figure 24. Stepwise surface Bezier curve generation for bifurcations. Step I: B(t) = P_0, C_0, C_1, P_1 are the Bezier curve information for one bifurcation region, P_0^I are a point in bifurcation sire region and P_1^I is a point on the outlet. Our aim is to find C_0^I & C_1^I in way that $B^I(t)$ is perpendicular to B(t). Step II: P_0^{II} is a point on B(t) which has the minimum distance to P_0^I. Step III: Using subdivision method, C_0^{II} and C_1^{II} are calculated. Step IV: Bezier offset equation were used to calculate C_0^I & C_1^I.Step V shows another Bezier surface $B^{II}(t) = P_0^{II}, C_0^{II}, C_1^{II}, P_1^{II}$.

To complete the surface mesh generation, control points are transferred to create parallel Bezier curves using Bezier offset algorithm for one Bezier surface curve, as shown in Figure 25A. All Bezier surface curves were generated using Bezier offset algorithm, Figure 25B. A number of the Bezier surface curves depends on the desired circumferential mesh density. Figure 25C shows the longitudinal refinement of the Bezier surface curves along the vessel wall. For example, all Bezier curves with t = 0, 0.1, 0.2... 1 are grouped and connected to finalize the surface mesh. Figure 25C illustrates a completed surface mesh on a single branch of a *Bif* segment.

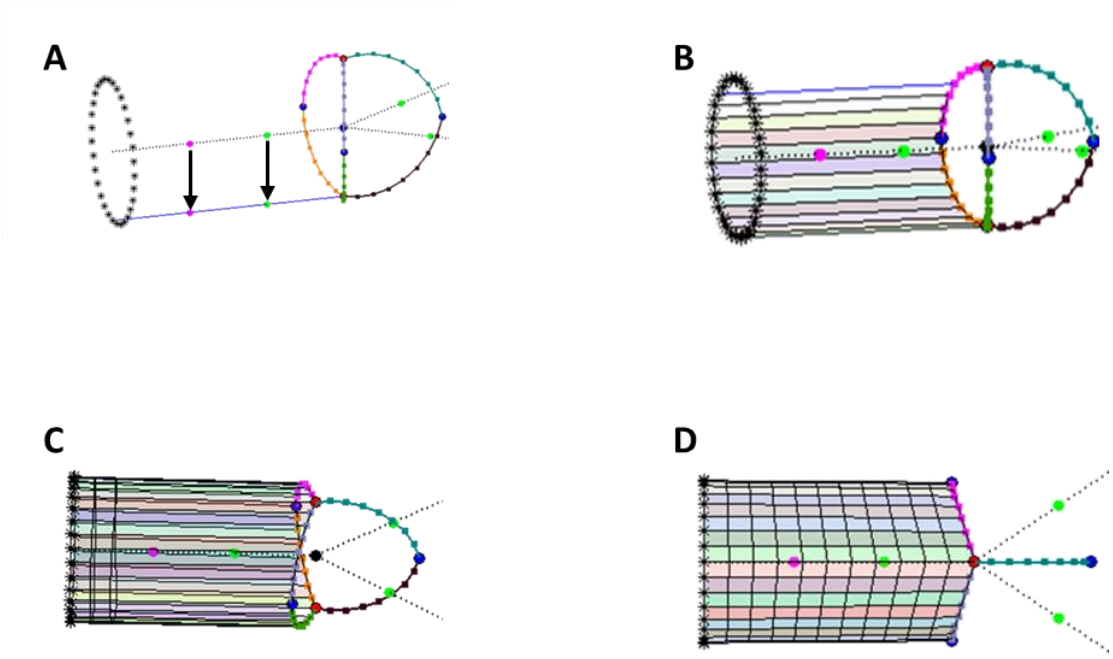

Figure 25. Surface mesh generation for bifurcations. (A) Control points are transferred to create parallel Bezier curves using Bezier offset algorithm. (B) More Bezier surface curves were generated using Bezier offset algorithm. (C) Depending on the desired density, longitudinal mesh is developed. For example, all Bezier curves with t = {0, 0.1, 0.2... 1} are grouped and connected to finalize the surface mesh. (D) Completed surface mesh for one branch of bifurcation.

Minimum distance algorithm and Bezier offset algorithm are explained here in details. These two algorithms were used to accomplish Bezier surface mesh generation as discussed in Figure 24.

2.3.5.8. Minimum distance algorithm

Table 5 is a detailed explanation of minimum distance algorithm.

Table 5. Algorithm to compute minimum distance from a single point to a Bezier curve.

//Return a single point ($\widehat{Q}$) on the Bezier curve given point Q and the Bezier curve of $B_1(t) = P_0, C_0, C_1, P_1$.

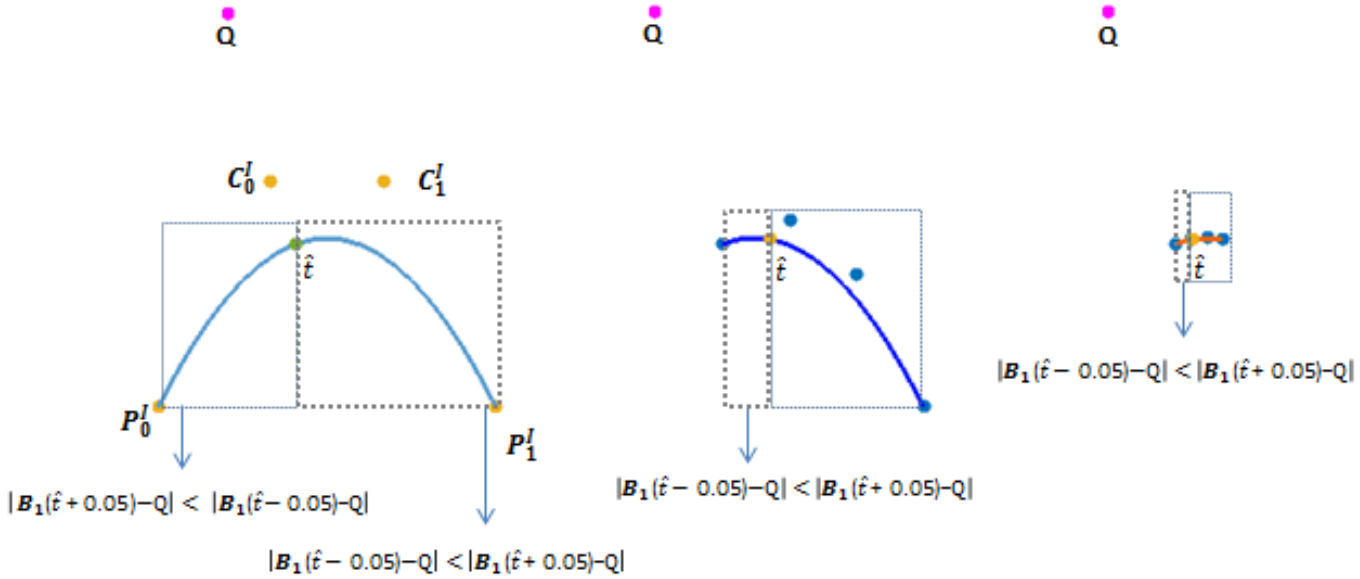

Set MaxIteration
iteration ← 1
while *iteration* ≤ *MaxIteration* **do**
    if $|Q - C_0| \leq |Q - C_1|$ **then**
    $\widehat{Q} \leftarrow C_0$
    else
    $\widehat{Q} \leftarrow C_1$
    end if
    $[\hat{t}] \leftarrow Parametrized\ t(\widehat{Q}, [P_0, C_0, C_1, P_1])$
    $B_{11}, B_{12} \leftarrow Subdivide(B_1, \hat{t})$
        if $|B_1(\hat{t} - 0.05)| < |B_1(\hat{t} + 0.05)|$ **then**
        $B_1 \leftarrow B_{12}$
        else
        $B_1 \leftarrow B_{11}$
        end if
    return $(B_1, \widehat{Q})$
end while

2.3.5.9. Bezier offset algorithm

In some vessels with high tortuosity and bifurcations circular cross-section may results in penetrating elements. Instead, we can first create surface Bezier curve and then partition the Bezier surface to complete surface meshes. Here, we explain Bezier offset algorithm to create longitudinal Bezier curve on the surface.

Parallel Bezier curves are developed by enforcing offset around the centerline to compute new control points for surrounding surface Bezier curve. Figure 26 shows the schematic of offset algorithm to calculate parallel Bezier curve using Equations (21)-(24). This technique can be used for *Bif-Term* and *Bif-Bif* mesh generation.

$$\overrightarrow{d_0} = P_0^I - P_0 \tag{21}$$

$$\overrightarrow{d_1} = P_1^I - P_1 \tag{22}$$

$$C_0^I = C_0 + \left(\frac{2}{3}\overrightarrow{d_0} + \frac{1}{3}\overrightarrow{d_1}\right) \tag{23}$$

$$C_1^I = C_0 + \left(\frac{1}{3}\overrightarrow{d_0} + \frac{2}{3}\overrightarrow{d_1}\right) \tag{24}$$

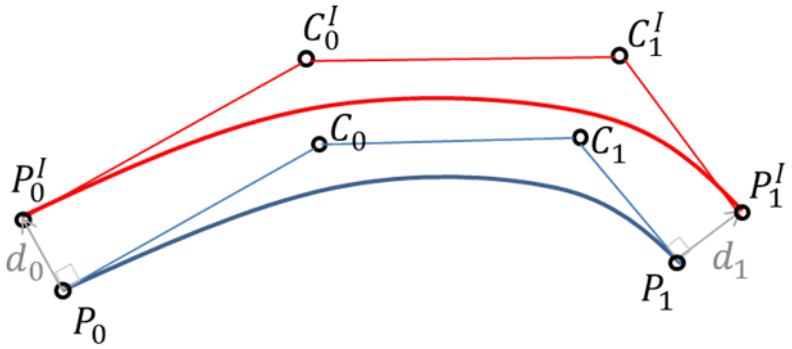

Figure 26. Offset development to compute new control points for parallel Bezier curves. Blue Bezier curve is the centerline and red Bezier curve is a surface Bezier curve.

2.3.5.10. Geometrical continuity between branches

The aim of this section is to show the method to keep the geometrical continuity in bifurcations. Initially, parallel Bezier curves were found for all three branches. Then, two by two branched were

smoothed by updating the bifurcation site points, Figure 28. Please note that ($P_0^I = P_0^{II}$). Euclidian distance between C_0^I to P_0^I as well as C_0^{II} to P_0^{II} were calculated using Equations (25) and (26). P^* is the updated point which will be replaced of P_0^I and P_0^{II} to keep the continuity, Equation (27). Geometrical continuity between two curves are shown in Figure 27.

$$D_1 = \sqrt{{C_0^I}^2 + {P_0^I}^2 - 2C_0^I \cdot P_0^I} \tag{25}$$

$$D_2 = \sqrt{{C_0^{II}}^2 + {P_0^{II}}^2 - 2C_0^{II} \cdot P_0^{II}} \tag{26}$$

$$P^* = \left(\frac{D_2}{D_1+D_2}\right) C_0^I + \left(\frac{D_1}{D_1+D_2}\right) C_0^{II} \tag{27}$$

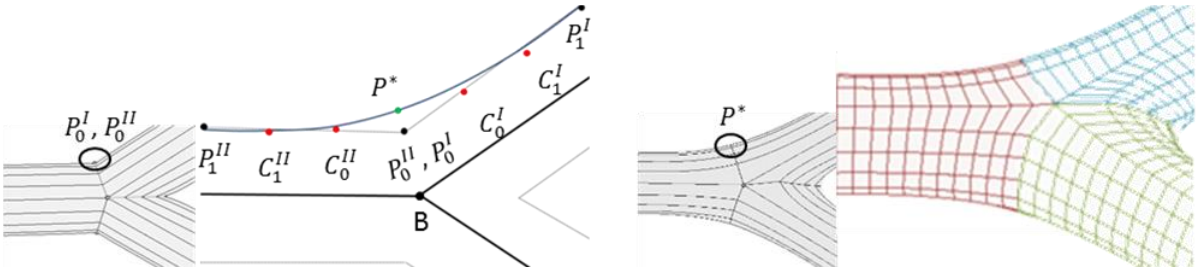

Figure 27. Geometrical continuity between two bifurcation branches. Smooth connections between branches avoid tangent discontinuity in the bifurcation surface geometry (as illustrated in left panel). A new control point P^* (marked in green) is inserted so that both branches connect smoothly (G^1-continuity). For each bifurcation branch, Bezier surface curves are partitioned longitudinally to span a structured parametric bifurcation surface mesh (as shown in the right panel). Note that resulting grids are shown with lower mesh density so that grid lines are better visible.

In Figure 28, step II shows the G1 continuous bifurcation. However, some elements are too stretched due to the extension of bifurcation region. To overcome this problem control points, shown in red color, are also updated. The average of three orange points was used as a substitution for control points. Pseudo code for G1 continuity at bifurcations is written in Table 6.

When the surface mesh generation is completed, volume mesh generation was implemented to create inner elements. This technique will be discussed in section 2.3.7.1.

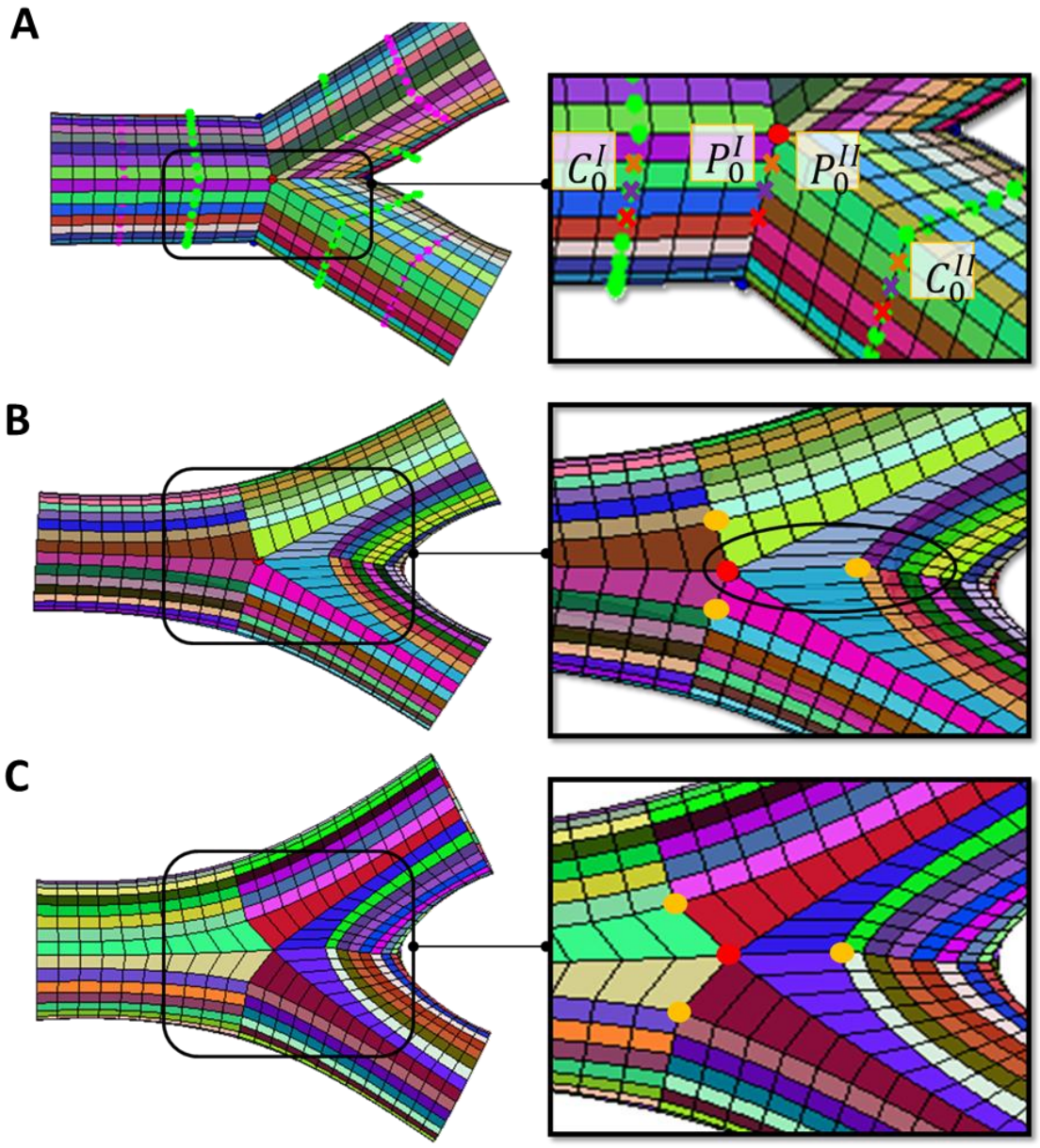

Figure 28. Geometrical continuity between bifurcation branches. (A) Two by two, Bezier curves are grouped for keeping the continuity. C_0^I & P_0^I as well as C_0^{II} & P_0^{II} are an example of grouped curves ($P_0^I = P_0^{II}$), shown in an orange cross. (B) P_0^I & P_0^{II} are updated using Equation (27) to keep the G1 continuity. (C) The mean of the orange circle points locations was used to update control points.

Table 6. Pseudo code projection of a bifurcation site point on each inlet/outlet.

Algorithm (Generation of smooth surface mesh for bifurcation)

Input: a set of two Bezier curves (C_0^I, P_0^I & P_0^{II}, C_0^{II}) which $P_0^I = P_0^{II}$

Output: Return an update point P^* which should be replaced by P_0^I& P_0^{II}

$D_1 \leftarrow$ Computer Distance(C_0^I, P_0^I)

$D_2 \leftarrow$ Computer Distance(C_0^{II}, P_0^{II})

$P^* \leftarrow \left(\frac{D_2}{D_1+D_2}\right) * C_0^I + \left(\frac{D_1}{D_1+D_2}\right) * C_0^{II}$ //Update P_0^I& P_0^{II}

$P_0^I \leftarrow P^*$

$P_0^{II} \leftarrow P^*$

return ($P_{0,}^I P_0^{II}$)

2.3.6. Bifurcation to Bifurcation

2.3.6.1. Preprocessing, circle points

We used the obj2msh matrix, as shown in Figure 13, to find the neighboring bifurcations for each *Bif-Bif* vessel. Then we extract corresponding attached point to the bifurcation regions using the coupling-points. Coupling-points are the points on the wall of the inlets or outlets of the bifurcation. Two sets of coupling-points at the first and at the last of each *Bif-Bif* section segment are required to generate parametric meshes.

2.3.6.2. Check coupling-point rotation

The order of the points is of great importance in mesh development, which will be more discussed in *Bif-Bif* network part. In *Bif-Bif* matrix, the same clockwise or counterclockwise rotation of coupling-points is of great importance to avoid twisting problem. Figure 29 illustrates a twisting problem in Bif-Bif where the coupling-points were the same rotation format.

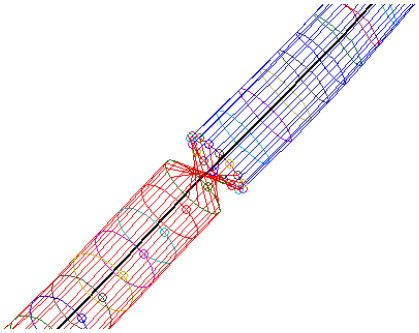

Figure 29. Twisting problem in *Bif-Bif*. This problem happens when both inlet and outlet coupling-points do not have the same clockwise or counterclockwise rotation.

Table 7 is the pseudo code to align coupling-points orientation to avoid twisting problem. If multiplication of two scalar value of N_1 and N_2, Equations (28) and (29), are positive, one of the coupling-point need to be reversed to avoid mesh twisting.

$$N_1 = \left|(\overrightarrow{A_1 - O_1} \times \overrightarrow{A_2 - O_1})\right| . \left|(\overrightarrow{C_1 - O_1})\right| \quad (28)$$

$$N_2 = \left|(\overrightarrow{B_1 - O_1} \times \overrightarrow{B_2 - O_1})\right| . \left|(\overrightarrow{C_2 - O_2})\right| \quad (29)$$

In which O_1 and O_2 are the first and the last terminal points of the Bezier spline of the *Bif-Bif* centerline. Similarly, C_1 and C_2 are the first and the last control points of the Bezier spline of the *Bif-Bif* centerline. In other words, C_1 and C_2 are the closest Bezier control points to the inlet and outlet of the Bif-bif segment. "$\cdot$", and "$\times$" are dot and cross product, respectively. $|.|$ denotes the norm of a vector.

Table 7. Coupling-points rotation algorithm to avoid twisting problem

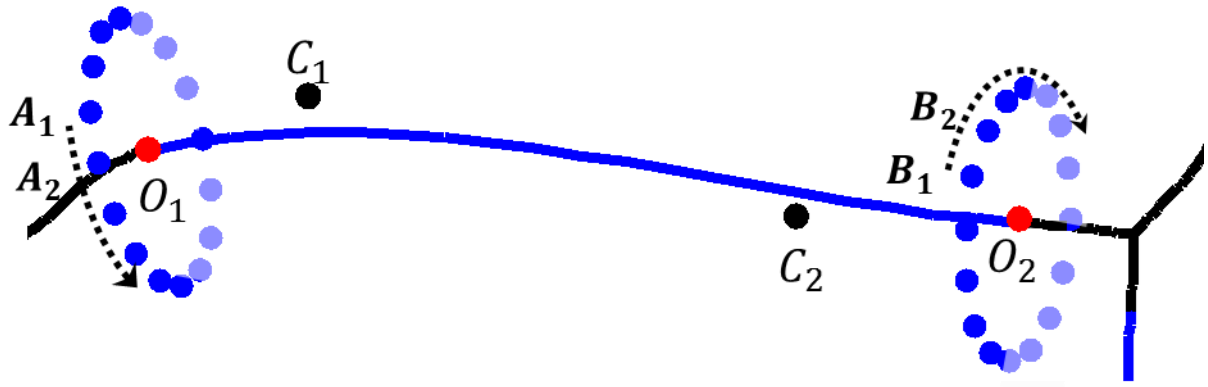

Input: Coupling-points set of two bifurcation branches A (inlet), B (outlet).
$\text{CouplingPoints}_1 = \{A_1, A_2, \dots A_n\}$, $\text{CouplingPoints}_2 = \{B_1, B_2, \dots B_n\}$
The Bezier spline of the *Bif-Bif* segment, O_1 and O_2 are the first and the end terminal points of the Bezier spline of the *Bif-Bif* centerline. C_1 and C_2 are the first and the last control points of the Bezier spline.
Output: Aligned coupling-points rotation to eliminate the twisting problem

1 $N_1 \leftarrow \left|(\overrightarrow{A_1 - O_1} \times \overrightarrow{A_2 - O_1})\right| . \left|(\overrightarrow{C_1 - O_1})\right|$;
2 $N_2 \leftarrow \left|(\overrightarrow{B_1 - O_1} \times \overrightarrow{B_2 - O_1})\right| . \left|(\overrightarrow{C_2 - O_2})\right|$;
3 $\varphi \leftarrow N_1 * N_2$;
4 //Check alignment of coupling-points direction based on γ
7 **If** $\varphi < 0$
8 $\text{CouplingPoints}_2 = \{B_n, B_{n-1}, \dots, B_2, B_1\}$;
9 **end If**
10 **Return** CouplingPoints_2;

2.3.6.3. Minimum torsion algorithm

In this section, we will show how two bifurcations can be attached together. First, we will define a critical point in the butterfly pattern of cross-sectional meshes. As shown in Figure 30, *critical points* are the points in the circumference of the cross-section, which are along the corner of the inner square inside the pattern. There are eight critical points in each cross-sectional mesh of vascular tree.

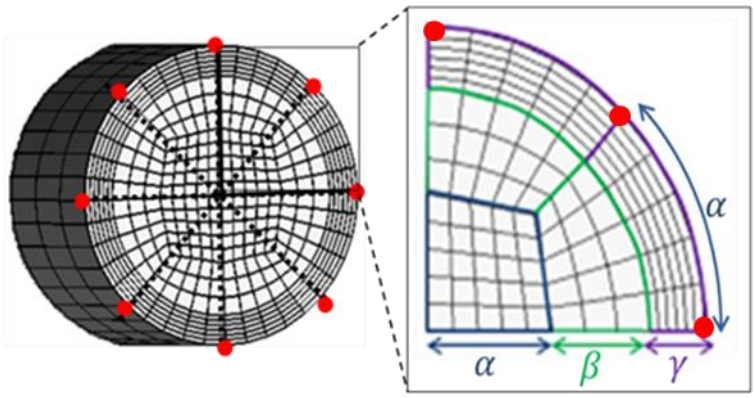

Figure 30. Schematic of critical points. For generating the volumetric meshes, cross-sections are swept and rotated along the longitudinal coordinate systems. Suitable selection of surface reference points (marked red) connect two bifurcation cross-sections to minimize rotation. The butterfly pattern allows for desired cross-sectional mesh refinement with the help of control parameters (α, β and γ).

In Figure 31, there is an angular difference between *i* and *j* in the cross-sectional patterns. To quantify the angular displacement, we define four critical points in j-cross-section, Bi (i ϵ [1, … , 4]). A critical point of i-cross section, Ai, is projected onto the other cross section ($\boldsymbol{A_i} \rightarrow \boldsymbol{A_j'}$). The minimum angular displacement ($\boldsymbol{\beta}$) is calculated between the $\boldsymbol{A_j'}$ and critical points on j-cross section. To complete the mesh, i-cross section will sweep and rotate along the centerline to fit the j-cross section. Table 8 shows the stepwise algorithm to connect two branches of bifurcations with minimum torsion algorithm.

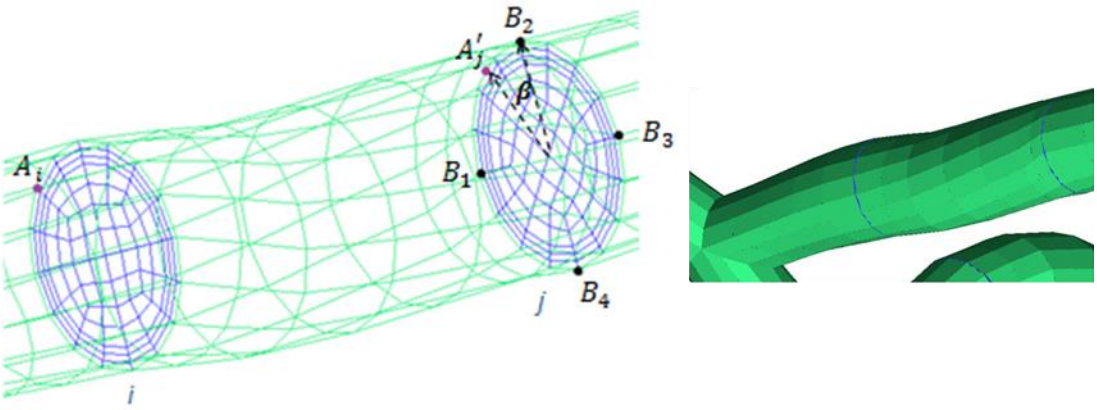

Figure 31. Bifurcation to bifurcation connection. A critical point on i-cross section is projected onto the j-cross section ($\mathbf{A_i} \rightarrow \mathbf{A'_j}$). The minimum angular displacement ($\boldsymbol{\beta}$) is calculated between the $\mathbf{A'_j}$ and critical points on j-cross section. *i*-cross section sweeps and rotated along the centerline to connect two bifurcations.

Table 8. Minimum torsion algorithm

Input: Cross-sectional point set of two bifurcation branches A, B.
Number of the required cross-sections in this Bif-bif segment: n.
Output: Bif-bif mesh section: BB

$S(A_1, A_2, A_3, A_4) \leftarrow$ Extract critical point of A;
$S(B_1, B_2, B_3, B_4) \leftarrow$ Extract critical point of B;
Project arbitrary point of $S(A)$, A_i on plane B
$A_{iB} \leftarrow$ ProjectPointOnPlane(A_i, B) //Project an arbitrary critical point of A onto Plane B
$B_i \leftarrow \text{FindClosetPoint}\big(A_{iB}, S(B_1, B_2, B_3, B_4)\big)$;
$\varphi \leftarrow \text{FindAngle}\big(A_{iB}, S(B_i)\big)$;
for each $\text{Cross} - \text{sectional point set of i} = \{1{:}\, n\}$ **do**
$BB_{\text{i}} \leftarrow \text{RotatePoints}(A, i \cdot \varphi/\text{n})$;
end for
Return BB;

Angular different from A1 and A2 will be calculated to detect required torsion. Maximum required torsion $\frac{pi}{(number\ of\ walls)}$, which can be minimize by increasing the number of surface walls.

Then we will use the Isoplanar mapping to project the point from each cross-section to the next cross-section to complete the mesh generation. The maximum angular difference between two neighboring cross-sections is $\frac{\varphi}{n}$, which φ is the angular difference between the projected critical point of plane A to the closest critical point of plane B. n is the number of required cross-sections to connect the vessel from plane A to plane B. Figure 32 is the completed *Bif-Bif* meshes forming a loop in the entrance of the anterior cerebral artery territory.

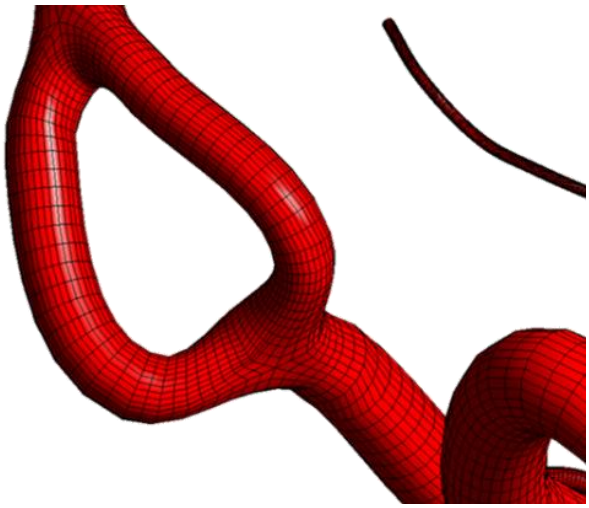

Figure 32. Subject-specific parametric mesh showing a section with two *Bif-Bif* segments forming a loop in the entrance of the anterior cerebral artery territory of *subject II*.

2.3.7. Volume mesh generation

To generate volume meshes, we first require the surface meshes for a single cross-section. In this section, we explained butterfly cross-sectional mesh generation using surface points which is applicable for all *Bif-Term*, *Bif* and *Bif-Bif* segments. Figure 33 illustrates the step-by-step progress of inner mesh generation. The topology is the butterfly pattern which requires the wall point to be divisible by four. Critical green points called (N_1, …, N_4) as shown in Figure 33A.

To develop butterfly topology, we first require selecting a critical point (Green point in Figure 33A), as well as eight inner points (blue and red points in Figure 33B). Then near-wall points were generated between close to the surface wall between 0.8R to R, which R is the local radius, Figure 33C. The intermediate-region between inner square and near-wall region were filled using linear line parametrization as visualized in Figure 33D. Figure 33E shows the completion of the intermediate-region. The inner square point was easily generated with dotted line parameterization of in Figure 33F.

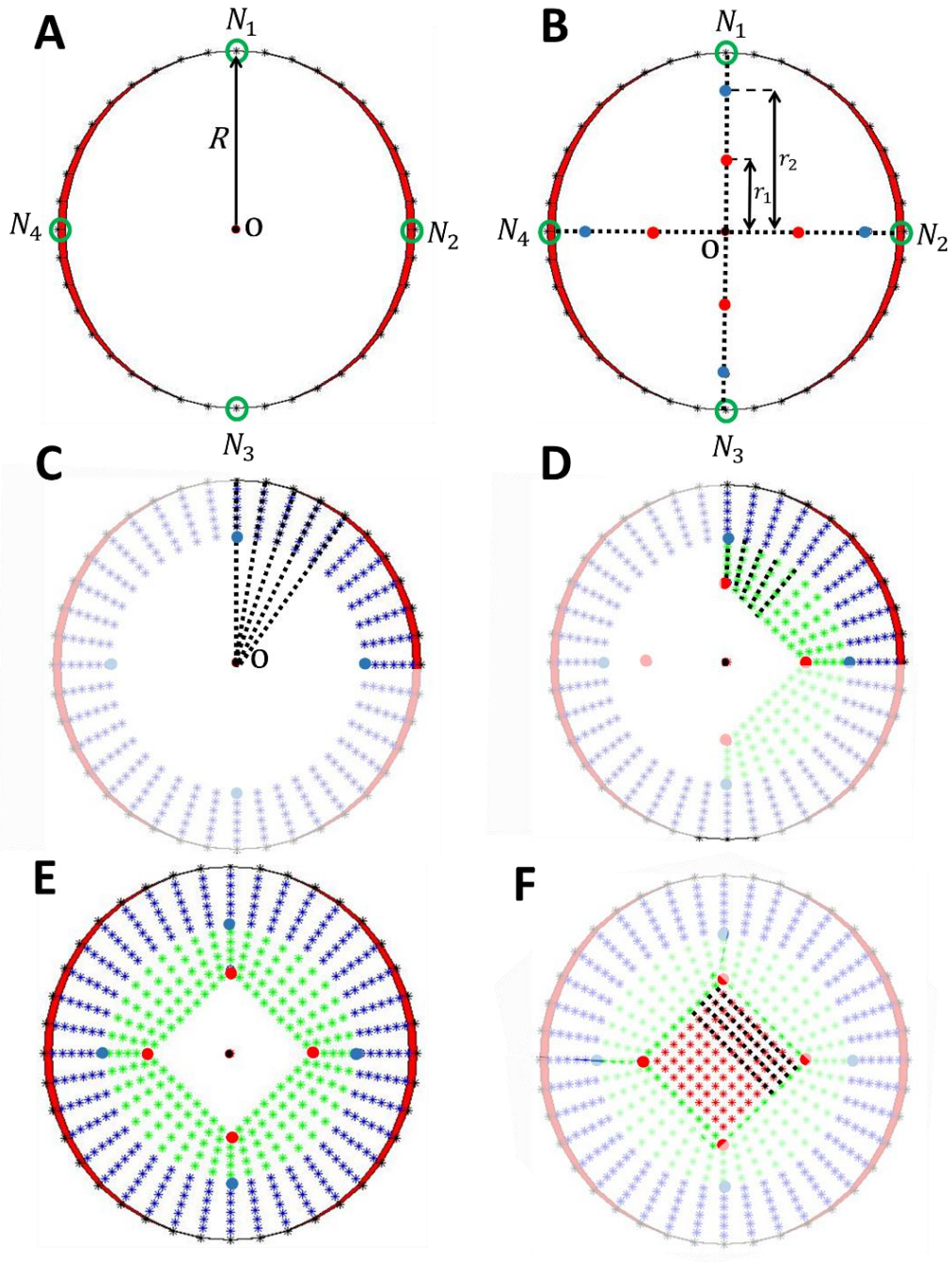

Figure 33. Inner cross-sectional mesh generation with Butterfly topology. (A) The surface points were categorized into four regions and the critical points (N_1, …, N_4) are shown in green. The centerline point is "O". (B) Four straight-lines from critical points to the center are used to find blue and red points. The distance from blue to center points are 0.8R; and from red to the center points are 0.4R, which R is the radius of circle. (C) Straight-lines from the surface points to the center (dotted-lines) were used to define the point near the surface point. These lines have been parametrized from 0.8R to R. (D) Red points were connected and parametrized to create green point using dotted straight lines. (E) The green region were completed for the cross-section. (F) Inner-square region were calculated using straight-parametrized meshes dotted-lines.

2.3.7.1. Mesh indexing

A mesh topology is a set of mesh entities (vertices, faces, and cells) and their connectivity. A quadrilateral shape that is formed by connecting four vertices is called face and six faces form a cell as shown in Figure 34. In this part, we present an efficient approach for mesh topology in vascular network. In meshing a complex geometry, a central task is to discretize a domain of interest into the simplified region.

We took advantage of the regularity of meshes to generate an optimal algorithm to create and index for the meshes. The local coordinate system has three axes of the longitudinal, circumferential, and radial have been used for numbering the mesh topology. In circumferential axes, point indices are increasing clock wisely in ($P_i \rightarrow P_{i+1}$). Then, ($P_i \rightarrow P_{i+n}$) shows the formation of points from peripheral to the center of rotation in a radial direction, which "8α*" is* the total number of points in a circumferential of a circular cross-section. β, and γ are the number of elements in intermediate and near-wall region of butterfly topology as shown in Figure 34C.

Point numbering is swiped in the longitudinal direction to complete volumetric mesh ($P_i \rightarrow P_{i+d}$), which "d" is the total number of vertices in each cross section. Mesh parameters are utilized to calculate the total number of vertices by Equation (30).

$$d = [8\alpha \cdot (\beta + \gamma)] + [(8\alpha + 1)]^2 \quad (30)$$

Minimum point index in each element was considered as the cell index, which allows the rapid store and retrieve of all the elements surrounding a point. To construct the neighboring relationships from element to element, let's consider k = Neigh (i,j) in which element "i" is adjacent to the element "j" and face "k" is the shared face (while i | j = 0 if the face "k" is a boundary surface face). Appendix 1 shows the example of generated mesh index for all possible boundary faces.

In this section, we present a geometry-based efficient algorithm to mesh automatically indexing that can be used for any *O-grid* or *butterfly-grid* cross-sectional patterns. The uniqueness of vertices, faces, and cells are guaranteed in this grid indexing algorithm. Such regularity in grid numbering allows for the rapid store and retrieves the single and neighboring cell information.

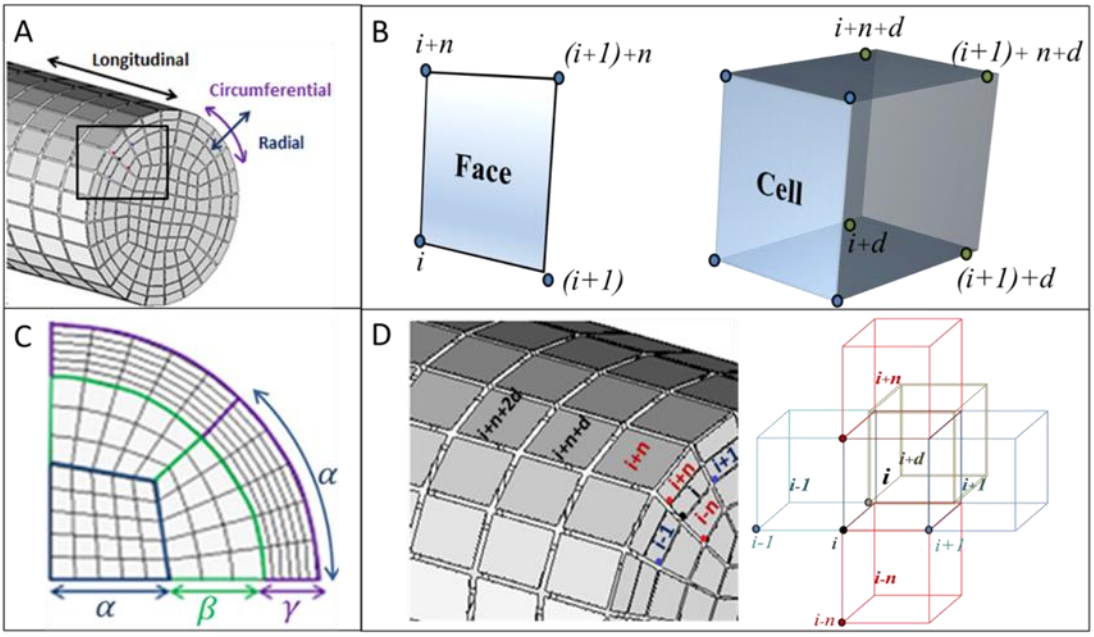

Figure 34. Mesh indexing algorithm. (A) The local coordinate system in a meshed vessel. (B) Mesh topology consists of vertices, faces, and cells. (C) Parameters (a, b and c) govern cross-sectional element resolution. The boundary layer near the vessel wall can independently be refined with the parameter, a. Longitudinal mesh refinement can be adjusted to local diameter and centerline curvature. (D) A magnified view of Celli and its adjacent elements are illustrated. Point indices are increased in circumferential (Pi → Pi+1), radial (Pi → Pi+n) and longitudinal (Pi → Pi+d) directions. The minimum point index of Celli gives the information of circumferential element neighbors (Celli-1, Celli+1), radial element neighbors (Celli+n, Celli-n) and longitudinal elements (Celli+d, Celli-d), [Celli-d is not shown]. Such a regular mesh indexing will help us to efficiently enhance mesh indexing, allows for the rapid store, and retrieve the mesh information.

2.3.8. Preliminary Blood flow simulation of PRM and UNST meshes

To systematically study the potential benefits of parametric mesh generation method (PRM), we also generated UNST meshes for comparison. All our attempt of direct unstructured meshing of the entire large portion of the arterial tree failed due to surface discontinuities, holes and overlap between neighboring surface patches. To overcome this problem for large-scale modeling, we synthesized unstructured tetrahedral/prism meshes by using parametric surface meshes (PRM) and Delaunay method in ANSYS ICEMCFD (ANSYS Inc., Canonsburg, Pa., USA). We compared the performance of PRM with UNST meshes using parallel 14-core processing on dual 2.4 GHz Xenon CPUs. Unsteady CFD analysis were simulated using ANSYS Fluent 18.1 (ANSYS Inc., Canonsburg, PA) using the finite volume method (FVM). For both PRM and UNST, the numerical simulations were carried out using "semi-implicit method for pressure-linked equations (SIMPLE) solver" [62] with a second-order upwind scheme with 40 iterations per time-step, and time-step size of 0.001 s.

The vessel walls were assumed rigid. Blood rheology is modeled as a viscous, incompressible, single-phase Newtonian fluid with dynamic viscosity of 4.265×10^{-3} *Pa.s* as well as blood flow density of 1055 kg/m^3 [63].

2.4. Results

This section presents the results for meshing and blood flow simulations of image-based subject-specific vascular trees. We applied PRM meshing was applied to reconstruct a large portion of the cerebral arterial tree in six human subjects with an average of 227 ± 68 vessel segments and 95 ± 17 bifurcations. To analyze the geometric accuracy, we first quantified geometric overlap between the vessel surface in the reconstructed meshes and the MRA image. Moreover, mesh quality of PRM meshes were compared against conventional UNST meshes. For

computational validation, hemodynamic simulations on all subjects were executed and compared the results and calculation-speed between PRM and UNST meshes. Finally, the PRM method was applied to reconstruct anatomy and to perform blood flow simulations in two pathological cases. Statistics of the reconstructed arterial trees are listed in Table 9.

Table 9. Statistics of reconstructed cerebral arterial trees with parametric meshing technique for six volunteers.

Subjects	#Bezier curves	#Branches	#Bif	Wall surface (m^2)	Blood volume (ml)	Meshing time (min)
I	391	133	68	0.0122	4.01	15.6
II	538	294	100	0.0134	4.28	18.4
III	433	175	89	0.0151	5.36	16.8
IV	574	309	122	0.0141	4.75	19.6
V	496	247	99	0.0146	4.76	17.5
VI	462	206	93	0.0138	4.70	17.4
Mean	482	227	95	0.0138	4.64	17.6

2.4.1. Mesh quality

Mesh quality is important in term of the accuracy and stability of the numerical computation. Three critical metrics, scaled *Jacobian*, *equiangle skew* and *orthogonality* were assessed. The scaled-Jacobian determinants generally range from -1 (worst) to +1 (well-shaped rectangular hexahedral) [64]. Negative values of scaled-Jacobian may not be acceptable for numerical analysis [65]. None of PRM meshes for healthy or pathological cases had cells with negative scale-Jacobians. Figure 5 displays magnified PRM meshes with histograms of the scaled Jacobian matrix determinant for three subjects. High-quality PRM meshes were generated for three problematic locations; non-planar bifurcation (Figure 35A), short *Bif-Bif* segments (Figure 35B) and vessels with high tortuosity such as intracranial arteries (Figure 35C).

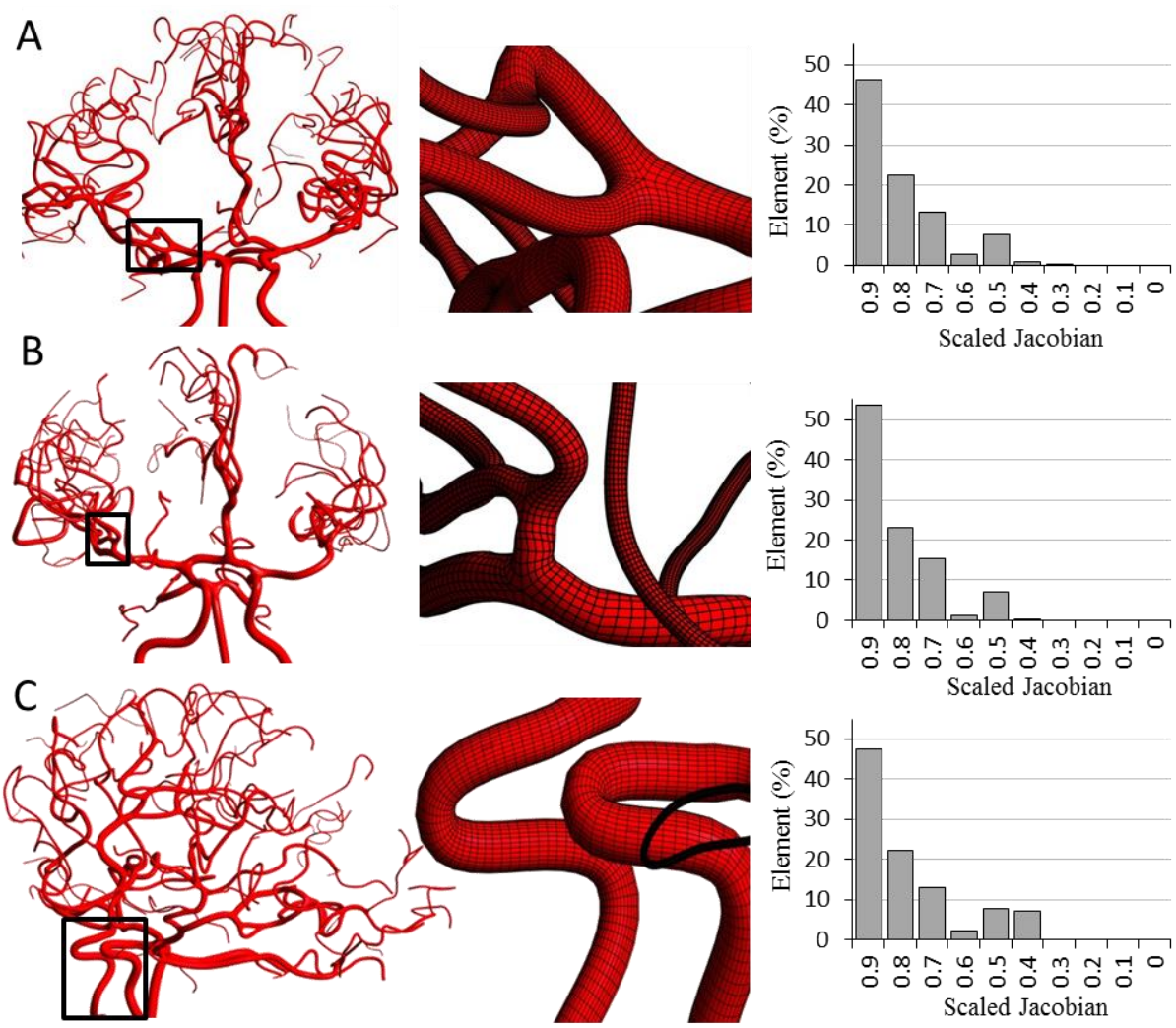

Figure 35. Parametric mesh generation for subject-specific cerebral arterial trees (only three specimens are shown here). Histograms quantify mesh quality in terms of scaled Jacobian for each subject (A) Magnified view visualizes planar and non-planar bifurcations. (B) Insert show details of a *Bif-Bif* segment connecting branches of several bifurcations. (C) The highly tortuous region of the internal carotid siphon.

The equiangular skewness quality (Q_{skew}) [9] ranges between zero (worst) and unity (best) as defined in Equation (31). For all six subjects, the average of equiangular skew was 0.85 ± 0.03. In addition, mesh orthogonality ranging from 0 (worst) to 1 (best) was quantified using ANSYS ICEMCFD, Based on Equation (32).

$$Q_{skew} = 1 - \max\left(\frac{\alpha_{max} - \alpha_e}{180 - \alpha_e}, \frac{\alpha_e - \alpha_{min}}{\alpha_e}\right) \quad (31)$$

$$Q_{ortho} = \min\left(\frac{\vec{F_i} \cdot \overrightarrow{CF_i}}{|\vec{F_i}||\overrightarrow{CF_i}|}, \frac{\vec{F_i} \cdot \overrightarrow{CC_i}}{|\vec{F_i}||\overrightarrow{CC_i}|}\right) \quad (32)$$

Here, α_{max} and α_{min} are the largest and smallest angles in the cell, respectively. α_e is the angle for an equiangular cell ($\alpha_e = 60$ for UNST, $\alpha_e = 90$ for PRM)[9]. For each face *i*, $\vec{F_i}$ is the face normal vector, $\overrightarrow{CF_i}$ is a vector connecting the center of the cell to the center of the face, $\overrightarrow{CC_i}$ is the vector connecting the center of the cell to the center of the adjacent cell sharing a face [66].

Mean orthogonality quality for all subjects was 0.97 ± 0.01. We also report the minimum internal angle in cells for both PRM and UNST mesh. Table 10 summarizes mesh quality statistics for both PRM and UNST models. In addition to mesh quality metrics, we calculated the aspect ratio and volume change as summarized in Table 11.

2.4.2. CPU performance

We compared the performance of PRM with UNST mesh generation using the single-core processor on a 2.4 GHz Xenon CPU. The CPU time for vascular network decomposition and PRM mesh generation of the cerebrovascular tree takes less than 17 minutes on average using MATLAB R2013b (MathWorks Inc.) as listed in Table 9. Even with excellent smooth surface meshes (STL file), ICEM ANSYSCFD required more than 32 hours to generate tetrahedral/prism volumetric meshes for the arterial trees of the volunteers.

We also checked the *Courant-Friedrichs-Lewy* (CFL) number in our mesh models. Figure 36A-B shows the CFL contour and histogram comparison of PRM and UNST meshes. For the same time discretization, more than 80% of the cells exhibited high CFL number (>1), while PRM

meshes with fewer cell numbers meet CFL condition for the first healthy subject. We also visualized the contour map and histogram mesh equiangular skewness (Figure 36C) and orthogonality quality (Figure 36D) of the UNST and PRM meshes.

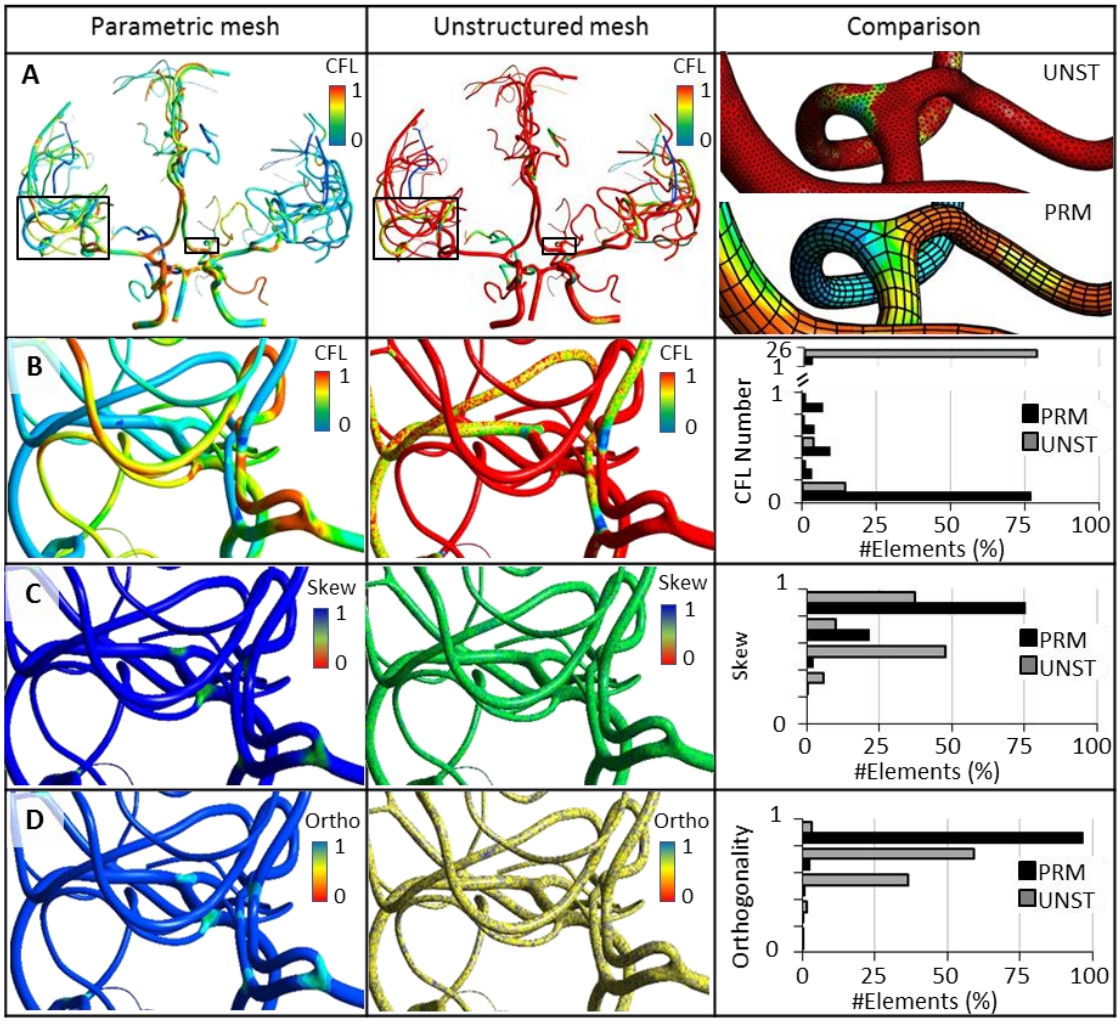

Figure 36. Comparison of mesh quality and computational stability in 3D CFD blood flow simulations of cerebral arterial trees reconstructed with parametric (PRM) versus unstructured meshing (UNST). (A) Global view of CFL contours for a subject-specific cerebral arterial tree mesh with PRM and UNST. The magnified insert shows a small portion of the meshes. (B) For a given step size, all cells in the PRM meshes meets the CFL condition at much lower mesh density. For the same time step, more than 80% of the cells violate the CFL criterion (>1) in UNST. (C) Equiangular skew (abbr. as Skew). PRM meshing improves mean skewness by 20%. (D) Orthogonality (abbr. as Ortho); more than 97% of the PRM cells are almost perfectly orthogonal.

Table 10. Comparison of quality (angle, orthogonality, skew) for PRM and UNST meshes.

Subjects	Min angle		Orthogonality		Equiangle Skew	
	PRM (mean, min)	UNST (mean, min)	PRM (mean, min)	UNST (mean, min)	PRM (mean, min)	UNST (mean, min)
I	77.2, 39.0	44.4,13.8	0.97, 0.79	0.78, 0.38	0.85, 0.56	0.74, 0.23
II	77.6, 21.6	40.2, 5.0	0.96, 0.40	0.69, 0.04	0.84, 0.39	0.67, 0.07
III	79.7, 25.4	45.3, 8.3	0.97, 0.56	0.67, 0.12	0.84, 0.47	0.68, 0.12
IV	78.3, 22.4	42.3, 9.2	0.97, 0.67	0.68, 0.07	0.86, 0.47	0.69, 0.22
V	80.4, 32.3	43.6, 8.6	0.98, 0.72	0.71, 0.17	0.83, 0.42	0.70, 0.09
V1	76.9, 34.5	44.1, 6.0	0.96, 0.55	0.68, 0.22	0.86, 0.51	0.65, 0.04
Mean	78.3, 29.2	43.3, 8.4	0.97, 0.62	0.71, 0.17	0.85, 0.47	0.69, 0.13

PRM: Parametric hexahedral mesh, UNST: Unstructured tetrahedral mesh. Tc: Total CPU time for a one cardiac cycle.

Table 11. Comparison aspect ratio and volume change for PRM and UNST meshes.

Subjects	Aspect ratio		Volume change	
	PRM (mean, min, max)	UNST (mean, min max)	PRM (mean, min, max)	UNST (mean, min, max)
I	0.36, 0.18, 0.99	0.76, 0.21, 0.99	1.31, 0.66, 10.39	1.29, 0.51, 09.38
II	0.48, 0.12, 0.97	0.63, 0.02, 1.00	1.31, 0.72, 26.68	1.50, 0.25, 26.28
III	0.37, 0.16, 0.96	0.66, 0.12, 1.00	1.34, 0.72, 20.25	1.52, 0.36, 07.53
IV	0.38, 0.12, 1.00	0.69, 0.15, 0.98	1.30, 0.86, 22.50	1.49, 0.49, 12.56
V	0.42, 0.09, 0.98	0.59, 0.03, 1.00	1.28, 0.76, 18.23	1.37, 0.39, 10.11
V1	0.37, 0.11, 0.99	0.60, 0.08, 0.98	1.33, 0.69, 16.33	1.22, 0.33, 18.30
Mean	0.39, 0.13, 0.98	0.65, 0.10, 0.99	1.31, 0.73, 19.06	1.39, 0.38, 14.03

PRM: Parametric hexahedral mesh, UNST: Unstructured tetrahedral mesh.

Table 12. Comparison of mesh density, quality (angle, orthogonality, skew) and computational speed for PRM and UNST meshes.

Subjects	#Elements		CPU time	
	PRM	UNST	PRM Tc (min)	UNST Tc (min)
I	1783K	29940K	78	1917
II	2158K	22455K	86	1980
III	1876K	26342K	103	2466
IV	2115K	32536K	89	2745
V	1918K	22547K	72	2035
V1	1897K	27986K	82	2785
Mean	1958K	26967K	85	2321

PRM: Parametric hexahedral mesh, UNST: Unstructured tetrahedral mesh. Tc: Total CPU time for one cardiac cycle.

2.4.3. Mesh independence test

We compared the dynamic 3D CFD results for one cardiac cycle between UNST and PRM models with results shown in Figure 37 and Figure 38. Polylines starting from internal carotid arteries (ICA), and basilar artery (BA) passing through a large portion of the vascular tree were generated. These polylines were used for point-to-point comparisons of computed pressure,

velocity and vorticity magnitudes at peak-systole, mid-diastole, and end-diastole of the cardiac cycle. Additional polylines located on the vessel walls were created for WSS comparison. Simulation results of vorticity magnitude and WSS results between mesh-independent UNST and PRM reconstruction are illustrated in Figure 37 and Figure 38. Maximum WSS and vorticity magnitude differences were less than 5% and 3% over one cardiac cycle.

Table 4 summarizes percentage difference of WSS between PRM and UNST at peak-systole, mid-diastole and end-diastole of the cardiac cycle. The predicted values between the two methods differed less than accepted relative error threshold of the mesh independence, indicating that the results are numerically equivalent. The accepted relative error for mesh-independence was set to 3% for pressure and velocity and 5% for vorticity and WSS [67], [68].

Figure 39 A-B displays results of simulated pressure and WSS contour in six healthy subjects. The minimum number of cells needed to reach grid-independent pressure, velocity, vorticity, and WSS-based predictions were 1,957,000 (PRM) and 26,967,000 (UNST). In these case studies, UNST meshes required on average 13.7 times more cells to reach a mesh-independent hemodynamic variable, leading to 27.3 times longer CPU time compared to PRM meshes.

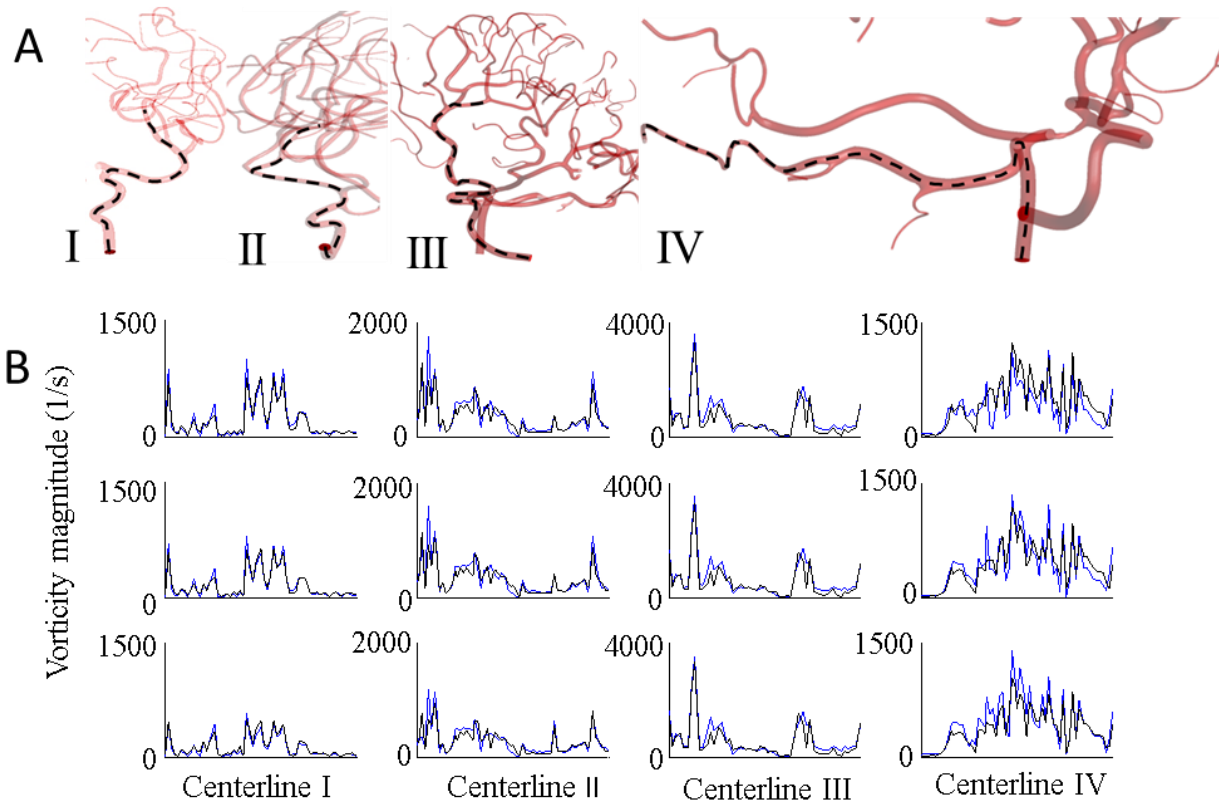

Figure 37.Vorticity profile comparison of unsteady CFD blood flow simulation between PRM and UNST for subject-specific cerebrovascular trees. Hemodynamic states along polylines (marked as dashed lines) passing from ICA and BA to downstream vessels of the arterial tree were plotted to compare predictions of blood pressure, velocity, wall shear stress and vorticity magnitude of parametric and unstructured meshes. Simulation results for vorticity magnitude of the UNST (black solid-line) and PRM meshes (blue solid-lines). The first, second and third rows correspond to the results at peak-systole, mid-diastole, and end-diastole of the cardiac cycle, respectively. Maximum vorticity magnitude differences were less than 3% over one cardiac cycle.

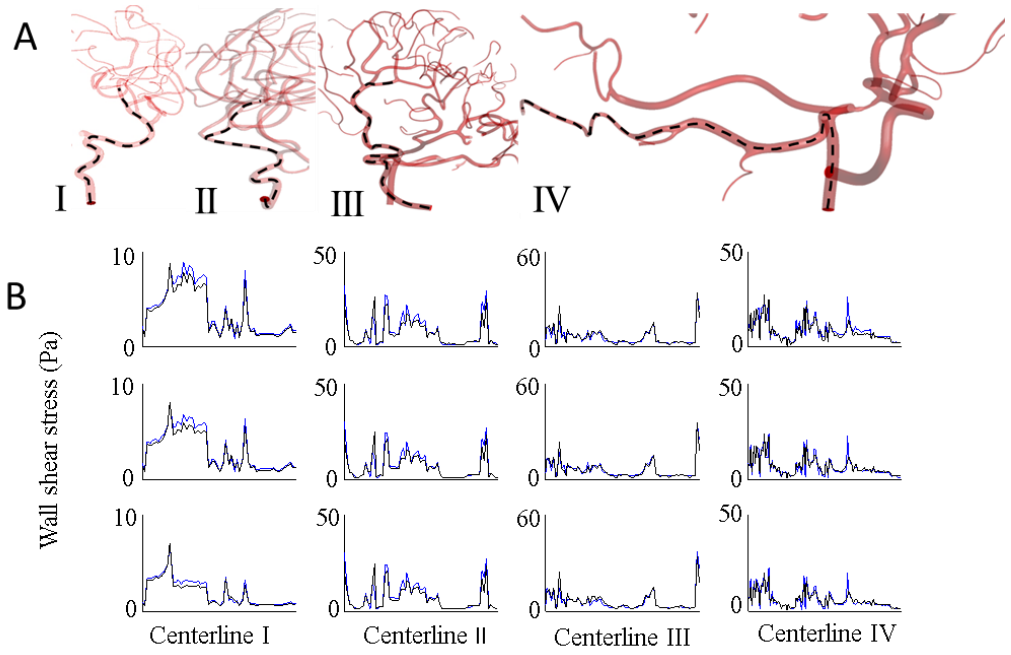

Figure 38. Wall shear stress (WSS) comparison of unsteady CFD blood flow simulation between PRM and UNST for subject-specific cerebrovascular trees. Simulation results for WSS of the UNST (black solid-line) and PRM meshes (blue solid-lines) are visualized. The first, second and third rows correspond to the results at peak-systole, mid-diastole, and end-diastole of the cardiac cycle, respectively. Maximum WSS magnitude differences were less than 5% over one cardiac cycle.

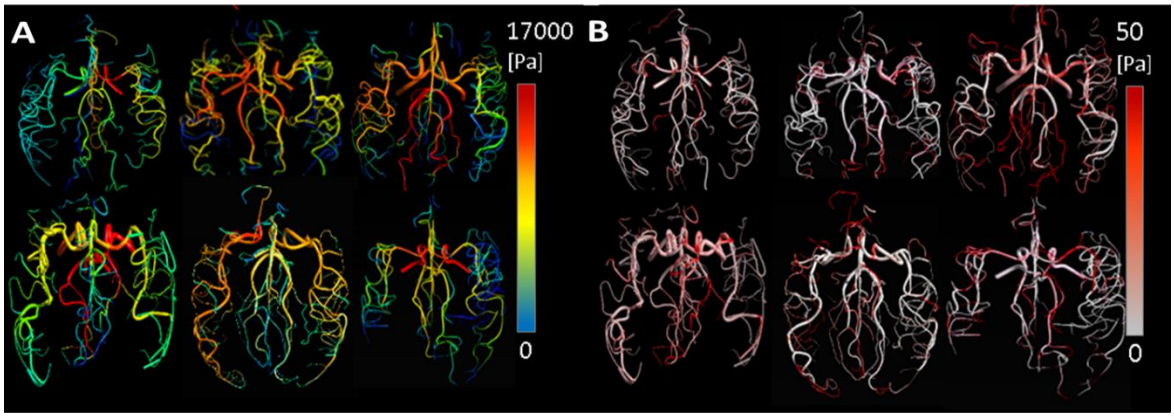

Figure 39. Preliminary 3D hemodynamic CFD analysis using parametric meshes in healthy arterial trees. (A) Predicted 3D pressure field for a large portion of cerebral arterial tree simulation at peak-systole in six volunteers. (B) Predicted wall shear stress distribution.

2.4.4. Preliminary blood flow analysis in pathological cases

In addition to CFD blood flow simulations in six healthy data sets, we also tested the PRM methodology in two pathological cases: an MCA stenosis lesion case and a severe aneurysm in the left vertebral artery. We successfully generated a parametric mesh for a vascular tree of a patient with MCA (M2) stenosis from digital subtraction angiography. The stenosed region was readily meshed parametrically. Reconstructed meshes and unsteady blood flow simulation results are shown in Figure 40.

For irregular pathological regions, such as saccular aneurysms, unstructured meshing is the method of choice [12], [13], [45], [46]. We combined the benefits of unstructured meshing for complex irregular pathologies with the efficient parametric meshing for normal segments by fusing the unstructured grid for the aneurysm with a parametric mesh for the remaining portion of the patient's arterial tree. To create a seamless connection between the aneurysm and the parametric arterial tree, an axial cross-section containing surface and interior points were used as seeding points for initiating unstructured mesh generation of the aneurysm. This task was supported by ICEM CFD mesh editing tools (e.g. merge-nodes, split-edges). The unstructured aneurysm mesh was connected at the proximal and the distal end to the parametric mesh of the "healthy" arterial tree. Figure 40D illustrates the combined *hybrid* PRM-UNST mesh with an unstructured (pathological) and a parametric (healthy) portion. We succeeded in performing preliminary hemodynamic simulation on a large portion of the vertebrobasilar system down to small arteries of the posterior cerebral territory for a patient with a massive aneurysm. Hybrid meshing enabled highly dense mesh refinement in the irregular pathology, combined with very economic reconstruction of the normal portion of the patients' cerebral circulation.

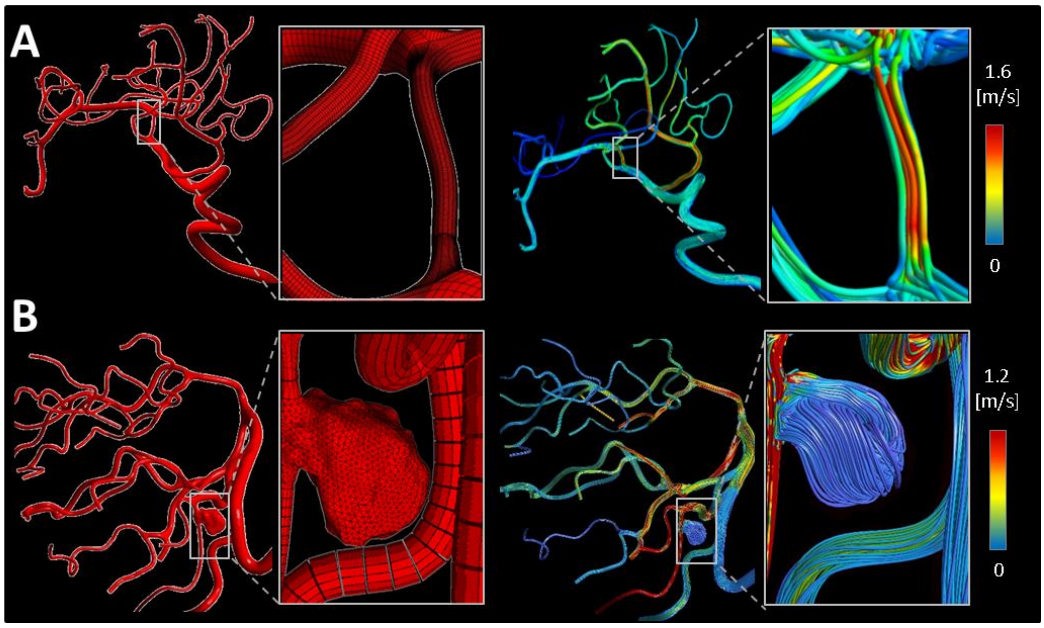

Figure 40. Preliminary 3D hemodynamic CFD analysis using parametric meshes in healthy and pathological cerebral arterial trees. Panel (A) illustrates the application of PRM method for a patient with MCA stenosis. Panel (B) summarizes results for a saccular aneurysm in the vertebral artery. It shows unstructured mesh for a saccular aneurysm in the right vertebral arteries fused to a parametric mesh of the vertebrobasilar system down to posterior cerebral arteries. The magnified insert depicts the hybrid mesh of unstructured aneurysm with parametric vascular tree meshes. The blood flow streamlines are shown for both stenosis and aneurysm pathological cases (right column of C and D panel).

2.5. Discussion

We presented a fully automated parametric mesh generation method tailored for large-scale hemodynamic analysis. It succeeded in generating high-quality meshes including challenging locations such as non-planar bifurcations, very short segments between bifurcations, and bifurcations with significant diameter differences, loops and high tortuosity arteries in both healthy and pathological cases.

2.5.1. PRM vs. UNST comparison

In all subjects, over 86% positions of the centroid in the reconstructed meshes differed less than the resolution limit from the corresponding points in the MR image. Geometric accuracy

evaluation showed a good agreement, with an AUC value of 0.87, between the constructed mesh and raw MRA data sets.

The required mesh generation time for PRM was almost 112 times faster than UNST mesh generation on the same computer with single core processor. Unsteady 3D CFD blood flow simulations for one cardiac cycle on a PC with 14-core parallel processors, required over 27 times more CPU time for the UNST meshes compared to the PRM model. Overall, the use of hexahedral PRM meshing decreases numerical diffusion error; mesh independence of the flow solution was achieved with significantly fewer elements in all subject-specific cases presented here. For the same time step, the value of local CFL number was visualized for both UNST and PRM models. It should be noted that the comparison of CFL numbers is not a direct measure of solver stability and convergence acceleration. High aspect ratio cells can also increase the bound of stability limits of a specific time-step and would allow the use of a larger CFL value to achieve fast convergence [69].

PRM meshes reached mesh-independent hemodynamic results with only 7% of the number of elements required for UNST. This is at least one order of magnitude savings in mesh size. PRM meshing yielded on-average, 36.6% and 21.7% orthogonal and equiangular skew quality improvement over unstructured meshes. The mean orthogonality quality and equiangular skew quality of PRM models for all six subjects were 0.97 ± 0.01 and 0.85 ± 0.03, respectively. However, the average of aspect ratio and volume changes of PRM and UNST are 0.39 ± 0.04 and 0.655 ± 0.06 as well as, 1.31 ± 0.02 and 1.39 ± 0.11, respectively. It is important to note that cells with large aspect ratio are undesirable in UNST, because stretching tetrahedral cells invariably introduces element distortion which in turn causes errors in the CFD analysis. In contrast, for structured hexahedral meshes, a large aspect ratio aligned longitudinally does not degrade skewness and

orthogonality quality. Moreover, good alignment of mesh edges in the dominant flow direction reduces numerical diffusion [70]. “Unstructured meshes with randomly oriented cells are reported to introduce relevant numerical diffusion in the flow solution, especially in predominantly unidirectional flow systems” [1], [3], [71]. In summary, some judgment needs to be taken into consideration in addition to the pure high-quality metrics, because of the role of quality parameters (aspect ratio, skewness, orthogonality) shifts, due to the differences in the construction principles of tetrahedral unstructured meshes versus PRM meshes.

2.5.2. Anisotropic mesh refinement

Fast and accurate 3D computational hemodynamic results may benefit from mesh refinement to better resolve complex local blood flow patterns. Anisotropic mesh refinement has been previously shown to reduce the numerical diffusion [1], [3], [50], [72]. The purpose of anisotropic meshing is to perform a flow or geometric-dependent mesh refinement in the region of interest, where higher precision is required. In our PRM method, mesh resolution in longitudinal and cross-sectional directions was varied to optimize the number of required grid cells. For each branch, the number of longitudinal subdivisions depends on the degree of curvature and local diameter of the vessel. To increase the solution accuracy near the boundary layers where higher velocity gradients are expected, higher cell density was implemented close to vessel walls using the boundary-layer refinement parameter (γ). Local orientation (longitudinal, circumferential and radial) aides defining flow- or geometry-dependent refinement in the vascular models. Flow gradients are generally smaller in the longitudinal direction than in the radial direction; therefore the mesh density should be high in the steep gradient regions. Accordingly, structured grid parametrized by a body-fitted coordinate system provides direct control over mesh alignment to improve

computational efficiency for large vascular hemodynamic simulations and minimizing unnecessary mesh elements.

2.5.3. Limitations and future work

In this current state, the project has a few limitations which need to be addressed in the future work. Although the actual study was limited to finite volumes methods, the parametric meshes could further be explored for use in *finite element methods* for blood flow simulations or vascular wall dynamics. In this paper, 3D unsteady simulation results provide quality metrics, CPU time cost, and accuracy, to compare the computational results between UNST and PRM meshing.

A next step simulation using parametric meshing techniques could include 3D fluid-structure interaction (FSI), because the body-fitted coordinate system enables a simple extension of the luminal wall to create a cylindrical wall domain of desired thickness. Our hexahedral orthogonal elements allow layered modeling of the detailed biomechanics of vessel walls [73]. However, reliable mechanical properties and vessel thickness measurements of the intracranial vasculature are necessary before attempting more rigorous 3D FSI simulations [74] for large sections of the cerebral vasculature.

In this paper, complex vascular features such as bifurcations and loops were parametrically meshed, but multifurcations will require a further generalization of Equations (4-8). Although the current focus is on the cerebral arterial tree, this methodology is applicable to other arterial networks such as coronary, pulmonary and retinal circulatory systems. Future work using the PRM method should address the venous system and irregular pathological regions such as a saccular aneurysm.

A future step incorporating increased clinical significance will entail an assessment of disturbed flow in pathological cases, and compare the near-wall hemodynamic parameters before

and after endovascular intervention for quantifying surgical outcomes. The automatic PRM method enables detailed hemodynamic analysis for a large portion of the arterial tree, including small downstream vessels. A large-scale approach of assessing hemodynamic risk factors for regions far away from the site of intervention could aid in elucidating poorly understood phenomena such as *delayed hemorrhage* (DH) [75], [76].

Moreover, automation of the workflow presented here would address an important clinical need, because it enables image segmentation and dynamic simulation of patient-specific images on the same day. Near real-time hemodynamic analysis is a clinical requirement that has the potential to inform physicians about disturbed blood flow based on subject-specific meshes and rigorous CFD computations.

3. MESH VALIDATION

In this chapter, we will show the details of a pipeline to validation parametric meshes of six cerebral vascular trees. The results of this chapter are under revision "Validation of parametric mesh generation for subject-specific cerebroarterial trees using modified Hausdorff distance metrics." Computers in Biology and Medicine (2018).

3.1. Abstract

Accurate subject-specific vascular network reconstruction is a critical task for the hemodynamic analysis of cerebroarterial circulation. Vascular skeletonization and computational mesh generation for large sections of cerebrovascular trees from magnetic resonance angiography (MRA) is an error-prone, operator-dependent, and very time-consuming task. Validation of reconstructed computational models is essential to ascertain their accuracy and precision, which directly relates to the confidence of the hemodynamic analysis. The aim of this study is to generate a pipeline to validate and quantify the spatial accuracy of computational models of subject-specific cerebral arterial trees. We used a parametric structured mesh (PSM) generation method to automatically reconstruct six subject-specific cerebral arterial trees containing 1364 vessels and 571 bifurcations in total. We performed sampling frame extraction for all vascular segments and bifurcations. Our comprehensive study quantifies the spatial accuracy of PSM against the original MRA images by correlating lumen area, pixel-based statistical analysis, area overlap and centerline accuracy measurements. In addition, we propose a pointwise offset surface distance metric (PSD) based on a modified Hausdorff distance to quantify the extent to which reconstructed arteries and bifurcation match the in-vivo datasets. Accurately reconstructed vascular trees could

be useful for morphological analysis of large patient data banks or subject-specific hemodynamic simulations of the cerebral arterial circulation.

3.2. Introduction

Thanks to advances in medical imaging technologies in the past decade, the use of subject-specific models is becoming more practical for diagnosis and treatment planning. Moreover, researchers and physicians have begun to perform cerebral hemodynamic simulations to acquire more insights into the cause of cerebrovascular diseases (CVDs). Especially, wall shear stress (WSS) components were implicated as critical hemodynamic factors for predicting endovascular lesions such as a cerebral aneurysm [19], [77], [78], plaque formation, and atherosclerosis [13]. Even small changes in vascular network configuration or geometry can substantially alter WSS in arteries [26]. Therefore, surgical interventions inducing geometrical changes may inadvertently induce undesired wall shear stress, which can lead to further lesions both local and distal to the site of intervention [75], [76], [79], [80]. Hence, accurate reconstruction of large-scale cerebral arterial trees topology can be of significance to anticipate the endovascular lesion-prone sites.

Many image reconstruction and mesh generation tools (VMTK [81], [82], Materialize Mimics, etc.) are available for surface reconstruction of blood vessels, which needs to be performed by a skilled technician. Often these processes require hands-on repair of surface discontinuity, holes and surface overlap which are highly operator-dependent, tedious, time-consuming, and difficult to reproduce; making manual reconstruction impractical for large-scale cerebral arterial tree reconstruction. Thus there is a need to generate fully-automatic high-quality vascular tree meshes from angiographic images.

We have recently presented an anatomic image processing and computational fluid dynamics (CFD) analysis pipeline based on a *parametric structured meshing* (PSM) technique [83]–[85]. In this paper, we perform comprehensive statistical analysis of the spatial fidelity of the subject-specific PSM reconstruction. Specifically, we will use crisp statistical image metrics to assess the accuracy of the centerline, diameter, and connectivity of the reconstructed vascular networks. For this purpose, we will compare raw MRA data with the automatically reconstructed computational meshes using the Walk-In Brain virtual reality software [86]. Due to the size of the datasets, we have automated the image validation protocol to effectively generate similarity measures between the MRA voxel data and the 3D reconstructed vectorized data.

Pixel-based Statistical similarity indices, such as Dice or Jaccard, have been widely used to measure the area alignment between two graphical objects. However, those indices do not quantify the alignment of borders (edges) [87]. The Hausdorff distance (HD) is a suitable measure of boundary similarity between two objects. Hausdorff distance has been commonly used for video sequences matching [88], trajectory comparison [89], and for evaluating the performance of medical segmentation and image registration [90]–[93]. However, the simple *pixel-based* statistical analysis is inadequate for comparing a smooth reconstructed mesh (PSM) with jagged-edge discrete MRA image, because the exact spatial location of the edge points on the boundaries is ignored[87]. To sharpen the analysis for evaluating the spatial alignment of reconstructed vascular tree surfaces, we introduce the *pointwise surface distance* (PSD) index based on a modified Hausdorff distance metric.

This paper is organized as follow. First, in-vivo data from MRA image acquisition, segmentation, and registration of six human subjects are presented. We then automatically capture sampling frames from important topological regions of the vascular trees. We quantify the

accuracy of centerline approximation using the original MR angiography images as the reference. We also perform pixel-based statistical analysis and calculate the similarity index between the PSM and MRA images. Moreover, we deploy a pointwise surface distance index to quantify the fidelity of diameter reconstruction. Finally, the reconstructed PSM meshes were used for morphological and CFD hemodynamic analysis.

3.3. Methods

A stepwise procedure for vascular mesh reconstruction validation techniques for cerebral arterial trees is summarized in Figure 41. The details of the applied methods are introduced next.

1.1.Image acquisition and segmentation (Step 1a)

Six healthy human subjects with no known cerebrovascular diseases were recruited and underwent MR imaging on a *General Electric 3T Discovery MR750* scanner using a 32-channel phased-array coil (Nova Medical, Inc., Wilmington, MA, USA) under *Institute Review Board* approval at the University of Illinois at Chicago, MRA images were acquired using a three-dimensional (3D) time of flight (TOF) pulse sequence to capture major cerebral arterial tree branches. No motion artifacts affecting the scan were observed in any of the six cases. The key data acquisition parameters were: repetition time (TR)=26 *ms*, echo time (TE)=3.4 *ms*, flip angle=18°, matrix size=512×512×408, voxel size=0.39×0.39×0.3 mm^3, acceleration factor=2, number of slab=4, magnetization transfer=on, and scan time = 30 *min*.

To reconstruct even small branches of the cerebral arterial tree, we enhanced the vessel contrast with our in-house *multi-scale vesselness* filter [58], [59]. Filtered images were processed to create logically connected networks and morphological descriptors of the cerebral arterial tree. A fast marching algorithm with the cutoff intensity of 0.01 was used to generate a binary mask of the connected vascular network [58], [94].

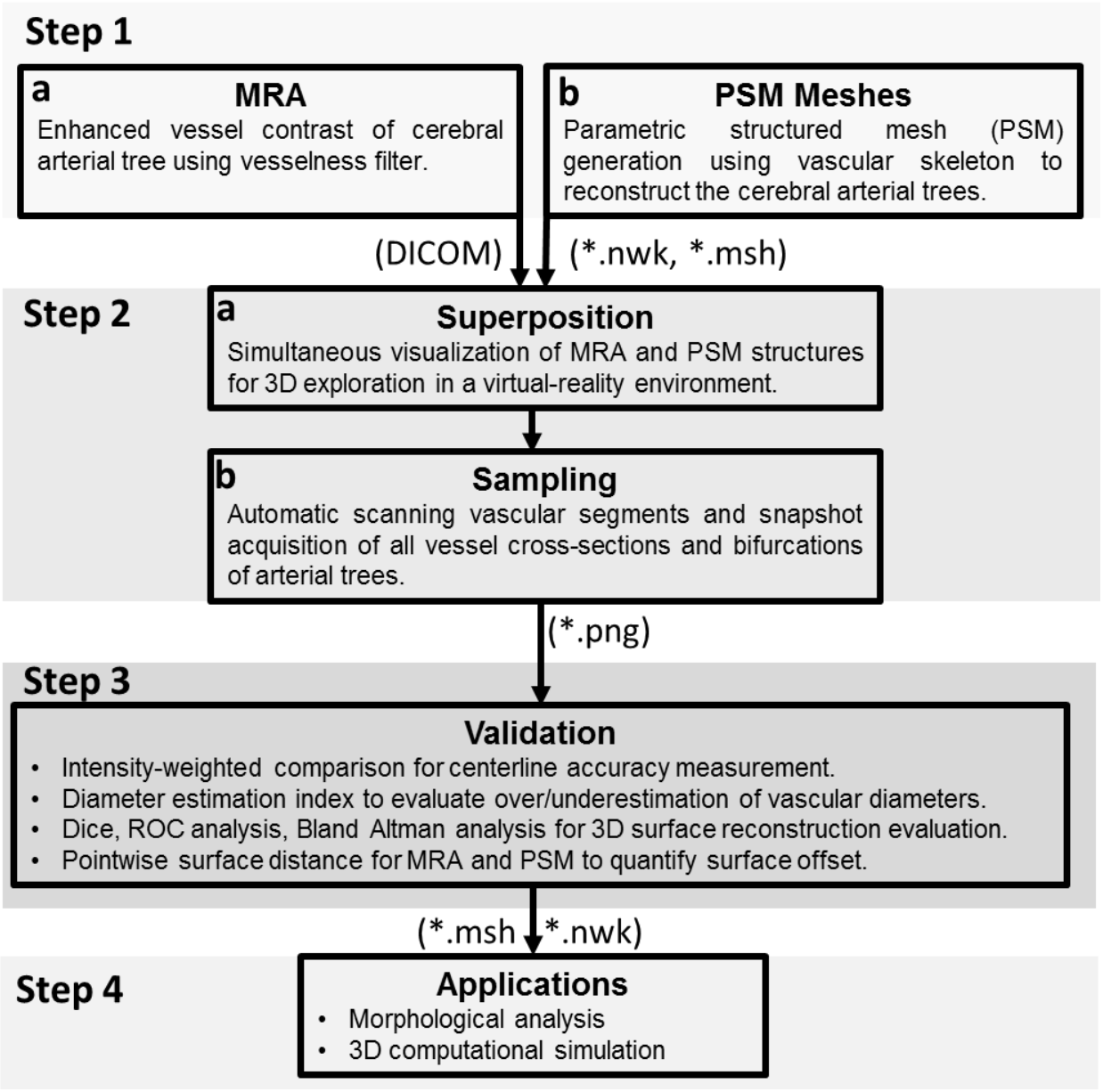

Figure 41. Information flow for validation of the spatial parametric structured meshes (PSM) validation from original MRA images. (Step 1) Cerebrovascular trees are reconstructed from MRA using PSM method. (Step 2) MRA and PSM reconstruction are superimposed in a virtual reality environment. Vascular segments and bifurcations are scanned and several 2D sampling frames are acquired. (Step 3) Spatial accuracy evaluation between PSM with original MRA images by correlating lumen area, pixel-based statistical analysis, area overlap measurements and centerline accuracy measurements. (Step 4) Applications of PSM meshes in cerebrovascular morphometric analysis and hemodynamic simulation.

3.3.1. Image acquisition and segmentation (Step 1a)

We used the exact imaging dataset as explained in Chapter 2. To reconstruct even small branches of the cerebral arterial tree, we enhanced the vessel contrast with our in-house *multi-scale vesselness* filter [58], [59]. A fast-marching algorithm with the cutoff intensity of 0.01 was used. Based on this cuttoff a binary mask were generated for the vascular network [58], [94], [95].

3.3.2. Skeletonization and mesh generation (Step 1b)

Morphological descriptors including centerlines, vessel diameters, and network connectivity were acquired from the filtered images using Vascular Modelling Toolkit (VMTK). Diameter information was obtained from the inscribed sphere method [81]. Vascular skeleton data was partitioned into *point coordinates*, *connectivity,* and *diameter* information. The *point coordinate* matrix contains the location of the nodes on the vessel centerline with its *diameter* information. Logical connections between two points were encoded via a *connectivity* matrix. Using *point coordinate* and *connectivity* matrices, the network was partitioned into *segments* and stored in persistent file (**.nwk* file). Vascular *segments* were encoded with cubic Bezier splines. To eliminate the non-physiological noisy variation of the *diameter* information, raw diameter data were smoothed with a moving average filter. In high tortuosity segments such as internal carotid arteries, a linear fit was implemented to enforce monotonically decreasing diameters along the blood flow direction.

We used a full-hexahedral *parametric structure mesh* (PSM) generation method described previously [59], [60], [85]. In brief, hexahedral meshes were parametrized along the vessels (Bezier splines) in radial, cross-sectional and longitudinal directions to build anisotropic meshes.

For each branch, the number of longitudinal subdivisions was chosen based on the local curvature and vessel diameter. PSM meshes satisfy C1-continuity condition over the entire surface.

3.3.3. Virtual exploration of superimposed MRA and PSM (Step 2a)

Both the MRA image and the reconstructed vascular tree were registered in the *Walk-in Brain* virtual-reality software [86]. Figure 42 depicts a 3D rendering of the separated different anatomical compartment in the virtual immersive environment of *Walk-in Brain.*

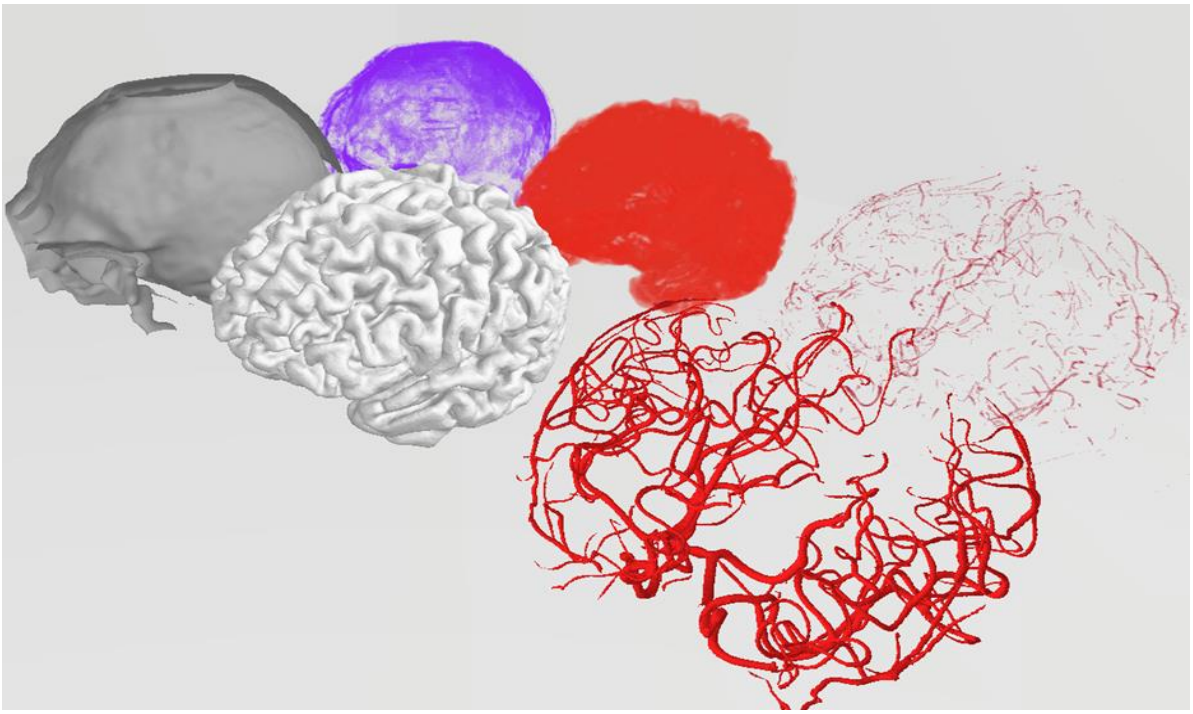

Figure 42. Virtual reality rendering of the raw data as well as the reconstructed meshes in WalkInBrain. In the back row, there are 3D rendering of the raw voxel matrices to visualize effective labeling according to the anatomical compartment. The voxel point clouds of the raw data including CSF surface, cortical surface, and the arterial tree are represented. In the front, reconstructed meshes of various anatomical compartments are shown. The comparison is between the reconstructed arterial tree and raw data.

Arterial trees in the MRA images and the reconstructed 3D PSM meshes were rendered semi-transparently to allow for simultaneous 3D visualization and exploration of both structures as shown in Figure 43.

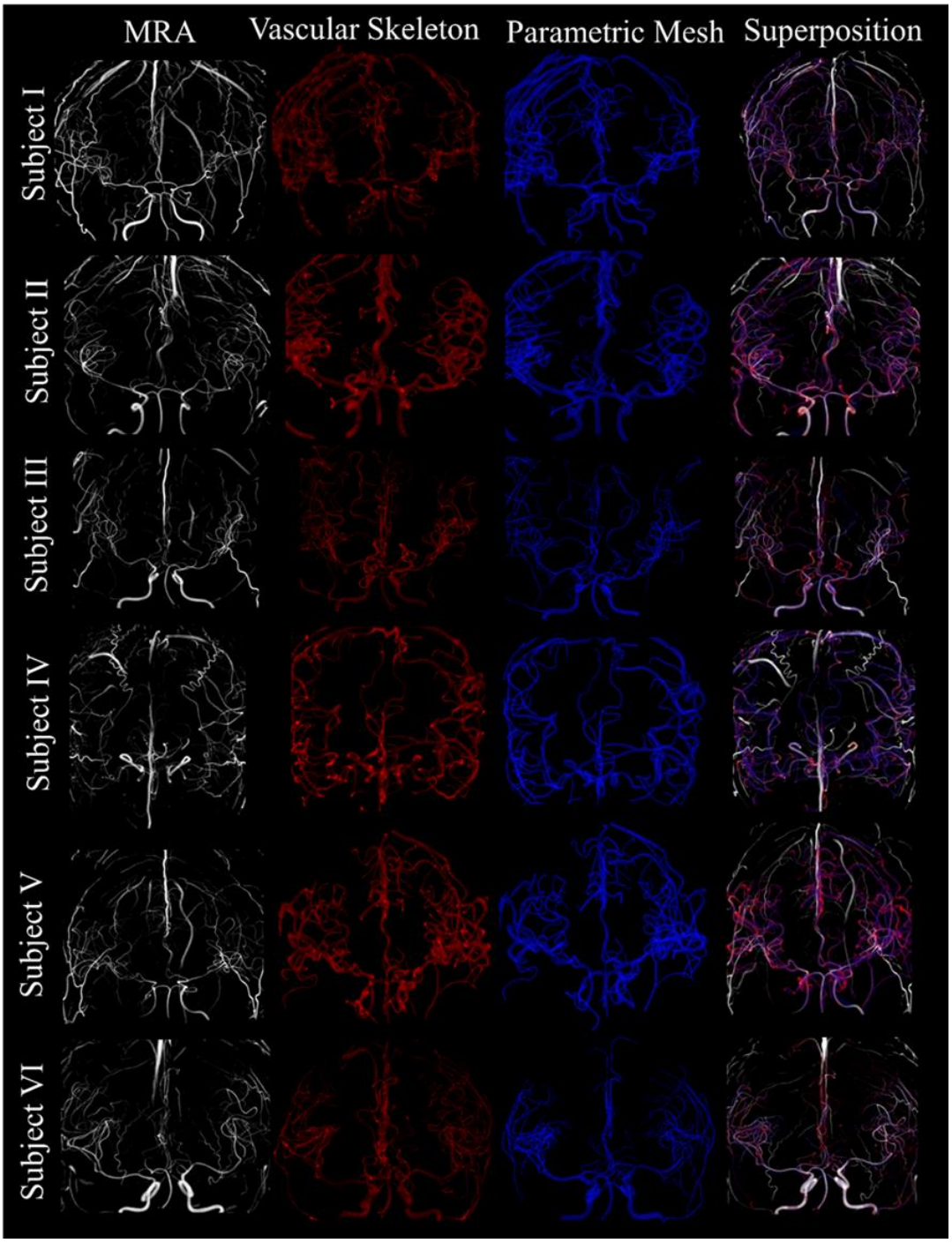

Figure 43. Global superposition of six cerebral arterial trees in virtual reality space. The first column shows the original gray-scale MRA images. The reconstructed vascular skeleton (red) of the arterial tree which includes diameter, centerline, and network connectivity information is depicted in the second column. Three-dimensional parametric structured meshes (blue) are shown in the third column. The last column is the global superposition with MRA (white), vascular skeleton (red) and parametric mesh (blue).

3.3.4. Automatic sample framing acquisition (Step 2b)

We implemented a procedure to automatically capture 2D image snapshots to assess *vascular cross-sections* (CRSs) and *bifurcations* (BIFs). Examples for a cross-section (CRS) and a bifurcation (BIF) are shown in Figure 44A.

For cross sections (CRS), multiple two-dimensional snapshots were generated along the centreline perpendicular to the velocity of the Bezier spline representation of a segment as shown in Figure 44B. Typically between 10 to 120 snapshots depending on the length of Bezier splines. For bifurcations, we first established the *separation region*. The *separation region* is defined by the bifurcation point *B*, three separation points, *S*, and two control points, *C*. The three branches of each bifurcation were indexed as *a*, *b*, and *c* as shown in Figure 4B. Bifurcation sampling frames were generated as 2D snapshots of the *separation planes* spanned by the separation points. By scanning the entire vascular networks on average 19,956 CRSs for the vascular segments, and 95 BIFs snapshots were created for each subject as listed in Table 13. We used MATLAB R2017a (MathWorks Inc.) for all image filtration and statistical analysis using a PC with a single-core 2.4 GHz Xenon CPU processor.

Table 13. Statistics of the sampling frames for each reconstructed cerebral arterial tree and CPU time for pre- and post-processing. The pre-processing includes all sampling frame acquisition and image filtration. Post-processing includes all pixel-based, surface-based statistical analysis.

Subjects	#CRS	#BIF	#Vessels	Pre-processing Time (min)	Post-processing Time (min)
I	15685	68	133	50	13.4
II	22540	100	294	73	18.8
III	17425	89	175	58	13.3
IV	24465	122	309	81	19.4
V	20439	99	247	66	17.8
VI	19184	93	206	63	16.6
Total	119738	571	1364	391	99.3

Vessel geometry in MRA angiograms was distinguished from the reconstructed meshes and segmentation using RGB (red-green-blue) channel separation. Then, a binary mask (silhouette) of

the filtered images was generated. A *Canny edge-detection* algorithm was applied on all sequentially acquired images to extract the border of the vascular cross-section and bifurcations for statistical analysis, as shown in Figure 44C.

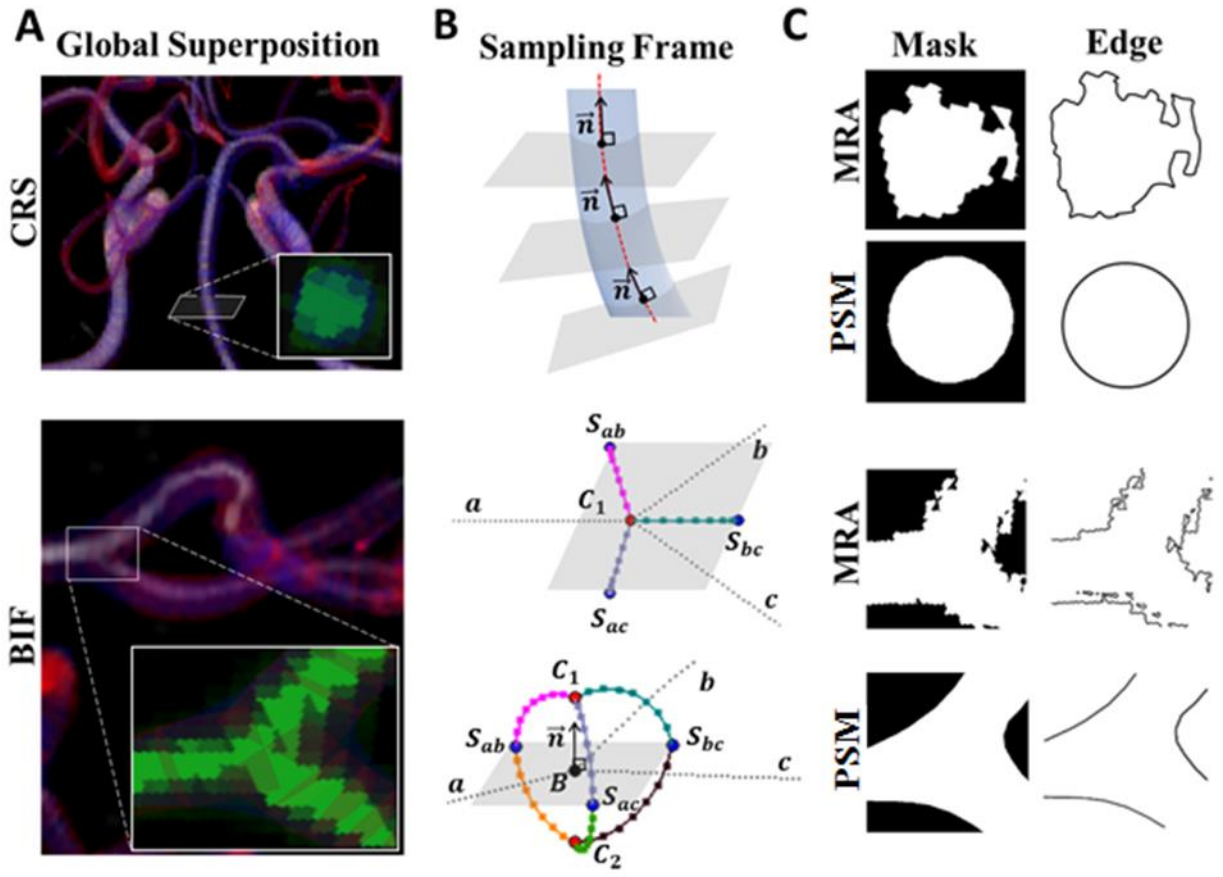

Figure 44. Sampling frame analysis of the vascular cross-sections (CRSs) and bifurcations (BIFs) for cerebral vascular tree reconstruction. (A) Superposition. Two-dimensional snapshots containing information of MRA and the reconstructed mesh were captured. (B) Sampling frame acquisition. The software automatically positions the 2D snapshots (gray planes) so that their normals, $\vec{n}$, are collinear to the centerline velocities for the vascular segment. In BIF, the snapshot belongs to the separation plane spanned by separation points S_{ab}, S_{bc}, S_{ac} of the branches of *a*-*b*, *b*-*c*, and *a*-*c*, respectively). The detailed schematic of the separation region also depicts the control points of C_1 and C_2, as well as the bifurcation points, B. In total, 119,738 vascular CRSs and 571 BIFs snapshots were automatically created for validation of vascular tree reconstruction. (C) Binary masks and boundary edges of vascular CRSs and BIFs were processed for further statistical analysis.

3.3.5. Statistical metrics for PSM evaluation (Step 3)

We performed *pixel-by-pixel analysis* to compare the reconstructed PSM vessel geometry to the MRA images by calculating the true negative (T_N), true positive (T_P), false negative (F_N) as well as false positive (F_P). We also evaluate the mesh reconstructions using the *receiver operating characteristic* (ROC) curves. All results of the pixel-based comparison are summarized in Figure 45.

Sensitivity (S_E), positive predictive value (P_{PV}), specificity (S_P), total accuracy (A_{CC}), negative predictive value (N_{PV}), and Dice similarity coefficient (D_{SC}) were computed using Equation (33) - (38) on a pixel-by-pixel basis. The sensitivity S_E represents the ratio of the correctly meshed pixels in all the vessel pixels. Specificity S_P is the ratio of correctly not meshed pixels in all the non-vessel pixels MRA images. P_{PV} is that the probability that a mesh cells are truly vessel in the raw image. A_{CC} is a global validation metric providing the ratio of total well-meshed pixels. Finally, D_{SC} is a statistical validation metric to evaluate area spatial overlap.

$$S_E = \frac{T_P}{T_P + F_N} \tag{33}$$

$$S_P = \frac{T_N}{T_N + F_P} \tag{34}$$

$$P_{PV} = \frac{T_P}{T_P + F_P} \tag{35}$$

$$N_{PV} = \frac{T_N}{T_N + F_N} \tag{36}$$

$$A_{CC} = \frac{T_N + T_P}{T_P + T_N + F_P + F_N} \tag{37}$$

$$D_{SC} = \frac{2T_P}{2T_P + F_P + F_N} \tag{38}$$

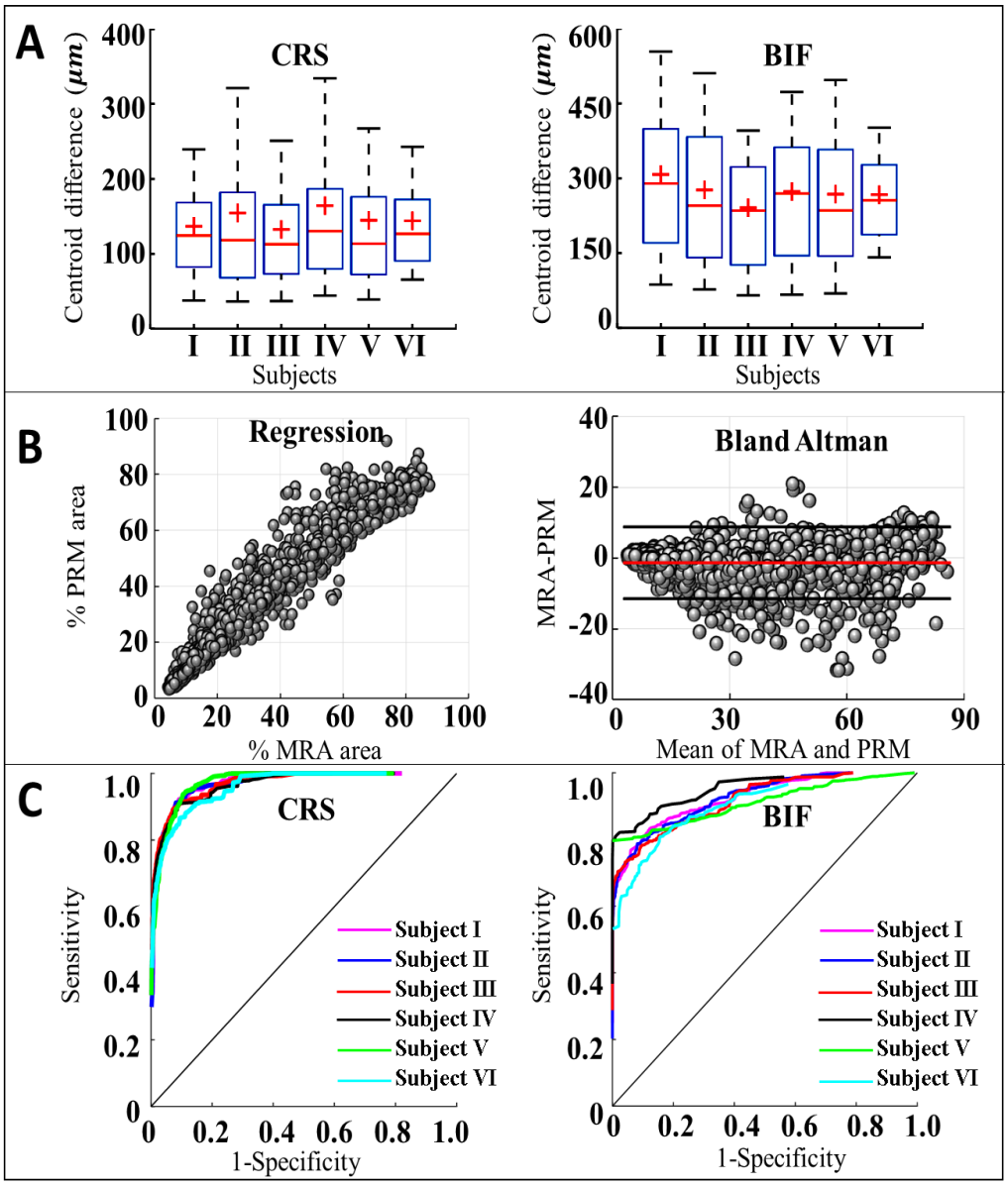

Figure 45. Pixel-based statistical analysis of the PSM reconstructed vascular models. (A) The accuracy of centerline reconstruction based on intensity-weighted centroids of PSM and reference images of MRA image for the six subjects. The vascular centerline accuracy reached a sub-resolution precision ($\sim 400\ \mu m$) for vascular cross-sections (CRSs) and bifurcations (BIFs) (B) Linear regression (left) and Bland Altman plot (right) to assess the agreement between the the reference MRA and reconstructed PSM in vascular CRSs and BIFs sampling frames. The regression plot shows the correlation with $R^2 = 0.9489$. The red line in Bland Altman plot is the mean of the difference and the two black lines are the upper and lower 95% limit of agreement (mean $\pm$ 1.96SD). (C) Receiver Operating Characteristic curves (ROC) of CRSs and BIFs for six subjects. Using MRA images as the ground truth, the area under the curve (AUC) was calculated with AUC = 0.96 for CRSs, and AUC = 0.88 for BIFs.

3.3.6. Pointwise surface distance (Step 3)

We propose a new *pointwise surface distance* (PSD) index to assess the quality of boundary reconstruction. The binary mask of "A" is defined as all pixels with intensity above the threshold in the reference image of the MRA, shown as the white convex region in Figure 44C. Equally, the binary mask of "B" stands for pixels that delineate the vascular lumen in PSM reconstruction. The boundary (edge) is defined as the subset, $S(A) = \{a_1, a_2, \dots, a_n\}$ that embodies pixels the border points of the binary mask A. Similarly, $S(B) = \{b_1, b_2, \dots, b_m\}$ with m pixels delineates the boundary of *B.* The *one-sided Hausdorff distance* is defined as the maximum of the distances between each point $a \in S(A)$ to the nearest point in $b \in S(B)$, Equation (39). Similarly, from $S(B)$ to $S(A)$ another one-sided Hausdorff distance can be calculate based on Equation (40) with notation summarized in Table 14. Finally, the two-sided Hausdorff distance, $H\big(S(A), S(B)\big)$, is the larger of the two one-sided Hausdorff distances as given in Equation (41).

$$h\big(S(A), S(B)\big) = \max_{\forall a \in S(A)} \left\{ \min_{\forall b \in S(B)} \{\|a, S(B)\|\} \right\} \tag{39}$$

$$h\big(S(B), S(A)\big) = \max_{\forall b \in S(B)} \left\{ \min_{\forall a \in S(A)} \{\|b, S(A)\|\} \right\} \tag{40}$$

$$H\big(S(A), S(B)\big) = \max\big\{h\big(S(A), S(B)\big), h\big(S(B), S(A)\big)\big\} \tag{41}$$

where $\|.\|$ is the Euclidean distance operator. Note that the one-sided HD is an asymmetric function, $h\big(S(A), S(B)\big) \neq h\big(S(B), S(A)\big)$. Since the Hausdorff distances only detect for extreme deviations, which could be caused by a single noisy point, it is not a robust metric for tracking entire boundaries.

Table 14. The mathematical notation for pointwise surface distance calculation.

Notation	Definition
$\boldsymbol{A}$	All pixels that have non-zero intensity on the MRA image.
$\boldsymbol{B}$	All pixels that have non-zero intensity on the PSM reconstruction.
$\boldsymbol{S(A)}$	Set of all the pixels on the boundary of the binary mask A.
$\boldsymbol{S(B)}$	Set of all the pixels on the boundary of the binary mask B.
$\boldsymbol{\|a, S(B)\|}$	Set of Euclidian distances for a point from $a \in S(A)$, to all the points of $S(B)$.
$\mathbf{d}(\boldsymbol{a}, \mathbf{S}(\mathbf{B}))$	Minimum distance from $a \in S(A)$ to the closest point of $S(B)$.
$\boldsymbol{h(S(A), S(B))}$	One-sided Hausdorff distance from $S(A)$ to $S(B)$.
$\boldsymbol{H(S(A), S(B))}$	Two-sided Hausdorff distance between $S(A)$ and $S(B)$.
$\boldsymbol{g(S(A), S(B))}$	One-sided pointwise surface distance from $S(A)$ to $S(B)$.
$\boldsymbol{G(S(A), S(B))}$	Two-sided pointwise surface distance (PSD) between $S(A)$ and $S(B)$.

Therefore, we propose a new parameter, which we call the *pointwise surface distance*. It uses the traditional HD, for all surface point to obtain a compact measurement for the degree of alignment of the entire boundary. We first calculate a *modified Hausdorff distance*, from the specific points $a \in S(A)$ to the closest point of $S(B)$, as shown in Equation (4). Then we multiplies the modified HD to the scalar parameter of either 1 or -1 depending on the position of the select point with respect to other binary mask. For example, if the point $a \in S(A)$ lies inside B, parameter α is 1 showing that the PSM reconstruction is overestimated. Conversely, if the point a is outside the PSM binary mask (outside of *B*), then the PSM reconstruction was underestimated as shown in A. The one-sided p*ointwise surface distance* from $S(A)$ to $S(B)$ was calculated using Equations (42)-(44).

We also defined the one-sided PDS from $S(B)$ to $S(A)$ as $g[S(B), S(A)]$ using Equations (45)-(47). Similarly, if the point $b \in S(B)$ is inside the MRA binary mask (inside *A*) then PSM was underestimated and vice versa as shown in Figure 46A.

$$d\big(a, S(B)\big) = \min_{\forall b \in S(B)} \{\|a, S(B)\|\} \tag{42}$$

$$g\big(S(A), S(B)\big) = \frac{1}{n}\sum_{i=1}^{n} \alpha_i . d\big(a_i, S(B)\big), \forall a \in S(A) \tag{43}$$

$$\alpha_i = \begin{cases} 1 & if\ a_i \in B \\ -1 & if\ a_i \notin B \end{cases} \quad (44)$$

$$d\big(b, S(A)\big) = \min_{\forall a \in S(A)} \{\|b, S(A)\|\} \quad (45)$$

$$g\big(S(B), S(A)\big) = \frac{1}{m}\sum_{i=1}^{m} \beta_i . d\big(b_i, S(A)\big), \forall b \in S(B) \quad (46)$$

$$\beta_i = \begin{cases} -1 & if\ b_i \in A \\ 1 & if\ b_i \notin A \end{cases} \quad (47)$$

Finally, we defined the two-sided *pointwise surface distance* (PSD) between $S(A)$, and $S(B)$ as the average of the two one-sdied PSD as in Equation (48). The pseudo-code algorithm to calculate PSD is written in Table 15.

$$G\big(S(A), S(B)\big) = \frac{1}{2}\big\{g\big(S(A), S(B)\big) + g\big(S(B), S(A)\big)\big\} \quad (48)$$

Figure 46B shows three vascular segments: the first overestimates the cross-sectional diameter, the second underestimates, the third example covers the diameter approximately correct. Despite these qualitative differences, all three examples of Figure 46B have identical the two-sided HD, which shows the limitation of the HD metrics to assess over and underestimation. Fortunately, the PSD metric G, correctly detect the trends as desired. Therefore, the jagged-edged MRA images and smooth PSM meshes were analyzed according to PSD criteria.

The reconstructed PSM meshes were evaluated as acceptable, over- or underestimated based on the PSD index, where, if PSD is positive, there are more positive *pointwise surface distance* than negative ones so the PSM reconstructed was totally overestimated. PSD value close to zero indicate perfectly align diameter overlap.

Table 15. Algorithm of two-sided *pointwise surface distance* (PSD) calculation

Input: Binary mask dataset of A, B.

Output: $G\big(S(A), S(B)\big)$

$S(A) = \{a_1, a_2, \dots, a_n\}$ ← Edge extraction of A;
$S(B) = \{b_1, b_2, \dots, b_m\}$ ← Edge extraction of B;
Compute one-sided PSD from A to B
  for each Point a in $S(A)$ **do**
  $d(a, S(B))$ ← The minimum distance from a to $S(B)$;
    if $a \in B$ **then**
      $\alpha \leftarrow +1$; //Overestimation of PSM
    else $a \notin B$ **then**
      $\alpha \leftarrow -1$; //Underestimation of PSM
    end if
  $d_g\big(a, S(B)\big) \leftarrow \alpha \cdot d\big(a, \mathrm{S(B)}\big)$;
  end for
$g\big(S(A), S(B)\big) \leftarrow \sum_{i=1}^{n} d_g\big(a, S(B)\big)/n$;
Compute one-sided PSD from B to A
  for each Point b in $S(B)$ **do**
  $d\big(b, S(A)\big)$ ← The minimum distance from b to $S(A)$;
    if $b \notin$ A **then**
      $\beta \leftarrow +1$; //Overestimation of PSM
    else $b \in$ A **then**
      $\beta \leftarrow -1$; //Underestimation of PSM
    end if
  $d_g\big(b, S(A)\big) \leftarrow \beta \cdot d\big(b, S(A)\big)$;
  end for
$g\big(S(B), S(A)\big) \leftarrow \sum_{i=1}^{m} d_g\big(b, S(A)\big)/m$;
Compute two-sided PSD index of *A* and *B*
$G\big(S(A), S(B)\big) \leftarrow 0.5\,\{g\big(S(A), S(B)\big) + g\big(S(B), S(A)\big)\}$
Return $G\big(S(A), S(B)\big)$;

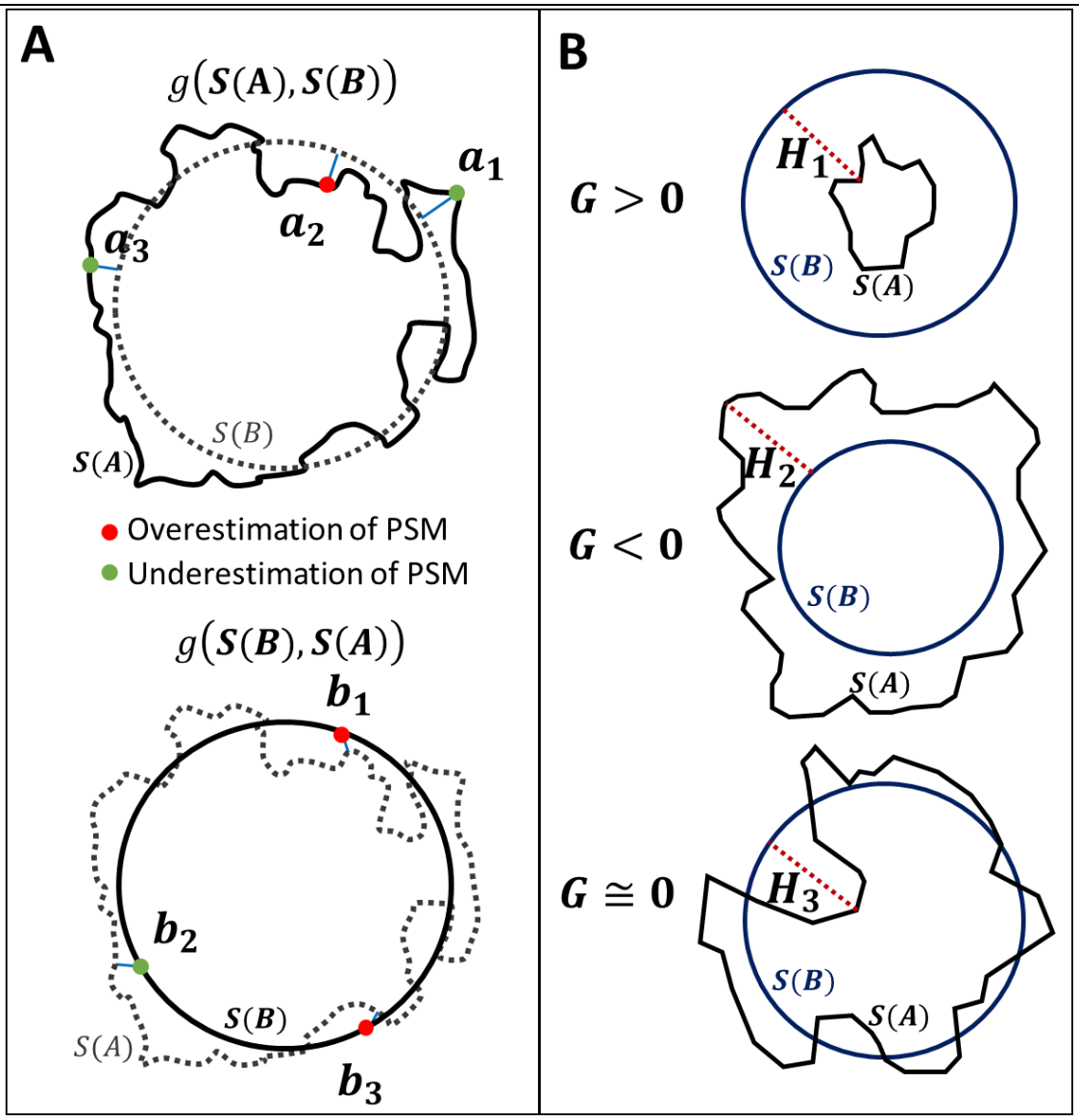

Figure 46. Pointwise surface distance (PSD) analysis and comparison with Hausdorff distances (HD). (A) Schematic of the one-sided PSD analysis. $S(A)$, and $S(B)$ are the boundaries of MRA and reconstructed parametric structured meshes (PSM) regions, respectively. The top panel represents the one-sided PSD from $S(A)$ to $S(B)$. The green and red points indicate under and overestimation of PSM at each point, respectively. The modified HD from $\{a_1, a_2, a_3\}$ to their nearest point in $S(B)$ are visualized in solid blue lines. Points $\{a_1, a_3\} \notin B$ indicates underestimated of PSM diameter for those specific points. In the lower panel, we calculated the one-sided PSD from $S(B)$ to $S(A)$ by calculating minimum distances from $\{b_1, b_2, \dots, b_m\} \in S(B)$ to their nearest neighbor in $S(A)$. (B) A schematic of the difference between HD and PSD. Three different cross-sectional vessel samples with identical calculated HD are shown in red-dotted lines ($H_1 = H_2 = H_3$). "G" is the average of the two one-sided PSD, which enables us to quantify the diameter estimation error when comparing PSM with the reference MRA images. PSD index shows overestimation $(G > 0)$ of the top, underestimation$(G < 0)$ in the middle, and an accurate diameter approximation $(G \cong 0)$ on the lower panel of B.

3.4. Results

Figure 41 illustrates the information flow diagram for the statistical analysis of reconstructed cerebrovascular trees. To detect gross errors in the tree connectivity, we first visualized MRA and PSM by global superposition in virtual reality environment *Walk-in Brain* software. For all six subjects, a total of 1364 vascular segments were automatically scanned and 119,738 CRS and 571 BIF sampling frames were captured for quantitative analysis.

3.4.1. Centerline accuracy

We first performed statistical analysis to evaluate the spatial accuracy of the centerline extraction for the vascular segments. Cross-sectional sampling frames were taken perpendicular to the centerlines of the vessel segments. The comparison of the *intensity-weighted centroid* of the RGB (red-green-blue) filtered image of the MRA and PSM showed a mean value of $145.1 \pm 111.5\ \mu m$ for the vascular CRSs (Figure 45A). Vascular centerline accuracy reached a sub-pixel size precision ($< 400\ \mu m$) for the arterial trees in this study.

3.4.2. Pixel-based statistical analysis

The binary mask areas of MRA and PSM were compared by performing linear regression and Bland Altman analysis as shown in Figure 45B. Linear regression showed a correlation efficient of 0.9489. Horizontal lines are placed at the mean of the difference and at the 95% limits of agreement. Using Bland Altman analysis, we calculated the limits of agreement within the mean of the difference as ±1.96 of the standard deviation.

We also quantified the pixel-based relative area overlap using *Dice similarity coefficient.* The *Dice coefficient* is computed for all sampling frames with a mean of Dsc_{CRS}=0.70±0.09 and Dsc_{BIF}=0.88±0.11. Total pixel-based reconstruction accuracy, Acc_{CRS}=0.91±0.08 for

Acc_{BIFs}=0.83±0.09. The area under the curve (AUC) of the ROC curves are on average 0.96±0.01 for the cross-sectional images of the six subjects as shown in Figure 45C. Table 16 and Table 17 summarize the pixel-based statistical analysis for all vascular CRSs and BIFs, respectively.

Table 16. Pixel-based statistical analysis of the vascular cross-sections.

Subjects	I	II	III	IV	V	VI	Mean±SD
Se	0.80	0.79	0.78	0.81	0.80	0.79	0.80±0.12
Sp	0.93	0.94	0.93	0.90	0.91	0.92	0.92±0.10
Ppv	0.93	0.76	0.76	0.66	0.75	0.73	0.73±0.13
Npv	0.73	0.96	0.96	0.96	0.94	0.96	0.96±0.06
Acc	0.92	0.92	0.92	0.89	0.89	0.91	0.91±0.08
Dsc	0.71	0.72	0.72	0.65	0.69	0.70	0.70±0.09
AUC	0.96	0.96	0.96	0.95	0.96	0.94	0.96±0.01

Se: sensitivity; *Sp*: specificity; *Ppv*: predictive positive value; *Npv*: Negative predictive values; *Acc*: accuracy; *Dsc*: Dice similarity coefficient; *AUC*: Area under the curve.

Table 17. Pixel-based statistical analysis of the vascular bifurcations.

Subjects	I	II	III	IV	V	VI	Mean±SD
Se	0.90	0.88	0.88	0.91	0.89	0.90	0.90±0.06
Sp	0.89	0.69	0.88	0.49	0.69	0.63	0.63±0.20
Ppv	0.64	0.86	0.99	0.90	0.87	0.87	0.88±0.12
Npv	0.86	0.70	0.46	0.53	0.71	0.67	0.65±0.19
Acc	0.82	0.81	0.88	0.84	0.83	0.83	0.83±0.09
Dsc	0.87	0.86	0.93	0.91	0.87	0.87	0.88±0.11
AUC	0.88	0.89	0.86	0.90	0.89	0.87	0.88±0.01

Se: sensitivity; *Sp*: specificity; *Ppv*: predictive positive value; *Npv*: Negative predictive values; *Acc*: accuracy; *Dsc*: Dice similarity coefficient; *AUC*: Area under the curve.

3.4.3. Point-based surface offset calculation

The *pointwise surface distance* method was deployed to quantify the difference between the jagged edges of the MRA images and the smooth surface edge of PSM. A schematic of the proposed one-sided *pointwise surface distance* (Figure 46A). Figure 46B illustrates the ability of the PSD index to differentiate between three different illustrative CRSs with the same Hausdorff distances. The calculated HD was identical for these three cross-sections, while PSD could categorize them into overestimated, underestimated and acceptable PSM reconstruction. Therefore, using PSD we can quantify the outcome of our diameter approximation for vascular CRSs. Table 18 summarizes the computed HD and PSD for CRSs and BIFs of the six human subjects.

We also introduced *diameter estimation index* (DEI) which is a nondimensional parameter defined as the two-sided PSD over the vascular diameter. Figure 47 deployed the DEI for vascular CRSs of the six cerebral arterial trees to assess the percentage of the over/underestimation of the diameters in vascular cross-sections. Vessel diameter between 0.8 to 3.2 *mm* exhibited an accuracy DEI of 2.5%. The PSM index showed a tendency of diameter underestimation for the vessels less than 1.7 *mm*, as well as overestimation for the vessels over 2.5 *mm*.

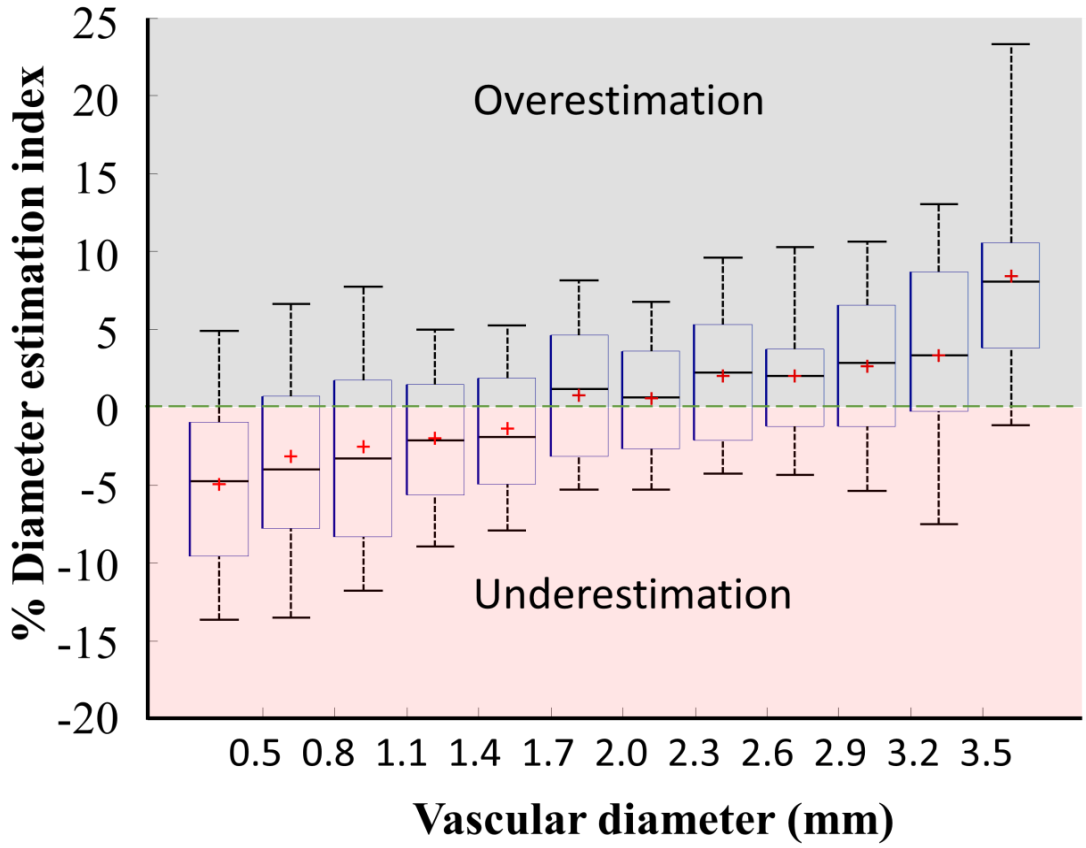

Figure 47. Diameter estimation index (DEI) of vascular cross-sections (CRSs) of six cerebral arterial trees. The DEI percentage was calculated for more than 119,000 CRSs. Positive DEI represents over-estimation of PSM diameter and negative DEI shows the under-estimated reconstructed diameters. Vessel diameters in the range of 0.8-3.2 *mm* have diameter accuracy of DEI $\leq \pm 2.5\%$. The PSM method exhibited a tendency of diameter underestimation for the vessels less than 1.7 *mm*, as well as overestimation for the vessels over 3.5 *mm*.

Table 18.Surface-based Hausdorff distances (HD) and pointwise surface distance (PSD) for cross-sections (CRSs) and bifurcation (BIFs) of the six human subjects.

	Mean Hausdorff Distances, HD (*mm*)		**Mean Pointwise Surface Distance, PSD (*mm*)**	
	CRS	**BIF**	**CRS**	**BIF**
Subject I	0.4513	0.8247	0.0146	0.0004
Subject II	0.4433	0.7861	0.0048	0.0018
Subject III	0.4721	1.3576	0.0045	0.0021
Subject IV	0.4715	1.2958	0.0083	0.0008
Subject V	0.5010	0.6987	0.0011	0.0021
Subject V1	0.4671	0.9190	0.0090	0.0030
Mean	0.47±0.02	0.98±0.28	0.0071±0.0047	0.0017±0.0009

3.4.4. Morphological and CFD analysis

Morphological analysis. We performed a preliminary study on morphological and CFD analysis to show applications of the PSM vascular reconstruction. Morphological matrices such as curvature, tortuosity, and torsion are measured for all vascular networks as shown in Figure 48 and Figure 49. Tortuosity is the ratio between the actual arc-length over the straight-line distance. Curvature and torsion uniquely determine the shape of a 3D vessels' space curve based on the speed of the bending and twisting of the curvature plane in space.

Morphological index calculation of curvature, torsion, and tortuosity using Equations (49)-(51), respectively.

$$\text{Curvature} = \frac{\left\|\vec{r'} \times \vec{r''}\right\|}{\left\|\vec{r'}\right\|^3} \tag{49}$$

$$\text{Torsion} = \frac{\left(\vec{r'} \times \vec{r''}\right) \cdot \vec{r'''}}{\left\|\vec{r'} \times \vec{r''}\right\|^2} \tag{50}$$

$$\text{Tortuosity} = \frac{L}{L_0} - 1 \tag{51}$$

With $\|\vec{.}\|$ the norm of a vector $\vec{r'}$, $\vec{r''}$, and $\vec{r'''}$ are the first, second, and third derivative of the parametric curve of the centerline. L is the total arc length and L_0 the end-first length of the vessel.

Using the probability density function (PDF), we found that the vascular segments have the diameters of 1.63±0.75 *mm*, tortuosity 0.2±0.4, curvature 0.33±0.63 mm^{-1}, and torsion 0.33±0.57 mm^{-1}.

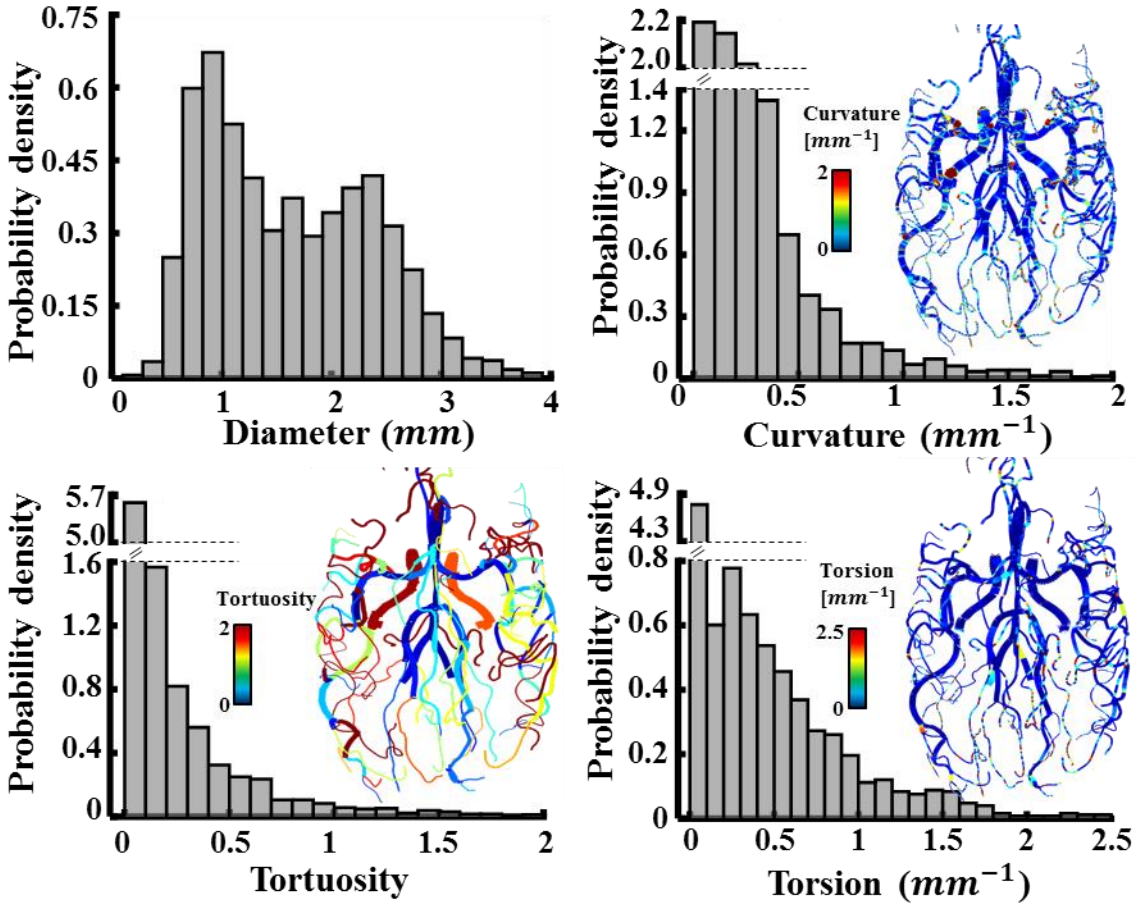

Figure 48. Morphological and computational analysis of reconstructed subject-specific cerebroarterial tree. Probability density function (PDF) and contour map were used to visualize the distribution of the vascular biometrics including diameter, curvature, torsion and tortuosity for six human subjects.

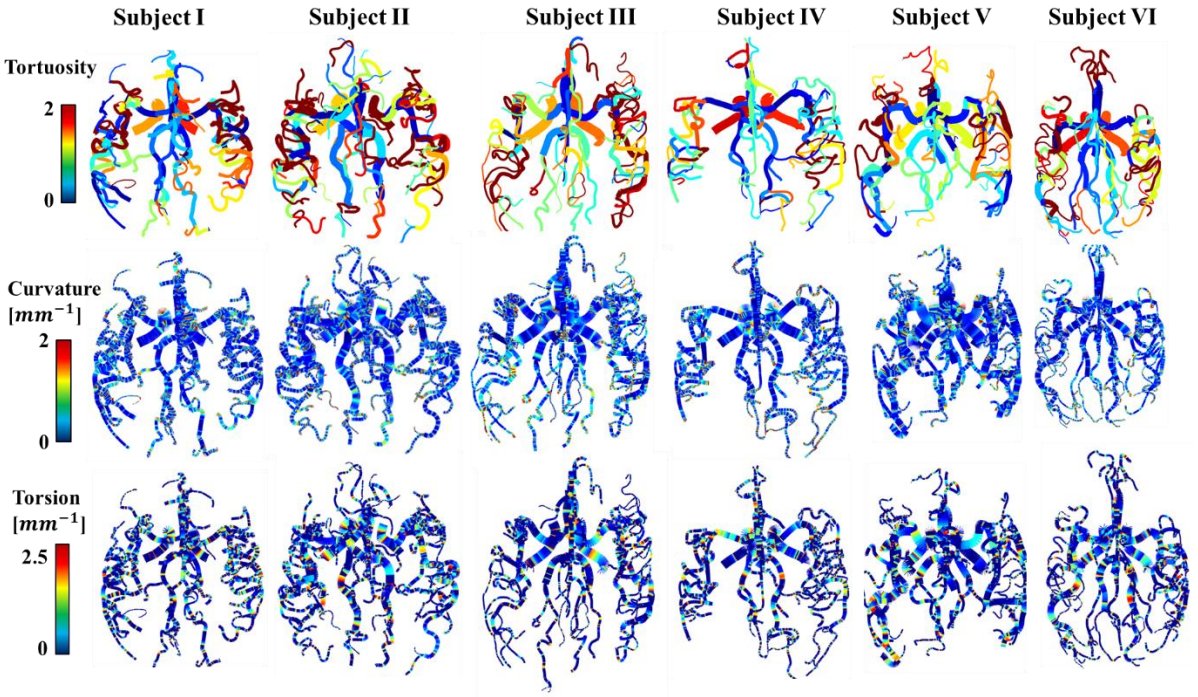

Figure 49. Morphological analysis. Tortuosity, curvature, and torsion map are illustrated for six human subjects.

Large-scale CFD analysis. The image-derived reconstruction of vascular tree can be used for both visualization and computational CFD analysis to quantify the hemodynamic risk factors such as relative residence time (RRT) for prediction of CVDs. For example, the occurrence of atherosclerosis-prone regions strongly correlates with high RRT [20], [21]. Hemodynamic analysis with the elevated RRT region in the basilar artery is shown in Figure 50. A manuscript explaining details of hemodynamic risk factor analysis for all six subjects is shown elsewhere [84].The automatic mesh generation and vascular reconstruction may be particularly suitable for computer analysis of large datasets such as patient's medical records database in hospitals. The rigorous and unbiased analysis of imaging data may become a useful enabling technology to better differentiate critical pathological factors for subject-specific variations.

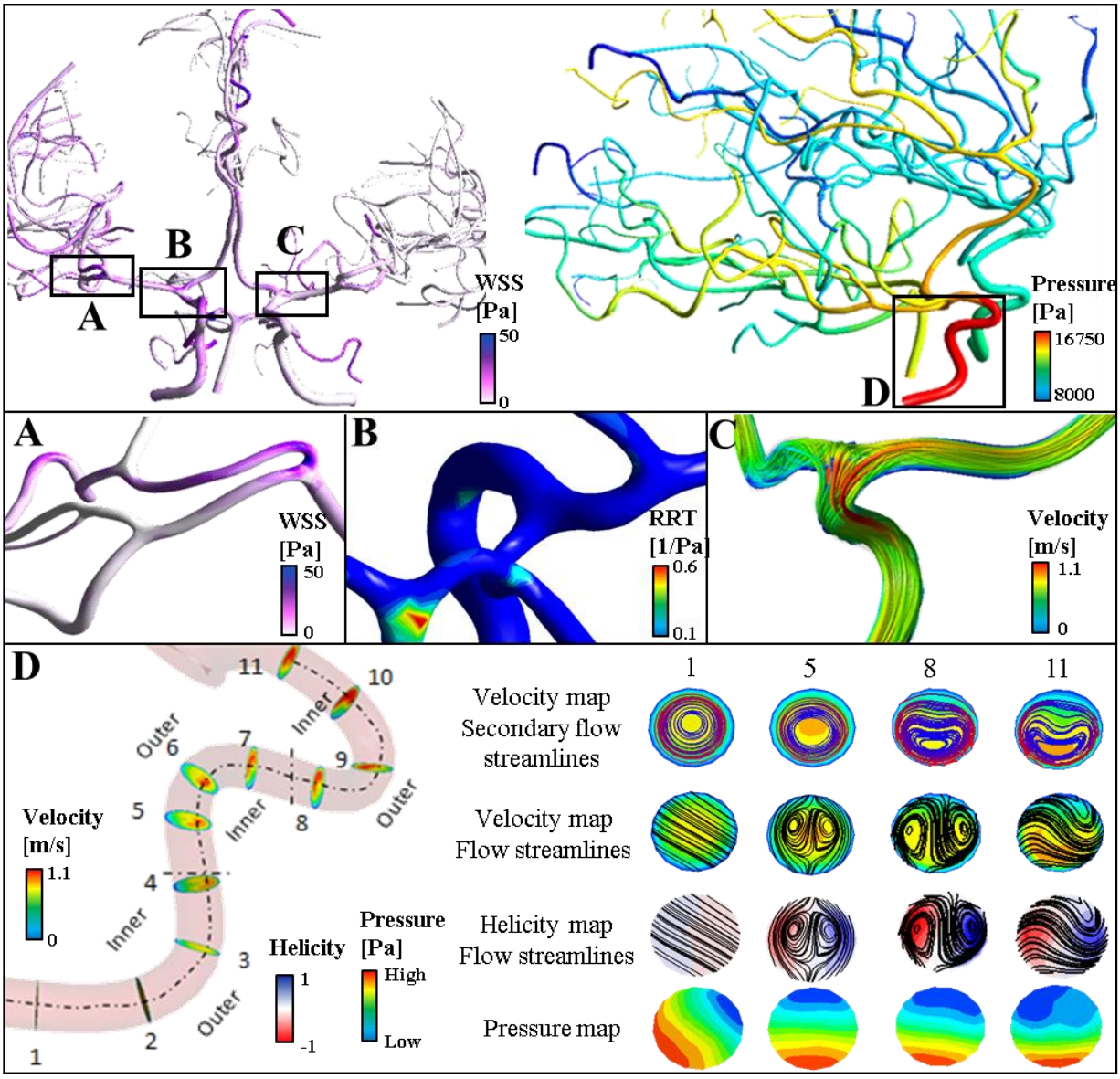

Figure 50. Preliminary 3D computational analysis. Validated reconstructed model was used for hemodynamic analysis of cerebral arterial tree. (A) Distribution of Wall shear stress for a small portion of right middle cerebral arteries, MCA. (B) Elevated Relative residence time (RRT) in the basilar artery. (C) Blood flow streamlines in the M_1 branch of left MCA. (D) Development of secondary flow in the high-tortuous RICA. Vorticity and normalized helicity are shown in select planes. Diameters are scaled to the same size for better visualization. In the vessels with high curvature, blood moves from the inner wall towards the outer wall which forms recirculation zones.

3.5. Discussion

The aim of this study is to validate the spatial accuracy of a recently proposed automatic mesh generation method for reconstruction of large-scale cerebral arterial trees. Intensity-based centerline evaluation, pixel-based statistical analysis, and pointwise surface distance were used to quantify the shape similarity between the reconstructed PSM meshes and the MRA images of arterial trees for six subjects. The proposed framework quantifies the degree of over/underestimation of the anatomically reconstructed PRM for the cerebroarterial trees.

Intensity-weighted centroid analysis showed that the extracted vascular centerline reached sub-pixel precision. Variability in the cross-sectional area portion between MRA images and PSM was assessed by performing regression and Bland Altman analysis showed a good agreement in terms of lumen area and bifurcation topology (R^2=0.95). Sensitivity and specificity of mesh reconstruction were evaluated by assessing the AUC for all vascular networks (0.96 ± 0.01 and 0.88 ± 0.01 for CRSs and BIFs, respectively).

Unlike prior vascular segmentation validation, which did not address the accuracy of the bifurcation geometry due to the discontinuity nature of the segmentation[96], our study analyzed the mesh surface near bifurcating forks. The mean of *Dsc*=0.88, and PSD=1.7 μm for 571 bifurcations underscore the ability of the reconstructed PSM to faithfully preserve endovascular bifurcation topology in human arterial trees.

Subject-specific abnormalities in the cerebroarterial vasculature such as an increased tortuosity might provide an indication of pathologies such as diabetes [97], vasculopathies [98], tumours [99] or dementia [100], [101], which affects the blood circulation and may lead to stroke, hemorrhage or hypoxia. Morphometric analysis of vascular networks like the vessel curvature or tortuosity [94]–[96] can be used for diagnostic, prediction, and therapeutic monitoring of the endovascular

diseases [102]. A comprehensive morphological analysis and territorial distributions of the cerebral arterial tree with a comparison between age and genders have been previously studied [105], [106].

The validated centerline and diameter data allows us to study morphological data of the large portion of cerebrovascular trees. In this study, the use of Bezier spline in vascular skeletons facilitates the speed and acceleration computation of vessel bending, enabling unique biometric visualization of torsion and curvature as shown in Figure 48. Automatic biometrics extraction would enable automatic morphological analysis on a large healthy population and patients with intracranial diseases before and after endovascular treatment.

The sampling frame acquisition required on-average 65.1 *min* for each subject using a single-core 2.4 GHz Xenon CPU processor. It takes almost 16.5 *min* to compute pointwise surface distances for all 2D sampling frames of all BIFs and CRSs (~20,050 snapshots) for each subject (Table 13). The current implementation of the PSD algorithm analyzes every single edge points of MRA and PRM in 2D sampling frames. Future extension of PSD algorithm should perform a direct 3D surface comparison with more efficient surface point sampling techniques [93], [107].

In this manuscript, PSD was demonstrated for mesh validation, however, it may also be applicable for crisp evaluation of the registration [108], segmentation, morphological data acquisition [109] and motion detection. The PSD index can be also extended to optimize current smoothing algorithm by evaluating the surface mesh in each iteration to avoid deformation and shrinkage of noisy surface meshes.

The reconstruction validation and dataset presented here should be extended for future studies of the pathological cases with endovascular diseases such as stenosis or aneurysm. In addition expansion to different imaging modalities to evaluate vein dataset is another possible future study.

Another direction pertains to assessment of arterial wall biomechanics [110], [111] by using high-resolution MRI vessel wall imaging.

4. SIMULATION

In this chapter, we will show the details of 3D computational simulation for six human subjects and two pathological cases. This chapter is previously published by Ghaffari, Mahsa, et al. "Quantification of near-wall hemodynamic risk factors in large-scale cerebral arterial trees." International Journal for Numerical Methods in Biomedical Engineering (2018).

4.1. Abstract

In the last decade, detailed hemodynamic analysis of blood flow in pathological segments close to aneurysm and stenosis has provided physicians with invaluable information about the local flow patterns leading to vascular disease. However, these diseases have both local and global effects on the circulation of the blood within the cerebral tree. The aim of this paper is to demonstrate the importance of extending subject-specific hemodynamic simulations to the large-scale cerebral arterial tree with hundreds of bifurcations and vessels, as well as evaluate hemodynamic risk factors and waveform shape characteristics throughout the cerebral arterial trees. Angioarchitecture and *in vivo* blood flow measurement were acquired from healthy subjects and in cases with symptomatic intracranial aneurysm and stenosis. A global map of cerebral arterial blood flow distribution revealed regions of low to high hemodynamic risk that may significantly contribute to the development of intracranial aneurysms or atherosclerosis. Comparison of pre- and post-intervention of pathological cases further show large angular phase shift (~33.8°), and an augmentation of the peak-diastolic velocity. Hemodynamic indexes of waveform analysis revealed on average a 16.35% reduction in the pulsatility index after treatment from lesion site to downstream distal vessels. The lesion regions not only affect blood flow streamline of the proximal sites, but also generate pulse wave shift and disturbed flow in downstream vessels. This

necessitates the use of large-scale simulation to visualize both local and global effects of pathological lesions.

4.2. Introduction

Quantitative magnetic resonance angiography (qMRA) is a commonly used non-invasive imaging modality to quantify blood flow in the cerebral arteries. However, it is limited to large cerebral arteries [12] and cannot reliably measure slow flow in small arteries. Moreover, qMRA does not provide enough spatial and, more importantly, temporal resolution to assess *near-wall hemodynamic factors* that are important in understanding of *cerebrovascular disease* (CVD). *Near-wall hemodynamic factors* include wall shear stress (WSS), time-averaged WSS (TAWSS), oscillatory shear index (OSI), relative residence time (RRT). The importance of disturbed flow as well as WSS vector directional changes [13], [14], [16] in CVD have been shown in the vascular tree. OSI has been correlated with plaque formation [18], [112] and high TAWSS initiates cerebral aneurysm formation [19]. The occurrence of atherosclerosis-prone regions strongly correlates with low TAWSS and high OSI (i.e. high RRT) [20], [21]. A clinical study by Kawaguchi et al. [22] demonstrated that there was a distinctive flow pattern between the ruptured and unruptured blebs and that the WSS was lower in the ruptured aneurysm. Animal and clinical studies have shown that sustainable secondary flow can significantly reduce the likelihood of thrombosis formation inside vascular grafts [23], [24]. Since none of these parameters can be measured directly, we propose to complement *in vivo* blood flow measurements by performing subject-specific CFD computations on a large cerebral arterial tree to assess hemodynamic risk factors.

Accurate cerebral arterial trees modelling require precise subject-specific reconstructions of the cerebral vasculature, which exhibits large profound geometrical variations between individuals. Any small changes in intracranial geometry can potentially create large effect on WSS and its derivatives [26]. For example, the *circle of Willis* (CoW) is an important pathway in maintaining and distributing cerebral blood supply. Its ability to redistribute blood depends highly on its morphology, presence and the shape of the communicating vessels. The effect of anatomical variation of CoW on CVDs has been well explained [113]–[115]. A close correlation has been reported between a low distribution capacity of the CoW and an increased risk of stroke [36], [116]. Beyond the CoW, the pial arterial networks extending in the other territorial regions are highly variable between individuals. Small changes in resistance and configuration of these vascular territories give rise to different levels of collateral blood supply, which may result in vascular reserve. In order to address individual anatomical variations, we propose to generate subject-specific models of the entire vascular trees.

In recent years, numerous studies have been devoted to performing CFD hemodynamic analysis, while detailed 3D simulations were performed mostly on a few branches and small segments. Here, we propose the extension of excellent prior studies [117]–[121] to the *large-scale* segment of cerebral arterial tree. The ability of *multi-scale algorithms* to resolve important biophysical processes of brain blood flow has been well addressed [15], [46], [122]–[126]. However, global hemodynamic flow simulations were mostly performed on the simplified 1D cerebral arterial tree [127]–[130]. Our global approach also has the advantage of assessing *near-wall hemodynamic analysis* for the large portion of the arterial tree including downstream vessels where undesired hemodynamics changes could occur far away from the site of intervention. For example, *delayed ipsilateral parenchymal hemorrhage* (DIPH) was reported in vascular beds

distal to the site of flow diversion deployment [75], [76], [79], [80]. Assessment of changes in cerebral circulation for a large cerebral arterial tree would shed light into the pathophysiology of the unexplained DIPH [131]. The possibility of remote and delayed hemorrhage caused by endovascular intervention underscores the need for assessing hemodynamic changes not just on a local scale, but throughout a much larger portion of the cerebrovascular tree.

Since high-risk hemodynamic parameters cannot be measured directly, we propose to augment the value of *in vivo* flow measurements with subject-specific CFD analysis to infer hemodynamic risk factors. In this paper, we will assess risks regions throughout the large-scale cerebral circulation for six healthy and two illustrative cases with cerebrovascular before and after endovascular treatment.

4.3. Methods

Time-of-flight (TOF) and phase contrast magnetic resonance angiography (PC-MRA) were used to measure blood flow and obtain DICOM source imaging data used for anatomical reconstructions from six healthy volunteers and two pathological cases, one with intracranial aneurysms and the other with a stenosis. A *vesselness enhancement filter* [58] was used to enhance the contrast of cerebral angioarchitecture [60], down to pial arteries (400 μm). After image filtering, information on the vessel centerline and radius of the vascular network were extracted. We then applied an automatic *parametric meshing technique* to generate flow-aligned hexahedral meshes [59], [60], [85]. Regional *in vivo* volumetric cerebral blood flows were measured at major arteries in the Circle of Willis. Three-dimensional dynamic CFD analysis was performed to calculate blood flow and hemodynamic risk factors in the cerebral arterial tree for the healthy and illustrative pathological cases.

4.3.1. Image acquisition and enhancement

Six healthy human explained in Chapter 2 were used for this study too. In addition, we added pathological cases.

The first illustrative pathological case was a 74-year-old female who had a large aneurysm involving the right *posterior inferior cerebellar artery* (PICA), who was treated with aneurysm clipping. The second illustrative pathological case was a 59-year-old male diagnosed with a severe critical left middle cerebral artery stenosis, who was treated with angioplasty. In addition, single vessel (left ICA, Right VA) three-dimensional *digital subtraction angiography* (DSA) data set for the two illustrative pathological cases were also collected to enhance the image reconstruction.

Time-dependent blood flow data were obtained using TOF angiography and anatomical information was acquired with PC-MRA. For the illustrative cases with stenosis/aneurysm, the same flow data was acquired twice: one *pre-intervention* (PRI), and second *post-intervention* (PSI). Finally, raw TOF and Magnetic Resonance Angiography (MRA) images were passed to a vessel enhancement filter to successfully identify and segment small pial arteries. We used our in-house developed *vesselness filter* to enhance the contrast of the arterial tree in MRA images [58], [59]. The scan parameters of TOF and PC-MRA are documented in Table 19. MRA and DSA were acquired under Institute Review Board approval at the University of Illinois at Chicago.

Table 19. Scan parameters of time-of-flight (TOF) and phase contrast MRA (PC-MRA) flow measurement for investigated subjects.

Scan parameters	TOF	PC-MRA (NOVA protocol)
Number of excitations	1	2
Temporal resolution (ms)	26	10.9
Echo Time	3.4	4.2
Flip angle (deg)	18°	25°
Acceleration factor	2	-
Number of slabs	4	-
Magnetization transfer	on	-
Matrix size	512 × 512 × 408	-
Voxel size (mm)	0.39 × 0.39	-
Slice Thickness (mm)	0.6	-
Slice Spacing	0.3	5
Echo Train Length	1	1
Pixel Spacing	0.3906	0.625
Cardiac Number of Images	-	12
Velocity Encoding (VENC)	-	1000
Acquisition time (s)	18000	-

4.3.2. Large-scale parametric mesh generation

We used a parametric *mesh generation* method described previously [59], [60], [85]. In brief, geometrical descriptors such as centerline and radii were extracted using the Vascular Modelling Toolkit (VMTK) software [132]. A Bezier spline approximation was used to parametrize and smooth the vascular centerlines. To complete vascular network reconstruction, hexahedral meshes were parameterized along the vessels in radial, cross-sectional and longitudinal directions, as shown in Figure 51A. For each branch, the number of longitudinal subdivisions was chosen based on the curvature and local vessel diameter. Statistics of the reconstructed cerebral arterial tree with parametric meshing technique for six volunteers are summarized in Table 20-Table 21.

We also applied our parametric meshing method for two illustrative cases with vascular diseases: an MCA stenosis lesion case and a large saccular aneurysm involving the right *posterior inferior cerebellar artery* (PICA). The stenosed region was completely meshed parametrically. For aneurysm case, we used *hybrid meshing* to enable combination of highly dense mesh refinement

in the aneurysm with economic reconstruction of the disease-free portion of the cerebral circulation. For the outpouching of the aneurysm, we used an unstructured meshing approach [12], [13], [45], [46]. Unstructured meshes for the aneurysm were fused with the parametric meshes for the normal adjacent parent vessel.

Table 20. Statistics of vascular tree Skeletonization for six volunteers.

Subjects	#Points	#Branches	#Bifurcations	Blood volume (ml)
I	15688	133	68	4.01
II	22502	294	100	4.28
III	17436	175	89	5.36
IV	24485	309	122	4.75
V	20477	247	99	4.76
VI	19203	206	93	4.70
Mean	19965	227	95	4.64

Table 21. Statistics of CPU time for parametric mesh generation and simulation of cerebral arterial trees for six volunteers.

Subjects	#Elements	Meshing time (min)	CPU time T_c (min)
I	1783K	15.6	78
II	2158K	18.4	86
III	1876K	16.8	103
IV	2115K	19.6	89
V	1918K	17.5	72
VI	1897K	17.4	82
Mean	1958K	17.6	85

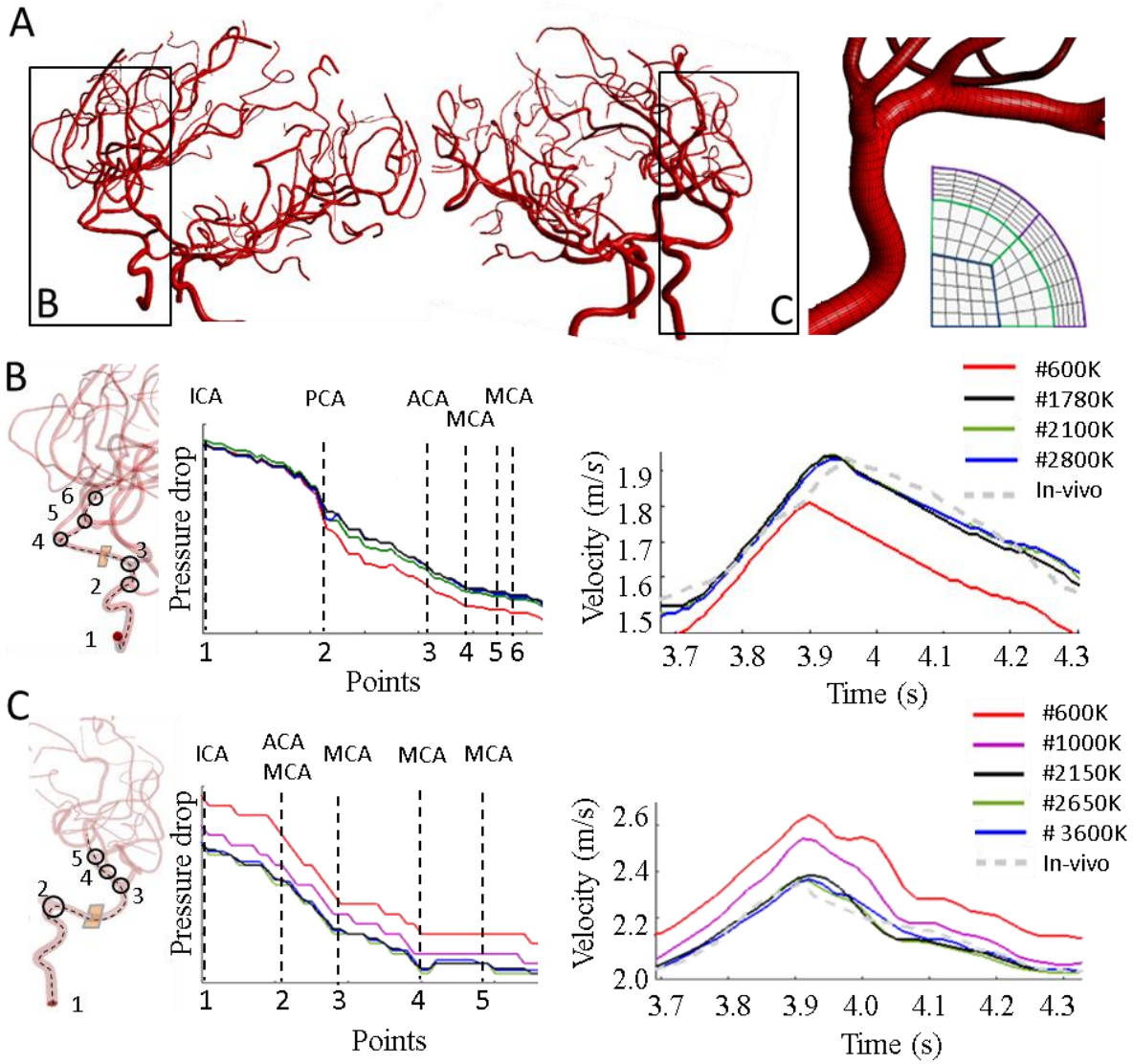

Figure 51. Mesh independence test for parametric meshes in two subject-specific cerebral arterial trees. (A) Parametric mesh of two subjects. Longitudinal and cross-sectional mesh density can be adjusted to control mesh resolution. Here, refinement was optimally performed based on the local diameter and centerline curvature. (B) Mesh independence for subject I. A centerline from RICA to RMCA passing through six main bifurcations was used to compare pressure values computed with different mesh element numbers. For each mesh, time-dependent velocity profiles for a plane marked in orange was also plotted. Meshes with the fewer cross-sectional element (black) slowly approached stable results shown for high-resolution models (green and blue) thus demonstrating mesh independence. (C) Mesh independence for subject II. Pressure trajectories for different resolution were plotted along large sections of the centerline spanning the LICA to LMCA regions. In addition, average velocity magnitude profiles are shown for a location at the entrance of the LMCA for different mesh resolution. Pressure and velocity results for green and blue are virtually identical with 2650K and 3600K elements. By varying cross sectional density, mesh-independent results were achieved with a 2150K mesh. These results demonstrate the achievement of mesh independence with parametric meshing technique.

4.3.3. Subject-specific blood flow measurement

Two imaging protocols, TOF and PC-MRA were used for acquiring anatomical and dynamic information to quantify volumetric pulsatile blood flow. These images were processed using a commercial flow analysis software, NOVA (Vassol Inc, River Forest, IL) [82]. Blood flow was measured from incoming flow to CoW including the left and right internal carotid arteries (LICA and RICA) and basilar artery (BA); in addition, "arteries leaving the CoW include the anterior cerebral arteries (LACA and RACA), middle cerebral arteries (LMCA and RMCA) and the left and the right posterior cerebral arteries (LPCA and RPCA)" [133]. Total scan time for each subject was 50-60 minutes. Acquired volumetric blood flow measurements are depicted in Figure 52 and summarized in Table 22.

Table 22. Comparison of volumetric blood flow rate acquired by PC-MRA (NOVA protocol) and CFD simulation results in cerebral arteries.

Average flow rate [mL/min]	Subject I			Subject II			Subject III		
	NOVA	CFD	% Diff	NOVA	CFD	% Diff	NOVA	CFD	% Diff
RACA	60.11	59.80	0.52	60.80	61.80	1.64	92.20	92.50	0.32
RMCA	103.4	105.0	1.55	165.7	168.9	1.93	118.5	114.9	3.03
RPCA	63.10	62.90	0.32	68.80	69.60	1.16	60.90	57.60	5.41
LACA	47.40	49.20	3.79	61.90	62.40	0.81	63.70	62.90	1.25
LMCA	103.1	102.3	0.78	172.6	171.4	0.69	124.9	132.7	6.24
LPCA	61.10	62.90	2.95	95.10	89.00	6.41	63.700	62.96	1.16
Avg. Frequency	1.330	1.35	-	1.470	1.460	-	1.550	1.520	-
Avg. Amplitude	15.09	15.9	-	20.02	21.31	-	18.69	21.50	-

LICA/RICA: left and right internal carotid arteries. BA: Basilar artery. LACA/ RACA: left and right anterior cerebral arteries. LMCA/RMCA: left and right middle cerebral arteries. LPCA/RPCA: left and right posterior cerebral arteries.

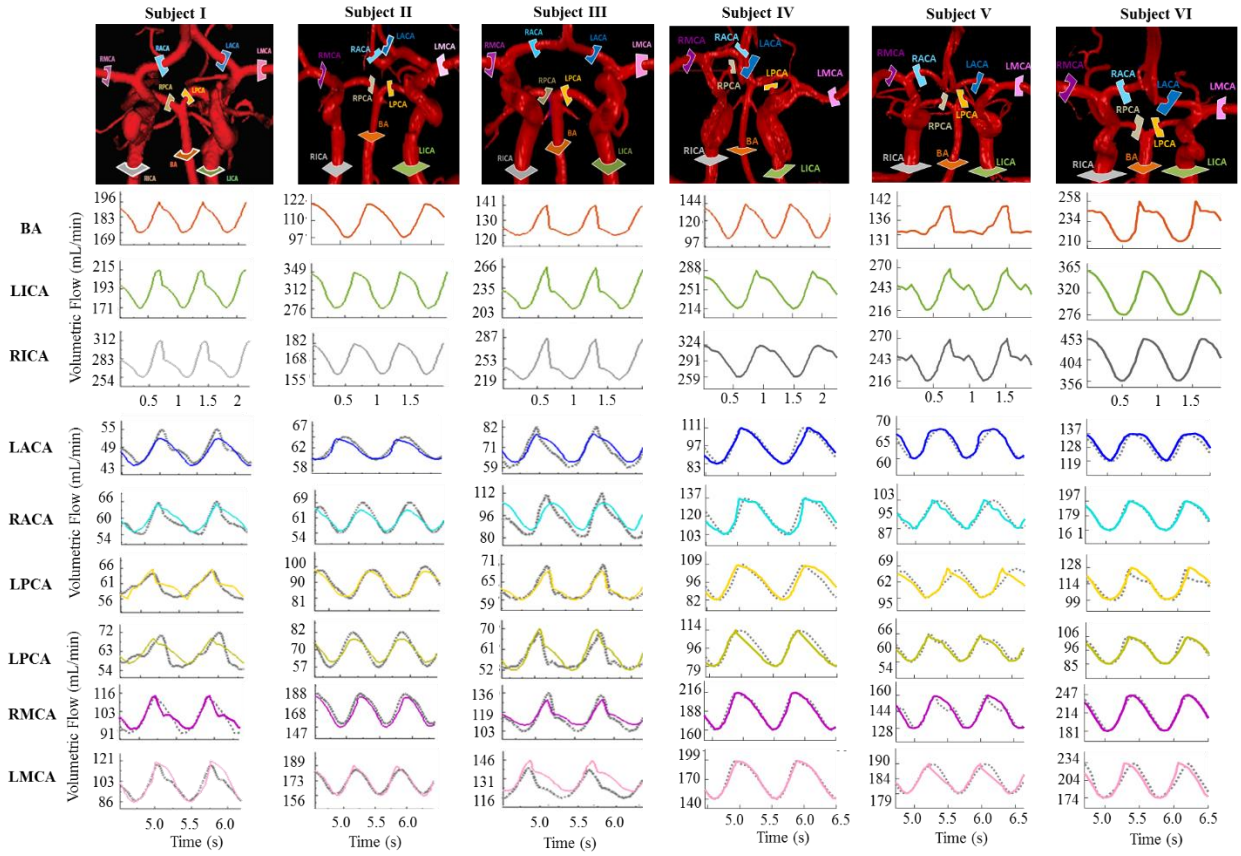

Figure 52. Comparison of regional blood flow measurement and subject-specific simulation using PC-MRA flow measurement. Three examples of *in vivo* measurements are shown in the first row. The color-coded slice plane is perpendicular to the longitudinal axis of a vessel segment showing where the measurement was made in the main cerebral arteries. The solid color-coded curves are measure blood flow and gray dotted profiles are the simulated blood flow in the main arteries of cerebral arterial tree.

4.3.4. Hemodynamic simulation and anatomical labeling

Transient hemodynamic simulations were carried out using ANSYS Fluent 18.0 (ANSYS Inc., Canonsburg, PA) with a *second-order upwind scheme* with 40 iterations per time-step, and time-step size of 0.001 seconds using the parallel 14-core processor on dual 2.4 GHz Xenon CPUs. Blood rheology is modeled as a viscous, incompressible, single-phase Newtonian fluid with a density of 1055 kg/m^3 and dynamic viscosity of 4.265×10^{-3} $Pa.s$. The vessel walls were assumed rigid with no-slip boundary condition. Convergence criterion of the simulation was set to 10^{-6} for residual error of continuity within each time step. The simulation results were reported after

multiple cardiac cycles to eliminate initial transients. Streamlines and hemodynamic variables were computed using *CFD-Post 18.0* and *MATLAB R2016b*.

We first classified the vessels based on their anatomical territories. The Inflow arteries are left and right internal carotid arteries (LICA and RICA) as well as either basilar artery (BA) or both right and left vertebral arteries (RVA and LVA), Outflow vessels were categorized based on their feeding anatomical regions in six groups of the left and right middle cerebral arteries (LMCA, RMCA), posterior cerebral arteries (LPCA, RPCA) and anterior cerebral arteries (LACA, RACA).

The blood flow measurements, obtained from the NOVA scans, at the RICA, LICA, as well as BA (or RVA, LVA) served as pulsatile inlet boundary conditions for our simulations. For all outlets, outflow pressure boundary conditions were assigned based on the volumetric flow rates from *in vivo* measurements at LMCA, RMCA, LPCA, RPCA, LACA, RACA vessels [40], as shown in Figure 52. Dynamic pressure boundary conditions were set for the six outflow territories including (LACA. RACA. LMCA, RMCA, LPCA, RPCA outlets) of 1D simulation to minimize the in-vivo PCMRA blood flow with computational fluid dynamic simulation [134]. The computed pressure values were used in the 3D simulation. A small modification of the pressure boundary condition to match the CFD blood flow distribution in the circle of Willis based on the regional measured blood flow distribution data.

Large-scale blood flow simulations required suitable boundary conditions selection. Here we describe a procedure to obtain optimal choices for terminal outflow pressures consistent with given blood flow measurements.

The desired pressures are calculated optimally by minimizing the difference between measured flow $f(t)$ and simulated flow $\hat{f}(t)$ at regions of interest. Clearly, a rigorous optimization would imply full 3D dynamic fluid flow inversion, which is impractical. Instead, a 1D network model

composed of cylindrical tubes was used to determine simultaneously the set of matching boundary pressures by solving the optimization problem in Equation (52). The optimal boundary condition adjustment can be performed for averaged flow rates (stationary flow), or extended to time dependent signals by solving the optimization problem for each frequency of a Fourier decomposed measurement signal. The optimization problem implies an assumption about territorial blood flow distribution in terminal nodes. Here we assumed that terminal branches discharge blood flow volume in proportion to their cross sectional area. Note that inlet pressures (we chose carotid and basilar artery inlet pressures) needs to be selected to calibrate the absolute pressure level. Hence, absolute pressure levels cannot be inferred from flow measurements alone. These boundary signals were used in the 3D CFD simulation.

$$\begin{aligned} z(p,f,t) &= \min_{f,p} \left\| \hat{f}(t) - f(t) \right\| \\ s.t. & \\ Af(t) - Z_1 p(t) &= 0 \\ Z_2 f(t) &= 0 \\ p(t) - \bar{p}(t) &= 0 \end{aligned} \tag{52}$$

Here, $\hat{f}(t)$ and $f(t)$ are the measured and the predicted flow, respectively. $p(t)$ is the predicted pressure. The symmetric matrix A contains the flow resistances, Z_1 is the network nodal matrix and $Z_2$is the flow incidence matrix of the vascular network.

If desired, boundary pressure choices obtained by optimization can be finely adjusted in the dynamic simulations to sharpen the alignment with the measured with the rigorous 3D computations. The blood flow measurements, obtained from the NOVA scans, at the BA, RICA, and LICA served as pulsatile inlet boundary conditions in our simulations. We performed a Fourier series approximation to set velocity boundary conditions at the inlet of the basilar and carotid arteries, which were implemented in ANSYS Fluent with user-defined functions (UDF).

The same procedure was used for each of the healthy and illustrative pathological cases with stenosis and aneurysm, each with their specific anatomical vascular trees, and intracranial flow measurements as an input and output for the CFD analysis. We performed a Fourier series approximation given in Equation (53) to set velocity boundary conditions at the inlet of the basilar (or vertebral arteries) and carotid arteries, using user-defined functions (UDF).

$$v_k(t) = a_0 + \sum_{n=1}^{N} (a_n \cos n\omega t + b_n \sin n\omega t), \tag{53}$$

For inlet boundary condition, including RICA, LICA as well as BA or both RVA, and LVA. N is the total number of the harmonic in the Fourier series. ω and t are the fundamental frequency and time domain of the flow profile. a_0, a_n, and b_n are the coefficients of the trigonometric Fourier series.

4.3.5. Near-wall hemodynamic risk factors

In this section, we will first introduce the near-wall hemodynamic factors chosen for this study. Then, we will quantify hemodynamic risks and classify the regions into normal, low-risk and high-risk regions. Changes in static or dynamic WSS have been implicated in cerebrovascular pathologies [135]. Several indicators were computed to account for biomechanical stresses in vessel walls throughout the entire arterial tree. The absolute value of WSS was calculated to illustrate its spatial distribution along the intracranial vessel wall. Using TAWSS and OSI, we will quantify the temporal distribution of WSS. Time-averaged wall shear stress is the integration of the WSS magnitude at each node over one single cardiac cycle, Equation (54) [136]. OSI is a nondimensional parameter quantifying the direction of WSS fluctuations during one cardiac cycle,

Equation (55) [112], [137]. The RRT is proportional to a combination of TAWSS and OSI Equation (56) [138].

$$TAWSS = \frac{1}{\tau}\int_0^{\tau} \left|\overrightarrow{WSS}\right| dt \tag{54}$$

$$OSI = \frac{1}{2}\left(1 - \frac{\left|\int_0^{\tau} \overrightarrow{WSS}\, d\tau\right|}{\int_0^{\tau}\left|\overrightarrow{WSS}\right| d\tau}\right) \tag{55}$$

$$RRT = \frac{1}{TAWSS(1 - 2\,OSI)} \tag{56}$$

$\left|\overrightarrow{\mathrm{WSS}}\right|$ is the magnitude of instantaneous WSS vectors ($\mathrm{N/m^2}$) and τ (sec) is a cardiac cycle. Regions with high OSI are predisposed to endothelial dysfunction, showing the high risk of local thrombosis and plaque formation [112], [139], [140]. The risk-free range of [141], [142]. WSS is between 1.0 to 7.0 Pa in the arterial network [68], [143], [144] and under 0.2 for OSI. On the other hand and high RRT (higher than 10 1/Pa) [145], [146] , low time-average wall shear stress values (less than 0.4 Pa), [68]are reported to increase the possibility of atherosclerosis. OSI greater than 0.3 have been also shown to promote atherogenesis [137], [147]. Considerably, we summarized the literature results into three regions of normal, low-risk and high-risk regions in Table 23. These classifications were used to categorize the level of hemodynamic risk in healthy and pathological cases.

Table 23. Problematic reported ranges of near-wall hemodynamic parameters (RRT, OSI, and TAWSS). Normal zone as well as low- to high-risk zone are defined based on literature reports.

Parameter	**Normal range** [68], [141]–[144]	**Low-risk range**	**High-risk range** [68], [145], [146]
TAWSS [Pa]	1.0 to 7.0	0.4 to 1.0	≤0.4
OSI	≤0.2	0.2 to 0.3	≥0.3
RRT [m2/N]	-	<10	≥10

TAWSS: time-averaged wall shear stress; OSI: oscillatory shear index; RRT: relative residence time.

4.4. Results

4.4.1. Mesh generation for cerebrovascular tree

We first report on the anatomical consistency of the reconstructed vascular trees. For each of the six healthy subjects, the large cerebral arterial tree was reconstructed with an average of 227 ± 68 vessel segments and 95 ± 17 bifurcations. Information about reconstructed arterial trees, computational meshes, CPU time for mesh generation and simulation for all volunteers are listed in Table 20. The computational meshes with subject-specific CoW anatomical variations are depicted in Figure 53A. For example, *Subject I* and *III* are missing left posterior communicating artery (PCOM). In *Subject II,* A1 part of the RACA and right PCOM are absent. *Subject IV* has an absent left PCOM and theACA. *Subject V* has both right and left PCOM absent. *Subject VI* possesses a complete CoW. The CPU time for vascular network segmentation and parametric mesh generation of the cerebrovascular tree takes less than 17 minutes on single-core processor of 2.4 GHz Xenon CPUs. The total number of required mesh cells after mesh-independence tests are listed and shown in Table 20 and Figure 51B-C.

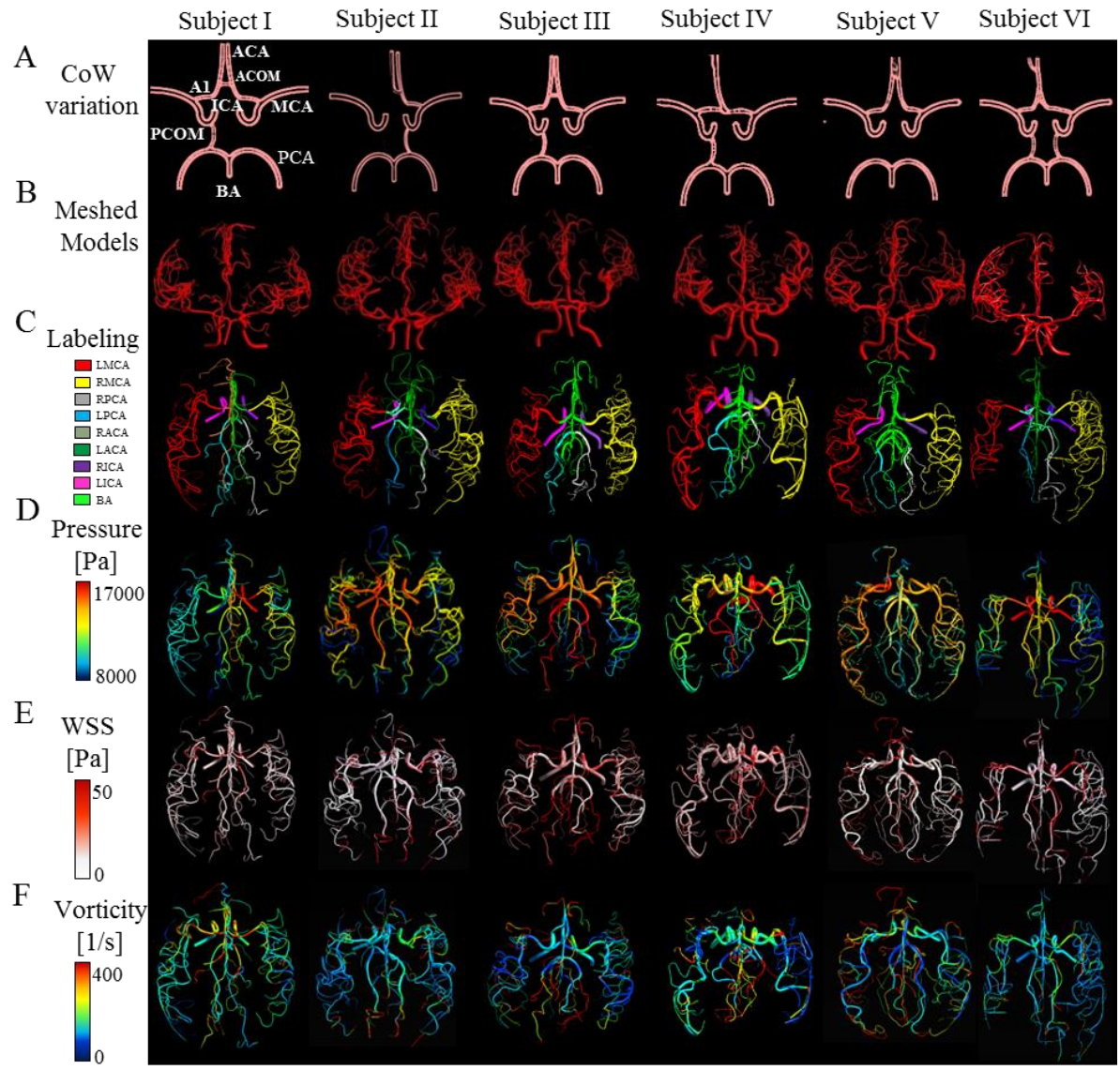

Figure 53. Cerebrovascular tree reconstructions (A-B), labeling (C), and simulation (D-F) for six healthy subjects. Each column represents a subject. (A) Schematic frontal views of anatomical variation of Circle of Willis. The absence of Left PCOM in *Subject I. Subject II:* Absence of A1 segment and right PCOM. In *Subject III: Absence of* Left PCOM. *Subject IV* Absence of left PCOM and presence of Azygos ACA present. *Subject V: Absence of* both PCOMs. Finally, a complete CoW in *Subject VI.* (B) An anterior view of parametric mesh of the subject-specific cerebral arterial trees. (C) Atlas of cerebral arterial tree. Cerebral arterial trees were labeled in their corresponding anatomical regions of LMCA, RMCA, LPCA, RPCA, LACA, RACA and BA. (D) Predicted pressure field at systole obtained by 3D CFD simulation for the entire cerebrovascular tree. Higher blood pressure in ICAs and BA, which gradually decreased towards the smaller outlet vessels. (E) Computed WSS on the arterial wall at peak-systole. (F) Visualization of blood flow vorticity magnitude in arterial trees to show the presence of secondary flow patterns at peak-systole.

4.4.2. Subject-specific blood flow simulation

PC-MRA blood flow measurements in the main arterial territories (RMCA, LMCA, RACA, LACA, RPCA and LPCA) for six healthy and two illustrative stenosis/aneurysm cases (pre- and post-intervention) were acquired. *In vivo,* PC-MRA flow results were compared with *CFD* predictions. Figure 52 illustrates color-coded slice planes perpendicular to the main flow direction, and plots dynamically measured and computed volumetric flow rates in the main cerebral arteries for the first three subjects with average volumetric flow error of $2.27 \pm 0.64\%$. The deviations between measurements and simulations for territories are summarized in Table 22. The blood flow analysis also includes average volumetric blood flow, frequency, and amplitude.

4.4.3. Hemodynamic analysis of low- to high-risk regions

Here we will illustrate quantification of near-wall hemodynamic risks as outlined in the method section and classify the regions into normal, low-risk and high-risk sites in Table 23. The large-scale analysis enabled us to detect lesion-prone sites through the wide portion of the cerebral arterial tree.

Low-risk regions: We first visualize the low-risk hemodynamic risks in healthy and stenosis/aneurysm cases. Figure 54A and Figure 54B exhibit the location of relative higher RRT in the both inner and outer portion of the carotid siphon of *subject II,* and *subject IV,* respectively. Low-risk sites were also found on a curved vessel following *the aneurysm lesion* in PRI as shown in Figure 54C. Figure 54D and Figure 54F show the relatively high level of RRT mostly at the side of the daughter branches at the bifurcations of *subject III* and *subject VI,* respectively. In *subject I* and *subject III* (data not shown), nearly perpendicular bifurcations such as the junction of PCOM and PCA or basilar tip were also found to have relatively high RRT as shown in Figure 54G. Distal

vessels of MCA in the *stenosis cases* were detected as risky regions while after angioplasty, no sign of low-risk was visualized in regions downstream of the MCA as shown in Figure 54H-I.

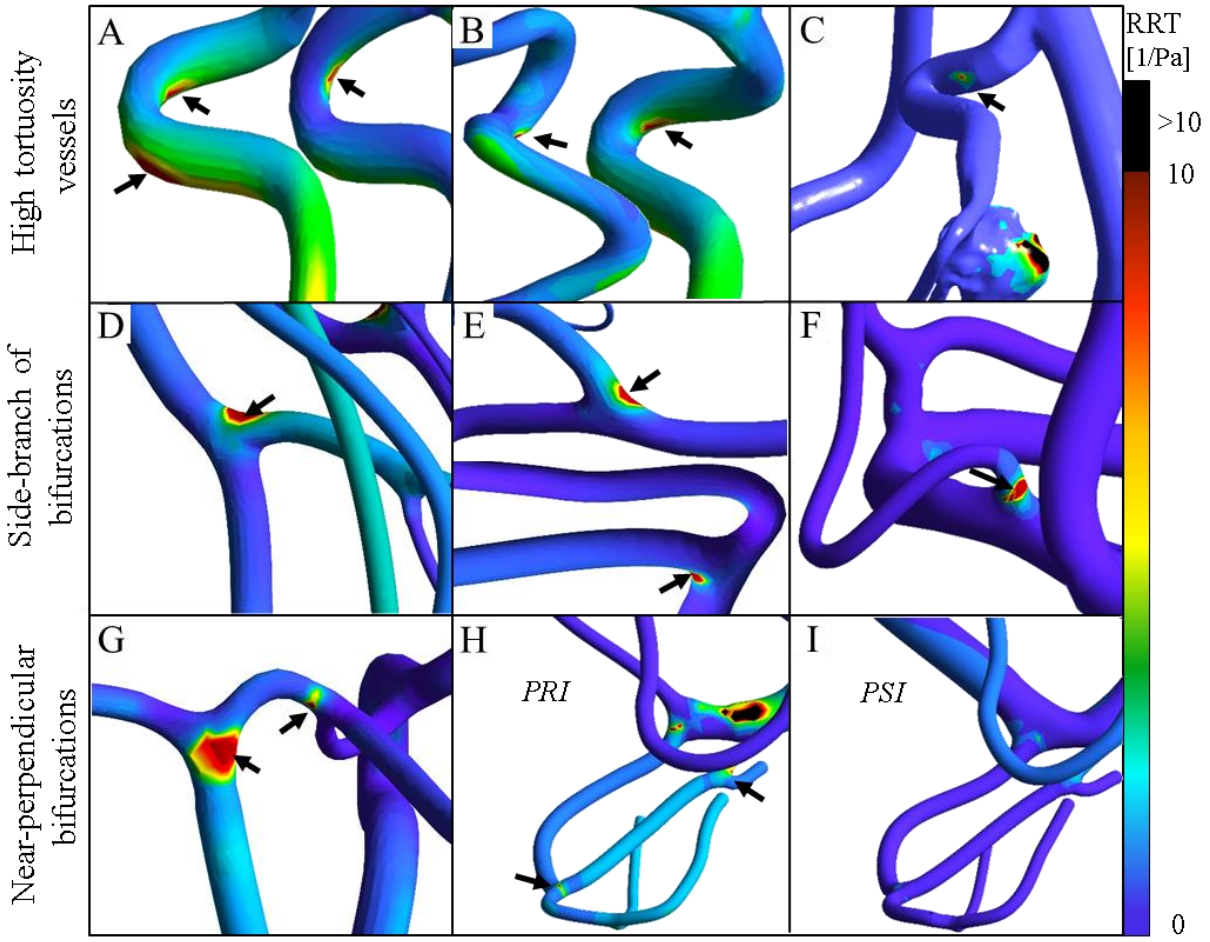

Figure 54. Assessment of hemodynamic *low-risk regions* in healthy and pathological cases. Black arrows indicate *low-risk regions* with high *relative residence time* (RRT). (A-B) Internal carotid arteries with high tortuosity exhibits hemodynamic risky regions mostly in inner curve of the carotid siphon of *subject II*, and *subject IV*. (C) The downstream artery of the aneurysm exhibits a low-risk area at the point of high curvature. (D-F) High RRT regions were observed at bifurcations with daughter branches of different diameter ratios in *subject III* and *subject VI*. (G) The walls of thinner side branches are more prone to atherosclerosis as indicated by the hemodynamic parameters. In *subject I*, low-risk regions were found to be located at near perpendicular-bifurcations such as the junction of PCOM and PCA and the basilar tip. High-velocity blood flow impinges on the opposite arterial wall in near perpendicular bifurcations. (H) High-velocity blood flow jets generate risky areas in the downstream vessels in *stenosis case* (PRI). (I) Risky regions in the patient shown in panel H were remedied after treatment (PSI).

High-risk regions: Figure 55 exhibits the reconstructed model and high-risk disturbed flow locations before and after aneurysm clipping. Figure 56 illustrates the inflow jet stream into the aneurysm sac on different planes oriented perpendicularly and horizontally to the aneurysm ostium before treatment. High-risk prolonged RRT sites were located on a bleb close to the separation of the inflow streamline in the aneurysm sac (Figure 57). The WSS vector plots captured during the different cycled phase of peak-systole, mid-diastole and end-diastole (Figure 58).

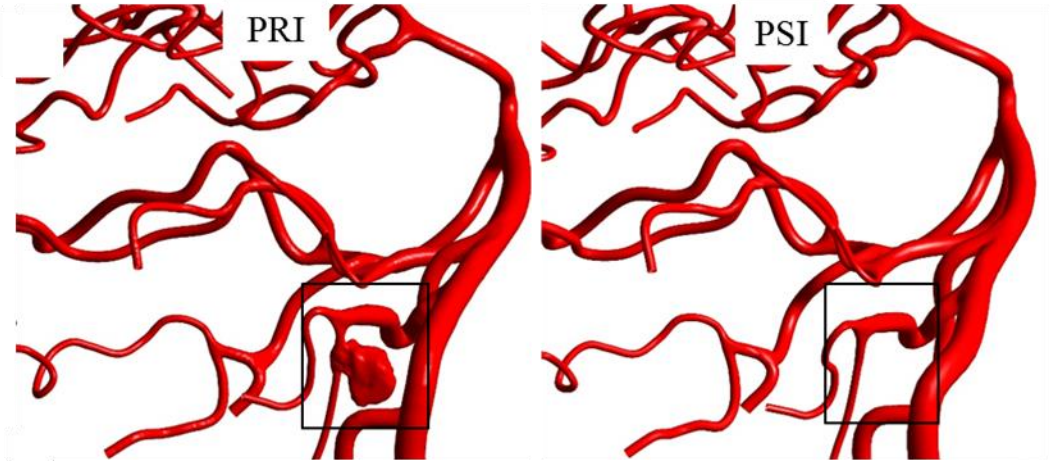

Figure 55. Reconstruction of vascular tree for a patient with aneurysm in the pre-intervention (PRI) and post-intervention (PSI).

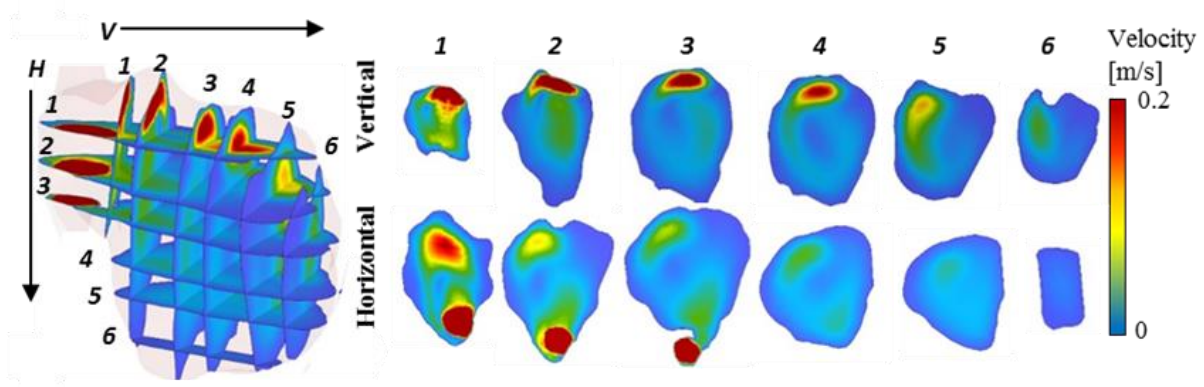

Figure 56. Several horizontal and vertical planes of the aneurysm neck were used to visualize the pattern of inflow into the aneurysm sac.

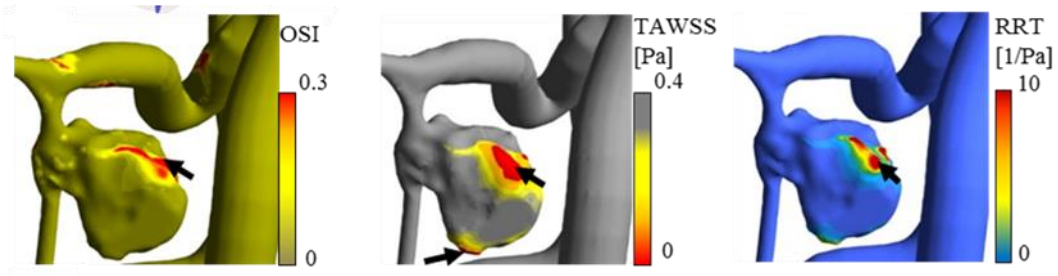

Figure 57. Disturbed flow quantification and high-risk region detection for a patient with a large saccular aneurysm on the PICA. The area of prolonged RRT (arrow) was found on a bleb of the aneurysm close to the stagnation of inflow jet.

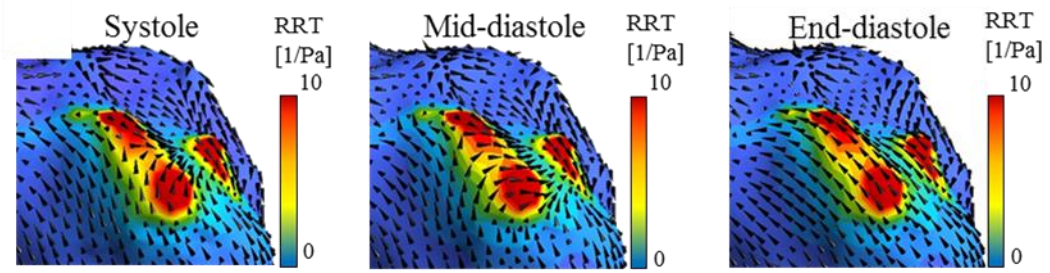

Figure 58. The WSS vector plots captured during different cycled time revealed that the WSS vector arrangement highly changed in diastole phase.

Figure 59 visualized the high-risk disturbed flow locations in a stenotic patient in PRI and PSI. Before the intervention, separation flow and recirculation were dominant in the post-stenotic region leading to elevated RRT sites (Figure 61). High-risk regions were mostly present in the post-stenotic zones as well as remotely in distal vessels, as shown in Figure 60A. These regions were monitored and compared in the post-treatment model, which is considered a high risk for developing atherosclerosis. "After angioplasty, our hemodynamic analysis showed the normalization of the high RRT segments both proximal and distal to the stenosis as shown in Figure 60B. Post-treatment, there was a 36% drop in the flow within the anterior cerebral artery (ACA)" [148]; 76% increase in flow within the MCA stenosis. Similarly, there was a 53% reduction in the mean velocity within the angioplasty segment. Based on these the measure blood flow before and after intervention, the decrease in the flow within the ACA post angioplasty may be related to a reduced demand from collateral pial vessels after a successful increase of the MCA

flow in the post angioplasty. Normalized WSS vectors were depicted at the various phased of the cardiac cycle as shown in Figure 61. Most WSS vector changes were detected between mid- to end-diastolic.

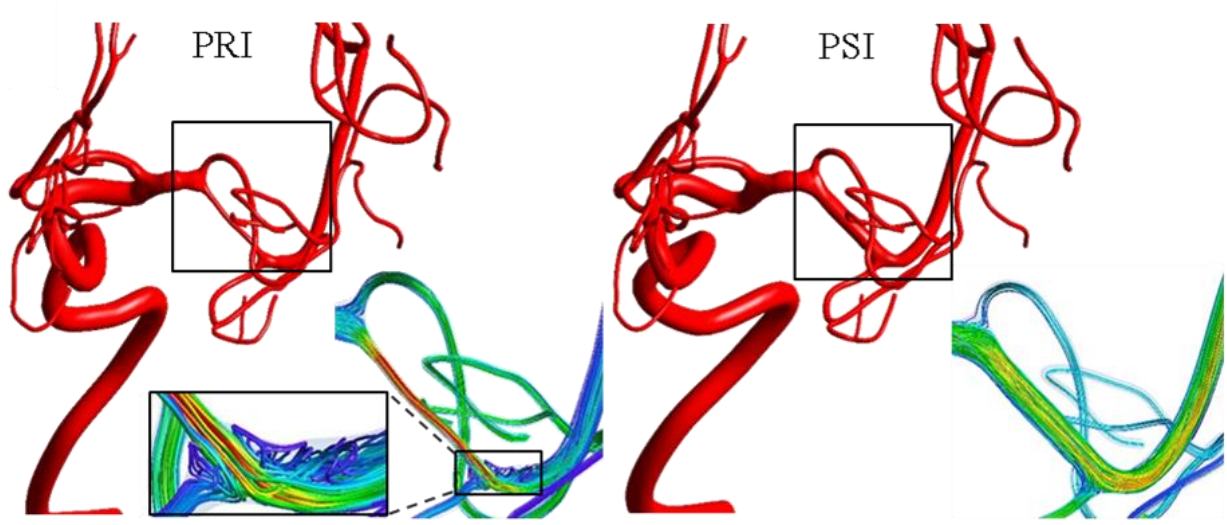

Figure 59. Reconstructed model with high-density blood flow streamline in pre-intervention (PRI) and post-intervention (PSI) at peak-systole. In PRI, the magnified view visualized the disturbed flow circulation at post stenosis region.

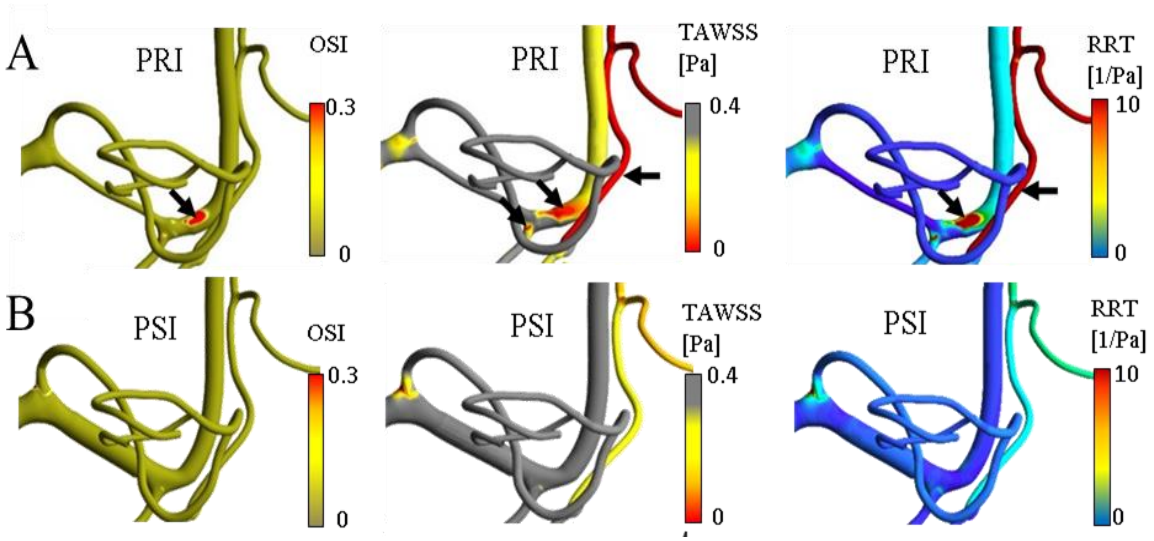

Figure 60. Disturbed flow generated regions with relative high OSI and low TAWSS, i.e. high RRT. (A) Black arrow indicated the high-risk locations at post-stenosis and distal down-stream vessel (arrow). (B) After angioplasty, it showed the normalization of the high risk regions in local and distal part of the lesion (red RTT zones).

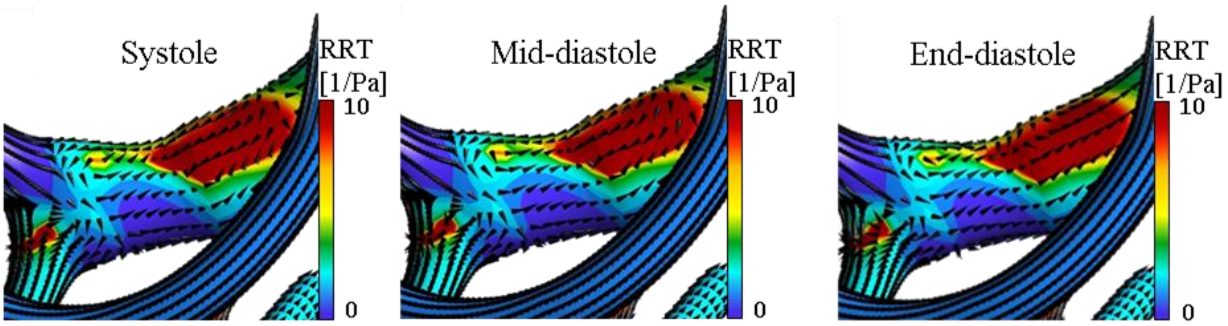

Figure 61. Visualize the normalized wall shear stress vectors on disturbed flow regions in systole, mid-diastole, and end diastole. Most changes are between mid to end-diastole.

4.4.4. Hemodynamic indices for waveform analysis

We observed pressure and flow rate attenuation of the blood flow pulsatility along the paths from the ICA to distal pial arteries in the MCA and PCA and ACA territories as shown in Figure 62 and Figure 63. The waveform shapes are depicted from lesion site to downstream distal vessels in Figure 64 and Figure 65 for pathological cases. We also calculated the hemodynamic indexes for waveform analysis using *pulsatility index* (PI), *resistance index* (RI), *systole to diastole ratio* (S/D) of the velocity profile, and *phase shift degree* at post-lesion regions using Equation (57)-(60).

$$PI = \frac{V_S - V_D}{V_{TA}} \tag{57}$$

$$RI = \frac{V_S - V_D}{V_S} \tag{58}$$

$$S/D = \frac{V_S}{V_D} \tag{59}$$

$$\Delta\phi = 360° \times \frac{\Delta t}{T} \tag{60}$$

Where, V_S and V_D are peak-systolic and end-diastolic velocity, respectively. V_{TA} is the time-averaged velocity over one cardiac cycle. $\Delta\phi$ is the phase shift in degrees; Δt is the time

difference between pre- and post-intervention velocity wave peaks; T is the wave period in seconds. Note that the wave periods were the same between the PRI and PSI stage.

Hemodynamic indexes for waveform analysis are summarized in Table 24 for post-lesion regions. PI, RI and S/D increased in the post-lesion downstream flows and were normalized after the intervention.

Table 24. Hemodynamic indexes for waveform analysis at post-lesion regions of aneurysm (*Case I*) and stenosis (*Case II*). A comparison between PRI and PSI.

Case Number	Point	Pulsatility Index		Resistance Index		S/D Ratio		Phase Shift	
		PRI	PSI	PRI	PSI	PRI	PSI	Δt	$\Delta\phi$
Case I	**#1**	1.82	0.69	0.84	0.49	6.36	1.95	0.03	10.58
Case I	**#3**	0.34	0.68	0.29	0.48	1.40	1.93	0.11	38.82
Case I	**#4**	0.59	0.47	0.43	0.37	1.75	1.59	0.03	10.58
Case I	**#5**	0.97	0.89	0.61	0.58	2.59	2.37	0.02	8.47
Case II	**#2**	1.06	0.64	0.67	0.47	3.03	1.90	0.02	6.95
Case II	**#3**	0.65	0.53	0.45	0.41	1.84	1.71	0.38	106.05
Case II	**#4**	1.18	0.50	0.66	0.39	2.94	1.66	0.28	78.14
Case II	**#5**	0.56	0.42	0.43	0.34	1.76	1.53	0.04	11.16

PRI: Pre-intervention, PSI: Post-intervention. $\Delta\phi$: Phase shift in degrees. Δt: Time difference between PSI and PRI velocity wave peaks. S/D: systolic/diastolic ratio.

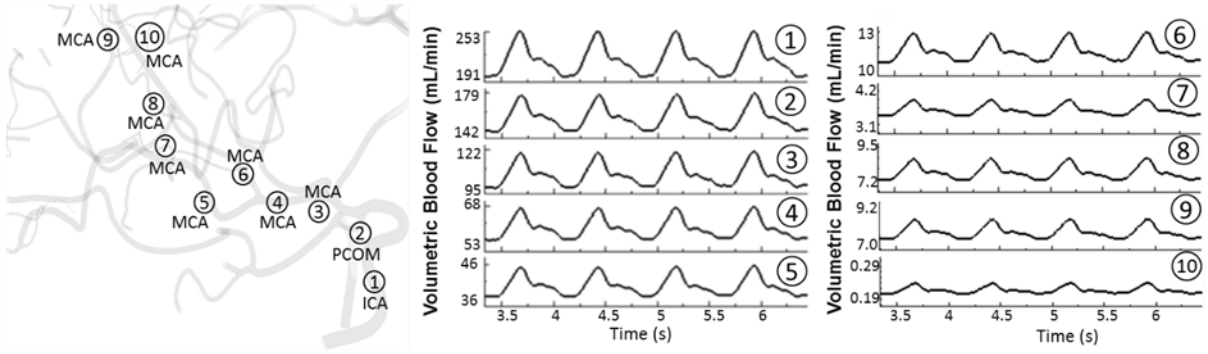

Figure 62. The map of dynamic flow rates shows attenuation of the blood flow pulsatility from ICA to the arteries in MCA territory down to distal pial arteries for *Subject I*.

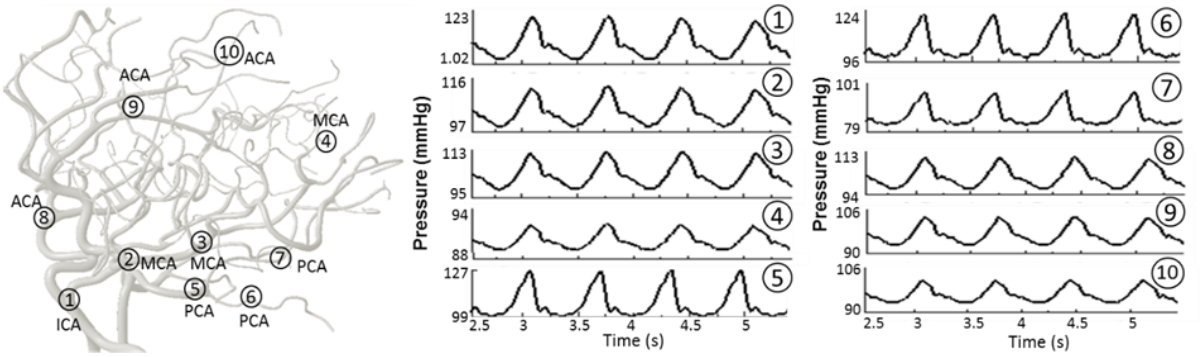

Figure 63. Pressure profile plotted from left ICA down to distal arteries in left MCA, PCA and ACA, for *Subject III*.

In the *post-aneurysm region*, there was a phase lag and an augmentation of peak-diastolic velocity (also known as secondary peak or notching) in the pre-intervention model as shown in Figure 64. The angular phase shift between PRI and PSI were 38.82° and 10.58° at points #3 and #4, respectively.

In Figure 65, phase shifts of 106.05° and 78.14° were calculated in the elevated RRT region at the *proximal post-stenotic region*. An angular phase difference of 11.16° was found in *distal* MCA vessels. Consequently, pre-intervention, the lesion region not only affect the proximal sites (ex. post-stenotic region), but also generates pulse wave delay in downstream vessels.

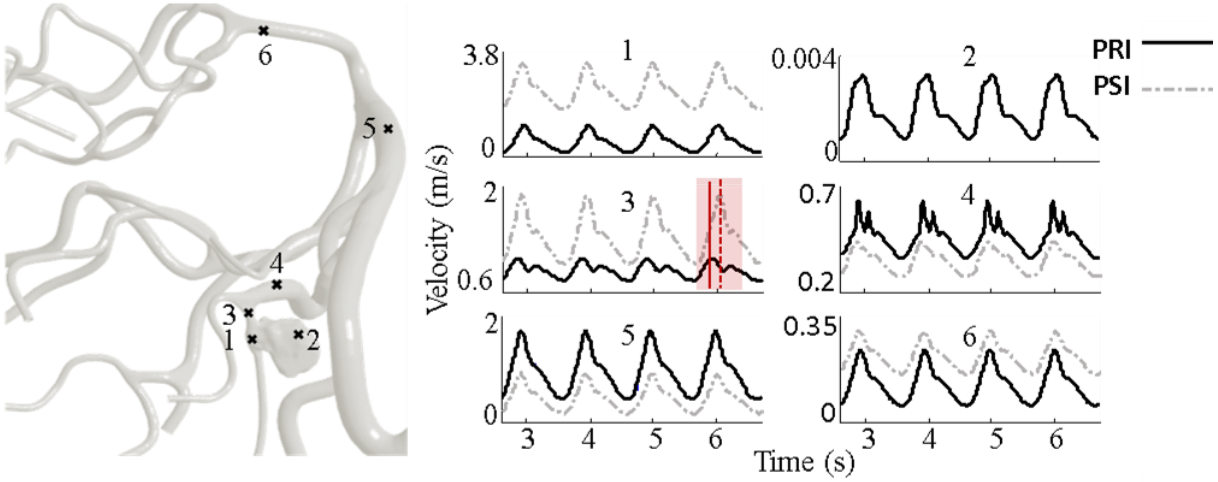

Figure 64. Computed blood flow velocity for the MCA stenosis illustrative case in pre- and post-intervention (PRI and PSI). It visualizes dynamic velocity profiles at different locations starting from the proximal to distal vessels. The transparent red area highlights the largest phase lag. In aneurysm case, a very low velocity of stagnated flow was recorded close to high RRT at point 2. In the post-aneurysm region, points 3 and 4, there was a phase lag and an augmentation of the secondary peak compared to the PSI. The angular phase shift between PRI and PSI are 38.82° and 10.58° at points 3 and 4, respectively.

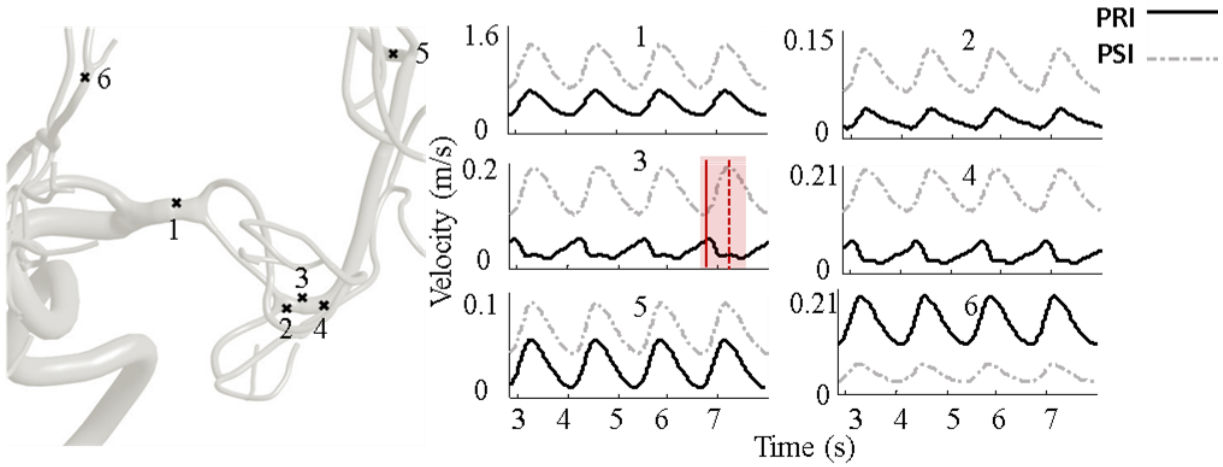

Figure 65. Computed blood flow velocity for the MCA stenosis illustrative case in pre- and post-intervention (PRI and PSI). It visualizes dynamic velocity profiles at different locations starting from the proximal to distal vessels. The transparent red area highlights the largest phase lag. In aneurysm case, a very low velocity of stagnated flow was recorded close to high RRT at point 2. In the post-aneurysm region, points 3 and 4, there was a phase lag and an augmentation of the secondary peak compared to the PSI. The angular phase shift between PRI and PSI are 38.82° and 10.58° at points 3 and 4, respectively.

Discussion

We deployed an image-based workflow specifically tailored for large-scale blood flow computations in subject-specific cerebral arterial trees. Predicted CFD flows were compared to *in vivo* qMRA measurements. Overall agreement between measured flow and CFD simulations was favorable with total average percentage difference in the flow of $2.27 \pm 0.64\%$. Flow measurements in combination with the computational analysis allow us to reconstruct the near-wall hemodynamic map throughout the cerebral arterial tree to better detect potential low- to high-risk sites. Global maps of hemodynamic risk parameters derived from *in vivo* measurements in combination with tree-wide CFD simulations provide unique observations about the hemodynamic status that no current imaging technique is capable of measuring directly.

4.4.5. Global maps of low- to high-risk hemodynamic analysis.

The illustrative cases of intracranial stenosis and aneurysm were chosen because the mechanism for the development of aneurysms or stenosis is affected by the *local* hemodynamic factors. In addition, once aneurysms or stenosis form that leads to further changes in the *local* and *global* blood flow redistribution. Adverse distal effects such as remote ipsilateral hemorrhage [149] may be located with our proposed more global hemodynamic analysis. The proposed method extends rigorous CFD analysis from a single site to large portions of the cerebrovascular network.

Low-risk regions were found to be located at nearly perpendicular bifurcations such as at the junction of PCOM and PCA and the basilar tip. At these bifurcations, the high-velocity blood flow impinges at the apex causing perpendicular forces on the arterial wall. Additionally, regions with relatively low WSS and high OSI were observed at bifurcations with daughter branches of largely different diameter ratios. The smaller side-wall branches are consequently more prone to atherosclerosis as indicated by the hemodynamic parameters. Moreover, internal carotid arteries

with high tortuosity exhibit an area of locally high residence time, mostly on the inner curve of the carotid siphon due to the predominant helical flow in curved vessels than parabolic velocity profile in semi-straight vascular segments [150]. In the illustrative cases of stenosis/aneurysm, disturbed laminar blood flow after stenosis and aneurysm generate low-risk sites in distal disease-free vessels as potential problem areas.

The simulation of the large-scale cerebral arterial tree helped identify and localize high-risk regions of disturbed flow in the pathological cases. The area of prolonged RRT was found on a bleb of the aneurysm close to the stagnation of the inflow jet. The velocity profile below this region shows low-velocity streamline at 0.62 mm beneath the wall with elevated RRT.

Our hemodynamic analysis was able to visualize potential problem spots in pathological cases. In the stenosis case, elevated levels of pre-operative RRT and TAWSS both upstream and downstream from the MCA stenosis were detected. Without the intervention (angioplasty) this MCA stenosis could eventually have initiated stenosis in other sites. After angioplasty, there was the normalization of the high RRT segments both proximal and distal to the stenosis. The visualization of normalized WSS vectors showed that the directional changes were mainly between mid- to end-diastole.

4.4.6. Blood flow waveform

We collected flow and velocity field from inlets and malformed vessels down to the small distal vessels. Post-intervention, we detected attenuation of the flow pulsatility in downstream flow streamline of the diseased vessels. Waveform indexes such as PI, RI and S/D ratio reduced by 16.3%, 11.52%, and 18.86%, respectively. Large angular phase difference was found between pre- and post-intervention flow profiles in downstream flow field following vascular lesions. The angular shift ranged from 106.87° in proximal to 7.06° in distal vessels from the malformed

vessels. We also visualized the augmentation of peak-diastolic flow waveform downstream of the diseased vessels. Since *in vivo* blood flow acquisition is not simultaneous, such phase shift differences cannot be studied with current *in vivo* blood flow measurements. Therefore, large-scale CFD analysis is capable of supplying critical temporal and spatial hemodynamic information throughout a large portion of the cerebral arterial tree that cannot be measured by imaging technologies.

Many researchers showed that hemodynamic parameter changes are highly associated with geometric features rather than physiological variations of the flow rate, blood pressure, and wave shapes [150]. Additionally, it has been reported that the augmented diastolic-peak of velocity correlates with age and is significantly higher in the blood flow waveforms of old adults [151], [152] leading to microvascular damage and impaired function [153]. However, it is unclear if lesion-induced phase lag and waveform dynamic changes encourage endovascular lesions in distal vessels; such as perhaps specific shear stress frequencies that correlate with inflammatory response in the endothelium [154]. We believe that the blood flow waveform should not be neglected; because near-wall hemodynamic analysis and WSS components are directly affected by blood flow shape of each cardiac cycle. A future study should evaluate the effect of post-lesion waveform changes on downstream distal vessels and quantify the physiological relevance of the waveform to endovascular diseases.

4.4.7. Same-day clinical screening modality.

The required time for mesh generation is on average 17.6 ± 1.24 *min* and simulation of one cardiac cycle is 85 ± 9.7 *min* for each subject. Our hemodynamic analysis cuts processing time for mesh generation and simulation, thus eliminating current bottlenecks, so that hemodynamic analysis can be realized on the same day. Availability of automated (*same day*) simulations will

provide surgeons with indicators for potential benefits and risks associated with endovascular procedures for individual patients. Tighter integration of imaging, endovascular interventions, and rigorous hemodynamic analysis will also eliminate barriers between surgeons and biomedical device designers aiming at better outcomes for cerebro-vascular diseases.

4.4.8. Boundary condition in large-scale simulation.

Current blood flow measurement does not allow direct measurement of the blood flow for each single outlet of the vascular tree. Therefore, multiple assumptions and solutions were introduced to provide a semi-realistic physiological outflow boundary conditions[46], [155]–[157]. The deeper the boundary condition lies in analyses, the less sensitive results are to such boundary conditions in large-mid size arteries. (The larger the simulation, the less sensitive the results are to boundary condition in large-mid size arteries). Appendix 4 shows different between RRT map and value of between a truncated and large-scale vascular model with the same velocity inlet boundary condition. Distal dynamic boundary condition provides wave propagation and maintains more realistic phase lag between blood flow and pressure and for a large portion of arterial tree [158]. Another goal arising from this study is to couple artificial 1D vascular tree [122], [159] or 2D cortical microcirculation [160] to further extend the size of the cerebrovascular tree.

4.4.9. Case study to compare small-scale and large-scale simulation.

In this study, we trimmed a small section of Subject II from the RICA to RMCA. We extracted pressure boundary condition from the large-scaled model and used them as pressure boundary condition for the cropped section using the same inlet velocity profile to ignore remove the effect of inlet boundary condition [161]. The distribution and the maximum value of RRT between the large-scale and truncated vascular model are shown in Figure 66.

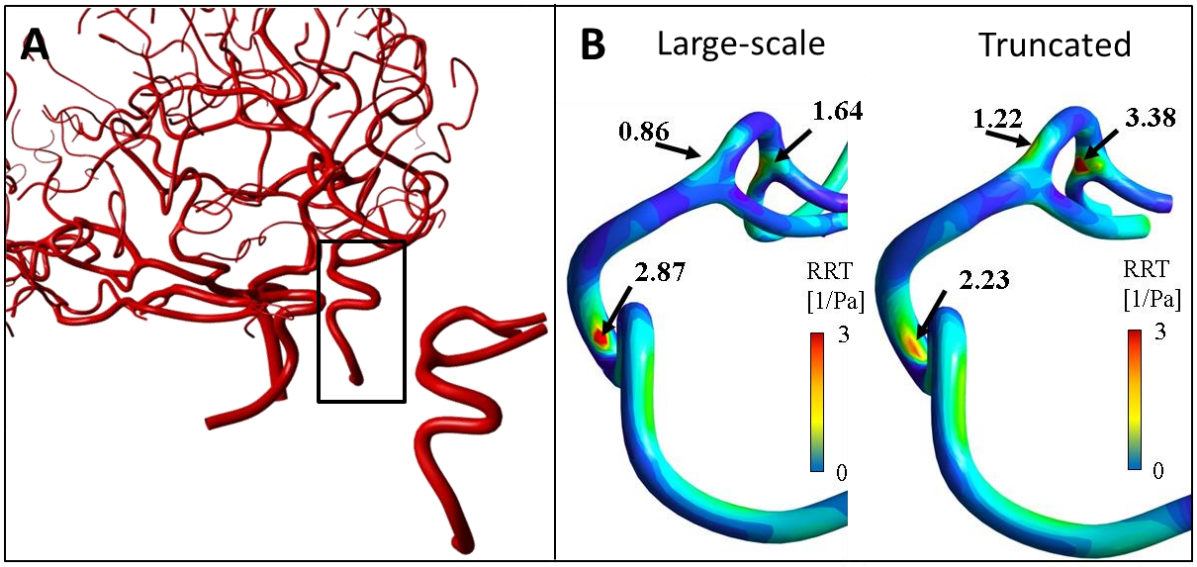

Figure 66. Hemodynamic risk-factor analysis of large-scale and truncated cerebrovascular tree. (A) A small section of Subject II's cerebroarterial tree with five segments from the RICA to RMCA was truncated. Dynamic pressure profiles were extracted from the large-scale model at three outlets and were used them as pressure boundary condition for the truncated model. (B) Distribution of relative residual time (RRT) of the truncated and large-scale vascular tree were different. The major different regions with the elevated RRT values are shown with black arrows.

4.4.10. Limitation and future work.

In the current model, we employed a rigid wall assumption for all simulation. Even though the deformations are small [162], wall deformations may significantly impact pressure attenuation, blood flow waveform and stress distribution in vessel walls. An extension to deformable vessels is a logical next step, which will benefit from the parametric structured meshes, because the wall geometry can easily be generated by extending the radial surface mesh to the desired wall thickness. However, reliable mechanical properties and vessel thickness measurements of all arterial blood vessels are necessary before attempting more rigorous 3D *fluid-structure interaction* (FSI) simulations for large sections of the cerebral vasculature. In addition, near-wall

hemodynamic risk analysis can be extended to more WSS components such as Lagrangian processing of the WSS vector field [14], [163].

Another future improvement concerns the use of non-Newtonian blood flow rheology [160]. This step would be critical for blood vessels less than 100 μm in diameter. In this study, we did not use complex rheology models because all arterial branches had diameters of D>400 μm due to the limited MRA resolution.

Future work should address the multi-scale arterial to venous system simulation with consideration of vein walls compliance. Another possible future step is to integrate rigorous 3D CFD arterial tree simulations with lower order microcirculatory closures [26,71,72].

5. CONCLUSIONS AND FUTURE WORK

An image-based automatic processing workflow specifically tailored for mesh generation of large-scale subject-specific cerebral arterial trees was presented. The tight integration of image processing, mesh generation and hemodynamics analysis with realistic, anatomically sound CFD tools is expected to narrow the gap between biofluid mechanic analysis and endovascular surgical practice aiming at providing more efficient interventions for cerebrovascular diseases.

Global maps of hemodynamic risk parameters derived from *in-vivo* measurements in combination with tree-wide CFD simulations provide unique observations about the hemodynamic status that no current imaging technique is capable to visualize directly. The large-scale subject-specific hemodynamic analysis is a promising next step for quantifying the surgical outcomes. This proposed method can be used to highlight the potential hemodynamic risks that might lead to aneurysm formation or increasing the risk of aneurysm rupture, as well as an understanding of the hemodynamic risks for atherosclerosis. Tree-wide simulation is expected to serve as a basis to predict changes to the large-scale flow redistribution after the endovascular intervention. To achieve this long-term goal, the global flow distribution model presented here may serve as a starting point for future research.

A large-scale approach of assessing hemodynamic risk factors for regions far away from the site of intervention, could aid in elucidating poorly understood phenomena such as *delayed hemorrhage* (DH) [75], [76].

The validated centerline and diameter data allows us to study morphological data of the large portion of cerebrovascular trees. The use of Bezier spline in vascular skeletons enables unique biometric visualization of torsion and curvature. Automatic biometrics extraction would enable

automatic morphological analysis on a large healthy population and patients with intracranial diseases before and after endovascular treatment.

Automation of the workflow presented here would address an important clinical need, because it enables image segmentation and dynamic simulation of patient-specific images on the same day. Availability of automated simulations will provide surgeons with indicators for potential benefits and risks associated with endovascular procedures for individual patients. Tighter integration of imaging, endovascular interventions, and rigorous hemodynamic analysis will also eliminate barriers between surgeons and biomedical device designers aiming at better outcomes for cerebrovascular diseases. The automatic mesh generation and vascular reconstruction may be particularly suitable for computer analysis of large datasets such as patient's medical records database in hospitals. The rigorous and unbiased analysis of imaging data may become a useful enabling technology to better differentiate critical pathological factors for subject-specific variations. In this current state, the project has a few limitations which need to be addressed in the future work.

Fluid structure interaction. In the current model, we employed a rigid wall assumption for all simulation. Even though the deformations are small [162], wall deformations may significantly impact pressure attenuation, blood flow waveform and stress distribution in vessel walls. A next step simulation using parametric meshing techniques could include 3D fluid-structure interaction (FSI) because the body-fitted coordinate system enables a simple extension of the luminal wall to create a cylindrical wall domain of desired thickness. Our hexahedral orthogonal elements allow layered modeling of the detailed biomechanics of vessel walls [73]. However, reliable mechanical properties and vessel thickness measurements of the intracranial vasculature are necessary before attempting more rigorous 3D FSI simulations [74] for large sections of the cerebral vasculature.

Blood flow in the rigid wall and compliance vessel wall may have a phase lag, which quantification of the phase lag and comparison with in-vivo blood flow measurement is of great importance.

Trifurcation. In this paper, complex vascular features such as bifurcations and loops were parametrically meshed, but multifurcations should be addressed in the future.

Applications. Although the current focus is on the cerebral arterial tree, this methodology is applicable to other arterial networks such as coronary, pulmonary and retinal circulatory systems. Future work using the PRM method should address the venous system and irregular pathological regions such as a saccular aneurysm.

Boundary conditions. Current blood flow measurement does not allow direct measurement of the blood flow in each outlet of a large-scale arterial tree. The deeper the boundary condition lies in analyses, the less sensitive results are to such boundary conditions in large-mid size arteries. (The larger the simulation, the less sensitive the results are to boundary condition in large-mid size arteries). Distal dynamic boundary condition provides wave propagation and maintains more realistic phase lag between blood flow and pressure and for a large portion of the arterial tree [158]. Another goal arising from this study is to couple artificial 1D vascular tree [122], [159] or 2D cortical microcirculation [160] to further extend the size of the cerebrovascular tree. Future work should address the multi-scale arterial to venous system simulation with consideration of vein walls compliance. Another extension can be assigning pulsatile pressure at the outlets which create a more realistic pressure change in the down-steam vessels. In addition, current enforcement of boundary condition assumed a constant pressure at each outlet. However, parabolic distribution of pressure should be enforced to the outlet's cross-section of vessels.

Blood flow rheology. The automatic PRM method enables detailed hemodynamic analysis for a large portion of the arterial tree, including small downstream vessels. Another future

improvement concerns the use of non-Newtonian blood flow rheology [160]. This step would be critical for blood vessels less than 100 μm in diameter. In this study, we did not use complex rheology models because all arterial branches had diameters of D>400 μm due to the limited MRA resolution.

Hemodynamic risk factors. In addition, near-wall hemodynamic risk analysis can be extended to more WSS components such as Lagrangian processing of the WSS vector field [14], [163].

Multi-scale simulation. Future work should address the multi-scale arterial to venous system simulation with consideration of vein walls compliance. Another possible future step is to integrate rigorous 3D CFD arterial tree simulations with lower order microcirculatory closures [26,71,72].

6. REFERENCES

[1] S. Vinchurkar and P. W. Longest, “Evaluation of hexahedral, prismatic and hybrid mesh styles for simulating respiratory aerosol dynamics,” *Comput. Fluids*, vol. 37, no. 3, pp. 317–331, Mar. 2008.

[2] F. Auricchio, M. Conti, A. Ferrara, S. Morganti, and A. Reali, “Patient-specific finite element analysis of carotid artery stenting: a focus on vessel modeling,” *Int. J. Numer. Methods Biomed. Eng.*, vol. 29, no. 6, pp. 645–664, Jun. 2013.

[3] G. De Santis, P. Mortier, M. De Beule, P. Segers, P. Verdonck, and B. Verhegghe, “Patient-specific computational fluid dynamics: structured mesh generation from coronary angiography,” *Med. Biol. Eng. Comput.*, vol. 48, no. 4, pp. 371–380, Apr. 2010.

[4] G. De Santis, M. De Beule, P. Segers, P. Verdonck, and B. Verhegghe, “Patient-specific computational haemodynamics: generation of structured and conformal hexahedral meshes from triangulated surfaces of vascular bifurcations,” *Comput. Methods Biomech. Biomed. Engin.*, vol. 14, no. 9, pp. 797–802, Sep. 2011.

[5] L. Antiga, B. Ene-Iordache, L. Caverni, G. P. Cornalba, and A. Remuzzi, “Geometric reconstruction for computational mesh generation of arterial bifurcations from CT angiography,” *Comput. Med. Imaging Graph. Off. J. Comput. Med. Imaging Soc.*, vol. 26, no. 4, pp. 227–235, Aug. 2002.

[6] T. C. Baudouin, J.-F. Remacle, E. Marchandise, F. Henrotte, and C. Geuzaine, “A frontal approach to hex-dominant mesh generation,” *Adv. Model. Simul. Eng. Sci.*, vol. 1, no. 1, pp. 1–30, Feb. 2014.

[7] C. S. Verma, P. F. Fischer, S. E. Lee, and F. Loth, “An All-Hex Meshing Strategy for Bifurcation Geometries in Vascular Flow Simulation,” in *Proceedings of the 14th International Meshing Roundtable*, B. W. Hanks, Ed. Springer Berlin Heidelberg, 2005, pp. 363–375.

[8] Z. Ali and P. G. Tucker, “Multiblock Structured Mesh Generation for Turbomachinery Flows,” in *Proceedings of the 22nd International Meshing Roundtable*, J. Sarrate and M. Staten, Eds. Springer International Publishing, 2014, pp. 165–182.

[9] G. De Santis, M. De Beule, K. Van Canneyt, P. Segers, P. Verdonck, and B. Verhegghe, “Full-hexahedral structured meshing for image-based computational vascular modeling,” *Med. Eng. Phys.*, vol. 33, no. 10, pp. 1318–1325, Dec. 2011.

[10] A. Wittek, N. M. Grosland, G. R. Joldes, V. Magnotta, and K. Miller, “From Finite Element Meshes to Clouds of Points: A Review of Methods for Generation of Computational Biomechanics Models for Patient-Specific Applications,” *Ann. Biomed. Eng.*, vol. 44, no. 1, pp. 3–15, Sep. 2015.

[11] Y. Zhang, Y. Bazilevs, S. Goswami, C. L. Bajaj, and T. J. R. Hughes, “Patient-Specific Vascular NURBS Modeling for Isogeometric Analysis of Blood Flow,” *Comput. Methods Appl. Mech. Eng.*, vol. 196, no. 29–30, pp. 2943–2959, May 2007.

[12] J. Cebral *et al.*, “Clinical Application of Image-Based CFD for Cerebral Aneurysms,” *Int. J. Numer. Methods Biomed. Eng.*, vol. 27, no. 7, pp. 977–992, Jul. 2011.

[13] A. Arzani and S. C. Shadden, “Characterizations and Correlations of Wall Shear Stress in Aneurysmal Flow,” *J. Biomech. Eng.*, vol. 138, no. 1, pp. 014503–014503, Dec. 2015.

[14] S. C. Shadden and A. Arzani, “Lagrangian postprocessing of computational hemodynamics,” *Ann. Biomed. Eng.*, vol. 43, no. 1, pp. 41–58, Jan. 2015.

[15] L. Grinberg, E. Cheever, T. Anor, J. R. Madsen, and G. E. Karniadakis, “Modeling Blood Flow Circulation in Intracranial Arterial Networks: A Comparative 3D/1D Simulation Study,” *Ann. Biomed. Eng.*, vol. 39, no. 1, pp. 297–309, Jul. 2010.

[16] D. Gallo, D. A. Steinman, and U. Morbiducci, “An insight into the mechanistic role of the common carotid artery on the hemodynamics at the carotid bifurcation,” *Ann. Biomed. Eng.*, vol. 43, no. 1, pp. 68–81, Jan. 2015.
[17] D. N. Ku, D. P. Giddens, C. K. Zarins, and S. Glagov, “Pulsatile flow and atherosclerosis in the human carotid bifurcation. Positive correlation between plaque location and low oscillating shear stress,” *Arterioscler. Dallas Tex*, vol. 5, no. 3, pp. 293–302, Jun. 1985.
[18] F. Rikhtegar *et al.*, “Choosing the optimal wall shear parameter for the prediction of plaque location-A patient-specific computational study in human left coronary arteries,” *Atherosclerosis*, vol. 221, no. 2, pp. 432–437, Apr. 2012.
[19] J. M. Dolan, J. Kolega, and H. Meng, “High wall shear stress and spatial gradients in vascular pathology: a review,” *Ann. Biomed. Eng.*, vol. 41, no. 7, pp. 1411–1427, Jul. 2013.
[20] J. R. Buchanan, C. Kleinstreuer, S. Hyun, and G. A. Truskey, “Hemodynamics simulation and identification of susceptible sites of atherosclerotic lesion formation in a model abdominal aorta,” *J. Biomech.*, vol. 36, no. 8, pp. 1185–1196, Aug. 2003.
[21] J. R. Buchanan, C. Kleinstreuer, G. A. Truskey, and M. Lei, “Relation between non-uniform hemodynamics and sites of altered permeability and lesion growth at the rabbit aorto-celiac junction,” *Atherosclerosis*, vol. 143, no. 1, pp. 27–40, Mar. 1999.
[22] T. Kawaguchi *et al.*, “Distinctive flow pattern of wall shear stress and oscillatory shear index: similarity and dissimilarity in ruptured and unruptured cerebral aneurysm blebs,” *J. Neurosurg.*, vol. 117, no. 4, pp. 774–780, Aug. 2012.
[23] C. G. Caro, N. J. Cheshire, and N. Watkins, “Preliminary comparative study of small amplitude helical and conventional ePTFE arteriovenous shunts in pigs,” *J. R. Soc. Interface*, vol. 2, no. 3, pp. 261–266, Jun. 2005.
[24] H. J. T. a. M. Huijbregts *et al.*, “A helical PTFE arteriovenous access graft to swirl flow across the distal anastomosis: results of a preliminary clinical study,” *Eur. J. Vasc. Endovasc. Surg. Off. J. Eur. Soc. Vasc. Surg.*, vol. 33, no. 4, pp. 472–475, Apr. 2007.
[25] *Arterial Variations in Man - Classification and Frequency | Hans Lippert | Springer*. .
[26] V. Peiffer, S. J. Sherwin, and P. D. Weinberg, “Does low and oscillatory wall shear stress correlate spatially with early atherosclerosis? A systematic review,” *Cardiovasc. Res.*, vol. 99, no. 2, pp. 242–250, Jul. 2013.
[27] D. Backes *et al.*, “Difference in Aneurysm Characteristics Between Ruptured and Unruptured Aneurysms in Patients With Multiple Intracranial Aneurysms,” *Stroke*, vol. 45, no. 5, pp. 1299–1303, May 2014.
[28] M. Korja, H. Lehto, and S. Juvela, “Lifelong Rupture Risk of Intracranial Aneurysms Depends on Risk Factors A Prospective Finnish Cohort Study,” *Stroke*, vol. 45, no. 7, pp. 1958–1963, Jul. 2014.
[29] P. Rissland, Y. Alemu, S. Einav, J. Ricotta, and D. Bluestein, “Abdominal aortic aneurysm risk of rupture: patient-specific FSI simulations using anisotropic model,” *J. Biomech. Eng.*, vol. 131, no. 3, p. 31001, Mar. 2009.
[30] Y. Wei, S. Cotin, J. Dequidt, C. Duriez, J. Allard, and E. Kerrien, “A (Near) Real-Time Simulation Method of Aneurysm Coil Embolization,” 2012.
[31] R. J. Damiano, D. Ma, J. Xiang, A. H. Siddiqui, K. V. Snyder, and H. Meng, “Finite element modeling of endovascular coiling and flow diversion enables hemodynamic prediction of complex treatment strategies for intracranial aneurysm,” *J. Biomech.*, vol. 48, no. 12, pp. 3332–3340, Sep. 2015.
[32] T. Ohshima, S. Miyachi, I. Takahashi, and K. Ishii, “Assessment of endovascular coil configuration for embolization of intracranial aneurysms using computational fluid dynamics,” *Nagoya J. Med. Sci.*, vol. 77, no. 3, pp. 383–388, Aug. 2015.

[33] B. Gao, M. G. Safain, and A. M. Malek, “Enterprise stenting for intracranial aneurysm treatment induces dynamic and reversible age-dependent stenosis in cerebral arteries,” *J. NeuroInterventional Surg.*, vol. 7, no. 4, pp. 297–302, Apr. 2015.
[34] M. Kim, D. B. Taulbee, M. Tremmel, and H. Meng, “Comparison of Two Stents in Modifying Cerebral Aneurysm Hemodynamics,” *Ann. Biomed. Eng.*, vol. 36, no. 5, pp. 726–741, May 2008.
[35] M. Tanemoto, T. Suzuki, M. Abe, T. Abe, and S. Ito, “Hemodynamic Index of Atheromatous Renal Artery Stenosis for Angioplasty,” *Clin. J. Am. Soc. Nephrol.*, vol. 4, no. 3, pp. 651–655, Mar. 2009.
[36] M. A. Maaly and A. A. Ismail, “Three dimensional magnetic resonance angiography of the circle of Willis: Anatomical variations in general Egyptian population,” *Egypt. J. Radiol. Nucl. Med.*, vol. 42, no. 3–4, pp. 405–412, Dec. 2011.
[37] R. H. C. Bisschops, L. J. Kappelle, W. P. T. M. Mali, and J. van der Grond, “Hemodynamic and Metabolic Changes in Transient Ischemic Attack Patients: A Magnetic Resonance Angiography and 1H-Magnetic Resonance Spectroscopy Study Performed Within 3 Days of Onset of a Transient Ischemic Attack,” *Stroke*, vol. 33, no. 1, pp. 110–115, Jan. 2002.
[38] B. P. Lemkuil, J. C. Drummond, and P. M. Patel, “Chapter 8 - Central Nervous System Physiology: Cerebrovascular,” in *Pharmacology and Physiology for Anesthesia*, H. C. Hemmings and T. D. Egan, Eds. Philadelphia: W.B. Saunders, 2013, pp. 123–136.
[39] A. Gahremanpour, E. C. Perin, and G. Silva, “Carotid Artery Stenting versus Endarterectomy,” *Tex. Heart Inst. J.*, vol. 39, no. 4, pp. 474–487, 2012.
[40] “3D Reconstruction of Cerebral Blood Flow and Vessel Morphology from X-Ray Rotational Angiography - Semantic Scholar.” [Online]. Available: /paper/3D-Reconstruction-of-Cerebral-Blood-Flow-and-Vessel-Waechter-Weese/0ffc81bb025e1308339e7aa84f3c454770d70f85. [Accessed: 08-Apr-2018].
[41] “Vascular Malformations - Alexander - - Wiley Online Books - Wiley Online Library.” [Online]. Available: https://onlinelibrary.wiley.com/doi/abs/10.1002/9781118704950.ch7. [Accessed: 06-Apr-2018].
[42] D. A. Steinman, J. S. Milner, C. J. Norley, S. P. Lownie, and D. W. Holdsworth, “Image-Based Computational Simulation of Flow Dynamics in a Giant Intracranial Aneurysm,” *Am. J. Neuroradiol.*, vol. 24, no. 4, pp. 559–566, Apr. 2003.
[43] M. A. Castro, C. M. Putman, and J. R. Cebral, “Patient-Specific Computational Modeling of Cerebral Aneurysms With Multiple Avenues of Flow From 3D Rotational Angiography Images,” *Acad. Radiol.*, vol. 13, no. 7, pp. 811–821, Jul. 2006.
[44] H. Schmitt *et al.*, “Reconstruction of blood propagation in three-dimensional rotational X-ray angiography (3D-RA),” *Comput. Med. Imaging Graph.*, vol. 29, no. 7, pp. 507–520, Oct. 2005.
[45] S. Sankaran, M. E. Moghadam, A. M. Kahn, E. E. Tseng, J. M. Guccione, and A. L. Marsden, “Patient-Specific Multiscale Modeling of Blood Flow for Coronary Artery Bypass Graft Surgery,” *Ann. Biomed. Eng.*, vol. 40, no. 10, pp. 2228–2242, Oct. 2012.
[46] L. Grinberg, T. Anor, J. Madsen, A. Yakhot, and G. Karniadakis, “Large-Scale Simulation of the Human Arterial Tree,” *Clin. Exp. Pharmacol. Physiol.*, vol. 36, no. 2, pp. 194–205, Feb. 2009.
[47] X. Liu *et al.*, “Three-dimensional hemodynamics analysis of the circle of Willis in the patient-specific nonintegral arterial structures,” *Biomech. Model. Mechanobiol.*, vol. 15, no. 6, pp. 1439–1456, Dec. 2016.
[48] M. Spiegel *et al.*, “Tetrahedral vs. polyhedral mesh size evaluation on flow velocity and wall shear stress for cerebral hemodynamic simulation,” *Comput. Methods Biomech. Biomed. Engin.*, vol. 14, no. 1, pp. 9–22, 2011.
[49] R. Lima, Y. Imai, T. Ishikawa, and V. Oliveira, *Visualization and Simulation of Complex Flows in Biomedical Engineering*. Springer Science & Business Media, 2013.

[50] O. Sahni, J. Müller, K. E. Jansen, M. S. Shephard, and C. A. Taylor, “Efficient anisotropic adaptive discretization of the cardiovascular system,” *Comput. Methods Appl. Mech. Eng.*, vol. 195, no. 41–43, pp. 5634–5655, Aug. 2006.
[51] J. Bols *et al.*, “Unstructured hexahedral mesh generation of complex vascular trees using a multi-block grid-based approach,” *Comput. Methods Biomech. Biomed. Engin.*, vol. 19, no. 6, pp. 663–672, Apr. 2016.
[52] Y. Otoguro, K. Takizawa, and T. E. Tezduyar, “Space–time VMS computational flow analysis with isogeometric discretization and a general-purpose NURBS mesh generation method,” *Comput. Fluids*, Apr. 2017.
[53] G. Xiong, S. Musuvathy, and T. Fang, “Automated Structured All-Quadrilateral and Hexahedral Meshing of Tubular Surfaces,” in *Proceedings of the 21st International Meshing Roundtable*, X. Jiao and J.-C. Weill, Eds. Springer Berlin Heidelberg, 2013, pp. 103–120.
[54] G. De Santis, M. De Beule, P. Segers, P. Verdonck, and B. Verhegghe, “Patient-specific computational haemodynamics: generation of structured and conformal hexahedral meshes from triangulated surfaces of vascular bifurcations,” *Comput. Methods Biomech. Biomed. Engin.*, vol. 14, no. 9, pp. 797–802, Sep. 2011.
[55] L. Antiga and D. A. Steinman, “Robust and objective decomposition and mapping of bifurcating vessels,” *IEEE Trans. Med. Imaging*, vol. 23, no. 6, pp. 704–713, Jun. 2004.
[56] M. Ghaffari, C. Y. Hsu, and A. A. Linninger, “Automatic Reconstruction and Generation of Structured Hexahedral Mesh for Non-planar Bifurcations in Vascular Networks,” *Comput. Aided Chem. Eng.*, vol. 37, pp. 635–640, 2015.
[57] J. Guo, S. Li, Y. P. Chui, J. Qin, and P. A. Heng, “Mesh quality oriented 3D geometric vascular modeling based on parallel transport frame,” *Comput. Biol. Med.*, vol. 43, no. 7, pp. 879–888, Aug. 2013.
[58] C.-Y. Hsu, B. Schneller, A. Alaraj, M. Flannery, X. J. Zhou, and A. Linninger, “Automatic recognition of subject-specific cerebrovascular trees,” *Magn. Reson. Med.*, vol. 77, no. 1, pp. 398–410, Jan. 2017.
[59] C.-Y. Hsu, B. Schneller, M. Ghaffari, A. Alaraj, and A. Linninger, “Medical Image Processing for Fully Integrated Subject Specific Whole Brain Mesh Generation,” *Technologies*, vol. 3, no. 2, pp. 126–141, May 2015.
[60] C.-Y. Hsu, M. Ghaffari, A. Alaraj, M. Flannery, X. J. Zhou, and A. Linninger, “Gap-free segmentation of vascular networks with automatic image processing pipeline,” *Comput. Biol. Med.*, vol. 82, pp. 29–39, Mar. 2017.
[61] M. P. Do Carmo, *Differential Geometry of Curves and Surfaces*. Prentice-Hall, 1976.
[62] J. H. Ferziger and M. Peric, *Computational Methods for Fluid Dynamics*, 3rd ed. Berlin Heidelberg: Springer-Verlag, 2002.
[63] A. Marzo *et al.*, “Computational hemodynamics in cerebral aneurysms: the effects of modeled versus measured boundary conditions,” *Ann. Biomed. Eng.*, vol. 39, no. 2, pp. 884–896, Feb. 2011.
[64] Y. Zhang and C. Bajaj, “Adaptive and Quality Quadrilateral/Hexahedral Meshing from Volumetric Data,” *Comput. Methods Appl. Mech. Eng.*, vol. 195, no. 9, pp. 942–960, Feb. 2006.
[65] O. C. Zienkiewicz and R. L. Taylor, *The Finite Element Method: Solid mechanics*. Butterworth-Heinemann, 2000.
[66] C. E. Quiroz Arita, “Anaerobic digestion comparison of manure leachate by high-rate anaerobic reactors,” M.S., Colorado State University, United States -- Colorado, 2013.
[67] E. Wellnhofer, L. Goubergrits, U. Kertzscher, K. Affeld, and E. Fleck, “Novel non-dimensional approach to comparison of wall shear stress distributions in coronary arteries of different groups of patients,” *Atherosclerosis*, vol. 202, no. 2, pp. 483–490, Feb. 2009.

[68] A. M. Malek, S. L. Alper, and S. Izumo, “Hemodynamic Shear Stress and Its Role in Atherosclerosis,” *JAMA*, vol. 282, no. 21, pp. 2035–2042, Dec. 1999.
[69] B. E. O. Buelow, S. Venkateswaran, and C. L. Merkle, “Convergence acceleration of implicit schemes in the presence of high aspect ratio grid cells,” presented at the 11th Workshop for Computational Fluid Dynamic Applications in Rocket Propulsion, 1993.
[70] G. De Santis, “Novel mesh generation method for accurate image-based computational modelling of blood vessels,” dissertation, Ghent University, 2011.
[71] P. W. Longest and S. Vinchurkar, “Effects of mesh style and grid convergence on particle deposition in bifurcating airway models with comparisons to experimental data,” *Med. Eng. Phys.*, vol. 29, no. 3, pp. 350–366, Apr. 2007.
[72] P. Mortier *et al.*, “A novel simulation strategy for stent insertion and deployment in curved coronary bifurcations: comparison of three drug-eluting stents,” *Ann. Biomed. Eng.*, vol. 38, no. 1, pp. 88–99, Jan. 2010.
[73] A. Swillens, J. Degroote, J. Vierendeels, L. Lovstakken, and P. Segers, “A simulation environment for validating ultrasonic blood flow and vessel wall imaging based on fluid-structure interaction simulations: Ultrasonic assessment of arterial distension and wall shear rate,” *Med. Phys.*, vol. 37, no. 8, pp. 4318–4330, Aug. 2010.
[74] J. Alastruey, K. H. Parker, J. Peiró, S. M. Byrd, and S. J. Sherwin, “Modelling the circle of Willis to assess the effects of anatomical variations and occlusions on cerebral flows,” *J. Biomech.*, vol. 40, no. 8, pp. 1794–1805, 2007.
[75] A. Amini, A. G. Osborn, T. D. McCall, and W. T. Couldwell, “Remote Cerebellar Hemorrhage,” *Am. J. Neuroradiol.*, vol. 27, no. 2, pp. 387–390, Feb. 2006.
[76] A. P. Mitha, J. P. Mynard, J. A. Storwick, Z. I. Shivji, J. H. Wong, and W. Morrish, “Can the Windkessel Hypothesis Explain Delayed Intraparenchymal Haemorrhage After Flow Diversion? A Case Report and Model-Based Analysis of Possible Mechanisms,” *Heart Lung Circ.*, vol. 24, no. 8, pp. 824–830, Aug. 2015.
[77] J. R. Cebral, F. Mut, J. Weir, and C. Putman, “Quantitative Characterization of the Hemodynamic Environment in Ruptured and Unruptured Brain Aneurysms,” *Am. J. Neuroradiol.*, vol. 32, no. 1, pp. 145–151, Jan. 2011.
[78] S. Omodaka *et al.*, “Local hemodynamics at the rupture point of cerebral aneurysms determined by computational fluid dynamics analysis,” *Cerebrovasc. Dis. Basel Switz.*, vol. 34, no. 2, pp. 121–129, 2012.
[79] J. P. Cruz *et al.*, “Delayed Ipsilateral Parenchymal Hemorrhage Following Flow Diversion for the Treatment of Anterior Circulation Aneurysms,” *Am. J. Neuroradiol.*, vol. 33, no. 4, pp. 603–608, Apr. 2012.
[80] M. J. H. Wermer, P. Greebe, A. Algra, and G. J. E. Rinkel, “Incidence of Recurrent Subarachnoid Hemorrhage After Clipping for Ruptured Intracranial Aneurysms,” *Stroke*, vol. 36, no. 11, pp. 2394–2399, Nov. 2005.
[81] L. Antiga, M. Piccinelli, L. Botti, B. Ene-Iordache, A. Remuzzi, and D. A. Steinman, “An image-based modeling framework for patient-specific computational hemodynamics,” *Med. Biol. Eng. Comput.*, vol. 46, no. 11, pp. 1097–1112, Nov. 2008.
[82] L. Antiga, B. Ene-iordache, and A. Remuzzi, “Centerline Computation and Geometric Analysis of Branching Tubular Surfaces with Application to Blood Vessel Modeling,” presented at the Proceedings of the 11th International Conference in Central Europe on Computer GraphicsWSCG, Plzen, Czech Republic, 2003, pp. 11–18.
[83] M. Ghaffari, K. Tangen, A. Alaraj, X. Du, F. T. Charbel, and A. A. Linninger, “Large-scale subject-specific cerebral arterial tree modeling using automated parametric mesh generation for blood flow simulation,” *Comput. Biol. Med.*, vol. 91, no. Supplement C, pp. 353–365, Dec. 2017.

[84] M. Ghaffari, A. Alaraj, X. Du, F. T. Charbel, and A. A. Linninger, “Quantification of near-wall hemodynamic risk factors in large-scale cerebral arterial tree,” *Int. J. Numer. Methods Biomed. Eng.*, p. (Under Review), 2018.
[85] M. Ghaffari, C.-Y. Hsu, and A. A. Linninger, “Automatic reconstruction and generation of structured hexahedral mesh for non-planar bifurcations in vascular network,” *Comput Aided Chem Eng*, 2015.
[86] G. Hartung, A. Alaraj, and A. Linninger, “Walk-In Brain: Virtual Reality Environment for Immersive Exploration and Simulation of Brain Metabolism and Function,” *Comput. Aided Chem. Eng.*, vol. 39, pp. 649–658, 2017.
[87] H. S. Kim, S. B. Park, S. S. Lo, J. I. Monroe, and J. W. Sohn, “Bidirectional local distance measure for comparing segmentations,” *Med. Phys.*, vol. 39, no. 11, pp. 6779–6790, Nov. 2012.
[88] S. H. Kim and R.-H. Park, “An efficient algorithm for video sequence matching using the modified Hausdorff distance and the directed divergence,” *IEEE Trans. Circuits Syst. Video Technol.*, vol. 12, no. 7, pp. 592–596, Jul. 2002.
[89] F. Shao, S. Cai, and J. Gu, “A modified Hausdorff distance based algorithm for 2-dimensional spatial trajectory matching,” in *2010 5th International Conference on Computer Science Education*, 2010, pp. 166–172.
[90] F. Morain-Nicolier, S. Lebonvallet, E. Baudrier, and S. Ruan, “Hausdorff Distance based 3D Quantification of Brain Tumor Evolution from MRI Images,” in *2007 29th Annual International Conference of the IEEE Engineering in Medicine and Biology Society*, 2007, pp. 5597–5600.
[91] H. Khotanlou, O. Colliot, J. Atif, and I. Bloch, “3D brain tumor segmentation in MRI using fuzzy classification, symmetry analysis and spatially constrained deformable models,” *Fuzzy Sets Syst.*, vol. 160, no. 10, pp. 1457–1473, May 2009.
[92] K. O. Babalola *et al.*, “Comparison and Evaluation of Segmentation Techniques for Subcortical Structures in Brain MRI,” in *Medical Image Computing and Computer-Assisted Intervention – MICCAI 2008*, 2008, pp. 409–416.
[93] M. Tang, M. Lee, and Y. J. Kim, “Interactive Hausdorff Distance Computation for General Polygonal Models,” in *ACM SIGGRAPH 2009 Papers*, New York, NY, USA, 2009, p. 74:1–74:9.
[94] J. A. Sethian, “A fast marching level set method for monotonically advancing fronts,” *Proc. Natl. Acad. Sci.*, vol. 93, no. 4, pp. 1591–1595, Feb. 1996.
[95] C.-Y. Hsu, B. Schneller, A. Alaraj, M. Flannery, X. J. Zhou, and A. Linninger, “Automatic recognition of subject-specific cerebrovascular trees,” *Magn. Reson. Med.*, vol. 77, no. 1, pp. 398–410, Jan. 2017.
[96] A. Suinesiaputra, P. J. H. de Koning, E. Zudilova-Seinstra, J. H. C. Reiber, and R. J. van der Geest, “Automated quantification of carotid artery stenosis on contrast-enhanced MRA data using a deformable vascular tube model,” *Int. J. Cardiovasc. Imaging*, vol. 28, no. 6, pp. 1513–1524, Aug. 2012.
[97] M. B. Sasongko *et al.*, “Retinal Vessel Tortuosity and Its Relation to Traditional and Novel Vascular Risk Markers in Persons with Diabetes,” *Curr. Eye Res.*, vol. 41, no. 4, pp. 551–557, 2016.
[98] B. J. Kim, S. M. Kim, D.-W. Kang, S. U. Kwon, D. C. Suh, and J. S. Kim, “Vascular tortuosity may be related to intracranial artery atherosclerosis,” *Int. J. Stroke Off. J. Int. Stroke Soc.*, vol. 10, no. 7, pp. 1081–1086, Oct. 2015.
[99] R. K. Jain, “Normalization of Tumor Vasculature: An Emerging Concept in Antiangiogenic Therapy,” *Science*, vol. 307, no. 5706, pp. 58–62, Jan. 2005.
[100] P. B. Gorelick *et al.*, “Vascular Contributions to Cognitive Impairment and Dementia,” *Stroke J. Cereb. Circ.*, vol. 42, no. 9, pp. 2672–2713, Sep. 2011.
[101] N. Nicolakakis and E. Hamel, “Neurovascular function in Alzheimer’s disease patients and experimental models,” *J. Cereb. Blood Flow Metab.*, vol. 31, no. 6, pp. 1354–1370, Jun. 2011.

[102] E. Bullitt, G. Gerig, S. M. Pizer, W. Lin, and S. R. Aylward, “Measuring tortuosity of the intracerebral vasculature from MRA images,” *IEEE Trans. Med. Imaging*, vol. 22, no. 9, pp. 1163–1171, Sep. 2003.
[103] D. Onkaew, R. Turior, B. Uyyanonvara, N. Akinori, and C. Sinthanayothin, “Automatic retinal vessel tortuosity measurement using curvature of improved chain code,” in *International Conference on Electrical, Control and Computer Engineering 2011 (InECCE)*, 2011, pp. 183–186.
[104] W. E. Hart, M. Goldbaum, B. Côté, P. Kube, and M. R. Nelson, “Automated measurement of retinal vascular tortuosity.,” *Proc. AMIA Annu. Fall Symp.*, pp. 459–463, 1997.
[105] S. N. Wright *et al.*, “Digital reconstruction and morphometric analysis of human brain arterial vasculature from magnetic resonance angiography,” *NeuroImage*, vol. 82, pp. 170–181, Nov. 2013.
[106] F. Mut, S. Wright, G. A. Ascoli, and J. R. Cebral, “Morphometric, geographic, and territorial characterization of brain arterial trees,” *Int. J. Numer. Methods Biomed. Eng.*, vol. 30, no. 7, pp. 755–766, Jul. 2014.
[107] M. Guthe, P. Borodin, and R. Klein, “Fast and accurate Hausdorff distance calculation between meshes,” *J. WSCG*, vol. 13, no. 2, pp. 41–48, Feb. 2005.
[108] H. Chui and A. Rangarajan, “A new point matching algorithm for non-rigid registration,” *Comput. Vis. Image Underst.*, vol. 89, no. 2, pp. 114–141, Feb. 2003.
[109] T. Luo, T. Wischgoll, B. Kwon Koo, Y. Huo, and G. S. Kassab, “IVUS Validation of Patient Coronary Artery Lumen Area Obtained from CT Images,” *PLoS ONE*, vol. 9, no. 1, Jan. 2014.
[110] M. Kontzialis and B. A. Wasserman, “Intracranial vessel wall imaging: current applications and clinical implications,” *Neurovascular Imaging*, vol. 2, p. 4, Feb. 2016.
[111] M. D. Alexander *et al.*, “High-resolution intracranial vessel wall imaging: imaging beyond the lumen,” *J Neurol Neurosurg Psychiatry*, vol. 87, no. 6, pp. 589–597, Jun. 2016.
[112] D. N. Ku, D. P. Giddens, C. K. Zarins, and S. Glagov, “Pulsatile flow and atherosclerosis in the human carotid bifurcation. Positive correlation between plaque location and low oscillating shear stress,” *Arterioscler. Dallas Tex*, vol. 5, no. 3, pp. 293–302, Jun. 1985.
[113] F. Liang, K. Fukasaku, H. Liu, and S. Takagi, “A computational model study of the influence of the anatomy of the circle of willis on cerebral hyperperfusion following carotid artery surgery,” *Biomed. Eng. Online*, vol. 10, p. 84, Sep. 2011.
[114] P. G. Huang and L. O. Muller, “Simulation of one-dimensional blood flow in networks of human vessels using a novel TVD scheme,” *Int. J. Numer. Methods Biomed. Eng.*, vol. 31, no. 5, p. e02701, May 2015.
[115] F. Liang, X. Liu, R. Yamaguchi, and H. Liu, “Sensitivity of flow patterns in aneurysms on the anterior communicating artery to anatomic variations of the cerebral arterial network,” *J. Biomech.*, vol. 49, no. 15, pp. 3731–3740, Nov. 2016.
[116] J. Alastruey, K. H. Parker, J. Peiró, S. M. Byrd, and S. J. Sherwin, “Modelling the circle of Willis to assess the effects of anatomical variations and occlusions on cerebral flows,” *J. Biomech.*, vol. 40, no. 8, pp. 1794–1805, 2007.
[117] I. Marshall, S. Zhao, P. Papathanasopoulou, P. Hoskins, and Y. Xu, “MRI and CFD studies of pulsatile flow in healthy and stenosed carotid bifurcation models,” *J. Biomech.*, vol. 37, no. 5, pp. 679–687, May 2004.
[118] P. Papathanasopoulou *et al.*, “MRI measurement of time-resolved wall shear stress vectors in a carotid bifurcation model, and comparison with CFD predictions,” *J. Magn. Reson. Imaging JMRI*, vol. 17, no. 2, pp. 153–162, Feb. 2003.
[119] D. A. Steinman, J. B. Thomas, H. M. Ladak, J. S. Milner, B. K. Rutt, and J. D. Spence, “Reconstruction of carotid bifurcation hemodynamics and wall thickness using computational fluid dynamics and MRI,” *Magn. Reson. Med.*, vol. 47, no. 1, pp. 149–159, Jan. 2002.

[120] J. S. Stroud, S. A. Berger, and D. Saloner, “Numerical analysis of flow through a severely stenotic carotid artery bifurcation,” *J. Biomech. Eng.*, vol. 124, no. 1, pp. 9–20, Feb. 2002.
[121] J. A. Moore, D. A. Steinman, and C. R. Ethier, “Computational blood flow modelling: errors associated with reconstructing finite element models from magnetic resonance images,” *J. Biomech.*, vol. 31, no. 2, pp. 179–184, Feb. 1998.
[122] P. Perdikaris, L. Grinberg, and G. E. Karniadakis, “Multiscale modeling and simulation of brain blood flow,” *Phys. Fluids*, vol. 28, no. 2, Feb. 2016.
[123] L. Formaggia, F. Nobile, A. Quarteroni, and A. Veneziani, “Multiscale modelling of the circulatory system: a preliminary analysis,” *Comput. Vis. Sci.*, vol. 2, no. 2–3, pp. 75–83, Dec. 1999.
[124] T. Passerini, M. de Luca, L. Formaggia, A. Quarteroni, and A. Veneziani, “A 3D/1D geometrical multiscale model of cerebral vasculature,” *J. Eng. Math.*, vol. 64, no. 4, p. 319, Aug. 2009.
[125] F. Liang, M. Oshima, H. Huang, H. Liu, and S. Takagi, “Numerical Study of Cerebroarterial Hemodynamic Changes Following Carotid Artery Operation: A Comparison Between Multiscale Modeling and Stand-Alone Three-Dimensional Modeling,” *J. Biomech. Eng.*, vol. 137, no. 10, p. 101011, Oct. 2015.
[126] F. Liang, S. Takagi, R. Himeno, and H. Liu, “Multi-scale modeling of the human cardiovascular system with applications to aortic valvular and arterial stenoses,” *Med. Biol. Eng. Comput.*, vol. 47, no. 7, pp. 743–755, Jul. 2009.
[127] L. O. Müller and E. F. Toro, “A global multiscale mathematical model for the human circulation with emphasis on the venous system,” *Int. J. Numer. Methods Biomed. Eng.*, vol. 30, no. 7, pp. 681–725, Jul. 2014.
[128] L. O. Müller and E. F. Toro, “Enhanced global mathematical model for studying cerebral venous blood flow,” *J. Biomech.*, vol. 47, no. 13, pp. 3361–3372, Oct. 2014.
[129] P. J. Blanco, S. M. Watanabe, M. A. R. F. Passos, P. A. Lemos, and R. A. Feijóo, “An Anatomically Detailed Arterial Network Model for One-Dimensional Computational Hemodynamics,” *IEEE Trans. Biomed. Eng.*, vol. 62, no. 2, pp. 736–753, Feb. 2015.
[130] P. J. Blanco, S. M. Watanabe, E. A. Dari, M. A. R. F. Passos, and R. A. Feijóo, “Blood flow distribution in an anatomically detailed arterial network model: criteria and algorithms,” *Biomech. Model. Mechanobiol.*, vol. 13, no. 6, pp. 1303–1330, Nov. 2014.
[131] M. R. Levitt *et al.*, “Cerebral aneurysms treated with flow-diverting stents: Computational models using intravascular blood flow measurements,” *AJNR Am. J. Neuroradiol.*, vol. 35, no. 1, pp. 143–148, Jan. 2014.
[132] L. Antiga, M. Piccinelli, L. Botti, B. Ene-Iordache, A. Remuzzi, and D. A. Steinman, “An image-based modeling framework for patient-specific computational hemodynamics,” *Med. Biol. Eng. Comput.*, vol. 46, no. 11, pp. 1097–1112, Nov. 2008.
[133] M. Abdi and M. Navidbakhsh, “Modeling internal carotid aneurysm utilizing lumped method to assess the effect of anatomical variation on efferent arteries pressures,” in *2012 19th Iranian Conference of Biomedical Engineering (ICBME)*, 2012, pp. 266–271.
[134] M. A. H. M. Adib, S. Ii, Y. Watanabe, and S. Wada, “Minimizing the blood velocity differences between phase-contrast magnetic resonance imaging and computational fluid dynamics simulation in cerebral arteries and aneurysms,” *Med. Biol. Eng. Comput.*, vol. 55, no. 9, pp. 1605–1619, Sep. 2017.
[135] S. Takeuchi and T. Karino, “Flow patterns and distributions of fluid velocity and wall shear stress in the human internal carotid and middle cerebral arteries,” *World Neurosurg.*, vol. 73, no. 3, p. 174–185; discussion e27, Mar. 2010.
[136] A. Sarrami-Foroushani, T. Lassila, A. Gooya, A. J. Geers, and A. F. Frangi, “Uncertainty quantification of wall shear stress in intracranial aneurysms using a data-driven statistical model of systemic blood flow variability,” *J. Biomech.*, vol. 49, no. 16, pp. 3815–3823, Dec. 2016.

[137] X. He and D. N. Ku, “Pulsatile flow in the human left coronary artery bifurcation: average conditions,” *J. Biomech. Eng.*, vol. 118, no. 1, pp. 74–82, Feb. 1996.
[138] H. A. Himburg, D. M. Grzybowski, A. L. Hazel, J. A. LaMack, X.-M. Li, and M. H. Friedman, “Spatial comparison between wall shear stress measures and porcine arterial endothelial permeability,” *Am. J. Physiol. Heart Circ. Physiol.*, vol. 286, no. 5, pp. H1916-1922, May 2004.
[139] D. M. Wootton and D. N. Ku, “Fluid mechanics of vascular systems, diseases, and thrombosis,” *Annu. Rev. Biomed. Eng.*, vol. 1, pp. 299–329, 1999.
[140] P. F. Davies, “Hemodynamic shear stress and the endothelium in cardiovascular pathophysiology,” *Nat. Clin. Pract. Cardiovasc. Med.*, vol. 6, no. 1, pp. 16–26, 2009.
[141] F. P. Glor *et al.*, “Image-based carotid flow reconstruction: a comparison between MRI and ultrasound,” *Physiol. Meas.*, vol. 25, no. 6, pp. 1495–1509, Dec. 2004.
[142] F. P. Glor *et al.*, “Reproducibility Study of Magnetic Resonance Image-Based Computational Fluid Dynamics Prediction of Carotid Bifurcation Flow,” *Ann. Biomed. Eng.*, vol. 31, no. 2, pp. 142–151, Feb. 2003.
[143] H. Meng *et al.*, “Complex Hemodynamics at the Apex of an Arterial Bifurcation Induces Vascular Remodeling Resembling Cerebral Aneurysm Initiation,” *Stroke*, vol. 38, no. 6, pp. 1924–1931, Jun. 2007.
[144] Z. Zeng *et al.*, “Sensitivity of CFD Based Hemodynamic Results in Rabbit Aneurysm Models to Idealizations in Surrounding Vasculature,” *J. Biomech. Eng.*, vol. 132, no. 9, p. 91009, Sep. 2010.
[145] U. Morbiducci *et al.*, “Quantitative Analysis of Bulk Flow in Image-Based Hemodynamic Models of the Carotid Bifurcation: The Influence of Outflow Conditions as Test Case,” *Ann. Biomed. Eng.*, vol. 38, no. 12, pp. 3688–3705, Jun. 2010.
[146] S.-W. Lee, L. Antiga, and D. A. Steinman, “Correlations Among Indicators of Disturbed Flow at the Normal Carotid Bifurcation,” *J. Biomech. Eng.*, vol. 131, no. 6, pp. 061013–061013, May 2009.
[147] Dong Jingliang, Wong Kelvin K.L., and Tu Jiyuan, “Hemodynamics analysis of patient-specific carotid bifurcation: A CFD model of downstream peripheral vascular impedance,” *Int. J. Numer. Methods Biomed. Eng.*, vol. 29, no. 4, pp. 476–491, Nov. 2012.
[148] M. Ghaffari, A. Alaraj, X. Du, F. T. Charbel, and A. A. Linninger, “Quantification of near-wall hemodynamic risk factors in large-scale cerebral arterial tree,” *Int. J. Numer. Methods Biomed. Eng.*, p. (Under Review), 2018.
[149] S. F. Shakur, V. A. Aletich, S. Amin-Hanjani, A. E. Hussein, F. T. Charbel, and A. Alaraj, “Quantitative assessment of parent vessel and distal intracranial hemodynamics following pipeline flow diversion,” *Interv. Neuroradiol.*, p. 1591019916668842, Oct. 2016.
[150] J. R. Cebral, M. A. Castro, S. Appanaboyina, C. M. Putman, D. Millan, and A. F. Frangi, “Efficient pipeline for image-based patient-specific analysis of cerebral aneurysm hemodynamics: technique and sensitivity,” *IEEE Trans. Med. Imaging*, vol. 24, no. 4, pp. 457–467, Apr. 2005.
[151] Y. Hoi *et al.*, “Characterization of volumetric flow rate waveforms at the carotid bifurcations of older adults,” *Physiol. Meas.*, vol. 31, no. 3, pp. 291–302, Mar. 2010.
[152] M. F. O’Rourke and M. E. Safar, “Relationship between aortic stiffening and microvascular disease in brain and kidney: cause and logic of therapy,” *Hypertens. Dallas Tex 1979*, vol. 46, no. 1, pp. 200–204, Jul. 2005.
[153] G. F. Mitchell *et al.*, “Arterial stiffness, pressure and flow pulsatility and brain structure and function: the Age, Gene/Environment Susceptibility--Reykjavik study,” *Brain J. Neurol.*, vol. 134, no. Pt 11, pp. 3398–3407, Nov. 2011.
[154] H. A. Himburg, S. E. Dowd, and M. H. Friedman, “Frequency-dependent response of the vascular endothelium to pulsatile shear stress,” *Am. J. Physiol. - Heart Circ. Physiol.*, vol. 293, no. 1, pp. H645–H653, Jul. 2007.

[155] F. Mut, D. Ruijters, D. Babic, C. Bleise, P. Lylyk, and J. R. Cebral, “Effects of changing physiologic conditions on the in vivo quantification of hemodynamic variables in cerebral aneurysms treated with flow diverting devices,” *Int. J. Numer. Methods Biomed. Eng.*, vol. 30, no. 1, pp. 135–142, Jan. 2014.
[156] I. E. Vignon-Clementel, C. Alberto Figueroa, K. E. Jansen, and C. A. Taylor, “Outflow boundary conditions for three-dimensional finite element modeling of blood flow and pressure in arteries,” *Comput. Methods Appl. Mech. Eng.*, vol. 195, no. 29–32, pp. 3776–3796, Jun. 2006.
[157] R. L. Spilker, J. A. Feinstein, D. W. Parker, V. M. Reddy, and C. A. Taylor, “Morphometry-Based Impedance Boundary Conditions for Patient-Specific Modeling of Blood Flow in Pulmonary Arteries,” *Ann. Biomed. Eng.*, vol. 35, no. 4, pp. 546–559, Feb. 2007.
[158] M. S. Olufsen, “Structured tree outflow condition for blood flow in larger systemic arteries,” *Am. J. Physiol. - Heart Circ. Physiol.*, vol. 276, no. 1, pp. H257–H268, Jan. 1999.
[159] A. A. Linninger, I. G. Gould, T. Marinnan, C.-Y. Hsu, M. Chojecki, and A. Alaraj, “Cerebral microcirculation and oxygen tension in the human secondary cortex,” *Ann. Biomed. Eng.*, vol. 41, no. 11, pp. 2264–2284, Nov. 2013.
[160] I. G. Gould and A. A. Linninger, “Hematocrit distribution and tissue oxygenation in large microcirculatory networks,” *Microcirc. N. Y. N 1994*, vol. 22, no. 1, pp. 1–18, Jan. 2015.
[161] J. Xiang, A. H. Siddiqui, and H. Meng, “The effect of inlet waveforms on computational hemodynamics of patient-specific intracranial aneurysms,” *J. Biomech.*, vol. 47, no. 16, pp. 3882–3890, Dec. 2014.
[162] A. Valencia, D. Ledermann, R. Rivera, E. Bravo, and M. Galvez, “Blood flow dynamics and fluid–structure interaction in patient-specific bifurcating cerebral aneurysms,” *Int. J. Numer. Methods Fluids*, vol. 58, no. 10, pp. 1081–1100, Dec. 2008.
[163] A. Arzani, A. M. Gambaruto, G. Chen, and S. C. Shadden, “Wall shear stress exposure time: a Lagrangian measure of near-wall stagnation and concentration in cardiovascular flows,” *Biomech. Model. Mechanobiol.*, vol. 16, no. 3, pp. 787–803, Jun. 2017.

7. APPENDIX

7.1. Licenses & permission

Following are the acquired permission to use my previously published articles in my dissertation.

Copyright Clearance Center RightsLink®

Home | Create Account | Help

Title: Large-scale subject-specific cerebral arterial tree modeling using automated parametric mesh generation for blood flow simulation

Author: Mahsa Ghaffari,Kevin Tangen,Ali Alaraj,Xinjian Du,Fady T. Charbel,Andreas A. Linninger

Publication: Computers in Biology and Medicine

Publisher: Elsevier

Date: 1 December 2017

LOGIN

If you're a copyright.com user, you can login to RightsLink using your copyright.com credentials.

Already a RightsLink user or want to learn more?

Please note that, as the author of this Elsevier article, you retain the right to include it in a thesis or dissertation, provided it is not published commercially. Permission is not required, but please ensure that you reference the journal as the original source. For more information on this and on your other retained rights, please visit: https://www.elsevier.com/about/our-business/policies/copyright#Author-rights

BACK | CLOSE WINDOW

7.2. Mesh Indexing

In this appendix, we discuss and solve an example of parametric mesh indexing of vascular. For a vascular cross section with α = 2, β = 1 and γ = 2 as shown in Figure 67 and Equation (61). All steps in parametric mesh generation are shown as follows. Total number of points in each cross-section is 73 points-index. Figure 68 to Figure 73 are different examples of circumferential, radial and longitudinal mesh indexing for butterfly cross-sectional topology.

$$d = [8\alpha \cdot (\beta + \gamma)] + [(8\alpha + 1)]^2$$
$$d = [8 \times 2 \cdot (1 + 2)] + [(4 \times 2 + 1)]^2 = 73 \quad (61)$$

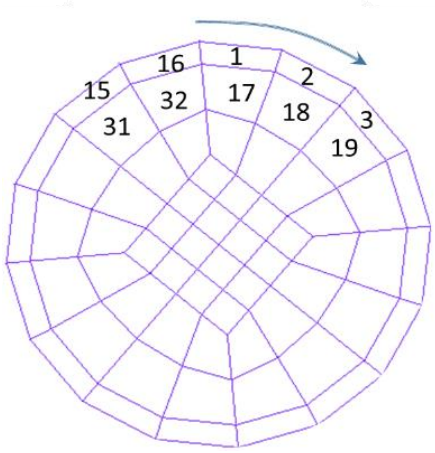

Figure 67. Cross-sectional illustration of parametric mesh generation. Cell mesh indices are shown for a butterfly cross-sectional topology

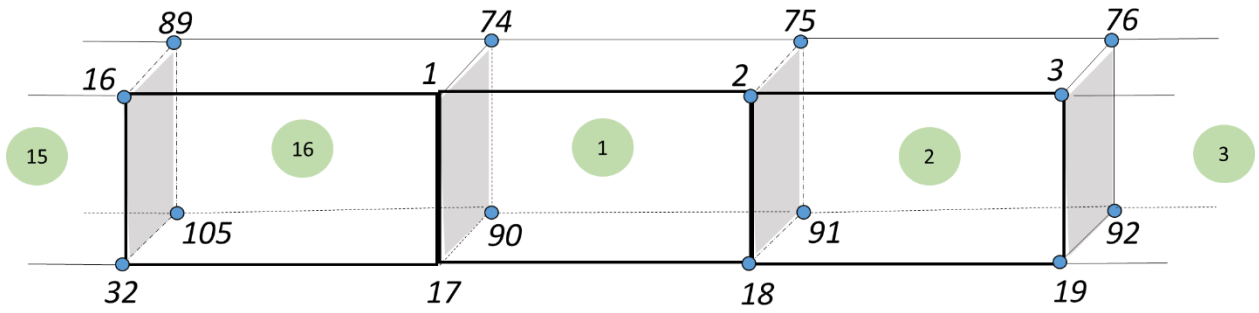

Point indices				Cell indices	
1	17	90	74	1	16
2	18	91	75	2	1
3	19	92	76	3	2
4	20	93	77	4	3
5	21	94	78	5	4
6	22	95	79	6	5
7	23	96	80	7	6
8	24	97	81	8	7
9	25	98	82	9	8
10	26	99	83	10	9
11	27	100	84	11	10
12	28	101	85	12	11
13	29	102	86	13	12
14	30	103	87	14	13
15	31	104	88	15	14
16	32	105	89	16	15

Figure 68. Circumferential mesh indexing. It starts from the first mesh element to the sixteenth element. Cell indices are shown in the green circle. The gray plane is in circumferential right-hand direction.

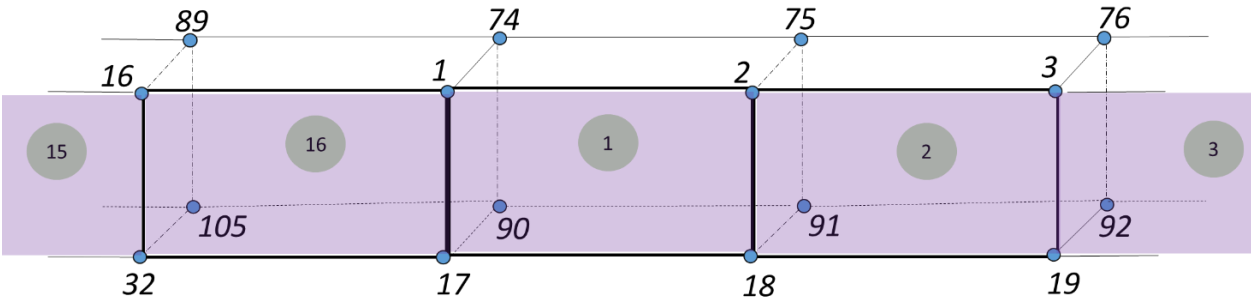

Point indices | Cell indices

1	2	18	17	1	0
2	3	19	18	2	0
3	4	20	19	3	0
4	5	21	20	4	0
5	6	22	21	5	0
6	7	23	22	6	0
7	8	24	23	7	0
8	9	25	24	8	0
9	10	26	25	9	0
10	11	27	26	10	0
11	12	28	27	11	0
12	13	29	28	12	0
13	14	30	29	13	0
14	15	31	30	14	0
15	16	32	31	15	0
16	1	17	32	16	0

Figure 69. Longitudinal mesh indexing. It starts from the first mesh element to the sixteenth element. Cell indices are shown in the green circle. One of the cell indices is zero, because it belongs to inlet cross-section.

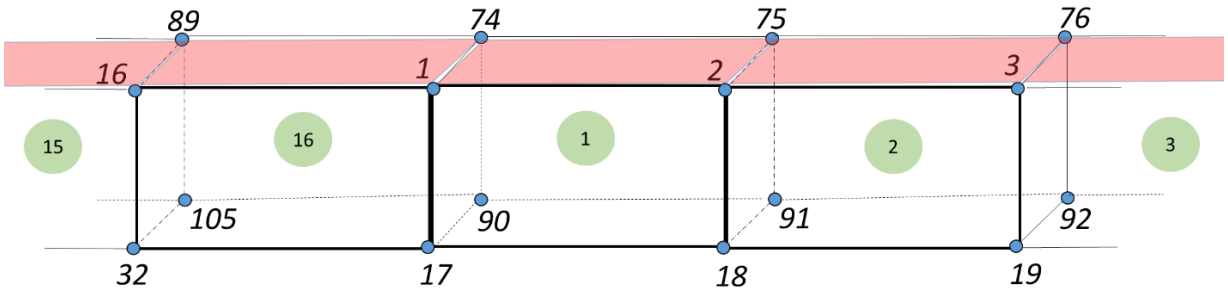

Point indices | Cell indices

1	74	75	2	1	0
2	75	76	3	2	0
3	76	77	4	3	0
4	77	78	5	4	0
5	78	79	6	5	0
6	79	80	7	6	0
7	80	81	8	7	0
8	81	82	9	8	0
9	82	83	10	9	0
10	83	84	11	10	0
11	84	85	12	11	0
12	85	86	13	12	0
13	86	87	14	13	0
14	87	88	15	14	0
15	88	89	16	15	0
16	89	74	1	16	0

Figure 70. Radial mesh indexing. It starts from the first mesh element to the sixteenth element. Cell indices are shown in the green circle. One of the cell indices is zero because it belongs to vessel wall region.

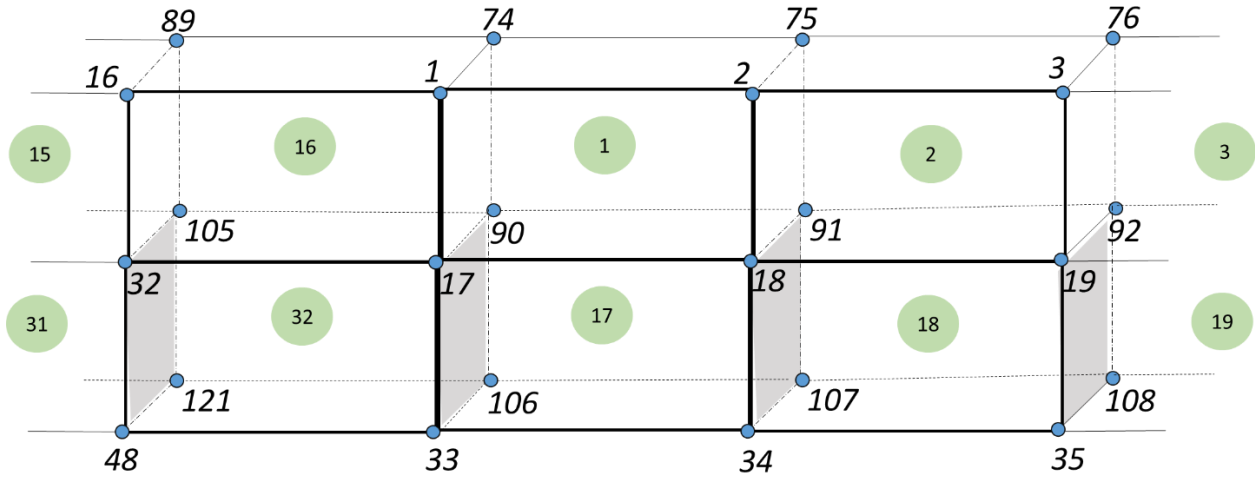

Point indices				Cell indices	
17	33	106	90	17	32
18	34	107	91	18	17
19	35	108	92	19	18
20	36	109	93	20	19
21	37	110	94	21	20
22	38	111	95	22	21
23	39	112	96	23	22
24	40	113	97	24	23
25	41	114	98	25	24
26	42	115	99	26	25
27	43	116	100	27	26
28	44	117	101	28	27
29	45	118	102	29	28
30	46	119	103	30	29
31	47	120	104	31	30
32	48	121	105	32	31

Figure 71. Circumferential mesh indexing. It starts from the 17th mesh element to the 32th element. Cell indices are shown in the green circle. The gray plane are in circumferential right-hand direction. These data set belong to lumen region.

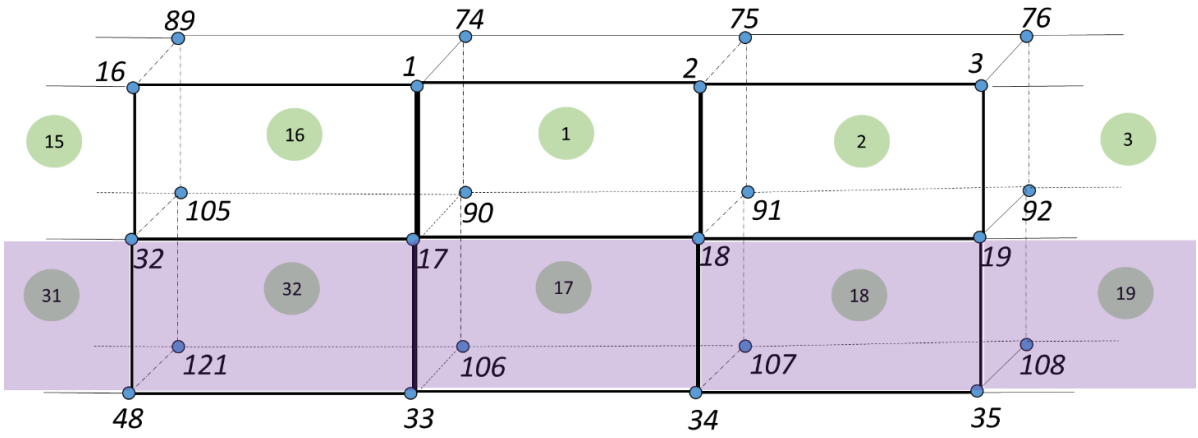

Point indices | Cell indices

17	18	34	33	17	0
18	19	35	34	18	0
19	20	36	35	19	0
20	21	37	36	20	0
21	22	38	37	21	0
22	23	39	38	22	0
23	24	40	39	23	0
24	25	41	40	24	0
25	26	42	41	25	0
26	27	43	42	26	0
27	28	44	43	27	0
28	29	45	44	28	0
29	30	46	45	29	0
30	31	47	46	30	0
31	32	48	47	31	0
32	17	33	48	32	0

Figure 72. Circumferential mesh indexing. It starts from the 17th mesh element to the 32nd element. Cell indices are shown in the green circle. One of the cell indices is zero, because it belongs to inlet cross-section.

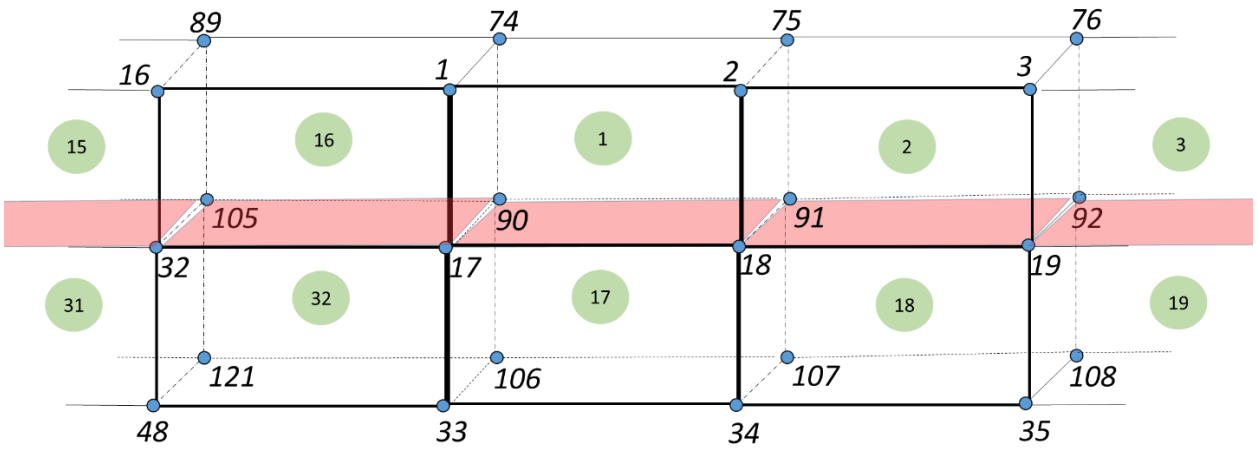

Point indices | Cell indices

17	90	91	18	17	1
18	91	92	19	18	2
19	92	93	20	19	3
20	93	94	21	20	4
21	94	95	22	21	5
22	95	96	23	22	6
23	96	97	24	23	7
24	97	98	25	24	8
25	98	99	26	25	9
26	99	100	27	26	10
27	100	101	28	27	11
28	101	102	29	28	12
29	102	103	30	29	13
30	103	104	31	30	14
31	104	105	32	31	15
32	105	90	17	32	16

Figure 73. Circumferential mesh indexing. It starts from the first mesh element to the sixteenth element. Cell indices are shown in the green circle. These data set belong to lumen region.

7.3. Data Inventory

This appendix lists the directory of used datasets to accomplish this thesis as well as a directory of the tutorials for local use of at Laboratory of Product and Process Design (LPPD). All of the files in this document exist on the share drive (S) or external hard-drive (E). This location has different directories each with its own chapter in this document. The naming conventions for the locations have all datasets appointed to a subdirectory under their own name with an example. All Tutorial are accessible on the share drive under \\share\25_Tutorial.

7.3.1. Subjects

7.3.1.1. Vascular network structures

Case and Network Files

We used Case and Network files to visualize cerebral arterial trees Skeletonization. Case and network files (cs31 and nwk) are the simplest way of organizing the data. They are a 1-dimensional logic expressed in 3-dimensions. They use points to represent vertices of importance (on a curve, at a bifurcation, at a diameter change) and radii between these points. There are spline versions (.cs4 and snwk) of the case and network file that enable vascular network cleaning faster. Figure 74 Figure 75 illustrates visualization of vascular skeletons in Delphi, WalInBrain and Cerebroview software. Statistics of the vascular network for six cerebral arterial trees are listed in Table 25.

Benefits: allows simple 1-dimensional simulation, does not take much space. Vascular network cleaning can be performed on 1-D network before generation of 3-D meshes.

Drawbacks: cannot be used in modern CFD tools, have to assign boundary conditions individually, not with groups.

Directory of case and network files:

Directory: E:/Inventory/Subjects/##name/NWK/##.nwk

Example: E:/Inventory/Subjects/bs/NWK/BS.nwk

Directory of spline format*:*

Directory: E:/Inventory/Subjects/##name/NWK/##.snwk

Example: E:/Inventory/Subjects/bs/NWK/BS.snwk

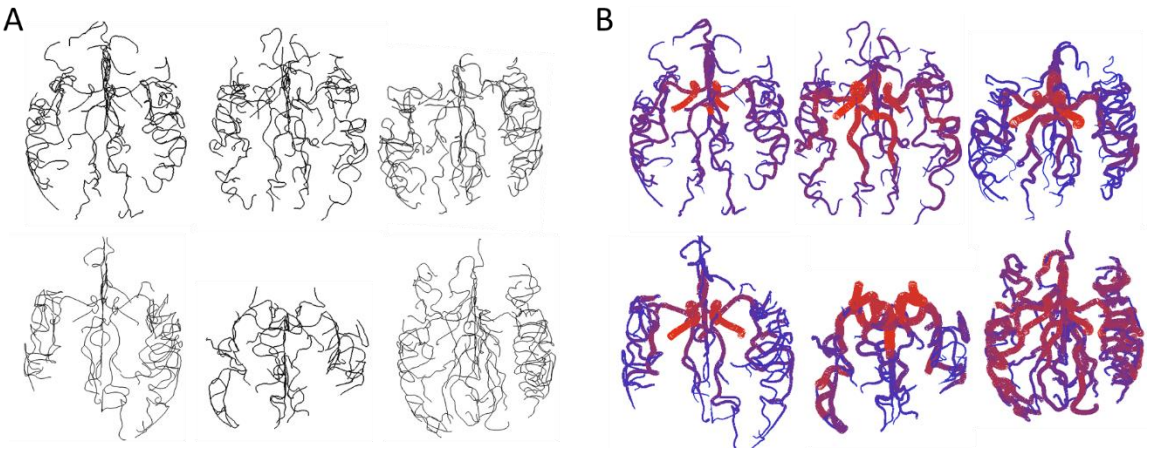

Figure 74. Visualization of cerebral arterial tree network. Delphi and WalkInBrain software were used to visualize the Case and Network files in Panel (A) and (B), respectively.

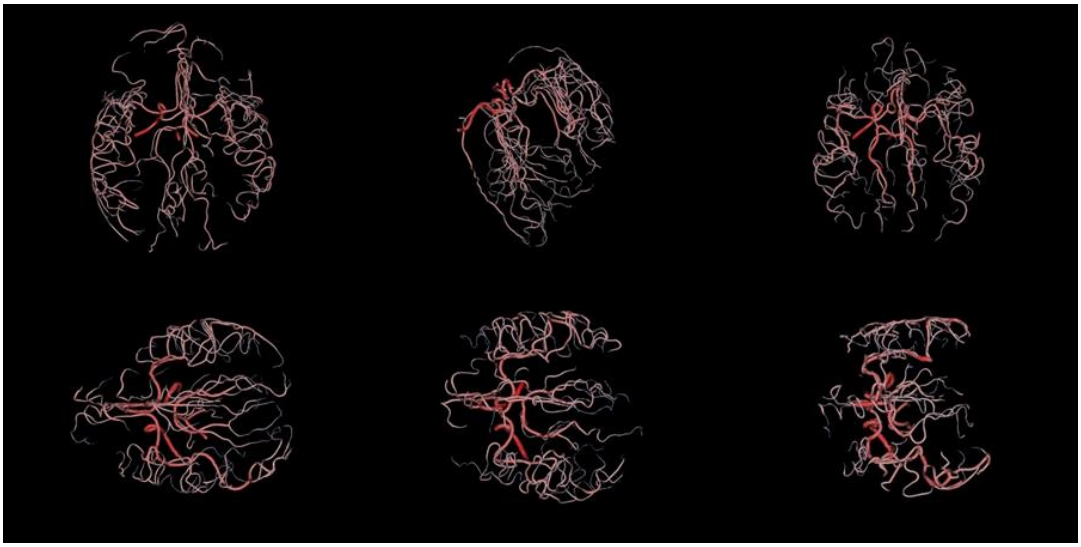

Figure 75. Visualization of cerebral arterial tree network in Cerebroview.

7.3.1.2. Surface Mesh

Meshes are an intermediate outcome during the centerline extraction procedure, mostly outputted in STL (stereo lithography) format. Surface meshes are an intermediate step between the original, unstructured mesh (STL) and the final volumetric mesh file. It is already smoothed using Bezier spline smoothing and fits the GAMBIT format (see MSH file report for more information).

Benefits: 3D Printing-ready, can be read by any 3D modeling or simulating software. Using surface mesh for visualization is faster to interpret that volumetric meshes

Shortcomings: Surface meshes cannot be directly used for 3D hemodynamic analysis.

Directory of STL files:

Directory: S: /19_ImageInventory/Subjects/#name/#nameSTL

Directory of surface meshes:

Directory: S: /19_ImageInventory/Subjects/#name/#nameSurfMSH

7.3.1.3. Volumetric Meshes

Volumetric meshes are the final step of creating a 3D object for simulation. A volumetric mesh adheres to the GAMBIT format and can be easily converted/imported to ANSYS for 3D CFD simulations. These meshes are not unstructured, but rather parametric which means the volume elements are hexahedrons (as opposed to tetrahedrons). Statistics of the parametric meshes for six cerebral arterial trees are listed in Table 25. Figure 76, Figure 77, and Figure 78 illustrate the visualization of computational meshes in WalkInBrain, ANSYS ICEM-CFD, and Cerebroview software, respectively.

Benefits: Easily ported to 3D CFD tools, can assign boundary conditions by groups. Parametric meshes are smaller that unstructured meshes and more suitable for both simulation and visualization.

Drawbacks: Volume meshes are very large datasets not suitable for visualization.

Directory: S:/19_ImageInventory/Subjects/#name/#nameMSH

3D Parametric meshes:
Directory: E:/Inventory/Subjects/#name/PRM/##.msh

3D Unstructured meshes:
Directory: E:/Inventory/Subjects/##name/UNST/##.msh

Table 25. Statistics of reconstructed, mesh generation of cerebral arterial trees with parametric meshing technique for six volunteers.

Subjects	#Points	#Branches	#Bifurcations	#Elements	Meshing time (min)
I	15688	133	68	1783K	15.6
II	22502	294	100	2158K	18.4
III	17436	175	89	1876K	16.8
IV	24485	309	122	2115K	19.6
V	20477	247	99	1918K	17.5
VI	19203	206	93	1897K	17.4
Mean	19965	227	95	1958K	17.6

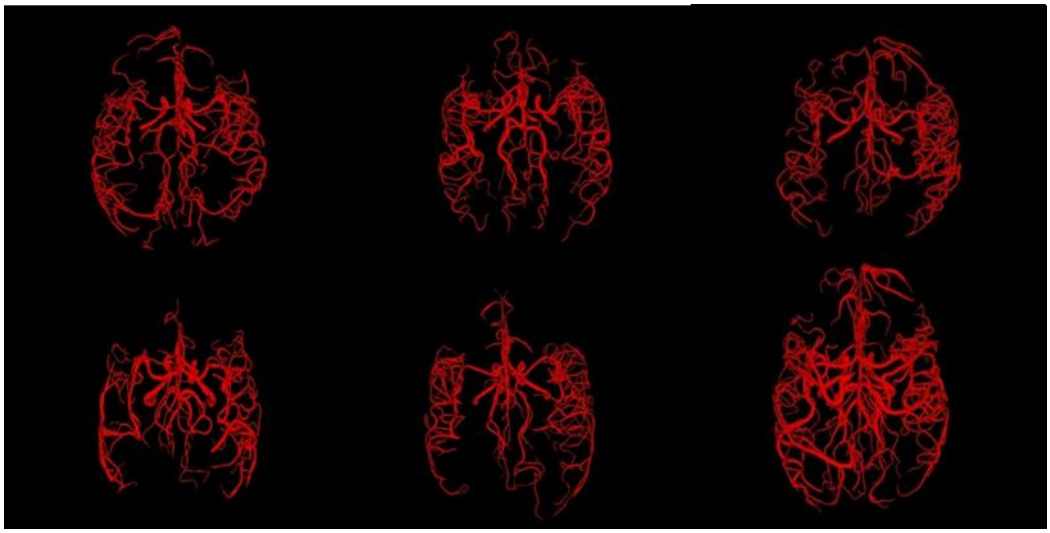

Figure 76. Visualization of STL surface mesh in WalkInBrain software.

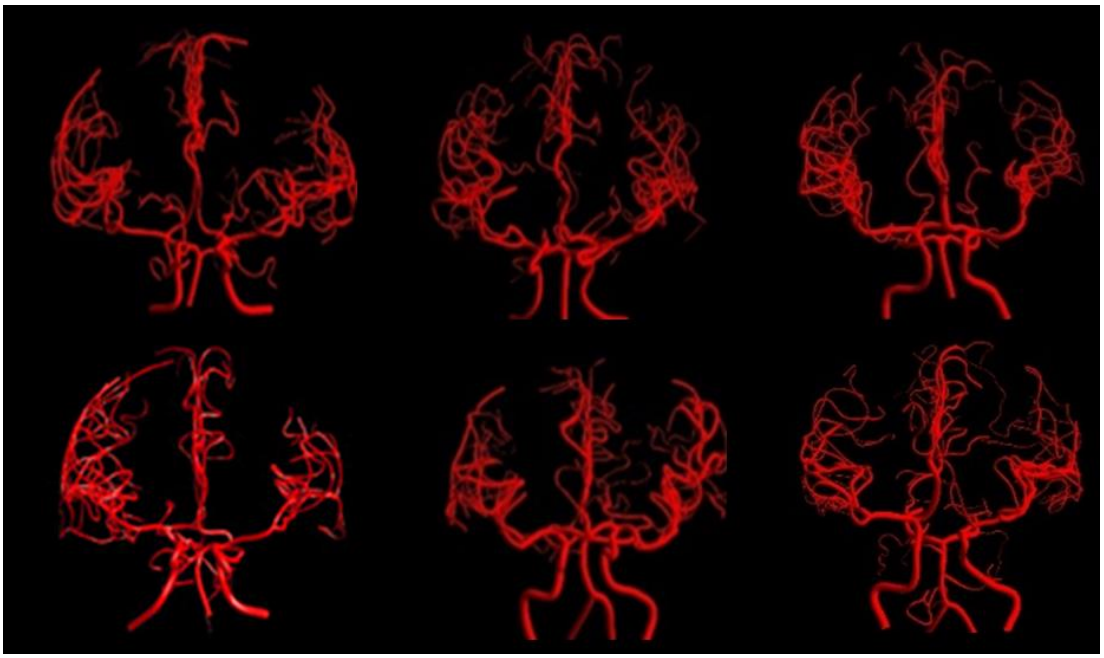

Figure 77.Visualization of 3D surface and volumetric meshes in ANSYS ICEM-CFD software.

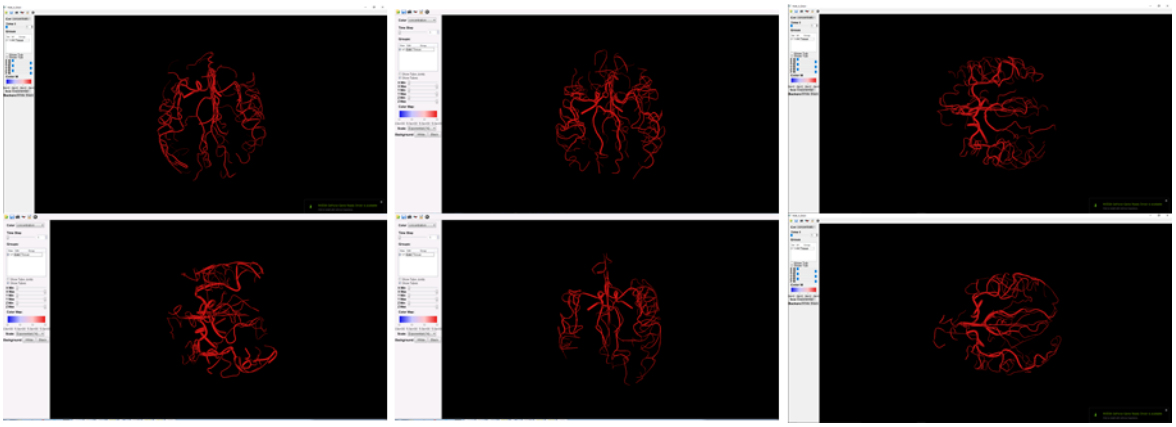

Figure 78. Visualization of 3D surface and volumetric meshes in Cerebroview software.

7.3.1.4. Superposition of the MRA, Segmentation, and Mesh

MRA images, network file, and volume meshes can be loaded together as shown in Figure 79. By the semi-transparent rending method, we can measure the overlap of the datasets and compare them using statistical analysis. The *.txt file indicates the name and the directory of all the files that should be loaded in WalkInBrain software, as shown in the directory example.

Benefits: Colors and transparency of the network and mesh can be changed to facilitate the differentiation (network in red and mesh in blue for example).

Drawbacks: Each datasets file need to be loaded in their correct order; first the raw images, then the vascular network and finally the mesh. Unfortunately, there is no "Save" option in WalkInBrain software.

Directory of Superposition of all datasets:

Directory:S:/19_ImageInventory/Unityloadable/6Subjects/XXCenterline/Structure.txt

Example: S:/19_ImageInventory/Unityloadable/6Subjects/BSCenterline/Structure.txt

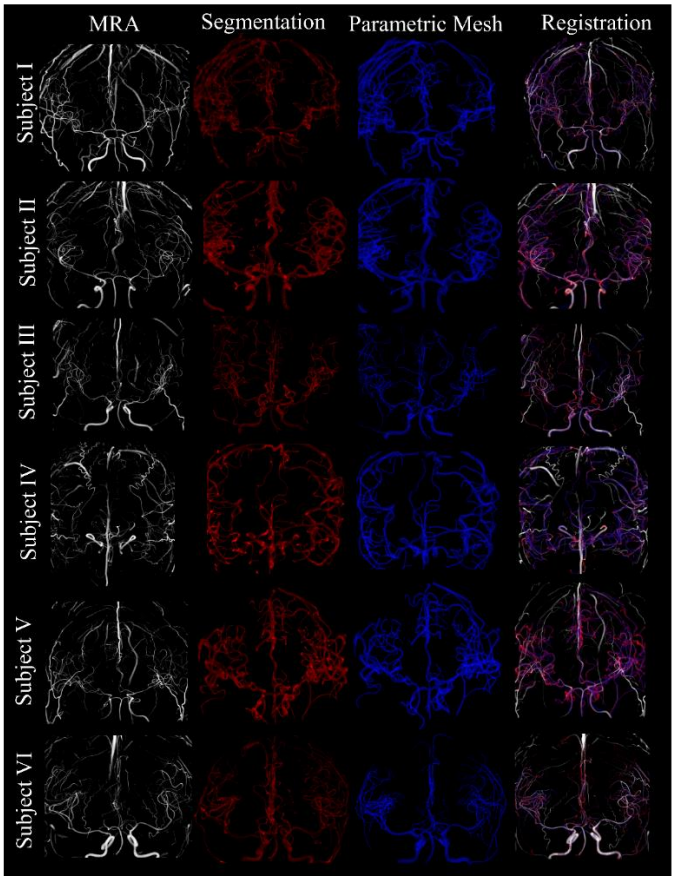

Figure 79. Simultaneous visualization of MRA (white), vascular network (red) and 3D parametric meshes (blue) in WalkInBrain.

7.3.1.5. NOVA measurement

Nova is commercial flow analysis software to quantify volumetric pulsatile blood flow. Blood flow was measured from incoming flow to CoW including the left and right internal carotid arteries (LICA and RICA) and basilar artery (BA); in addition, arteries leaving the CoW include the anterior cerebral arteries (LACA and RACA), middle cerebral arteries (LMCA and RMCA) and the left and the right posterior cerebral arteries (LPCA and RPCA).

The measured NOVA blood flow profile should be digitalized to enable computational analysis such as Fourier series approximation. To quantify the profiles, we used online plot digitizer software (https://apps.automeris.io/wpd/).

Benefits: Blood flow measurement with NOVA software is subject-specific and transient. It is also available at the University of Illinois at Chicago hospital.

Drawbacks: NOVA cannot measure blood flow in small arteries. In addition, it cannot simultaneously measure the blood flow from all desired arteries. An operator should assign perpendicular plane for each artery to measure the blood flow. This user-dependent procedure does not guarantee that the plane is fully perpendicular.

The accumulated inlet flow was more than accumulated outflows for Subject I (65 mL/min), Subject II (5 mL/min), Subject III (22 mL/min), Subject IV (11 mL/min), and Subject VI (60 mL/min). However, Subject V's accumulated outflow was 84 mL/min more than total blood flow in BA, RICA, and LICA. This error may be due to inaccurate (not-perpendicular) plane generation for vascular to measure blood flow.

Measured NOVA profiles:

Directory: E: /Inventory/Subjects/#name/NOVA/NOVA profile/*.jpg

Digitalized NOVA profiles:

Directory: E: /Inventory/Subjects/#name/NOVA/NOVA quantified/*.csv

Table 26.Volumetric blood flow rate acquired by quantitative MRA in major cerebral arteries (mL/min).

	Subject I	Subject II	Subject III	Subject IV	Subject V	Subject VI	Average
RICA	277	168	406	241	295	242	271.5
RACA	112	-	179	95	120	96	120.4
RMCA	102	166	213	145	190	116	155.3
RPCA	63	70	96	60	92	59	73.3
LICA	190	312	318	247	265	226	259.7
LACA	68	159	131	66	96	70	98.3
LMCA	102	172	202	184	171	131	160.3
LPCA	61	89	113	62	97	62	80.7
BA	106	181	232	135	122	126	150.3

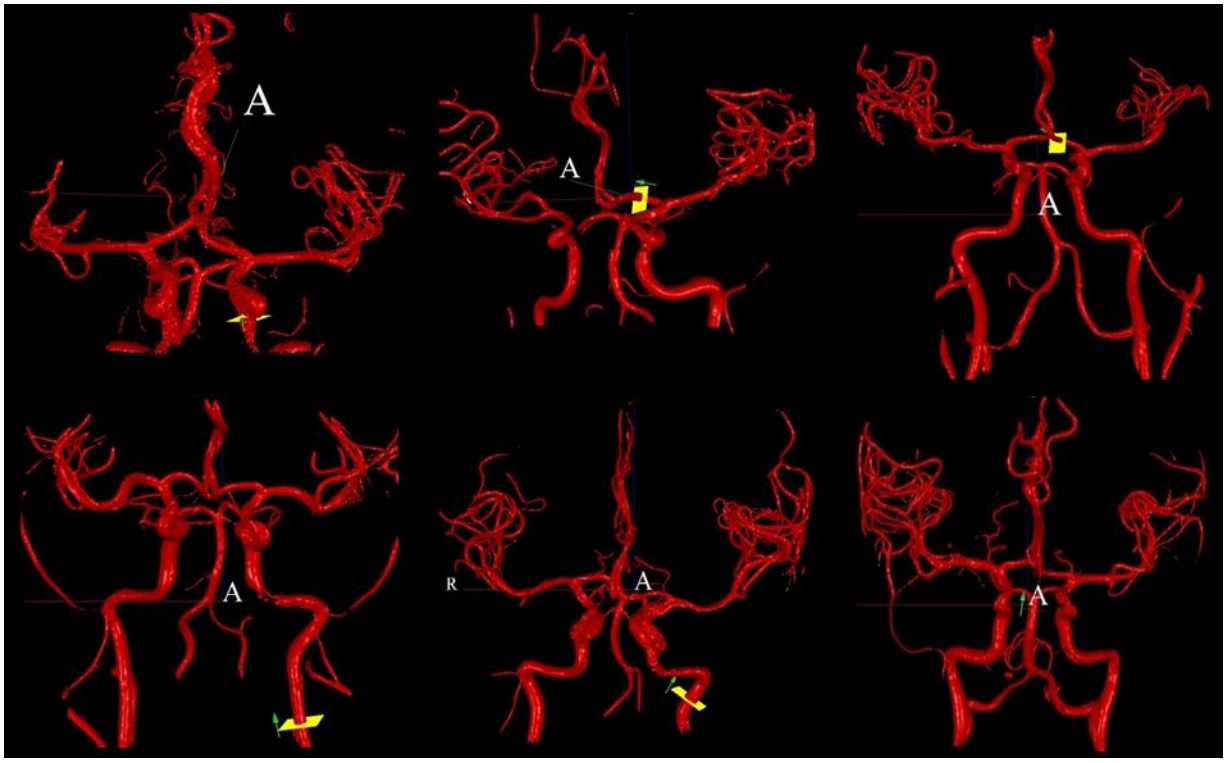

Figure 80. Visualization of NOVA blood flow measurement for six cerebral arterial trees.

7.3.1.6. Boundary condition assignment

Blood flow measurements obtained from the NOVA scans at the RICA, LICA, as well as BA (or RVA, LVA) served to set pulsatile inlet boundary conditions for our simulations. For all outlets, outflow pressure boundary conditions were assigned so as to match the volumetric flow rates from in vivo measurements at LMCA, RMCA, LPCA, RPCA, LACA, RACA vessels.

For velocity inlet calculation, the operator should calculate the area of the inlets to convert the flow to velocity.

We used a Fourier series approximation to set velocity boundary conditions at the inlet of the basilar and carotid arteries, which were implemented in ANSYS Fluent with user-defined functions (UDF).

Benefits: Enables subject-specific inlet/outlet boundary condition assignment in the hemodynamic flow simulation.

Drawbacks: Outlet boundary condition assignment requires multiple simulations to match CFD simulation with in vivo measurements at LMCA, RMCA, LPCA, RPCA, LACA, RACA vessels.

Important notes for future works:

In the NOVA measurement, there is no mass flow equilibrium between measured inflows and outflows. NOVA usually detects more flow in the inlets than outflow from Circle of Willis. Therefore, the operator should reduce the inlet flow to keep the flow conservation. 3D simulation is highly sensitive to the outlets' boundary conditions which are close to CoW. In these cases, it is suggested to label proximal outlets in a different group to enhance the NOVA and CFD blood flow matching. Moreover, the assigned pressure outlets are constant. Future works can address generation of a specific UDF which create pulsatile pressure.

Velocity boundary condition:

Directory: E:/Inventory/Subjects/#name/BC/#name.c

Pressure boundary condition

Table 27. Outlet pressure for vascular territories of cerebral arterial tree of six subjects.

	Subject 1 (KT)	Subject 2 (BS)	Subject 3 (NN)	Subject 4 (IG)	Subject 5 (CY)	Subject 6 (MG)
RACA	10666	12399	11599	10799	11500	11000
RMCA	13332	11999	12398	12398	9000	9500
RPCA	14932	13999	16665	11999	14500	10500
LACA	10799	12399	11999	12398	18500	12000
LMCA	11732	11999	11998	11199	7500	9000
LPCA	12266	10932	15998	12665	10000	14000

7.3.1.7. Blood flow, pressure and near-wall indices visualization

"To visualize the pressure and blood flow in the entire cerebral vascular tree, contour map and streamline generation are recommended in CFD-POST. If specific pressure and flow measurement from a single vascular segment are required, the operator should first generate a plane and measure the hemodynamic parameter in the plane. The tutorial of this process is in the following directory. Near-wall hemodynamic indices such as oscillatory shear index (OSI), relative residence time (RRT) and time-average wall shear stress (TAWSS) should be calculated separately in MATLAB software and visualized in CFD-Post. The tutorial for the process is in the following directory.

Tutorial of CFD-Post:

Directory 1: S:/25_Tutorials/CFD_Post/CFD_Post_PlaneGeneration.avi

Directory 2: S:/25_Tutorials/CFD_Post/CFD_Post_Tutorial.avi

Tutorial of Near-wall hemodynamic computation and calculation:

Directory: S:/25_Tutorials/OSI, RRT, TAWSS/OSI_tutorial.docx

7.3.2. Patients

Similar to the six subjects, here we are visualizing different datasets format of two patients with stenosis and aneurysm diseases.

7.3.2.1. Vascular network structures

Figure 81 illustrates the Case and Network file of the pathological cases including one aneurysm with two stenosis patients.

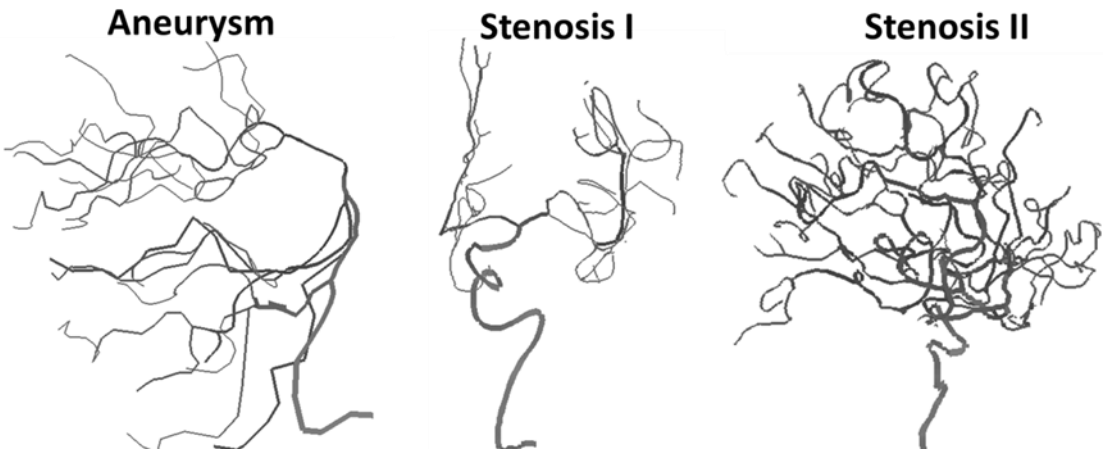

Figure 81. Visualization of vascular network of three pathological cases.

Directory of the case and network files:

Directory: E:/Inventory/Patients/##name/NWK/##.nwk

Directory of spline format:

Directory: E:/Inventory/Patients/##name/NWK/##.snwk

7.3.2.2. Volumetric Meshes

Volumetric meshes are the final step of creating a 3D object for simulation. For patient cases, we have 3D volumetric meshes from pre- and post-treatment of the lesion. Totally Aneurysm and stenosed tree have 3320606 and 474960 cells. Figure 82 visualized the 3D computational meshes of the pathological cases in pre- and post-treatment. Similar to the healthy human subject, all formats are listed as follows.

Benefits: Volumetric meshes enables 3D hemodynamic simulation.

Drawbacks: Extremely large data for visualization. In WalkInBrain, it is difficult and very slow import and rotates the subjects. In addition, the .msh file should be converted to .mm files to enable using WalkInBrain software to visualize the data.

Directory of parametric meshes:

Directory: E:/Inventory/Patients/##name/PRM/##.msh

Example: E:/Inventory/Patients/stenosis/PRM/stenosisPreTreat.msh

Example: E:/Inventory/Patients/stenosis/PRM/stenosisPostTreat.msh

Directory of unstructured meshes:

Directory: E:/Inventory/Patients/##name/UNST/##.msh

Example: E:/Inventory/Patients/stenosis/UNST/stenosisPreTreat.msh

Example: E:/Inventory/Patients/stenosis/UNST/stenosisPostTreat.msh

Directory of WalkInBrain:

Directory: E:/Inventory/Patients/##name/UNST/##.msh

Example: E:/Inventory/Patients/stenosis/WalkInBrainFormat/stenosisPreTreat.mm

Example: E:/Inventory/Patients/stenosis/WalkInBrainFormat/stenosisPostTreat.mm

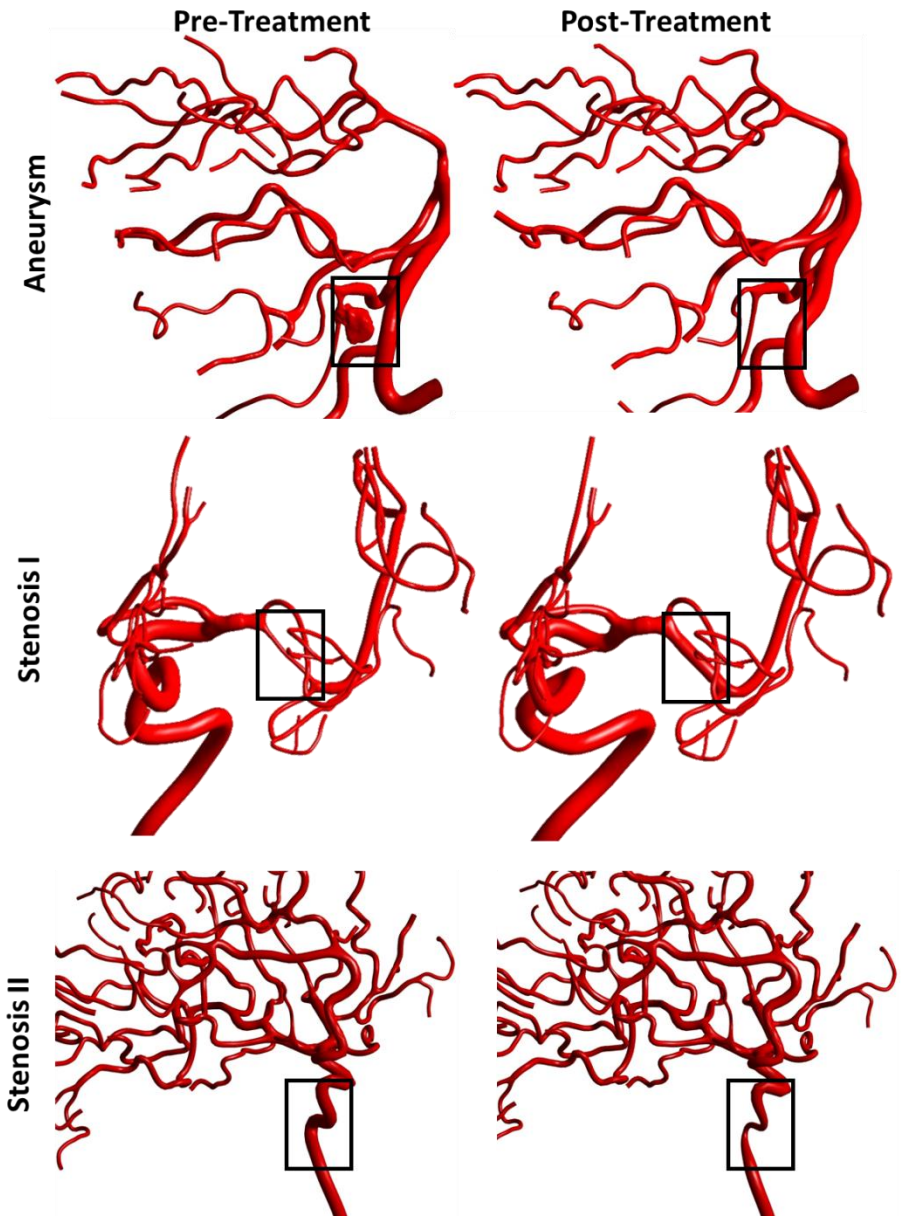

Figure 82. Visualization of the 3D computational model of the pathological cases in pre- and post-treatment.

7.4. Comparison of 1D-3D arterial blood flow simulation at steady state

This appendix summarizes the 1D-3D blood flow simulation for six cerebral arterial trees. Totally pressure was underestimated in 1D simulation. Geometric features of bifurcation and development of secondary flow generate on average 0.57 ± 7.60 percentage difference in flow field compared with 1D flow simulation.

7.4.1. 1D blood flow simulation results

In this study, we performed steady-state simulation of the 1D and 3D networks. We assumed a Dirichlet pressure boundary conditions of given 95 mmHg for outlets of RMCA, LMCA, RPCA, LPCA, RACA, LACA. We also assumed a flow inlet boundary condition of 200 mL/min for BA, RICA, and LICA segments.

For 1D simulation, we used the Hagen-Poiseuille Equations (62)-(63). We used the Point and Face matrix to get datasets of point connectivity for preserving conservation balance equations. The vascular resistance was calculated for each Face. The set of linear algebraic equations were solved in MATLAB R2013b.

$$\Delta P = F \ \alpha \tag{62}$$

$$\alpha = \frac{128\mu L}{\pi D^4} \tag{63}$$

Where ΔP here refers to the pressure drop, α is the resistance and F is the volumetric flow. μ is dynamic viscosity, D is the diameter of vessel and L is the length of the vessel.

Having the 1D Case and Network file, we performed the 1D simulation with the MATLAB code. For each subject, the inlet flow indices to assign inlet flow boundary conditions were used in the 1D simulation. Finally, results of the 1D simulate were saved as a new Case and Network

file with the inclusion of pressure and flow maps. 1D steady-state results can be visualized using "ViewerApplication.exe" executable software as shown in Figure 83.

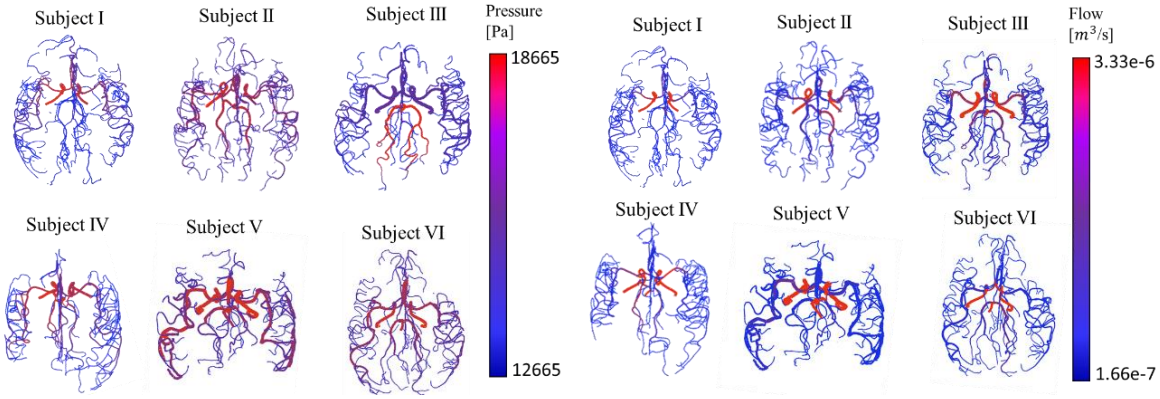

Figure 83. Pressure and flow field visualization of six cerebral arterial trees computed by 1D simulation.

Directory of 1D Case and Network files:

Directory:E:/Inventory/Subjects/##name/1D_3D_SteadyState/1D_Network/##.cs31 ##.nwk

Example: E:/Inventory/Subjects/NN/1D_3D_SteadyState/1D_Network/NN.cs31 NN.nwk

Directory of MATLAB code for 1D simulation:

Directory: E:/Inventory/Subjects/##name/1D_3D_SteadyState/1D_Matlab Code/##.m

Example: E:/Inventory/Subjects/NN/1D_3D_SteadyState/1D_Matlab Code/NN.m

Directory of 1D Simulation Results:

Directory:E:/Inventory/Subjects/##name/1D_3D_SteadyState/1D_Results/##.cs31 ##.nwk

Example: E:/Inventory/Subjects/NN/1D_3D_SteadyState/1D_Results//NN.cs31 NN.nwk

7.4.2. 3D blood flow simulation results

To perform 3D CFD simulation, we first generate the parametric meshes from the 1D Case and Network files. Then we import the "*.msh" files into the ICEM fluent to label the outlets in

RMCA, LMCA, RPCA, LPCA, RACA, LACA groups. Parametric meshes with the territorial labeled outlets are analyzed in ANSYS Fluent 18.1, the steady-state project is kept as "*.cas" file. The steady-state simulation results are exported as "*.dat" file. Finally, data files are analyzed in ANSYS CFD-Post to get the velocity streamline and pressure contour of cerebral vascular trees. Velocity streamlines of six cerebral arterial trees computed by 3D simulation are visualized in Figure 84. Figure 85 illustrates the pressure field of six cerebral arterial trees computed by 3D simulation.

To measure the flow of the vascular network, the operator should create several perpendicular planes to the vascular segment; small imprecision in the plane alignment will result in over-approximation of the blood flow. For this section, a code was written to calculate the point and the normal vector for the select vascular to get high-fidelity plane generation for 3D blood flow measurement.

Directory of 3D Parametric Structured Meshes:

Directory: E:/Inventory/Subjects/##name/1D_3D_SteadyState/3D_PRM mesh/##.msh

Example: E:/Inventory/Subjects/NN/1D_3D_SteadyState/3D_PRM mesh/NN.msh

Directory of 3D Simulation Results:

Directory: E:/Inventory/Subjects/##name/1D_3D_SteadyState/3D_Results/##.dat

Example: E:/Inventory/Subjects/NN/1D_3D_SteadyState/3D_Results/NN.dat

Directory of 3D ANSYS Fluent .cas File:

Directory: E:/Inventory/Subjects/##name/1D_3D_SteadyState/3D_Fluent/##.cas

Example: E:/Inventory/Subjects/NN/1D_3D_SteadyState/3D_Fluent/NN.cas

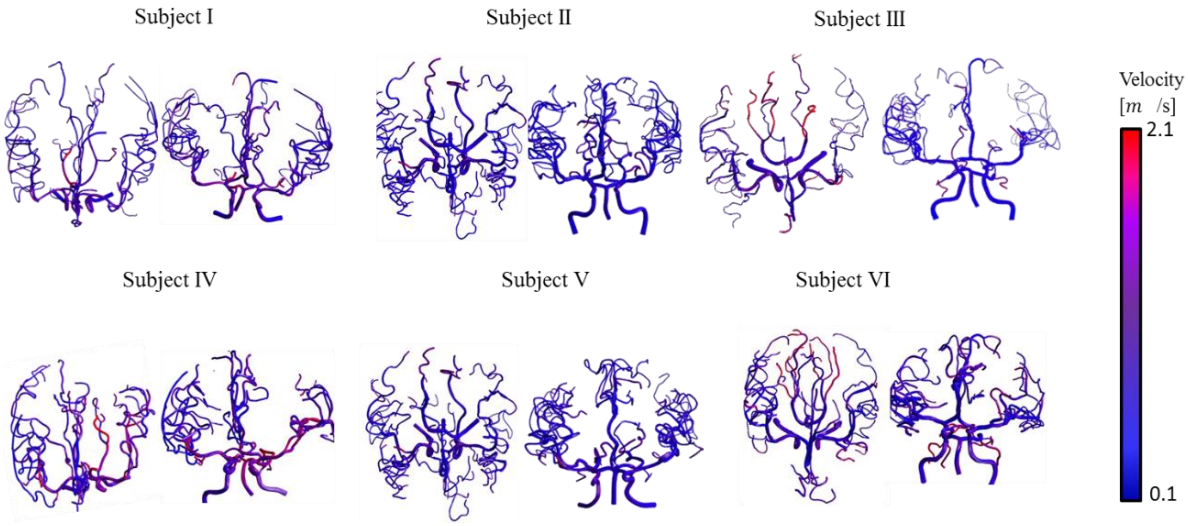

Figure 84. Velocity streamline of six cerebral arterial trees computed by 3D simulation.

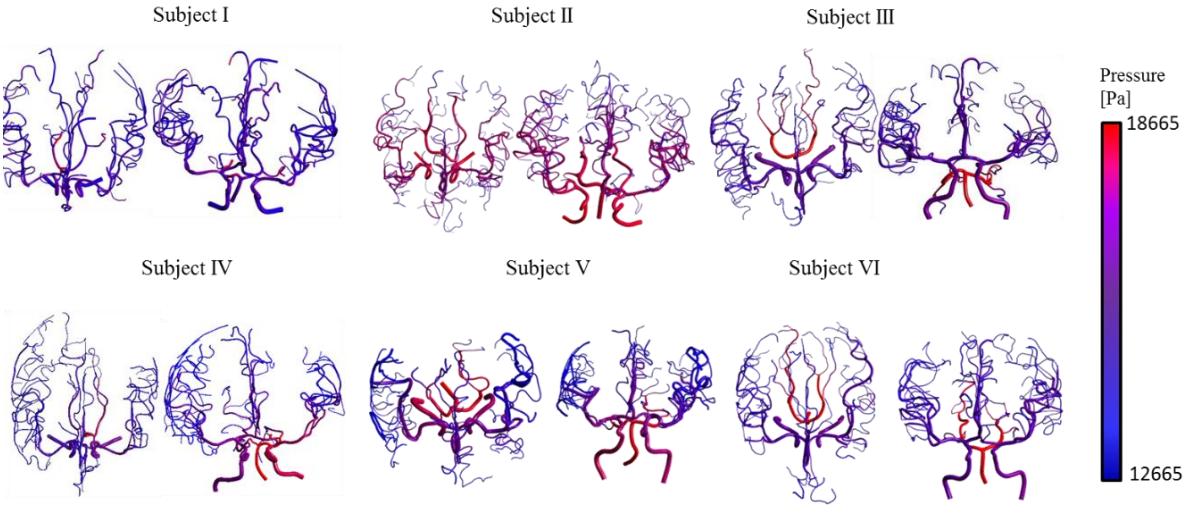

Figure 85. Pressure field of six cerebral arterial trees computed by 3D simulation.

7.4.3. Comparison of 1D and 3D simulation

In this section, we compared to pressure and flow value of the select faces of the inlet segment of vascular territories as shown in Figure 86. Table 37 to Table 45 summarize the comparison between 1D and 3D simulation for Subject I to Subject VI.

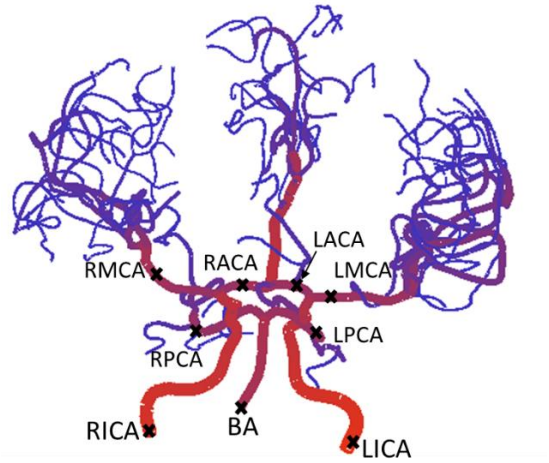

Figure 86. A sample of face numbers was used for 1D blood flow and pressure value acquisition. Pressure and a flow value of these select faces at the first segment of vascular territories RMCA, LMCA, RPCA, LPCA, RACA, LACA, as well as inflow segment of RICA, LICA, and BA are chosen for 1D-3D comparison.

Table 28. Flow and Pressure value of select faces between 1D and 3D hemodynamic simulation in different vascular territories for Subject I.

Region	#Face	1D simulation		3D Simulation	
		Pressure [mmHg]	Flow [mL/min]	Pressure [mmHg]	Flow [mL/min]
BA	155	130.66	200.00	159.87	200.00
RICA	101	133.07	200.00	158.78	200.00
LICA	33	127.89	200.00	134.90	200.00
RMCA	5001	125.92	116.15	140.30	110.40
LMCA	6102	121.12	133.88	122.25	148.16
RACA	4461	126.07	73.24	137.22	75.35
LACA	19098	120.86	66.12	119.88	80.91
RPCA	17951	116.20	148.52	118.63	159.79
LPCA	506	123.46	62.08	149.19	65.65

Table 29. Flow and Pressure comparison of select faces between 1D and 3D hemodynamic simulation in different vascular territories for Subject I.

Region	#Face	Flow comparison		Pressure comparison	
		Δf, mL/min $(F_{3D} - F_{1D})$	% Difference $\%(F_{3D} - F_{1D})/F_{3D}$	ΔP, mmHg $(P_{3D} - P_{1D})$	% Difference $\%(P_{3D} - P_{1D})/P_{3D}$
BA	155	0.00	0.00	29.22	18.28
RICA	101	0.00	0.00	25.72	16.20
LICA	33	0.00	0.00	7.02	5.20
RMCA	5001	-5.75	-5.21	14.38	10.25
LMCA	6102	14.29	9.64	1.13	0.92
RACA	4461	2.11	2.80	11.15	8.12
LACA	19098	14.78	18.27	-0.98	-0.82
RPCA	17951	11.27	7.05	2.42	2.04
LPCA	506	3.57	5.44	25.73	17.25

Table 30. Terminal points, faces, and simulated flow of all outlets based on 1D simulation for Subject I.

Terminal Point	Face Label	1D simulation Flow [mL/min]
18264	18095	19.95
18875	18707	5.24
5208	5148	3.29
5259	5199	20.72
4587	4533	3.84
3668	3617	9.04
6023	5960	3.77
18387	18221	15.94
21651	21490	120.22
6068	6005	2.72
6080	6017	5.88
18805	18639	9.00
3077	3032	11.58
6670	6598	13.98
9510	9413	8.55
4729	4673	4.81
3277	3231	8.08
7439	7363	0.82
7276	7200	7.88
17899	17731	4.73
19	18	8.32
6296	6231	4.96
4909	4849	2.06
8896	8806	6.97
8850	8760	0.63
6710	6638	1.23
6793	6721	1.18
5855	5794	19.59
6392	6325	1.90
7503	7421	4.60
5837	5776	4.77
8913	8823	4.97
7849	7800	3.26
12362	12252	7.41
8349	8262	7.21
10086	9983	14.50
9402	9306	9.48
13571	13443	6.14
11715	11608	9.00
10764	10660	22.77
11698	11591	3.70
10339	10236	12.70
13582	13454	20.60
20691	20532	6.07
16610	16455	4.80
16129	15978	9.30
11824	11715	14.43
12610	12501	6.54
16717	16562	5.96
14832	14691	2.53
12627	12529	25.38
12865	12749	6.03
15592	15445	1.97
15540	15393	2.23
10682	10578	7.49
12987	12870	8.40
12897	12780	12.09

9567	9469	22.18
16814	16658	6.14
14628	14494	3.21
10512	10408	17.12
20521	20360	2.12
17379	17214	2.20
21459	21301	5.96
15654	15506	11.97
21302	21144	2.36

Table 31. Flow and Pressure value of select faces between 1D and 3D hemodynamic simulation in different vascular territories for Subject II.

Region	#Face	1D simulation		3D Simulation	
		Pressure [mmHg]	Flow [mL/min]	Pressure [mmHg]	Flow [mL/min]
BA	1	116.94	200	116.93	200.00
RICA	13549	117.67	199.98	121.26	199.98
LICA	13597	121.48	200	117.64	200.00
RMCA	13947	114.67	200.33	115.22	200.33
LMCA	14113	111.49	114.84	111.41	111.44
RACA	4796	110.05	63.32	110.07	58.80
LACA	4770	109.90	43.79	110.14	46.62
RPCA	491	115.46	120.1	115.19	119.47
LPCA	743	115.05	64.53	114.11	64.39

Table 32. Flow and Pressure comparison of select faces between 1D and 3D hemodynamic simulation in different vascular territories for Subject II.

Region	#Face	Flow comparison		Pressure comparison	
		Δf, mL/min $(F_{3D} - F_{1D})$	% Difference $\%(F_{3D} - F_{1D})/F_{3D}$	ΔP, mmHg $(P_{3D} - P_{1D})$	% Difference $\%(P_{3D} - P_{1D})/P_{3D}$
BA	1	0.00	0.00	-0.01	-0.01
RICA	13549	0.00	0.00	3.59	2.96
LICA	13597	0.00	0.00	-3.85	-3.27
RMCA	13947	0.00	0.00	0.55	0.48
LMCA	14113	-3.40	-3.05	-0.08	-0.07
RACA	4796	-4.52	-7.69	0.01	0.01
LACA	4770	2.83	6.07	0.23	0.21
RPCA	491	-0.63	-0.53	-0.27	-0.24
LPCA	743	-0.14	-0.22	-0.94	-0.82

Table 33. Terminal points, faces, and simulated flow of all outlets based on 1D simulation for Subject II.

Terminal Point	Face Label	1D Simulation Flow [mL/min]
13777	13729	31.10
11	9	7.73
370	366	6.62
689	684	17.75
13974	13925	60.14
6	5	19.11
432	428	45.78
3877	3856	10.27
14407	14361	10.42
6512	6480	5.98
7804	7770	15.82
16583	6924	19.97
14603	14557	1.74
6233	6204	4.56
11689	11647	2.34
7830	7796	19.97
9160	9122	12.86
2012	1997	7.45
4053	4031	3.95
4217	4195	4.35
11440	11398	2.53
11504	11462	2.73
9222	9185	7.31
14159	14111	6.81
15225	15180	1.59
15089	15044	1.75
1178	1164	0.24
1317	1302	1.41
1482	1467	26.50
1485	1470	60.43
2786	2770	5.14
2969	2953	59.04
3118	3101	3.52
2421	2406	9.81
6059	6032	3.09
3337	3319	8.09
3562	3544	5.52
5106	5079	10.40
14604	14558	1.16
8622	8585	4.23
8756	8718	7.55
4610	4585	7.29
4660	4635	3.16
4695	4670	4.04
8999	8961	6.41
7437	7403	17.90
7744	7710	4.01
4465	4440	0.00
4465	4440	0.00
9373	9335	8.88
9479	9441	4.26
3915	3893	107.64
15226	15181	4.37
8457	8422	3.67
8309	8274	0.81
8139	8104	1.58
15843	15798	2.07

9719	9679	3.43
9714	9674	0.74
11285	11243	0.34
11289	11247	8.38
12092	12049	3.83
15629	15584	4.75
16085	16041	10.21
12031	11989	4.27
12244	12201	1.70
12127	12084	7.70
11114	11072	5.12
16251	16207	3.00
16514	16470	1.81
12982	12937	1.03
12706	12661	21.65
16515	16471	10.44
13486	13440	2.61
13595	13548	4.12

Table 34. Flow and Pressure value of select faces between 1D and 3D hemodynamic simulation in different vascular territories for Subject III.

Region	#Face	1D simulation		3D Simulation	
		Pressure [mmHg]	Flow [mL/min]	Pressure [mmHg]	Flow [mL/min]
BA	14	159.60	200.00	145.59	199.98
RICA	10283	119.12	200.00	116.07	199.98
LICA	1	119.35	200.00	116.49	199.98
RMCA	90	116.71	137.94	112.23	162.62
LMCA	957	116.65	133.40	113.37	117.52
RACA	181	116.44	62.13	113.04	62.90
LACA	955	116.97	66.65	113.03	59.50
RPCA	130	157.45	99.15	143.57	105.71
LPCA	158	157.16	100.91	143.57	98.16

Table 35. Flow and Pressure comparison of select faces between 1D and 3D hemodynamic simulation in different vascular territories for Subject III.

Region	#Face	Flow comparison		Pressure comparison	
		Δf, mL/min $(F_{3D} - F_{1D})$	% Difference $\%(F_{3D} - F_{1D})/F_{3D}$	ΔP, mmHg $(P_{3D} - P_{1D})$	% Difference $\%(P_{3D} - P_{1D})/P_{3D}$
BA	14	-0.02	-0.01	-14.01	-9.62
RICA	10283	-0.02	-0.01	-3.05	-2.63
LICA	1	-0.02	-0.01	-2.86	-2.46
RMCA	90	24.68	15.18	-4.48	-3.99
LMCA	957	-15.88	-13.51	-3.28	-2.89
RACA	181	0.77	1.22	-3.40	-3.01
LACA	955	-7.15	-12.01	-3.94	-3.49
RPCA	130	6.56	6.21	-13.88	-9.66
LPCA	158	-2.75	-2.80	-13.59	-9.46

Table 36. Terminal points, faces, and simulated flow of all outlets based on 1D simulation for Subject III.

Terminal Point	Face Label	1D Simulation Flow [mL/min]
10560	10468	71.46
2350	2320	10.97
2401	2371	18.50
1185	1169	43.40
10720	10627	55.67
2255	2227	79.09
13765	13671	3.05
7738	7657	3.85
13269	13176	6.63
8768	8680	12.20
6424	6352	6.84
2812	15911	6.84
7167	7089	8.47
7022	6945	6.64
14882	14786	6.66
1700	1681	4.50
5165	5104	6.62
11397	11303	2.56
2518	2488	4.54
11589	11495	5.85
4163	4109	4.95
6669	6594	16.81
5581	5520	11.12
13398	13305	11.63
11329	11236	4.46
2900	2859	24.61
12117	12023	12.90
5815	5754	7.29
12981	12887	10.23
5341	5280	9.85
13694	13601	4.45
6179	6108	50.81
8506	8418	12.09
8671	8583	13.47
15391	15295	7.99
7463	7382	9.14
9797	9707	5.64
16002	15906	5.66
9955	9865	15.75
10355	10265	3.62

Table 37. Flow and Pressure value of select faces between 1D and 3D hemodynamic simulation in different vascular territories for Subject IV.

Region	#Face	1D simulation		3D Simulation	
		Pressure [mmHg]	Flow [mL/min]	Pressure [mmHg]	Flow [mL/min]
BA	37	140.48	200.00	153.43	200.00
RICA	1	135.64	200.00	142.35	200.00
LICA	8720	125.61	200.00	136.88	200.00
RMCA	362	111.97	134.22	124.24	136.62
LMCA	257	117.15	150.11	122.56	143.18
RACA	279	98.46	48.38	109.64	54.39
LACA	243	98.36	64.77	105.54	67.24
RPCA	408	108.11	121.80	117.87	116.10
LPCA	939	125.44	80.35	138.67	84.60

Table 38. Flow and Pressure comparison of select faces between 1D and 3D hemodynamic simulation in different vascular territories for Subject IV.

Region	#Face	Flow comparison		Pressure comparison	
		Δf, mL/min $(F_{3D} - F_{1D})$	% Difference $\%(F_{3D} - F_{1D})/F_{3D}$	ΔP, mmHg $(P_{3D} - P_{1D})$	% Difference $\%(P_{3D} - P_{1D})/P_{3D}$
BA	37	0.00	0.00	12.95	8.44
RICA	1	0.00	0.00	6.71	4.71
LICA	8720	0.00	0.00	11.27	8.24
RMCA	362	2.40	1.75	12.27	9.87
LMCA	257	-6.93	-4.84	5.41	4.41
RACA	279	6.01	11.06	11.18	10.20
LACA	243	2.47	3.68	7.18	6.81
RPCA	408	-5.70	-4.91	9.76	8.28
LPCA	939	4.25	5.02	13.23	9.54

Table 39. Terminal points, faces, and simulated flow of all outlets based on 1D simulation for Subject IV.

Terminal Point	Face Label	1D simulation Flow [mL/min]
2406	2358	33.28
10194	10103	22.01
10512	10418	12.56
1825	1786	27.29
1989	1949	32.08
9676	9586	18.38
6251	6176	24.06
11710	11615	30.34
1180	1147	7.29
10230	10137	2.28
3065	3014	5.49
9997	9906	3.99
11205	11109	1.77
10779	10684	2.53
6757	6682	1.66
3989	4622	0.96
15504	15408	3.62
14330	14234	1.83
14680	14583	2.04
15384	15288	1.58
15077	14981	3.79
8009	7926	4.42
8227	8144	2.93
10898	10803	2.77
6098	6024	1.15
4647	4575	3.89
6979	6901	11.42
13848	13752	0.67
7623	7542	0.72
14439	14342	1.58
15670	15573	1.90
8787	8700	1.09
15669	15572	1.54
8672	8585	1.75
7410	7331	0.85
7263	7184	2.01
3563	3507	1.67
2632	2583	1.79
4409	4340	1.24
4233	4164	1.44
12157	12062	0.93
7786	7703	0.73
7694	7611	0.92
4019	3954	2.77
12158	12063	1.47
13060	12963	0.81
13262	13165	1.09
804	779	0.01

Table 40. Flow and Pressure value of select faces between 1D and 3D hemodynamic simulation in different vascular territories for Subject V.

Region	#Face	1D simulation		3D Simulation	
		Pressure [mmHg]	Flow [mL/min]	Pressure [mmHg]	Flow [mL/min]
BA	475	134.72	200.00	124.39	200.00
RICA	7129	119.13	200.00	117.07	200.00
LICA	8280	119.33	200.00	113.91	200.00
RMCA	4369	116.74	126.99	110.60	150.99
LMCA	3067	116.65	132.51	107.65	150.84
RACA	4360	116.92	78.63	109.35	69.52
LACA	3067	116.93	85.80	109.16	79.54
RPCA	8788	121.56	138.36	118.27	113.52
LPCA	2994	122.34	37.25	121.48	41.67

Table 41. Flow and Pressure comparison of select faces between 1D and 3D hemodynamic simulation in different vascular territories for Subject V.

Region	#Face	Flow comparison		Pressure comparison	
		Δf, mL/min $(F_{3D} - F_{1D})$	% Difference $\%(F_{3D} - F_{1D})/F_{3D}$	ΔP, mmHg $(P_{3D} - P_{1D})$	% Difference $\%(P_{3D} - P_{1D})/P_{3D}$
BA	475	0.00	0.00	-10.33	-8.30
RICA	7129	0.00	0.00	-2.06	-1.76
LICA	8280	0.00	0.00	-5.42	-4.76
RMCA	4369	23.99	15.89	-6.14	-5.55
LMCA	3067	18.33	12.15	-9.00	-8.36
RACA	4360	-9.11	-13.10	-7.57	-6.92
LACA	3067	-6.26	-7.87	-7.78	-7.12
RPCA	8788	-24.84	-21.88	-3.29	-2.78
LPCA	2994	4.42	10.61	-0.86	-0.71

Table 42. Terminal points, faces, and simulated flow of all outlets based on 1D simulation for Subject V.

Terminal Point	Face Label	1D simulation Flow [mL/min]
7024	6912	8.46
6499	6387	8.79
11031	10916	4.64
4550	4462	18.60
5477	5381	25.78
8542	8424	1.88
3653	3577	2.12
3833	3757	1.59
5	11340	10.54
625	609	2.55
3460	3382	1.69
1760	1710	1.09
8996	8879	1.16
2576	2512	9.94
2633	2568	24.27
6059	5949	2.23
6632	6521	17.66
5557	5457	2.73
6750	6639	3.04
6203	6093	0.95
7235	7123	20.06
7226	7112	0.69
11438	11392	4.07
8037	7919	1.03
66	59	8.59
1371	1337	1.93
6362	6252	2.01
3010	2937	1.29
3	488	1.74
2840	2773	0.23
1946	1892	0.16
11166	11050	2.34
5202	5109	1.20
173	162	1.51
5765	5658	2.13
2483	2426	2.39
4360	4275	1.85
9555	9439	6.89
9757	9640	0.71

Table 43. Flow and Pressure value of select faces between 1D and 3D hemodynamic simulation in different vascular territories for Subject VI.

Region	#Face	1D simulation		3D Simulation	
		Pressure [mmHg]	Flow [mL/min]	Pressure [mmHg]	Flow [mL/min]
BA	37	160.48	200.00	206.40	200.00
RICA	1	121.64	200.00	139.15	200.00
LICA	8720	142.61	200.00	147.20	200.00
RMCA	362	118.97	131.33	131.31	136.62
LMCA	257	108.15	149.20	137.06	143.18
RACA	279	118.46	63.66	131.60	54.39
LACA	243	112.36	63.80	134.66	67.24
RPCA	408	158.11	112.14	201.98	116.10
LPCA	939	158.44	79.86	203.59	84.60

Table 44. Flow and Pressure comparison of select faces between 1D and 3D hemodynamic simulation in different vascular territories for Subject VI.

Region	#Face	Flow comparison		Pressure comparison	
		Δf, mL/min $(F_{3D} - F_{1D})$	% Difference $\%(F_{3D} - F_{1D})/F_{3D}$	ΔP, mmHg $(P_{3D} - P_{1D})$	% Difference $\%(P_{3D} - P_{1D})/P_{3D}$
BA	37	0.00	0.00	45.92	22.25
RICA	1	0.00	0.00	17.51	12.59
LICA	8720	0.00	0.00	4.60	3.12
RMCA	362	5.28	3.87	12.34	9.40
LMCA	257	-6.02	-4.21	28.91	21.09
RACA	279	-9.28	-17.05	13.14	9.98
LACA	243	3.44	5.12	22.31	16.56
RPCA	408	3.96	3.41	43.87	21.72
LPCA	939	4.74	5.61	45.15	22.18

Table 45. Terminal points, faces, and simulated flow of all outlets based on 1D simulation for Subject VI.

Terminal Point	Face Label	1D simulation Flow [mL/min]
2406	2358	33.28
10194	10103	22.01
10512	10418	12.56
1825	1786	27.29
1989	1949	32.08
9676	9586	18.38
6251	6176	24.06
11710	11615	30.34
1180	1147	7.29
10230	10137	2.28
3065	3014	5.49
9997	9906	3.99
11205	11109	1.77
10779	10684	2.53
6757	6682	1.66
3989	4622	0.96
15504	15408	3.62
14330	14234	1.83
14680	14583	2.04
15384	15288	1.58
15077	14981	3.79
8009	7926	4.42
8227	8144	2.93
10898	10803	2.77
6098	6024	1.15
4647	4575	3.89
6979	6901	11.42
13848	13752	0.67
7623	7542	0.72
14439	14342	1.58
15670	15573	1.90
8787	8700	1.09
15669	15572	1.54
8672	8585	1.75
7410	7331	0.85
7263	7184	2.01
3563	3507	1.67
2632	2583	1.79
4409	4340	1.24
4233	4164	1.44
12157	12062	0.93
7786	7703	0.73
7694	7611	0.92
4019	3954	2.77
12158	12063	1.47
13060	12963	0.81
13262	13165	1.09
804	779	0.01

We also perform a comparison between 1D, 3D and measured flow using NOVA software for Subject I. In this study, we used validated 3D simulation analysis with NOVA measured blood flow as shown in Figure 52. Territorial outlets of 1D network were categorized in RMCA, LMCA, RACA, LACA, RPCA and LPCA to assign the proper boundary conditions as listed in Table 46. Then, we compared 1D and 3D blood flow with NOVA measured blood flow. 3D blood flow showed on average -0.28±2.57 percentage difference with NOVA measured blood flow. However, 1D simulated blood flow were on average -2.90±20.6 percentage difference with NOVA measured blood flow.

Table 46. Boundary conditions used for 3D and 1D simulation of Subject I.

Region	Pressure Outlet	Velocity Inlet
	Pressure [mmHg]	Flow [mL/min]
BA	-	109
RICA	-	232
LICA	-	167
RMCA	100	-
LMCA	88	-
RACA	80	-
LACA	81	-
RPCA	112	-
LPCA	92	-

Table 47. Flow and Pressure value of select faces of 1D and 3D hemodynamic simulation as well as NOVA measurement in different vascular territories for Subject I.

Region	#Face	3D simulation		1D Simulation		NOVA
		Pressure [mmHg]	Flow [mL/min]	Pressure [mmHg]	Flow [mL/min]	Flow [mL/min]
BA	14	127.41	109.00	148.94	109.01	109
RICA	10283	135.28	232.00	173.19	232.00	232
LICA	1	113.15	167.00	125.93	167.00	167
RMCA	90	127.66	103.89	152.95	100.17	102
LMCA	957	107.65	100.71	116.24	101.62	102
RACA	181	126.45	109.49	147.22	88.41	112
LACA	955	106.93	66.29	113.22	85.79	68
RPCA	130	121.23	64.64	130.52	81.26	63
LPCA	158	120.87	62.98	116.26	52.16	61

Table 48. Flow and Pressure comparison of select faces of 1D and 3D hemodynamic simulation with NOVA measurements in different vascular territories for Subject I.

Region	Flow comparison 3D-Nova		Flow comparison 1D-Nova	
	Δf [mL/min] $(F_N - F_{3D})$	% Difference $\%(F_N - F_{3D})/F_N$	Δf [mL/min] $(F_N - F_{1D})$	% Difference $\%(F_N - F_{1D})/F_N$
BA	0.00	0.00	-0.01	-0.01
RICA	0.00	0.00	0.00	0.00
LICA	0.00	0.00	0.00	0.00
RMCA	-1.89	-1.86	1.83	1.80
LMCA	1.29	1.27	0.38	0.38
RACA	2.51	2.24	23.59	21.06
LACA	1.71	2.51	-17.79	-26.16
RPCA	-1.64	-2.61	-18.26	-28.99
LPCA	-1.98	-3.24	8.84	14.50

7.4.4. Discussion and Future work

The average of percentage error for pressure field is 3.56 ± 8.89. Totally pressure drop was underestimated in 1D simulation compared with 3D simulation, which may be due to secondary flow ignorance in the 1D simulation.

Average of all percentage error for flow field is 0.57 ± 7.60. In 3D simulation, the geometric feature of bifurcation plays important role in blood flow distribution. These features are not considered in the 1D simulation. For example, the topology of the bifurcation of communicating arteries highly affects the blood distribution in CoW. The maximum deviations of flow rate were found about 21% for Subject V. Subject II had the minimum average percentage error of -0.60 ± 3.57 and -0.08 ± 1.59 for flow and pressure field, respectively. This subject lack A1 branch and RPcoM. Such incomplete Circle of Willis may create this close 1D-3D results.

Hemodynamic indices such as wall shear stress, are highly sensitive to the vascular geometry. For example, T-shape (near-perpendicular) bifurcation topology highly affect the WSS patterns and generates the oscillation of wall shear stress vectors on the surface. Such important geometrical features are not taken into consideration for 1D hemodynamic simulation.

In addition, cerebral arteries with high-tortuosity generate secondary flow which results in cross-sectional pressure difference in these vessels. Due to the curvature, local pressure gradient created by the centrifugal force acts on the blood. Therefore, initially, blood at the center of the wall moves towards the outer wall and later it comes back to outer wall thereby creating double spiral secondary flow field. Secondary flow affects the pulsatility index of the blood flow and it can only be visualized in 3D blood flow simulation.

1D, 3D, and NOVA comparison. 3D blood flow showed on average -0.28$\pm$2.57 percentage difference with NOVA measured blood flow. However, 1D simulated blood flow was on average -2.90$\pm$20.6 percentage difference with NOVA measured blood flow. The difference between 1D and 3D flow map showed us that the 1D simulation is a suitable tool to get an initial guess for pressure boundary condition assignment for 3D simulation. However, additional slight changes are necessary to perfectly match 3D with NOVA measurements

We require multiple software to accomplish 3D blood flow simulation. Especially, CFD-Post takes reasonable time for blood flow and pressure map generation. Thanks to sparse matrix setting, 1D simulation is fast and does not require a skilled operator for flow and pressure visualization. However, 3D simulation accounts for all geometrical features and secondary flow development, which generate a more realistic simulation of vascular tree. Therefore, 1D simulation is a suitable substitution for an initial guess of flow distribution to estimate correct boundary condition assignment.

Territorial labeling of the vascular network should be automated in future studies. Here we only analyzed and compared the steady-state simulation, transient simulation with NOVA results should be addressed in 1D simulation as well.

In this study, we used a constant velocity for inlet boundary condition of the 3D simulation. Future works can improve the simulation by inserting parabolic velocity profile for inlets boundary conditions.

VITA

NAME: Mahsa Ghaffari

EDUCATION: B.S., Biomedical Engineering, Azad University, Tehran, Iran, 2010

M.S., Biomedical Engineering, Amirkabir University of Technology, 2012

Ph.D., Bioengineering, University of Illinois at Chicago, 2018

HONORS: Provost-Deiss Scholarship, University of Illinois at Chicago, Illinois, 2016.

Travel Presenter Award, 25th European Stroke Conference, Venice, 2016.

The best Master research award, Tehran Polytechnics, 2013.

PUBLICATIONS: M. Ghaffari, A. Alaraj, X. Du, X. Zhou, F. Charbel, A. Linninger. "Quantification of near-wall hemodynamic risk factors in large-scale cerebral arterial trees" International Journal of Numerical methods in Biomedical Engineering, 2018.

M. Ghaffari, K. Tangen, A. Alaraj, X. Du, F. Charbel, A. Linninger. "Large-scale subject-specific cerebral arterial tree modeling using automated parametric mesh generation for blood flow simulation" Computers in Biology and Medicine, 91, 353-365, 2018.

M. Ghaffari, C. Hsu, A. Linninger. "Automatic reconstruction and generation of structured hexahedral mesh for non-planar bifurcations in vascular network." Computer Aided Chemical Engineering, 37, 2015,

C. Hsu, M. Ghaffari, A. Alaraj, Flannery X J Zhou, A. Linninger, "Gap-free segmentation of vascular networks with automatic image processing pipeline," Computers in Biology and Medicine, 82, 29–39, 2017.

C. Hsu, B. Schneller, M. Ghaffari, A. Alaraj and A. Linninger, "Medical Image Processing for Fully Integrated Subject Specific Whole Brain Mesh Generation." Technologies, 3(2), 126-141, 2015.

M. Sheikholeslami, M. Ghaffari, et al. "Site-Dependence Scalp Cooling System to Prevent Hair Loss during Chemotherapy", Journal of Bioengineering & Biomedical Science 5 (2), 2015.

M. Ghaffari, M. Rostami, M. Zoghi, N. Abolfathi "Fluid Structure Interaction of Traumatic Brain Injury: Effects of Material Properties on SAS Trabeculae", Journal of Modern Engineering, 14(2), 2014.

M. Ghaffari, M. Rostami, M. Zoghi, N. Abolfathi "A new approach to model subarachnoid trabeculae resistance in cerebrospinal fluid flow", IEEE, ICBME , 2012.

M. Ghaffari, R. Nickmanesh, N. Tamanaee, F. Farahmand "The impingement-dislocation risk of total hip replacement: Effect of cup orientation and patient maneuvers", IEEE EMBS, 2012.

Conferences: M Ghaffari , C Hsu , A Alaraj , A Linninger, "Cerebral hemodynamic changes after angioplasty of intracranial stenosis", 28th Symposium on Cerebral Blood Flow, Metabolism and Function 13th Conference on Quantification of Brain Function with PET.

M Ghaffari, C Hsu, B Schnellera, X J Zhoub, A Alaraj, A. Linninger "Automatic and patient-specific reconstruction of the cerebral vasculature, CSF spaces and parenchyma for hemodynamic assessment of vascular pathologies" Stroke conference Vienna.

M Ghaffari, C Hsu, A Alaraj, A. Linninger, "Hemodynamic simulation of the patient-specific cerebral blood flow towards a personalized surgical planning for vascular disorders"

M Ghaffari, A Alaraj, A. Linninger, "Subject-specific simulation of entire cerebral arterial tree: implementation of automatic parametric mesh generation". SB3C2016 Summer Biomechanics, Bioengineering and Biotransport Conference

M Ghaffari, C Hsu, A Alaraj, A. Linninger, "Computational Fluid Dynamics for Flow Assessment in Digital Subtraction Angiography" XXVIIthInternational Symposium of Cerebral Blood Flow, Metabolism and Function XIIthInternational Conference on Quantification of Brain Function with PET June 27th-30th2015, Vancouver, Canada

M Ghaffari, N. Gascuel, A. Alaraj, A. Linninger, "Hemodynamic Simulation of Intracranial arteries." 2015 UIC College of Medicine Research Forum